2009

Integrated Servomechanism And Process Control For Machining Processes

Yan Tang
University of Central Florida

INTEGRATED SERVOMECHANISM AND PROCESS
CONTROL FOR MACHINING PROCESSES

by

YAN TANG
B.S. NANJING UNIVERSITY OF SCIENCE & TECHNOLOGY, 1995
M.S. NANJING UNIVERSITY OF SCIENCE & TECHNOLOGY, 1999

A dissertation submitted in partial fulfillment of the requirements
for the degree of Doctor of Philosophy
in the Department of Mechanical, Materials, and Aerospace Engineering
in the College of Engineering and Computer Science
at the University of Central Florida
Orlando, Florida

Summer Term
2009

Major Professor: Chengying Xu

ABSTRACT

In this research, the integration of the servomechanism control and process control for machining processes has been studied. As enabling strategies for next generation quality control, process monitoring and open architecture machine tools will be implemented on production floor. This trend brings a new method to implement control algorithm in machining processes. Instead of using separate modules for servomechanism control and process control individually, the integrated controller is proposed in this research to simultaneously achieve goals in servomechanism level and the process level.

This research is motivated by the benefits brought by the integration of servomechanism control and process control. Firstly, the integration simplifies the control system design. Secondly, the integration promotes the adoption of process control on production floor. Thirdly, the integration facilitates portability between machine tools. Finally, the integration provides convenience for both the servomechanism and process simulation in virtual machine tool environment.

The servomechanism control proposed in this research is based on error space approach. This approach is suitable for motion control for complex contour. When implement the integration of servomechanism control and process control, two kinds of processes may be encountered. One is the process whose model parameters can be aggregated with the servomechanism states and the tool path does not need real time offset. The other is the process which does not have direct relationship with the servomechanism states and tool path may need to be modified real time during machining. The integration strategies applied in error space are proposed for each case. Different integration strategies would propagate the process control goal

into the motion control scheme such that the integrated control can simultaneously achieve goals of both the servomechanism and the process levels.

Integrated force-contour-position control in turning is used as one example in which the process parameters can be aggregated with the servomechanism states. In this case, the process level aims to minimize cutting force variation while the servomechanism level is to achieve zero contour error. Both force variation and contour error can be represented by the servomechanism states. Then, the integrated control design is formulated as a linear quadratic regulator (LQR) problem in error space. Force variation and contour error are treated as part of performance index to be minimized in the LQR problem. On the other hand, the controller designed by LQR in error space can guarantee the asymptotic tracking stability of the servomechanism for complex contour. Therefore, the integrated controller can implement the process control and the servomechanism control simultaneously.

Cutter deflection compensation for helical end milling processes is used as one example in which the process cannot be directly associated with the servomechanism states. Cutter deflection compensation requires real-time tool path offset to reduce the surface error due to cutter deflection. Therefore, real time interpolation is required to provide reference trajectory for the servomechanism controller. With the real time information about surface error, the servomechanism controller can not only implement motion control for contour requirement, but also compensation for the dimensional error caused by cutter deflection. In other words, the real time interpolator along with the servomechanism controller can achieve the goals of both the servomechanism and process level.

In this study, the cutter deflection in helical end milling processes is analyzed first to illustrate the indirect relationship between cutter deflection and surface accuracy. Cutter

deflection is examined for three kinds of surfaces including straight surface, circular surface, and curved surface. The simulation-based deflection analysis will be used to emulate measurement from sensors and update the real-time interpolator to offset tool path. The controller designed through pole placement in error space can guarantee the robust tracking performance of the updated reference trajectory combining both contour and tool path offset required for deflection compensation. A variety of cutting conditions are simulated to demonstrate the compensation results.

In summary, the process control is integrated with the servomechanism control through either direct servomechanism controller design without tool path modification or servomechanism control with real time interpolation responding to process variation. Therefore, the process control can be implemented as a module within machine tools. Such integration will enhance the penetration of process control on production floor to increase machining productivity and product quality.

To: my parents Wang Lizhen and Tang Zhenyu,

my husband Wu Xuan,

and my daughter Wu Ruohan.

ACKNOWLEDGMENTS

I would like to acknowledge and extend my sincere gratitude to my advisor Dr. Chengying Xu. Her guidance, patience, and continuous support have helped me go through the most difficult stage during completing the research. I am deeply influenced by her passion, commitment, and endurance. My appreciation also goes to Dr. Robert Landers for bringing me into the machining control research area. I should also thank Dr. Alexander Leonessa for his continuous support and encouragement. I am very fortunate to receive guidance from them.

Besides my advisors, I would like to thank the rest of my dissertation committee, Dr. Chi-Kuo Lin, Dr. Aravinda Kar, and Dr. Quanfang Chen, for spending time reviewing the manuscript. Their valuable insights have helped me to think through research problems from different perspectives. My thanks also go to Dr. Wang Jing, Dr. Marc Compere, Dr. Omar Omar, Dr. Anil Srivastava, and Dr. Mark Jackson, for their helpful discussions and suggestions.

I gratefully acknowledge the financial support from Department of Mechanical, Materials, and Aerospace Engineering (MMAE) through teaching assistantship, and I^2lab through I^2lab fellowship.

My appreciation also goes to all MMAE staff for their assistance throughout my study.

I owe many thanks to my colleagues at Reconfigurable Intelligent System Engineering (RISE) lab for interesting discussions and making RISE a wonderful workplace.

Additionally, I would like to thank all my friends who have being an important part in my life during my stay at UCF over the years, especially to Dong Mi, Wang Qing, Shi Zheng, Dr. Liu Miao, Dr. Lou Lifang, Lv Jian, Sun Shan, Yang Boyi, Wang Xuexin, Jia Hongwei. Dr. Yang

TABLE OF CONTENTS

LIST OF FIGURES

LIST OF TABLES

CHAPTER 1 INTRODUCTION

1.1 <u>Background and Motivation</u>

Machining productivity and product quality are essential winning factors for manufacturers facing fierce global competition. The sustaining competitiveness requires high performance machine tools, efficient process planning, and effective quality control. Machine tools and process planning have overseen revolutionary changes brought by rapid development in servomechanism control and information technology. Quality control, however, still utilizes traditional methods, *i.e. pre-process* Taguchi design method and *post-process* statistical process control (SPC) [1]. Next generation of quality control requires *in-process* monitoring and control to eliminate expensive SPC. Although in-process quality control has obvious advantage, its adoption in current industry practice is limited due to lack of process measuring techniques and open architecture machine tools [1, 2]. With the increasing demand on flexibility, adaptability and reconfiguration of manufacturing processes, process monitoring and open architecture machine tools will become indispensable in next generation manufacturing. This trend will enable in-process monitoring and control to increase productivity, improve quality, and relax design constraints [2].

The implementation of process monitoring and open architecture machine tools will improve the productivity of traditional Computer Numerical Control (CNC) machine tools, which usually work on fixed cutting conditions programmed before machining. The cutting conditions in CNC machine tools are typically programmed by operators based on design criterions and operators' knowledge about cutting processes, and conservative values are usually chosen to avoid cutter breakage or other rare severe situations. Therefore, CNC machine tools do not work at their potentials, and productivity is reduced. The productivity of CNC machine tools

1

can only be improved by optimizing cutting conditions during machining, which is implemented by sensor-based process control. Due to lack of in-process monitoring and the closed architecture of CNC machine tools, process control is only studied in laboratory settings. The trend of adopting process monitoring and open architecture machine tools will enable process control on production floor.

Although process control is not widely used in industry, tremendous research on process control has been conducted mainly at university research labs. By manipulating process variables (such as feed, speed, depth-of-cut) during machining, process controller can regulate the cutting process (such as cutting forces variation, chip formation, and chatter etc.) to maximize the productivity and quality. Research activities on process control have generated promising results to demonstrate technical and economic advantages of process results. On the other hand, servomechanism control is another research focus in machining control. The goal of servomechanism control is to improve the speed and precision of feed drives to meet demanding requirements of high-speed machining.

Although both process control and servomechanism control are essential to improve outcomes of machining processes, these technologies are not tightly integrated. The separation is partly due to the closed architecture of CNC machine tools which do not provide interface interacting with external controllers for process control. Therefore, the process controller, the module functioning outside the servomechanism controller, sends control signals (such as reference feedrate or depth-of-cut) to the interpolator to regenerate the reference trajectory, which is the input to the servomechanism controller. Such separation will cause problems in reliability due to interactions between subsystems. Given the flexibility offered by open architecture machine tools, users can integrate the process control module with the

servomechanism controller such that the resulting controller can simultaneously regulate both process phenomena and feed drives.

The integration of servomechanism control and process control is motivated by the following reasons. Firstly, the integration simplifies the control system design. Instead of designing two control systems, one integrated control could simultaneously achieve goals of two systems. Secondly, the integration promotes the adoption of process control in industry practice. With the integration, process control becomes a bundled function of machine tools, rather than a module installed separately in machining processes. It will eliminate the extra effort for installation and learning. Thirdly, the integration facilitates portability between different machine tools. Portability is referred to the ability of modules in machining tools to operate on different hardware platforms, and it is one of requirements for open architecture machine tools. Instead of considering portability for two control systems, one integrated system relaxes the design constraints on portability. Four, the integration provides convenience for both servomechanism and process simulation in virtual machine tool environment. Virtual machine tool technology could save time and cost for machine tool builders by utilizing virtual prototyping, and it is essential for modern machine tool development. Virtual machine tool should simulate not only the process phenomena, but also the rigid body motion of the machine tool [3]. The integration simplifies the system composition, and therefore straights out the cause-effect relationship between the controller and the machining process together with feed drive dynamics, which is easier for simulation in the virtual machine tool.

In order to make use of advantage brought by process monitor and open architecture machine tools in the intelligent manufacturing environment, this dissertation research aims to study the integration of servomechanism control and process control for machining processes.

The integration is expected to bundle process control function with machine tools, and simplify the control system design for machining processes. The proposed integration scheme provides a new paradigm for control system design for the forthcoming open architecture machine tools. The ultimate goal is to enhance the penetration of process control as next generation quality control scheme to improve machining productivity and product quality.

1.2 Problem Statement and Research Objectives

The goal for servomechanism control is to reduce the axis position errors and the contour error in machining processes [4]. Error space approach is an effective motion control for complex contour [5], and therefore it is adopted in this study for the servomechanism control. On the other hand, the process control has a variety of goals depending on which process is controlled. In general, the process control is to make full use of production capability of machine tools to improve productivity and quality. Machining processes can be grouped to two categories. One is the process whose model parameters can be aggregated with the servomechanism states and the tool path does not need real time offset. The other is the process which does not have direct relationship with the servomechanism states and the tool path needs to be changed real time during machining. In this study, we aim to combine the error-space-based servomechanism control with process control for these two kinds of processes. Different integration strategies would propagate the process control goal into the servomechanism control design such that the integrated control can simultaneously achieve goals of both the servomechanism and the process levels.

Integrated force-contour-position control in turning is used as one example in which the process parameters can be aggregated with the servomechanism states. In this case, the process level aims to minimize cutting force variation while the servomechanism level is to achieve zero contour error. Both force variation and contour error can be represented by the servomechanism states. Then, the integrated control design is formulated as a linear quadratic regulator (LQR) problem in error space. Force variation and contour error are treated as part of performance index to be minimized in the LQR problem. On the other hand, the controller designed by LQR in error space can guarantee the asymptotic stability of the servomechanism for complex contour.

5

Therefore, the integrated controller can implement the process control and the servomechanism control simultaneously.

Cutter deflection compensation for helical end milling processes is used as one example in which the process cannot be directly associated with the servomechanism states and real time interpolation is required. In order to compensate for surface error due to cutter deflection, real time interpolation is applied to change the interaction between the cutter and the workpiece. With the real time information about surface error, the servomechanism controller can not only implement motion control for contour requirement, but also compensate for the dimensional error caused by cutter deflection. In other words, the servomechanism controller requires reference trajectory updated by the real time interpolator to achieve the goals of both the servomechanism and process level. In this study, the cutter deflection in helical end milling processes is analyzed first to illustrate the indirect relationship between cutter deflection and surface accuracy. The simulation-based analysis will be used to emulate measurement from sensors. The real time interpolation scheme, considering both part geometry and surface error due to cutter deflection, is developed to offset tool path. The controller designed through pole placement in error space can guarantee the robust tracking performance of the updated reference trajectory combining both contour and tool path offset required for deflection compensation.

In summary, the dissertation aims to study the integration of servomechanism control and process control to simplify control system design for machining processes. Two kinds of processes are addressed for such integration study. One is the process whose model parameters can be aggregated with the servomechanism states directly and the tool path does not require real time offset. The other is the process which does not have direct relationship with the

servomechanism states and the tool path needs real time offset to compensate for the process

error. Simulation studies are conducted to demonstrate the effectiveness of proposed solutions.

1.3   <u>Dissertation Outline</u>

The dissertation is organized as follows.

Chapter 1 lays out the background and motivation for the research. Literature review in Chapter 2 presents current research in servomechanism control and process control for machining processes to provide the research background and highlight the necessity of the integration. Further, since force control and cutter deflection are two processes to be addressed in this study, research activities in these two areas are also reviewed to illustrate the unique contribution of the proposed research.

In chapter 3, direct integration of servo-contour-force control is formulated through hierarchical optimal control methodology. The aggregation of process (cutting forces) parameters with servomechanism states is built such that the servomechanism controller can simultaneously regulate axis positions, contour, and cutting forces. The simulation studies demonstrate the effectiveness of the proposed integration scheme.

Chapter 4 and chapter 5 address how to integrate servomechanism control and process control for processes which are not directly related to servomechanism states. Helical end mill deflection compensation problem is raised as one example for such case. The resulting controller is expected to provide motion control along with deflection compensation to reduce surface error due to deflection. The controller is designed through two steps. In chapter 4, cutter deflection is analyzed, and the surface error due to deflection is simulated to show indirect relationship between surface accuracy and servomechanism states. Since deflection is compensated by offsetting tool path online, corresponding interpolation scheme is proposed to address both contour requirement and tool path offset. The simulation also serves as to emulate sensor measurements for real time interpolation. In chapter 5, the interpolation scheme is proposed for

three kinds of workpiece surface, including straight surface, circular surface, and the free-form surface. Simulations over a variety of cutting conditions are conducted to demonstrate the compensation performance. Conclusions and suggestions for future work conclude the dissertation in Chapter 6.

CHAPTER 2 LITERATURE REVIEW

2.1   Servomechanism and Process Control

Machine tool controls can be generally classified into three categories including servomechanism control, interpolation, and process control. The servomechanism control is to reduce the axial position errors and the contour errors in machining processes with the existence of adverse disturbances such as friction, backlash, and machining forces, etc [6, 7]. The interpolator is to coordinate multiple axes to maintain a specified tool path and orientation [8]. The process control is the automatic adjustment of process parameters in order to increase operation productivity and part quality. The servomechanism control and the interpolator have been integrated into today's machine tools, while process control has rarely found application in industry. These functions form a hierarchical structure of machine tools as shown in Figure 1.
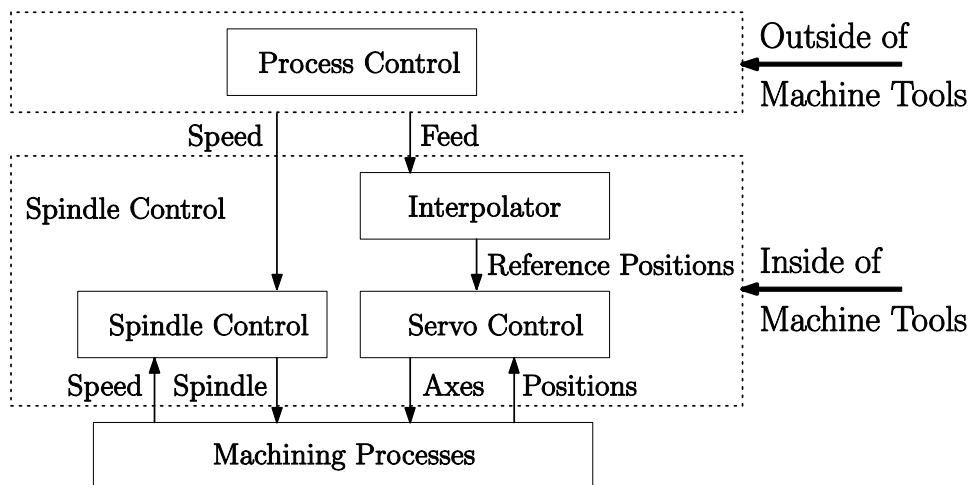
Figure 1 Hierarchical Structure of Machine Tool Controls

The control of single axes has been well–researched for many decades. Many comprehensive controllers are investigated to reduce in the position errors of each individual axis and consequently the contour error [9-14]. Another approach is to utilize a feedforward controller (such as Zero Phase Tracking Error Control (ZPTEC)) to compensate for the axial

position errors [15-19]. For example, in the ZPTEC technique, feedback and feedforward controllers are utilized to achieve good tracking and zero phase error between the reference and the output. This technique has been applied to complex contours [20] and was extended to time–varying, uncertain systems via the integration of adaptive techniques [21]. The issues involved in servomechanism motion control are reviewed in Ellis and Lorenz [22]. These two approaches intend to reduce contour error indirectly by drive the individual axis errors to zero. On the contrary, cross coupling control intends to reduce the contour error to zero directly [6, 23-25]. In this methodology, an additional algorithm is added to the control architecture that, based on the contour error, calculates offsets for each servomechanism control signal. Typically, cross coupling control design does not take the individual servomechanism controllers into account. In a recent work by Landers and Balakrishnan [26], hierarchical optimal control techniques were utilized to integrate servomechanism and contour control for two–axis motion control systems.

Force control is a commonly applied process control. Constant machining forces can prevent tool breakage and increase productivity. Fixed-gain controllers were used at early work in machining force control [27]. However, the system performance and stability is problematic when there exist variations in processes. As a result, adaptive machining control is required to maintain the performance over a variety of cutting conditions [28]. In the adaptive machining force control methodology, model parameters are estimated on–line and control gains adjusted to maintain stability over a wide range of parameter variations. Although adaptive controllers can address the problems encountered by fixed-gain controllers, the systems are complex to design, and have rare acceptance in industry.

Another popular method is robust machining force control [29] where, given bounds on model parameter variations, robust control techniques are utilized. The robust methodology was

extended in Kim *et al*. [30], which decreased model uncertainty by directly accounting for known process parameter variations. Other types of machining force control techniques include log transform [31], nonlinear with process compensation [32], neural network [33], and fuzzy logic [34]. A review of model–based techniques is given in Landers *et al*. [35]. In a recent work by Pandurangan *et al*. [36], hierarchical optimal control techniques were used to integrate machining force and servomechanism position control in a lathing operation. However, contour control was not incorporated into the methodology and only simple contours were considered.

As shown in Figure 1, the process control is not integrated with machine tools. Such separation will increase the complexity of machine tool control systems, and may affect the reliability. It is intended to design a control system within machine tools to simultaneously achieve goals of process level and the servo level. Such integration will enhance the application of process control in industry to improve the productivity and quality.

2.2   <u>Cutter Deflection Compensation in End Milling Processes</u>

Milling is one of the most versatile and widely used machining processes for generating surfaces in a variety of shapes and sizes. Supported and driven from one end, the milling cutter can be easily changed by automatic tool changers, which makes the milling process suitable for automatic mass production. Such cantilever beam like tool holding structure, however, induces the cutter deflection issue which affects the machining accuracy. Due to the importance of the milling process in manufacturing, especially in aerospace industry, it is critical to develop an effective strategy to reduce the geometric error caused by the cutter deflection.

Although the effect of cutter deflection on machining accuracy has been noticed by researchers for a long time, the earliest investigation on cutter deflection began in 1950s [37]. The study result suggested replacing shorter end mills with long end mills. Continuing this research effort, National Twist Drill & Tool Company conducted series of experiments to study the effect of cutter deflection on the accuracy of milled surfaces. Their work led to several strategies to reduce the cutter deflection, such as reducing feeds, using shallow depth of cut, using conventional milling instead of climb milling, etc. These suggestions have been adopted in the later studies on control system designs to avoid excessive cutter deflection.

In early 1980s, DeVor's group initiated the systematic investigation on cutter deflections [38-42] through computer simulation and experiments. The main objective was to provide CNC part programmers with the optimal process parameters when machining complex parts in aerospace industry, such as airframes. They developed instantaneous cutting force prediction model by combining the geometric analysis of milling processes by Martellotti [43] and empirical force estimation by Tlusty, etc., [44]. The instantaneous model can provide instant cutting force information even during transients, for example, varying radial depth of cut, which

13

is common in machining airframe structures. These models have been used for predicting cutter deflection in research on deflection compensation.

Many strategies have been proposed to address this issue, and can be categorized to 1) process design approach [45-52]; 2) online adaptive control approach [53-57]; 3) offline tool path compensation approach [52, 58-65].

The process design approach aims to reduce the load applied on the cutter to alleviate the deflection by choosing appropriate cutting conditions. In other words, the accuracy is improved at the cost of lower productivity, which is definitely not preferred in batch manufacturing. Such conservative approach may only be good for the production of a few of parts. Therefore the compensation-based strategy gains more attention in industry. Both online adaptive control and offline tool path compensation belong to this category.

Although online adaptive control approach was proposed as early as 1983 [53], there are only few work reported since then [54, 66]. This is partly due to the requirement for sensors or hardware modifications, which imposes a barrier for adoption in industry. Watanabe first proposed an online compensation method to reduce both the surface location error and the waviness error, which are computed from the measured moments [53]. Although both errors are induced by the deflection, they are reduced by different schemes. The surface error is reduced by controlling the servo program directly to shift the tool path while the waviness error is decreased by modifying the interpolation program to change the feed rate. The reason for applying different strategies is that reducing waviness error requires faster cycle motion and more accurate calculations than shifting the tool path so the servo program based on single precision data cannot meet the requirement while the interpolator can modify the program easily with required accuracy. For both cases, the proportional control is used. The experiment results show that the

14

proposed geometric adaptive controller can improve the accuracy of the surface for both rough and finish cut. Instead of modifying the servo program or the interpolator to change the relative position of the cutter and the workpiece, Yang and Choi designed a special tool adapter to tilt the cutter [54]. In this way, the control of the adapter is independent with the CNC system. The surface error is estimated by an empirical equation based on the mean and the fluctuation value of the measured cutting force, and the PI controller is applied to control the tool adapter.

Offline tool path compensation was studied in [52, 58-65]. In this approach, the deflection is estimated first according to the cutting force model, and the effect of cutter deflection on surface accuracy is predicted. Based on such estimation, the tool path is modified such that the resulting surface location error due to cutter deflection is still within the tolerance requirement. Although the offline approach allows the less conservative cutting conditions, the performance of this approach mainly depends on the modeling accuracy, which cannot be guaranteed. The literature review indicates inadequate work on the online cutter deflection compensation strategy which can ensure the quality and productivity simultaneously.

The difference between online compensation and offline tool path planning is that the former one is to change the path trajectory in real time based on the measurement of deflection, while the latter is to plan the tool path trajectory before machining according to the prediction of deflection. It can be concluded that, in addition to the compensation strategies for each approach, the effect of the online one relies on the real time measurement while the offline approach relies on the accuracy of the prediction.

In this research, the error space based online compensation approach will be developed and applied to workpiece with different surfaces including the straight surfaces, circular surfaces, and the free form surfaces.

15

CHAPTER 3 DIRECT AGGREGATION OF THE SERVO-PROCESS CONTROL

3.1 Introduction

From our literature review, the process control and the servomechanism control have not been tightly integrated. Separate controllers are required to control cutting forces, servomechanisms, and contour in machining tools. The resulting system complexity increases system costs and may cause reliability problem due to interactions among different modules. One of the dissertation research goals is to design a single control system to simultaneously control both the process and the servo level.

In this chapter, the process whose variables can be associated with the servomechanism states is addressed. The aggregation between the process and the servomechanism states is integrated in the servomechanism controller design such that the resulting controller can simultaneously achieve goals of the servomechanism control and the process control. Force-position-contour control in turning is used as one example for this type of integration study.

The chapter is organized as follows. The force-position-contour control methodology is presented in section 3.2. In this section, the error-state space approach for the servomechanism control is introduced first. Then the hierarchical optimal control scheme integrating control of force, position, and contour is described. The robustness to parameter variations of the cutting processes is examined in section 3.3. Simulation studies in section 3.4 demonstrate the effectiveness of the controller for a variety of cutting conditions. Section 3.5 concludes the chapter with summaries and conclusions.

16

3.2   <u>Force-Position-Contour Control Methodology</u>

A control methodology that simultaneously regulates forces, position errors, and contour error in machining operations is now presented. A multi–axis machine tool is conceptualized as a hierarchical system (Figure 2). The contour error and machining force are located at the top level, and the servomechanisms are located at the bottom level. While the top level has physical outputs (i.e., contour error and cutting force), it does not contain physical control signals. The bottom level consists of a number of axes whose coordinated motion allows the machine tool to produce complex contours. This level consists of physical outputs (e.g., position, velocity) as well as physical control signals (e.g., voltages, currents). The top–level goals are to maintain zero contour error to ensure quality and a constant machining force to maintain productivity, and the bottom level goal is to maintain zero servomechanism position errors, which indirectly guarantee the performance of quality. Since the top level does not contain physical control signals, the goals of zero contour error and a constant machining force must be realized via the bottom level control signals. Thus, the control methodology presented will propagate the top–level goals to the bottom level where a controller will simultaneously meet the top and bottom–level goals.
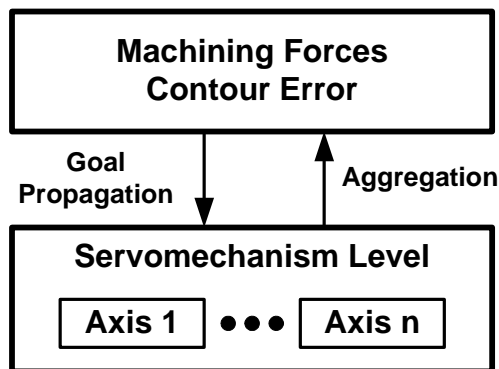
Figure 2 Hierarchical Representation of a Machining Operation for Force-Position-Contour Control

17

3.2.1 Error-state Space Approach

Motion control is a critical component in machining processes especially for parts with complex contours. Precision control of the relative displacement between the cutting tool and the workpiece is essential for achieving high machining accuracy. Simple motion controllers, such as Proportional plus Integral plus Derivative (PID) controllers, can only guarantee zero steady-state error for linear contours. The machining process can be interpreted as a tracking system, in which the cutting tool is controlled to track the desired trajectory. Since the cutting conditions and machining geometry vary for different operations and there also exist disturbances during machining, the robustness of the controller to parameter changes and disturbance is critical for machining quality. In order to realize the required robustness and achieve zero steady-state error, we can use error state space approach [67], which constructs an expanded space including both the system states and tracking errors. The transformation converts the tracking problem into a regulator problem, which aims to drive the states of the error state space to zero. In other words, the controller design is independent of the reference signals, so the robustness to process changes and disturbances can be achieved. In this section, this approach is briefly presented to illustrate how the robustness to reference signals is achieved.

The system state equations are:

$$\dot{x}(t) = Ax(t) + Bu(t),$$
$$y(t) = Cx(t), \tag{1}$$

where $x(t)$ is an n-dimensional vector of system states, $u(t)$ is the system input, $y(t)$ is the system output. A is an $n \times n$ state matrix, B is an $n \times 1$ input matrix, and C is an $1 \times n$ output matrix.

The reference signal can be represented by

$$\ddot{r}(t) + a_1\dot{r}(t) + a_2r(t) = 0, \tag{2}$$

18

and the tracking error is defined as

$$e(t) = r(t) - y(t).$$ (3)

Representing the reference signal by the tracking error and the output, equation (2) can be rewritten as

$$\ddot{e}(t) + a_1\dot{e}(t) + a_2 e(t) = -\ddot{y}(t) - a_1\dot{y}(t) - a_2 y(t)$$
$$= -C\left[\ddot{x}(t) + a_1\dot{x}(t) + a_2 x(t)\right].$$ (4)

Defining the error-space state ξ as

$$\xi \triangleq \ddot{x}(t) + a_1\dot{x}(t) + a_2 x(t),$$ (5)

equation (4) is replaced with

$$\ddot{e}(t) + a_1\dot{e}(t) + a_2 e(t) = -C\xi(t).$$ (6)

The derivative of ξ can be derived from the state space equation (1) by

$$\dot{\xi} = \dddot{x}(t) + a_1\ddot{x}(t) + a_2\dot{x}(t)$$
$$= A\left[\ddot{x}(t) + a_1\dot{x}(t) + a_2 x(t)\right] + B\left[\ddot{u}(t) + a_1\dot{u}(t) + a_2 u(t)\right].$$ (7)

Defining a dummy control input μ in the error space by

$$\mu(t) = \ddot{u}(t) + a_1\dot{u}(t) + a_2 u(t),$$ (8)

equation (7) can be rewritten as

$$\dot{\xi}(t) = A\xi(t) + B\mu(t).$$ (9)

If the plant (A,B) is controllable, $\xi(t)$ can be given arbitrary dynamics, including $\xi(t) = 0$ as time gets large, by state feedback. Tracking error states, $e(t)$ and $\dot{e}(t)$ and the defined state $\xi(t)$, form the so called error space which is given by:

$$\begin{bmatrix} \dot{e}(t) \\ \ddot{e}(t) \\ \dot{\xi}(t) \end{bmatrix} = \begin{bmatrix} 0 & 1 & 0 \\ -a_2 & -a_1 & -C \\ 0 & 0 & A \end{bmatrix} \begin{bmatrix} e(t) \\ \dot{e}(t) \\ \xi(t) \end{bmatrix} + \begin{bmatrix} 0 \\ 0 \\ B \end{bmatrix} \mu(t).$$ (10)

19

Defining the error space state vector $x_{es}^T(t) = \begin{bmatrix} e(t) & \dot{e}(t) & \xi(t) \end{bmatrix}$, equation (10) is represented by

$$\dot{x}_{es} = A_{es} x_{es}(t) + B_{es} \mu(t). \tag{11}$$

If $[A,B]$ is controllable and matrix C does not have common factors with a_1 and a_2, $[A_{es}, B_{es}]$ is controllable Consequently, the system can be assigned with desired dynamics by state feedback. This condition is not stringent for servomechanisms used in machining because they are usually approximated as 2nd order system without zeros.

3.2.2   Hierarchical Force-Position-Contour Control

The hierarchical optimal force–position–contour control methodology will propagate the top–level goals of zero contour error and a constant machining force to the bottom level via an aggregation relationship between the contour error/machining force and the servomechanism position errors. A single optimal controller will be constructed that is capable of simultaneously addressing three objectives: zero contour error, constant machining force, and zero servomechanism position errors. Therefore, the increased complexity of additional contour and force control algorithms is avoided. The methodology developed below provides an intuitive means for the designer to weight the relative importance of the three objectives.

The state space representation of the servomechanism dynamics is

$$\begin{aligned} \dot{x}(t) &= Ax(t) + Bu(t), \\ y(t) &= Hx(t), \end{aligned} \tag{12}$$

where $x(t)$ is an n-dimensional vector of servomechanism states, $u(t)$ is an m-dimensional vector of servomechanism inputs, $y(t)$ is an p-dimensional vector of servomechanism outputs where p is

20

the number of axes, A is an $n \times n$ state matrix, B is an $n \times m$ input matrix, and H is an $p \times n$ output matrix.

Each point on the reference tool path is approximated as a point on a circular arc in the hierarchical optimal control methodology. The controller requires the instantaneous radius of curvature and the instantaneous center of curvature. For linear trajectories, the radius of curvature is infinite. For circular trajectories, the radius of curvature and the instantaneous center of the radius of curvature are constant; however, for general trajectories, these parameters will constantly change. Knowing the radius of curvature and the desired linear velocity along the curve, the angular velocity can be calculated. The reference axial positions satisfy

$$\ddot{r}(t) + \omega^2 r(t) = 0, \tag{13}$$

where the value of ω varies for different trajectories. Note that $\omega = 0$ for linear trajectories, ω is constant for circular trajectories (assuming a constant velocity interpolator is employed), and ω is time–varying for complex trajectories. Using the error-space approach in [67] and extending it to MIMO systems, the augmented servomechanism system is

$$\dot{x}_{bot}(t) = A_{bot} x_{bot}(t) + B_{bot} u_{bot}(t) = \begin{bmatrix} E_{bot} & H_{bot} \\ 0_{(n)(2p)} & A \end{bmatrix} \begin{bmatrix} e(t) \\ \xi(t) \end{bmatrix} + \begin{bmatrix} 0_{(2p)(m)} \\ B \end{bmatrix} u_{bot}(t), \tag{14}$$

where

$$e^T(t) = \begin{bmatrix} e_1(t) & \cdots & e_p(t) & \dot{e}_1(t) & \cdots & \dot{e}_p(t) \end{bmatrix}, \tag{15}$$

$$\xi(t) = \ddot{x}(t) + \omega^2 x(t), \tag{16}$$

$$E_{bot} = \begin{bmatrix} 0_{(p)(p)} & I_p \\ -\omega^2 I_p & 0_{(p)(p)} \end{bmatrix}, \quad H_{bot} = \begin{bmatrix} 0_{(2p)(n)} \\ H \end{bmatrix}, \tag{17}$$

$$u_{bot}(t) = \ddot{u}(t) + \omega^2 u(t), \tag{18}$$

21

and p is the number of axes, $e(t)$ is a $2p$-dimensional vector of error signals, $e_i(t)= y_i(t) - r_i(t)$, i =1, …, p, $y_i(t)$ is the position of the ith servomechanism, $u_{bot}(t)$ is an m-dimensional vector of dummy control signals, $r(t)$ is an p-dimensional vector of servomechanism position reference signals, $\xi(t)$ is an n–dimensional vector of error space states, $0_{(i)(j)}$ is a matrix of zeros with i rows and j columns, and I_j is an identity matrix with j rows and j columns. Equation (14) describes the bottom level dynamics in the hierarchical optimal control methodology.

The next step in the hierarchical control formulation is to determine the top level goals and an aggregation relationship between the goals at the top and bottom levels such that the top–level goals are propagated to the bottom level. Such aggregation is expected to relate the values of the top level to the individual axis errors at the bottom.

One of the goals at the top level is to maintain zero contour error, which is the minimum distance between the actual tool position and the desired tool path. The contour error is related to the individual axis errors and may be expressed as

$$\varepsilon(t) = f\big[e(t)\big] = c_1(t)\, x_{bot}(t),\tag{19}$$

where $c_1(t)$ depends upon the tool path. It is assumed that all axis positions are measurable.
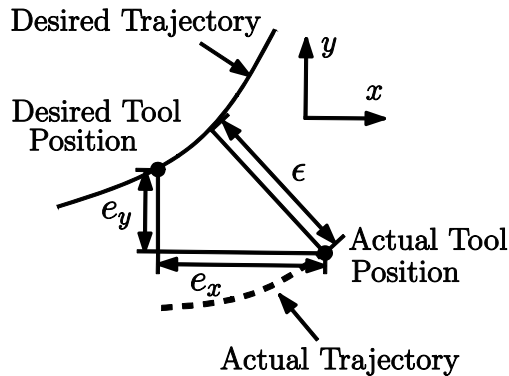
Figure 3 Contour Error and Axis Errors

The other goal at the top level is to maintain a constant cutting force. The cutting force depends on the feed, depth-of-cut and cutting speed, and is related to these parameters by the following nonlinear relation [32]

$$F(t) = Kf^{\alpha}(t)d^{\beta}(t)V_c^{\gamma}(t),$$ (20)

where K is the process gain, $f(t)$ is the feed, $d(t)$ is the depth of cut, and $V_c(t)$ is the cutting speed. A reference feed is calculated based on equation (20) to maintain a specified cutting force. This reference feed is then translated into a reference velocity, which is input to the interpolator. The parameters K, V, and d in equation (20) are nominal values and may change during the cutting processes. The structural vibrations are assumed to be small as compared to the feed, and the cutting tool angles are constant. Also, effects due to tool wear and cutting temperature are assumed to be reflected in the force process gain.

Linearizing equation (20) about the operating conditions, which is allowable maximum cutting forces, yields

$$\Delta F(t) = \left[KV_c^{\gamma}d^{\beta}\alpha f^{\alpha-1} \right] \Delta f(t) = \Theta \Delta f(t),$$ (21)

where

$$\Delta f(t) = f_r(t) - f(t) = g\left[\dot{e}(t) \right].$$ (22)

Equation (21) indicates that the force error can be related to the individual axis errors. The aggregation between the force error and the individual axis error derivative can be represented by

$$\Delta F(t) = \Theta g\left[\dot{e}(t) \right] = c_2(t) x_{bot}(t).$$ (23)

The contour error and the force error are related to the individual axis errors and their derivatives, and may be expressed through the aggregation relation

$$x_{top}(t) = \begin{bmatrix} \varepsilon(t) \\ \Delta F(t) \end{bmatrix} = \begin{bmatrix} c_1(t) \\ c_2(t) \end{bmatrix} x_{bot}(t) = C(t) x_{bot}(t).$$ (24)

23

3.2.2.1 Controller Formulation

Now the goals of the top level have been propagated to the bottom level, where the controller resides. This aggregation needs to be integrated into the controller formulation, so that the controller can control the bottom level directly and the top level indirectly. This problem can be formulated as an optimal tracking control problem [68] where the bottom level seeks to track the top level goals (i.e., zero contour error and constant cutting force). The cost function at the bottom is

$$J_{bot} = \frac{1}{2}\left[C(t_f)x_{bot}(t_f) - x_r(t_f)\right]^T S_{bot}\left[C(t_f)x_{bot}(t_f) - x_r(t_f)\right] + \int_0^{t_f} L_{bot}(t)dt, \qquad (25)$$

where

$$x_r(t_f) = \begin{bmatrix} \varepsilon_r(t_f) \\ \Delta F(t_f) \end{bmatrix}, \qquad (26)$$

$$L_{bot}(t) = \frac{1}{2}\left\{ \begin{matrix} \left[C(t)x_{bot}(t) - x_r(t)\right]^T Q_{bot}\left[C(t)x_{bot}(t) - x_r(t)\right] \\ +u_{bot}^T(t)R_{bot}u_{bot}(t) + x_{bot}^T(t)Qx_{bot}(t) \end{matrix} \right\}. \qquad (27)$$

Note that the goals at the top level require $\varepsilon_r(t) = 0$ and $\Delta F_r(t) = 0$. The first term in equation (25) ensures the goal of the top level is achieved at the final time. The first term in equation (27) ensures the aggregation relationship between the top and bottom levels is met. In effect, this term is used to send commands from the top level to the bottom level to ensure the top level objectives are met. The second term in equation (27) penalizes control usage at the bottom level, where the physical control signals reside. The third term in equation (27) penalizes deviations in the states at the bottom level. In effect, this term is used to ensure the objectives at the bottom level are met. The Hamiltonian at the bottom level is

$$H_{bot}(t) = L_{bot}(t) + \lambda_{bot}(t)\left[A_{bot}x_{bot}(t) + B_{bot}u_{bot}(t)\right], \qquad (28)$$

24

where the Lagrange multiplier is of the form

$$\lambda_{bot}(t) = P_{bot}(t)x_{bot}(t) + k_{bot}(t). \tag{29}$$

The optimal control law is found by taking the partial derivative of equation (18) with respect to $u_{bot}(t)$ and equating to zero

$$u_{bot}(t) = -R_{bot}^{-1}B_{bot}^{T}\lambda_{bot}(t) = -R_{bot}^{-1}B_{bot}^{T}\left[P_{bot}(t)x_{bot}(t) + k_{bot}(t)\right]. \tag{30}$$

The elements of the matrices $P_{bot}(t)$ and the vector $k_{bot}(t)$ are found by solving, respectively, the differential equations

$$\dot{P}_{bot}(t) = -P_{bot}(t)A_{bot} - A_{bot}^{T}P_{bot}(t) + P_{bot}(t)B_{bot}R_{bot}^{-1}B_{bot}^{T}P_{bot}(t) - C^{T}(t)Q_{bot}C(t) - Q, \tag{31}$$

$$\dot{k}_{bot}(t) = -A_{bot}^{T}k_{bot}(t) + P_{bot}(t)B_{bot}R_{bot}^{-1}B_{bot}^{T}k_{bot}(t) + C^{T}(t)Q_{bot}x_{top}(t). \tag{32}$$

These differential equations must be solved backward in time. The boundary conditions for equations (21) and (22), respectively, are

$$P_{bot}(t_{f}) = C^{T}(t_{f})S_{bot}C(t_{f}), \tag{33}$$

$$k_{bot}(t_{f}) = C^{T}(t_{f})S_{bot}x_{top}(t_{f}). \tag{34}$$

The matrix $P_{bot}(t)$ is used for regulation and the vector $k_{bot}(t)$ is used for tracking. However, the top level objectives are $\varepsilon_r(t) = 0$ and $\Delta F_r(t) = 0$. Therefore, $k_{bot}(t_f) = 0$ and $k_{bot}(t)$ is unforced and, thus, $k_{bot}(t) = 0$. Simulations of equation (31) reveal that the elements of $P_{bot}(t)$ are constant except near $t = t_f$. Therefore, the steady–state solution of equation (31) is utilized. This greatly aids the stringent real–time computational demands required by machining processes.

Note that $u_{bot}(t)$ is a vector of dummy control signals. The physical control signals are found by solving

$$\ddot{u}(t) + \omega^2 u(t) = -R_{bot}^{-1}B_{bot}^{T}P_{bot}(t)x_{bot}(t). \tag{35}$$

The tool path parameterization that is utilized in this research is a circular arc. If another curve parameterization were utilized, the differential equation that defines the reference signal, namely equation (13), would be modified. This, in turn, would change the structure of E_{bot} and, hence, the size of A_{bot}, as well as the definitions of $\xi(t)$ and $\boldsymbol{u_{bot}}(t)$. The hierarchical optimal control methodology is illustrated in the next section via an application to a two–axis lathe.

EXAMPLE: TWO–AXIS LATHE

The hierarchical optimal contour/force control methodology developed in the above section is now applied to a two–axis lathe consisting of two linear orthogonal axes, denoted x and z, and a spindle. The x and z–axis time constants are denoted τ_x and τ_z, respectively, and the x and z–axis gains are denoted K_x and K_z, respectively. The control–oriented system equations of a two–axis servomechanism, assuming the electrical dynamic response is much faster than the mechanical dynamic response [69], are

$$\tau_x \ddot{x}_x\left(t\right) + \dot{x}_x\left(t\right) = K_x u_x\left(t\right), \tag{36}$$

$$\tau_z \ddot{x}_z\left(t\right) + \dot{x}_z\left(t\right) = K_z u_z\left(t\right). \tag{37}$$

The state space representation is given by equation (1) where

$$\boldsymbol{x}^T\left(t\right) = \begin{bmatrix} x_x\left(t\right) & x_z\left(t\right) & \dot{x}_x\left(t\right) & \dot{x}_z\left(t\right) \end{bmatrix}, \tag{38}$$

$$\boldsymbol{u}^T\left(t\right) = \begin{bmatrix} u_x\left(t\right) & u_z\left(t\right) \end{bmatrix}, \tag{39}$$

$$\boldsymbol{y}^T\left(t\right) = \begin{bmatrix} x_x\left(t\right) & x_z\left(t\right) \end{bmatrix}, \tag{40}$$

$$A = \begin{bmatrix} 0 & 0 & 1 & 0 \\ 0 & 0 & 0 & 1 \\ 0 & 0 & -\dfrac{1}{\tau_x} & 0 \\ 0 & 0 & 0 & -\dfrac{1}{\tau_z} \end{bmatrix}, \quad B = \begin{bmatrix} 0 & 0 \\ 0 & 0 \\ \dfrac{K_x}{\tau_x} & 0 \\ 0 & \dfrac{K_z}{\tau_z} \end{bmatrix}, \quad H = \begin{bmatrix} 1 & 0 & 0 & 0 \\ 0 & 1 & 0 & 0 \end{bmatrix}. \tag{41}$$

The augmented servomechanism system is

$$\dot{x}_{bot}(t) = \begin{bmatrix} E_{bot} & H_{bot} \\ 0_{(4)(4)} & A \end{bmatrix} \begin{bmatrix} e(t) \\ \xi(t) \end{bmatrix} + \begin{bmatrix} 0_{(4)(2)} \\ B \end{bmatrix} u_{bot}(t), \tag{42}$$

where

$$e^T(t) = \begin{bmatrix} e_x(t) & e_z(t) & \dot{e}_x(t) & \dot{e}_z(t) \end{bmatrix}, \tag{43}$$

$$e_x(t) = x_x(t) - r_x(t), \tag{44}$$

$$e_z(t) = x_z(t) - r_z(t), \tag{45}$$

$$\xi^T(t) = \begin{bmatrix} \ddot{x}_x(t) + \omega^2 x_x(t) & \ddot{x}_z(t) + \omega^2 x_z(t) & \dddot{x}_x(t) + \omega^2 \dot{x}_x(t) & \dddot{x}_z(t) + \omega^2 \dot{x}_z(t) \end{bmatrix}, \tag{46}$$

$$E_{bot} = \begin{bmatrix} 0_{(2)(2)} & I_2 \\ -\omega^2 I_2 & 0_{(2)(2)} \end{bmatrix}, \qquad H_{bot} = \begin{bmatrix} 0_{(2)(4)} \\ H \end{bmatrix}, \tag{47}$$

$$u_{bot}(t) = \begin{bmatrix} \ddot{u}_x(t) \\ \ddot{u}_z(t) \end{bmatrix} + \omega^2 \begin{bmatrix} u_x(t) \\ u_z(t) \end{bmatrix}. \tag{48}$$

Before applying the control methodology, the controllability is examined to guarantee the stability of the augmented error space system. The controllability matrix for the original states is

$$\mathcal{C}_{ss} = \begin{bmatrix} B & AB & A^2B & A^3B \end{bmatrix}$$

$$= \begin{bmatrix} 0 & 0 & K_x/\tau_x & 0 & -K_x/\tau_x^2 & 0 & -K_x/\tau_x^3 & 0 \\ 0 & 0 & 0 & K_z/\tau_z & 0 & -K_z/\tau_z^2 & 0 & -K_z/\tau_z^3 \\ K_x/\tau_x & 0 & -K_x/\tau_x^2 & 0 & K_x/\tau_x^3 & 0 & -K_x/\tau_x^4 & 0 \\ 0 & K_z/\tau_z & 0 & -K_z/\tau_z^2 & 0 & K_z/\tau_z^3 & 0 & -K_z/\tau_z^3 \end{bmatrix}. \tag{49}$$

which is nonsingular, and the original system is controllable. The controllability matrix for the augmented error space is

$$\mathcal{C}_{es} = \begin{bmatrix} \boldsymbol{B}_{bot} & \boldsymbol{A}_{bot}\boldsymbol{B}_{bot} & \cdots & \boldsymbol{A}_{bot}^7\boldsymbol{B}_{bot}^7 \end{bmatrix}, \tag{50}$$

where

$$\boldsymbol{B}_{bot} = \begin{bmatrix} 0_{(4)(2)} \\ B \end{bmatrix} \in R^{8\times 2}, \tag{51}$$

$$\boldsymbol{A}_{bot} = \begin{bmatrix} E_{bot} & H_{bot} \\ 0_{(4)(4)} & A \end{bmatrix} \in R^{8\times 8}. \tag{52}$$

$\mathcal{C}_{es}$ is proved to be nonsingular by checking the rank. Therefore, the augmented error space system is controllable and the control signal can take the system from any initial state $\boldsymbol{x}_{bot}(0)$ to any desired final state $\boldsymbol{x}_{bot}(t_f)$ in a finite time interval [67]. The controllability check validates the optimal control formulation.

The contour error is given by equation (19) where

$$\boldsymbol{c}_1(t) = \begin{bmatrix} c_x(t) & c_z(t) & 0_{(1)(6)} \end{bmatrix}, \tag{53}$$

and $c_x(t)$ and $c_x(t)$ depend on the tool path. The change in feed is

$$\Delta f(t) = f_r(t) - f(t) = \frac{60V_{rz}(t)}{N_s} - \frac{60V_z(t)}{N_s} = -\frac{60}{N_s}\dot{e}_z(t). \tag{54}$$

28

The spindle speed N_s is assumed to be well regulated via another control scheme. From equation (21)

$$\Delta F(t) = c_2(t) x_{bot}(t) = -\frac{60\Theta(t)}{N_s} \dot{e}_z(t) = \left[0_{(1)(3)} \quad -\frac{60\Theta(t)}{N_s} \quad 0_{(1)(4)} \right].$$

(55)

The aggregation relation between the top level (i.e., contour error and cutting force) and the bottom level (i.e., servomechanism position errors) is given by equation (24) where

$$C(t) = \begin{bmatrix} c_x(t) & c_z(t) & 0 & 0 & 0_{(1)(4)} \\ 0 & 0 & 0 & -\frac{60\Theta(t)}{N_s} & 0_{(1)(4)} \end{bmatrix}.$$

(56)

Applying the hierarchical optimal contour/force control methodology, the physical control signals are found by solving

$$\begin{bmatrix} \ddot{u}_x(t) \\ \ddot{u}_z(t) \end{bmatrix} + \omega^2 \begin{bmatrix} u_x(t) \\ u_z(t) \end{bmatrix} = -R_{bot}^{-1} B_{bot}^T P_{bot}(t) x_{bot}(t).$$

(57)

3.3   <u>Robustness to Parameter Varations</u>

The force model given by equation (20) includes model parameters (i.e., K, α, β, and γ) that must be determined empirically and process parameters (i.e., d and V_c) that are functions of the machine tool's linear axis and the spindle motions. The controller derived above assumed no variation in these parameters; however, these parameters naturally vary during a machining operation. For example, the model gain K strongly depends on the tool wear and cutting temperature. Also, the depth–of–cut depends on the part geometry and the cutting speed will change when machining a tapered part if the spindle speed is held constant. When a model parameter varies, monitoring techniques must be used to determine the amount of variation, while process parameter variations may be determined from the part drawing and sensing the machine variables. When there is parameter variation, the linearized relation given by equation (21) is not valid. In this section, controllers are derived for uncertainties in the model gain and in the depth–of–cut.

Variations in Model Parameters and Process Parameters

Simultaneous variations in the force process model gain and the depth–of–cut are now considered. Expanding the force–feed relation given by (21) in a Taylor series expansion about the reference feed (f_r), the nominal value of the force process model gain (K_0) and the nominal value of the depth–of–cut (d_0)

$$
\begin{aligned}
\Delta F(t) \cong & \left[K_0 \alpha f_r^{\alpha-1} d_0^{\beta} V_c^{\gamma} \right] \Delta f(t) + \left[f_r^{\alpha} d_0^{\beta} V_c^{\gamma} \right] \Delta K(t) \\
& + \left[K_0 \beta f_r^{\alpha} d_0^{\beta-1} V_c^{\gamma} \right] \Delta d(t) + \left[\alpha f_r^{\alpha-1} d_0^{\beta} V_c^{\gamma} \right] \Delta f(t) \Delta K(t) \\
& + \left[K_0 \alpha \beta f_r^{\alpha-1} d_0^{\beta-1} V_c^{\gamma} \right] \Delta f(t) \Delta d(t) + \left[\beta f_r^{\alpha} d_0^{\beta-1} V_c^{\gamma} \right] \Delta d(t) \Delta K(t) \\
& + \frac{1}{2!} \left[K_0 \beta (\beta-1) f_r^{\alpha} d_0^{\beta-2} V_c^{\gamma} \right] \Delta d^2(t) + \frac{1}{2!} \left[K_0 \alpha (\alpha-1) f_r^{\alpha-2} d_0^{\beta} V_c^{\gamma} \right] \Delta f^2(t),
\end{aligned}
\tag{58}
$$

30

where $\Delta K(t) = K(t) - K_0$ and $\Delta d(t) = d(t) - d_0$. Assuming that the second order term in $\Delta f(t)$ in equation (58) is negligible

$$
\begin{aligned}
\Delta F(t) &- \left[f_r^\alpha d_0^\beta V_c^\gamma \right] \Delta K(t) - \left[K_0 \beta f_r^\alpha d_0^{\beta-1} V_c^\gamma \right] \Delta d(t) - \frac{1}{2!} \left[K_0 \beta (\beta-1) f_r^\alpha d_0^{\beta-2} V_c^\gamma \right] \Delta d^2(t) \\
&= \left[K(t) \alpha f_r^{\alpha-1} d_0^\beta V_c^\gamma + K_0 \alpha \beta f_r^{\alpha-1} d_0^{\beta-1} V_c^\gamma \Delta d(t) \right] \Delta f(t).
\end{aligned}
\tag{59}
$$

The term $-\left[f_r^\alpha d_0^\beta V_c^\gamma \right] \Delta K(t) - \left[K_0 \beta f_r^\alpha d_0^{\beta-1} V_c^\gamma \right] \Delta d(t) - \frac{1}{2!} \left[K_0 \beta (\beta-1) f_r^\alpha d_0^{\beta-2} V_c^\gamma \right] \Delta d^2(t)$ again

can be regarded as a bias to the top level goal of constant cutting force. The goal propagated from the top level of the hierarchy is $\Delta F_{eff} = 0$ where

$$
\begin{aligned}
\Delta F_{eff}(t) &= \Delta F(t) - \left[f_r^\alpha d_0^\beta V_c^\gamma \right] \Delta K(t) - \left[K_0 \beta f_r^\alpha d_0^{\beta-1} V_c^\gamma \right] \Delta d(t) \\
&\quad - \frac{1}{2!} \left[K_0 \beta (\beta-1) f_r^\alpha d_0^{\beta-2} V_c^\gamma \right] \Delta d^2(t) \\
&= \left[K(t) \alpha f_r^{\alpha-1} d_0^\beta V_c^\gamma + K_0 \alpha \beta f_r^{\alpha-1} d_0^{\beta-1} V_c^\gamma \Delta d(t) \right] \Delta f(t).
\end{aligned}
\tag{60}
$$

The effective aggregation matrix is

$$
C_{eff}(t) = \begin{bmatrix} c_x(t) & c_z(t) & 0 & 0 & 0_{(1)(4)} \\ 0 & 0 & 0 & -\dfrac{60 \left(K(t) \alpha f_r^{\alpha-1} d_0^\beta V_c^\gamma + K_0 \alpha \beta f_r^{\alpha-1} d_0^{\beta-1} V_c^\gamma \Delta d(t) \right)}{N_s} & 0_{(1)(4)} \end{bmatrix}.
\tag{61}
$$

The cost function to minimize at the lower level is given

$$
\begin{aligned}
J_{bot}(t) &= \frac{1}{2} \left[C_{eff}(t) x_{bot}(t_f) - \begin{bmatrix} \Delta F_{eff}(t_f) \\ \varepsilon_r(t_f) \end{bmatrix} \right] S_{bot} \left[C_{eff}(t) x_{bot}(t_f) - \begin{bmatrix} \Delta F_{eff}(t_f) \\ \varepsilon_r(t_f) \end{bmatrix} \right] \\
&\quad + \int_0^{t_f} L_{bot}(t) \, dt,
\end{aligned}
\tag{62}
$$

where C_{eff} is given by equation (61). The controller given by equation (57) is implemented where the steady–state solution for P_{bot} is utilized and the controller gains are updated, based on C_{eff}, each time the model gain and the depth–of–cut change. The vector k_{bot} is again identically zero

31

since $\Delta F_{eff}\left(t_f\right)=0$. Note that when only the force process model parameter changes equation (59) is reduced to

$$\Delta F\left(t\right)-\left[f_r^\alpha d^\beta V_c^\lambda\right]\Delta K\left(t\right)=\left[K_0\alpha f_r^{\alpha-1}d^\beta V_c^\gamma+\alpha f_r^{\alpha-1}d^\beta V_c^\gamma\Delta K\left(t\right)\right]\Delta f\left(t\right)$$
$$=\left[K\left(t\right)\alpha f_r^{\alpha-1}d^\beta V_c^\gamma\right]\Delta f\left(t\right).$$

(63)

Similarly, when only the depth-of-cut changes, equation (59) is reduced to

$$\Delta F\left(t\right)-\left[K_0\beta f_r^\alpha d_0^{\beta-1}V_c^\gamma\right]\Delta d\left(t\right)-\frac{1}{2!}\left[K_0\beta\left(\beta-1\right)f_r^\alpha d_0^{\beta-2}V_c^\gamma\right]\Delta d^2\left(t\right)$$
$$=\left[K_0\alpha f_r^{\alpha-1}d_0^\beta V_c^\gamma+K_0\alpha\beta f_r^{\alpha-1}d_0^{\beta-1}V_c^\gamma\Delta d\left(t\right)\right]\Delta f\left(t\right).$$

(64)

Therefore, when there exist uncertainties in the model gain and in the depth–of–cut, the controller should use the performance index, given in equation (62) rather than equation (25), to provide the robustness to process parameter variation.

3.4 Simulation Studies

Simulation studies are now conducted for the four lathing operations. The servomechanism parameters are from a laboratory–grade machine tool [70]: $\tau_x = 0.055$ *sec*, $\tau_z = 0.056$ *sec*, $K_x = 3.628$ (*mm/s*)/*V*, and $K_z = 3.706$ (*mm/s*)/*V*. The force process is given by $F(t) = 1.17d^{0.877}(t)V^{-0.273}(t)f^{0.891}(t)$. This data is based on machining experiments conducted for a steel part using a coated carbide insert ([71]). The maximum power is 10 *hp* (7.46 *kW*) and the spindle speed is $N_s = 6000$ *rpm*. Interpolators, described below, generate the reference axis trajectories. A Runge–Kutta fourth order integration routine with a sample period of 0.001 *sec* is utilized to solve the servomechanism and controller dynamic equations. The control signals are saturated at ± 20 *V*. For all the simulations, the tool starts at rest at the *x–z* coordinate system origin. The *z*–axis reference velocity is

$$\dot{r}_z(t) = \frac{f_r(t)N_s}{60},\tag{65}$$

where the reference feed is calculated via equation (20) using the reference cutting force. The *x*–axis reference velocity is calculated from the *z*–axis reference velocity and the contour curvature. If the *x*–axis reference velocity is greater than the maximum *x*–axis velocity, the *x*–axis reference velocity is set to this maximum value and the *z*–axis reference velocity is recalculated. Eight simulation case studies are investigated below. Each of the four operations consists of a case study where the force process gain is constant and where the force process gain changes by 0.001 kN/mm^2 at each sample period. The weighting matrices, which were determined via trial and error, are chosen as $R_{bot} = diag\begin{bmatrix} 10^{-6} & 10^{-6} \end{bmatrix}$, $S_{bot} = 0$, $Q_{bot} = diag\begin{bmatrix} 10^7 & 10^{-2} \end{bmatrix}$, and $Q = diag\begin{bmatrix} 10^7 & 10^7 & 10^{-2} & 10^{-2} & 10^{-8} & 10^{-8} & 10^{-8} & 10^{-8} \end{bmatrix}$.
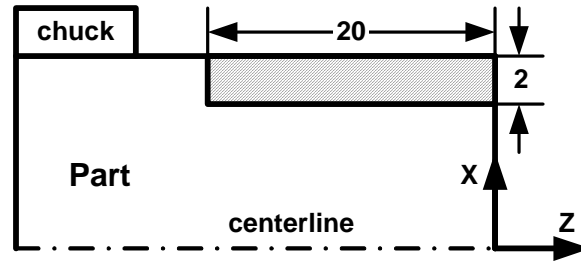
Figure 4 Operation I

Operation I

The contour of Operation I (Figure 4) is a straight line with a 2 *mm* depth–of–cut along a 20 *mm*
length–of–cut. This contour has an infinite radius of curvature and, thus, the reference angular
velocity is zero. The contour error is

$$\varepsilon(t) = e_x(t). \tag{66}$$

Two simulations were performed to illustrate how the hierarchical controller affects contour
error and cutting force for straight cuts, and the simulation results are shown in Figure 5 - Figure
8. In Case 1, the force process gain and depth–of–cut are constant; therefore, the aggregation
matrix is constant and the steady–state value of $P_{bot}(t)$ is calculated only once. In Case 2, the
depth – of – cut is constant and the force process gain varies; therefore, the force–feed relation is
given by equation (63). Also, the aggregation matrix is not constant and, thus, the steady – state
solution of $P_{bot}(t)$ is calculated at each sample period. For both cases, the steady–state contour
and force errors were zero. Since an exact contour error formulation is utilized, the steady–state
contour error was zero and, since the feed was able to track the reference feed, the steady–state
force error was zero. Note that the controller was able to track the reference feed even when the
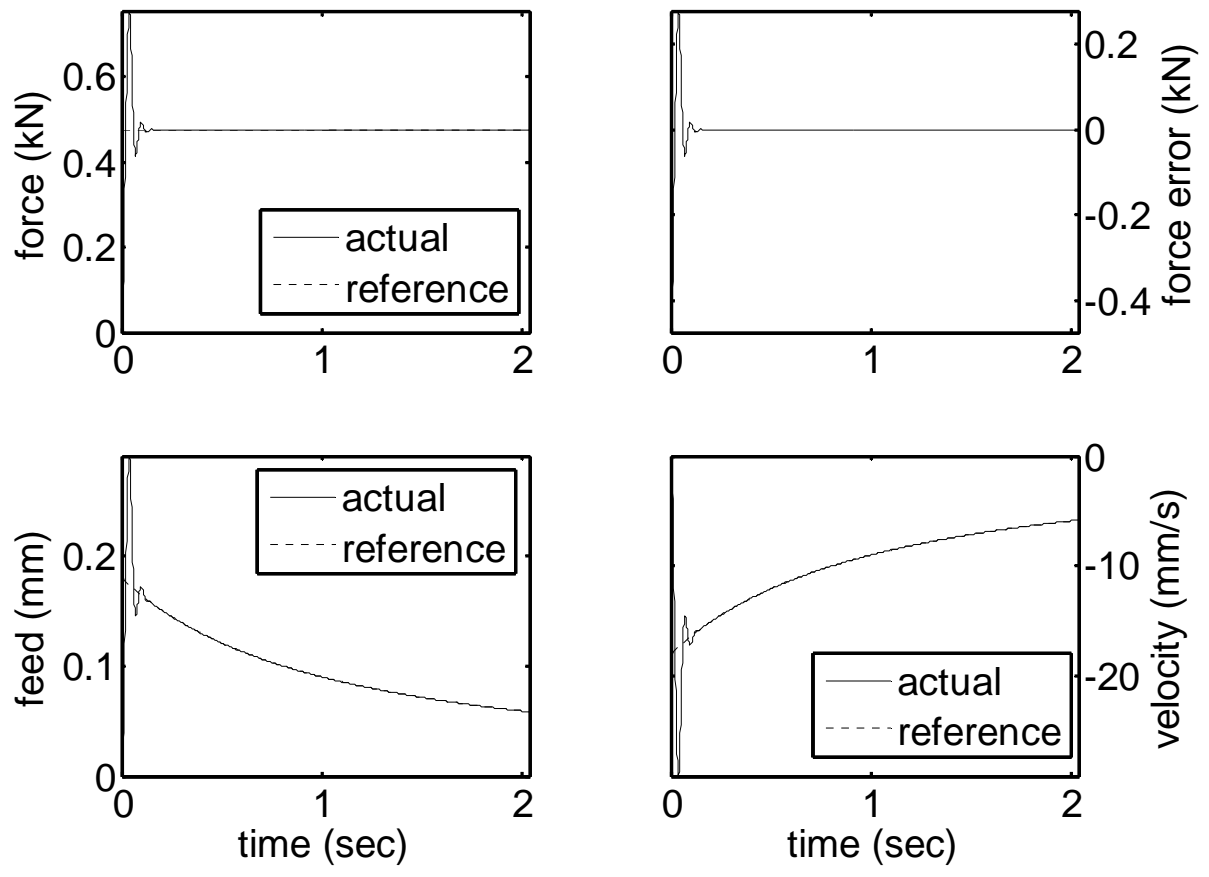reference feed decreased due to the increasing force process gain.

34
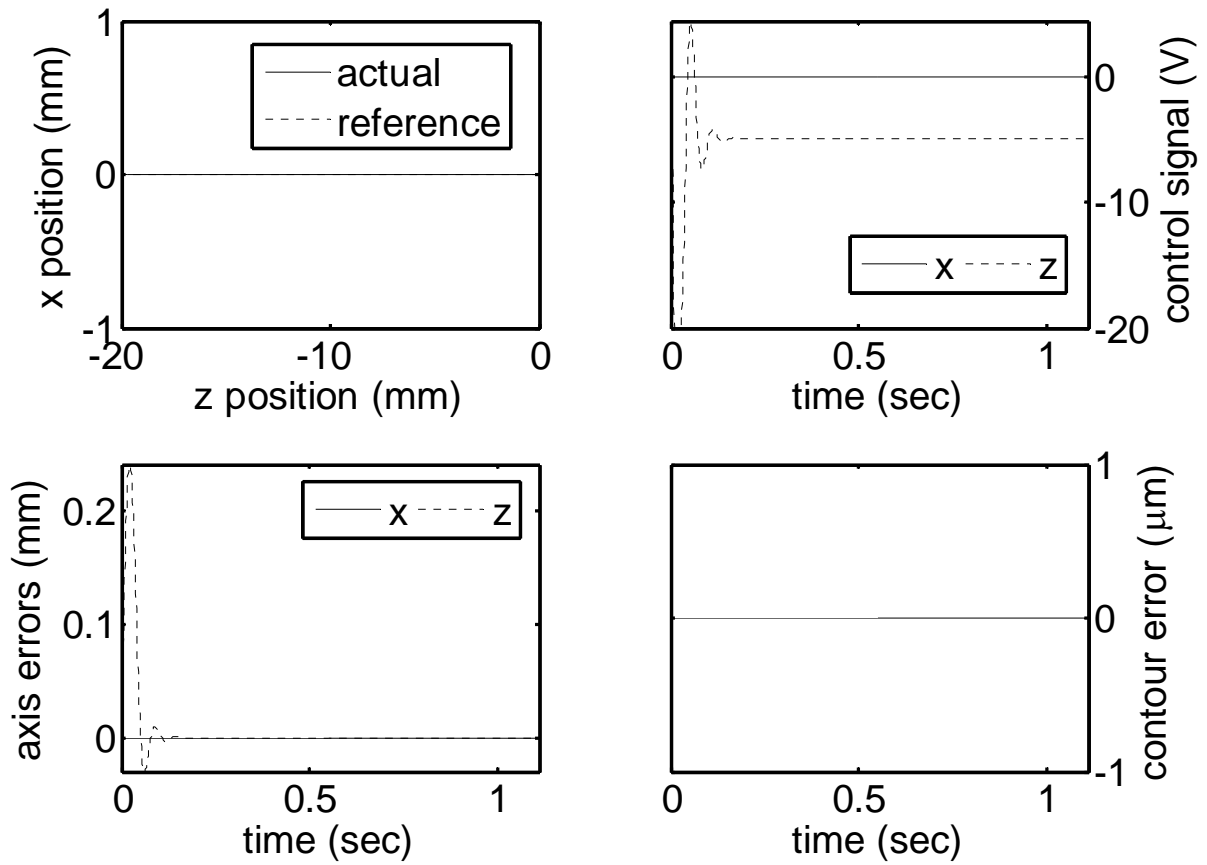
Figure 5 Case 1 (straight line with constant force process gain) simulation results (servo)

35
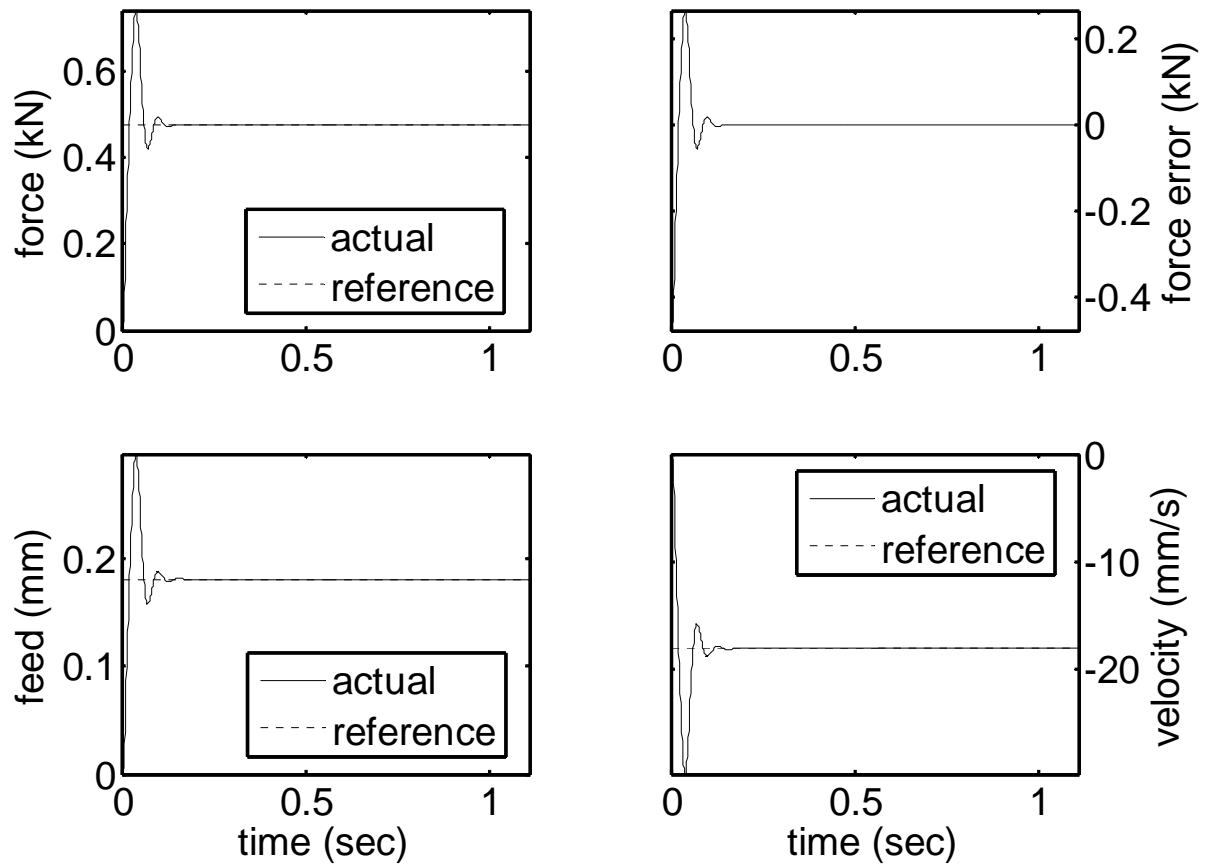
Figure 6 Case 1 (straight line with constant force process gain) simulation results (process)
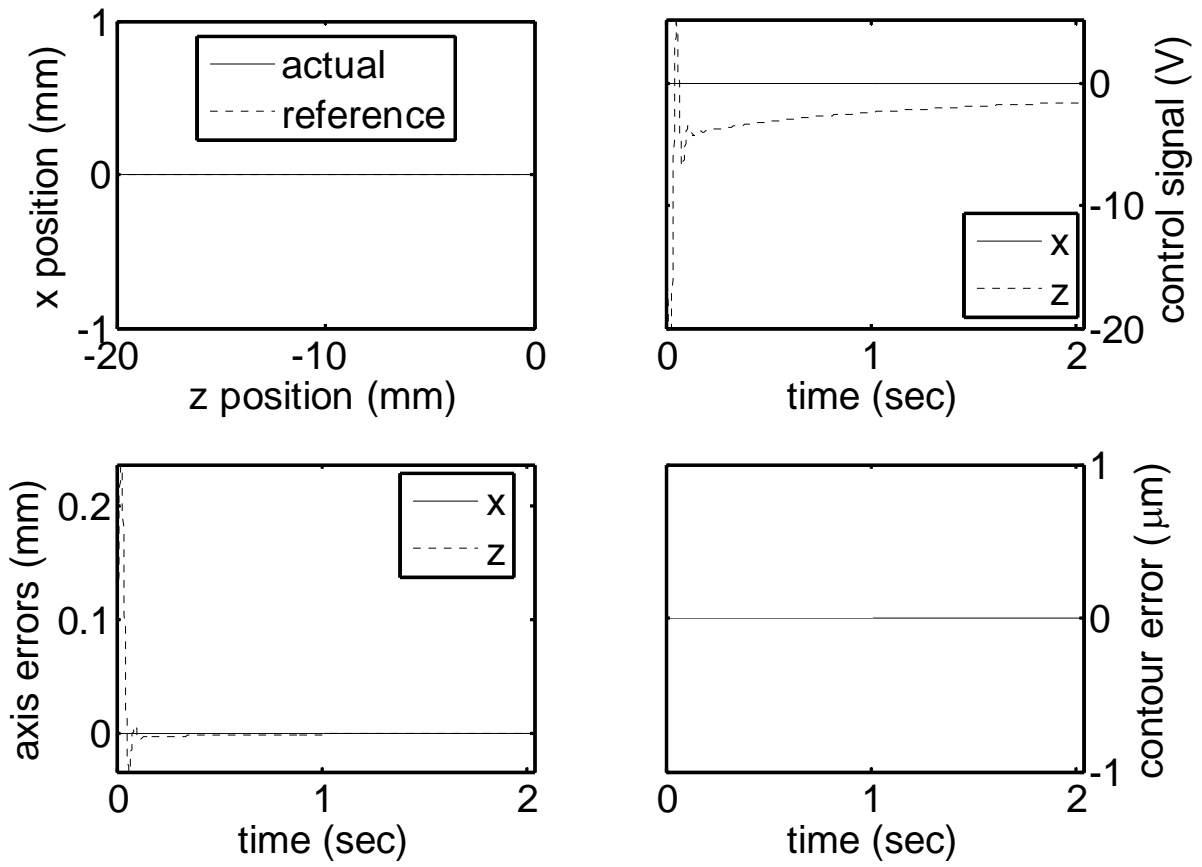
**Figure 7 Case 2 (straight line with variable force process gain)
simulation results (servo)**

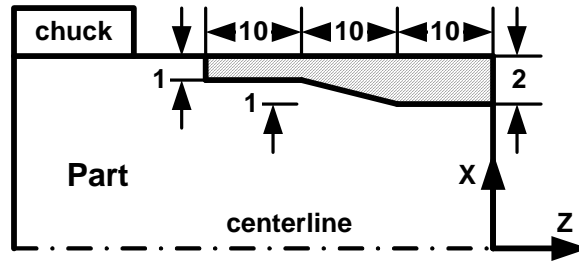**Figure 8 Case 2 (straight line with variable force process gain) simulation results (process)**
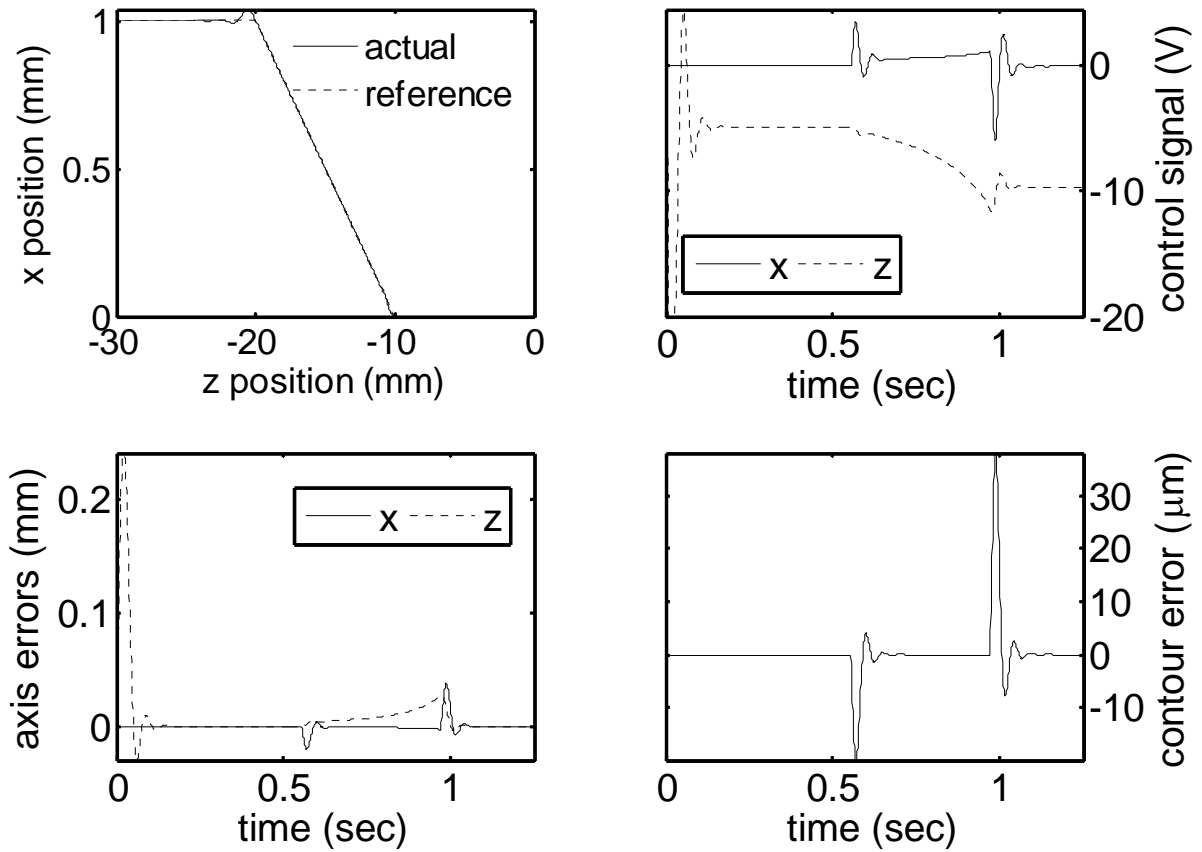
Figure 9 Operation II

Operation II

The contour of Operation II (Figure 9) comprises three sections. The first and third sections are straight lines with depths–of–cut of 2 *mm* and 1 *mm*, respectively and lengths–of–cut of 10 *mm*. The second section is a taper where the depth–of–cut continuously decreases from 2 *mm* to 1 *mm* over a length of 10 *mm*. The contour in each section has an infinite radius of curvature; thus, the reference angular velocity is zero at each section. The contour error in the first and third section is given by equation (66) and the contour error in the second section is

$$\varepsilon(t) = \frac{10}{\sqrt{1^2 + 10^2}} e_x(t) + \frac{1}{\sqrt{1^2 + 10^2}} e_z(t). \tag{67}$$

The simulation results for Cases 3 and 4 are shown in Figure 10 - Figure 13. In Case 3, the force process gain is constant and the depth–of–cut varies during the second section. Therefore, the force–feed relation is given by equation (64) and the steady–state value of $P_{bot}(t)$ is calculated at each sample period. In Case 4, the force process gain varies and the depth‑of‑cut varies during the second section. Therefore, the force–feed relation is given by equation (59) and the steady–state value of $P_{bot}(t)$ is calculated at each sample period. The steady–state contour and force errors are zero in all three sections and for both cases since an exact contour error formulation was utilized and the feed was able to track the reference feed. There is slight contour
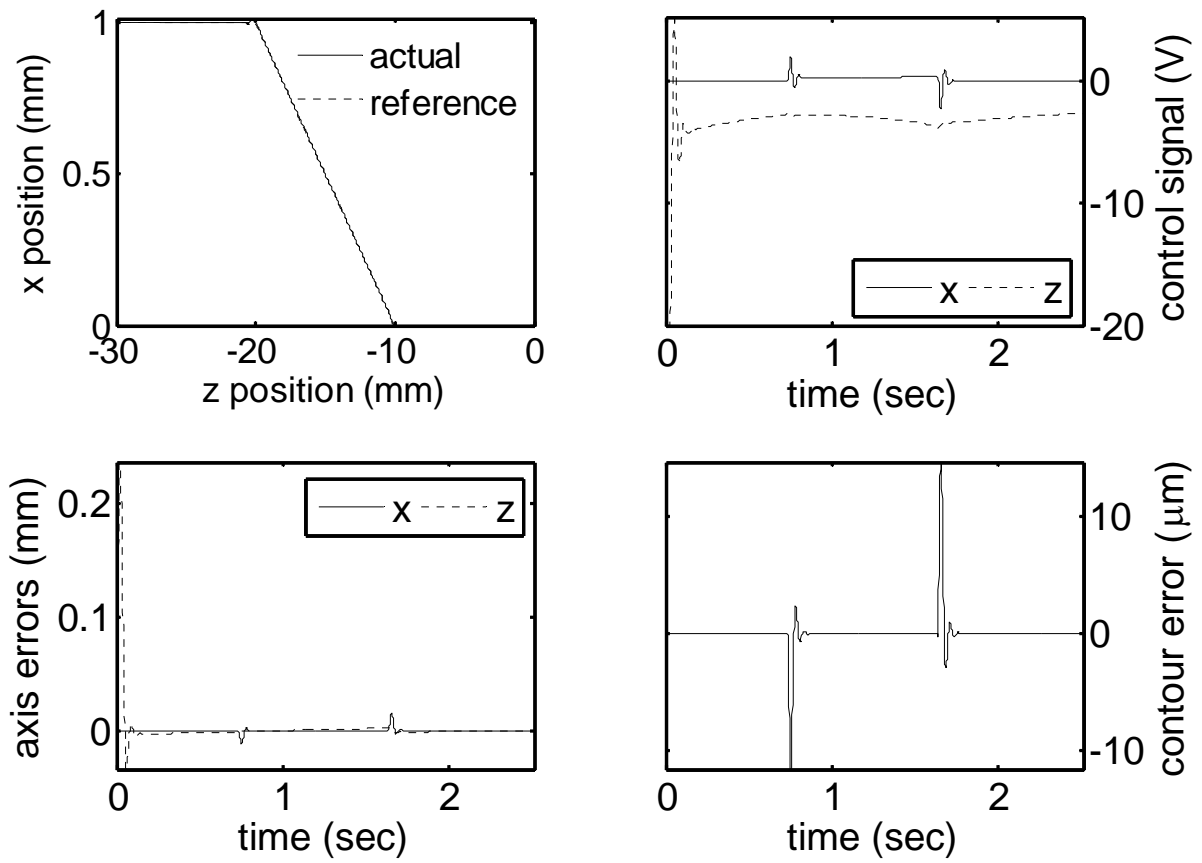
error at the transitions between the straight and taper sections due to the discontinuity in the reference velocity at these points and control signal saturation.

Figure 10 Case 3 (taper cut with constant force process gain)
simulation results (servo)
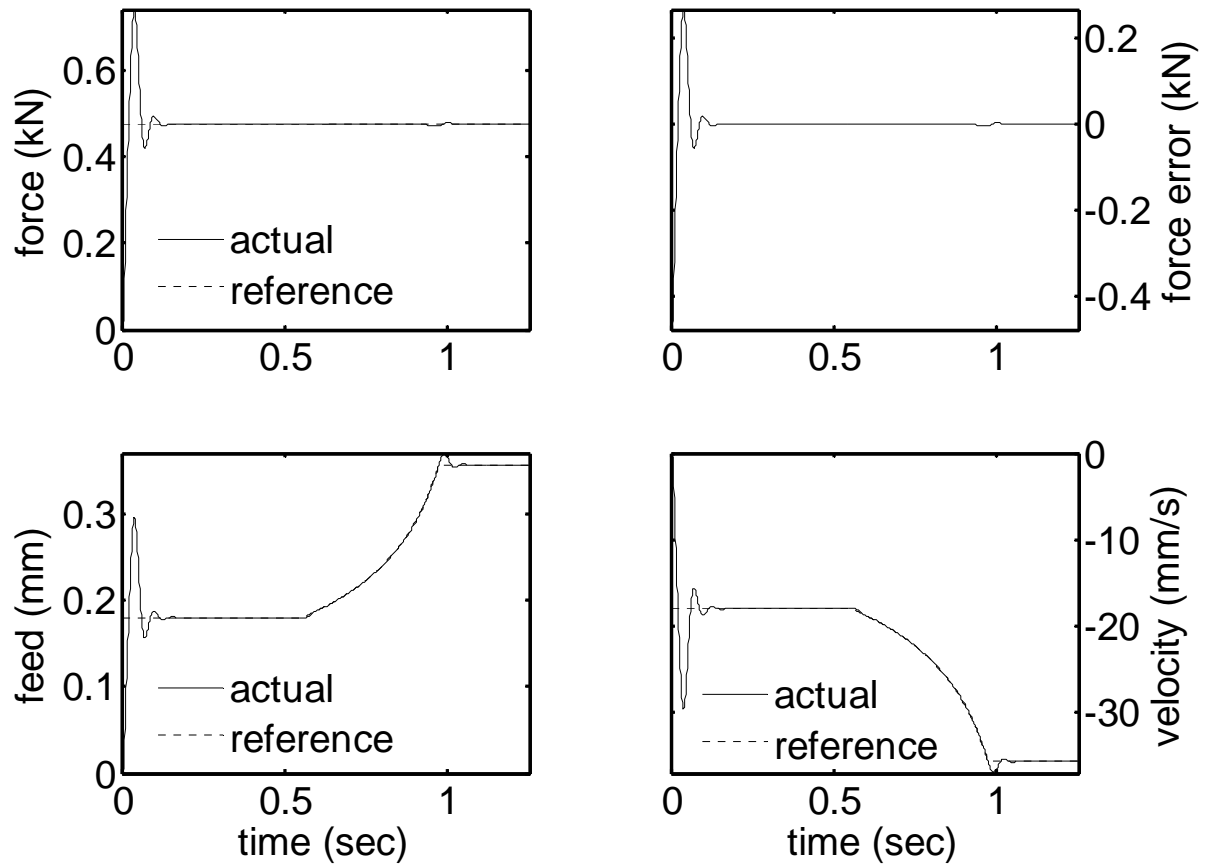
**Figure 11 Case 3 (taper cut with constant force process gain)
simulation results (process)**

Figure 12 Case 4 (taper cut with variable force process gain) simulation results (servo)
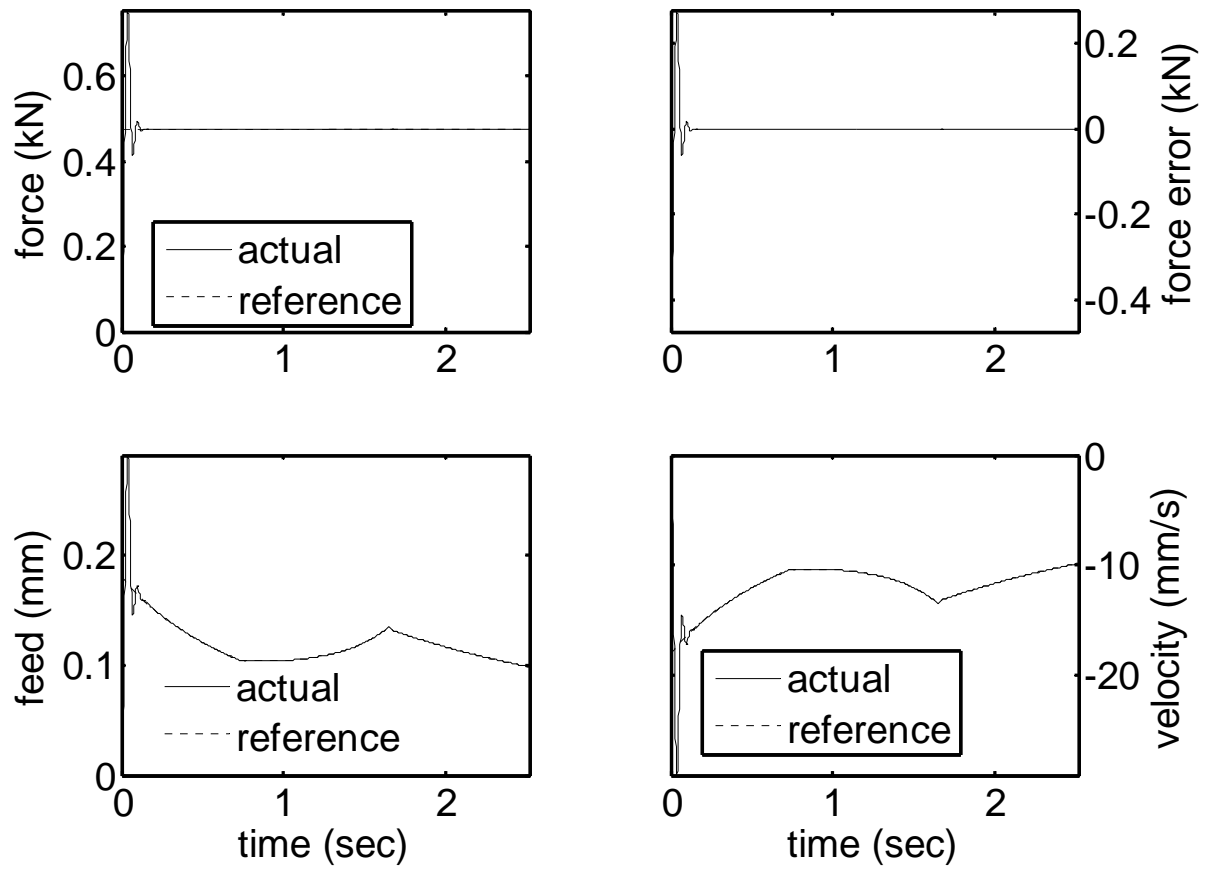
**Figure 13 Case 4 (taper cut with variable force process gain)
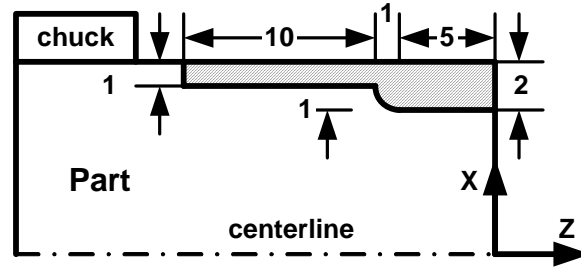simulation results (process)**

Figure 14 Operation III

Operation III

The contour of Operation III (Figure 14) comprises three sections. The first and third sections are straight lines with depths–of–cut of 2 *mm* and 1 *mm*, respectively and lengths–of–cut of 5 *mm* and 10 *mm*, respectively. The second section is a quarter circle with a radius of 1 *mm*. The contours in the first and third sections have an infinite radius of curvature; thus, the reference angular velocity is zero in these sections. The reference angular velocity in the second section is the tangential reference velocity divided by the radius. The reference angular velocity will constantly vary in this section since the reference feed will vary due to the changing depth–of–cut. The exact contour error is ([25])

$$\varepsilon(t) = \sqrt{\left\{\rho \sin\left[\phi(t)\right] + e_x(t)\right\}^2 + \left\{\rho \cos\left[\phi(t)\right] + e_z(t)\right\}^2} - \rho, \tag{68}$$

where the radius of curvature is constant and is the circle radius. The time–varying, nonlinear aggregation relationship is approximated via a Taylor series expansion

$$\varepsilon(t) = \left\{\sin\left[\phi(t)\right] + \frac{e_x(t)}{2\rho}\right\} e_x(t) + \left\{\cos\left[\phi(t)\right] + \frac{e_z(t)}{2\rho}\right\} e_z(t)$$

$$= c_x(t) e_x(t) + c_z(t) e_z(t), \tag{69}$$

The simulation results for Cases 5 and 6 are shown in Figure 15-Figure 18. In Case 5, the force process gain is constant and the depth–of–cut varies during the second section. Therefore, the force–feed relation is given by equation (64) and the steady–state value of $P_{bot}(t)$ is calculated at

44

each sample period. In Case 6, the force process gain and depth‑of‑cut vary during the second section. Therefore, the force–feed relation is given by equation (59) and the steady–state value of $P_{bot}(t)$ is calculated at each sample period. The steady–state contour and force errors are zero in the first and third sections and for both cases since an exact contour error formulation was utilized and the feed was able to track the reference feed. The contour error magnitude in the second section was less than 2 μm and the machining force error went towards zero. The non zero contour error was due to the approximation in equation (69). The tangent to the contour in this section changes from being solely in the z direction at the beginning of the contour to being solely in the x direction at the end of the contour. As a result, the reference z–axis velocity needed to maintain the machining force requires a x–axis reference velocity that exceeds its maximum value. Therefore, the x–axis reference velocity is set to its maximum value causing the reference z–axis velocity to decrease until it reaches zero at the end of the contour. This, in turn, causes the machining force to go towards zero. Again there is slight contour error at the transitions between the straight and circular sections due to the discontinuity in the reference velocity at these points and control signal saturation.
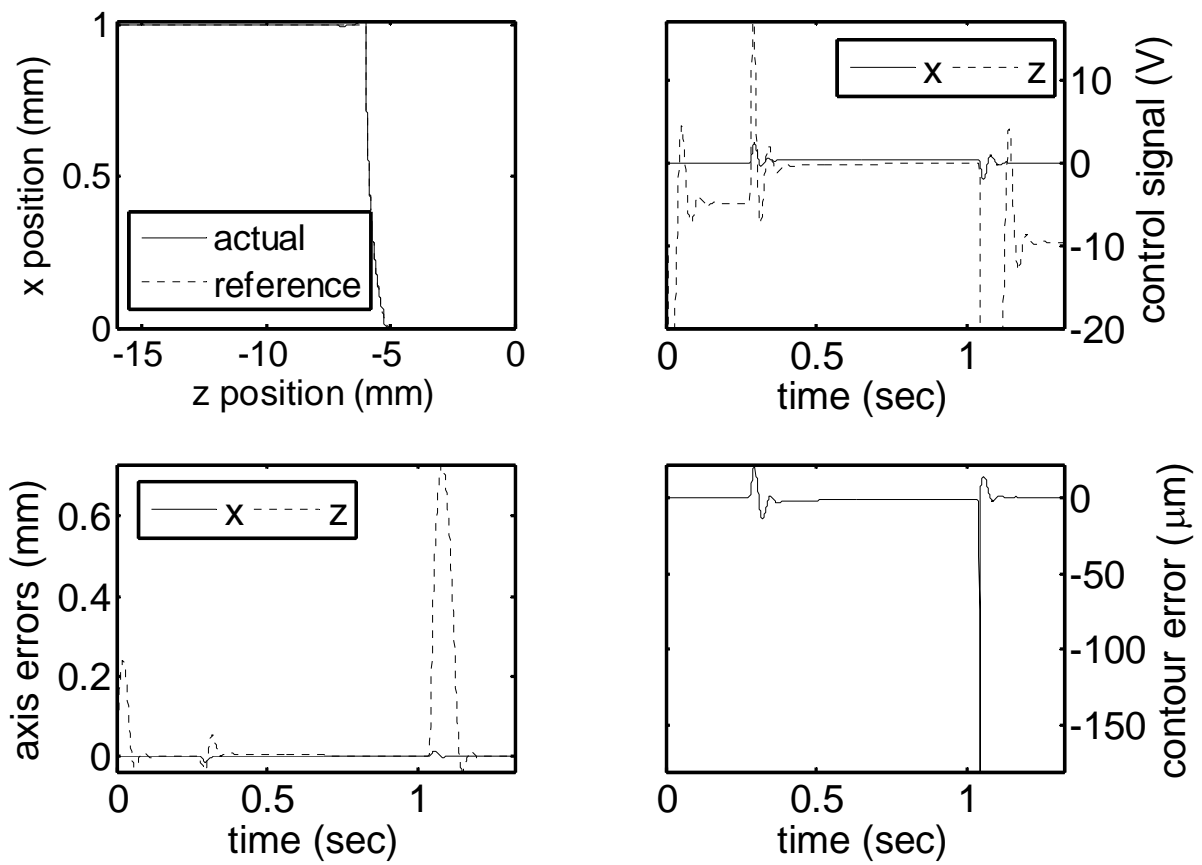
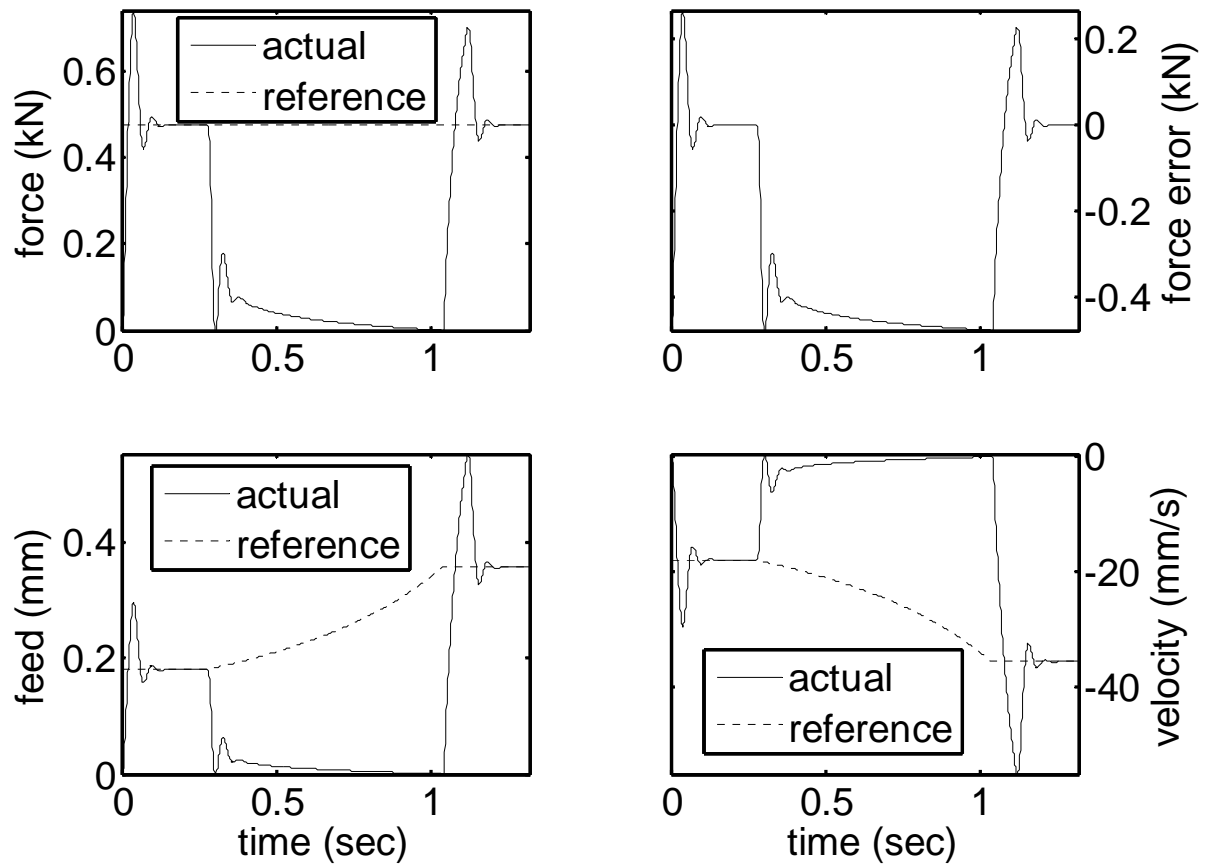**Figure 15 Case 5 (circular cut with constant force process gain) simulation results (servo)**

Figure 16 Case 5 (circular cut with constant force process gain) simulation results (process)
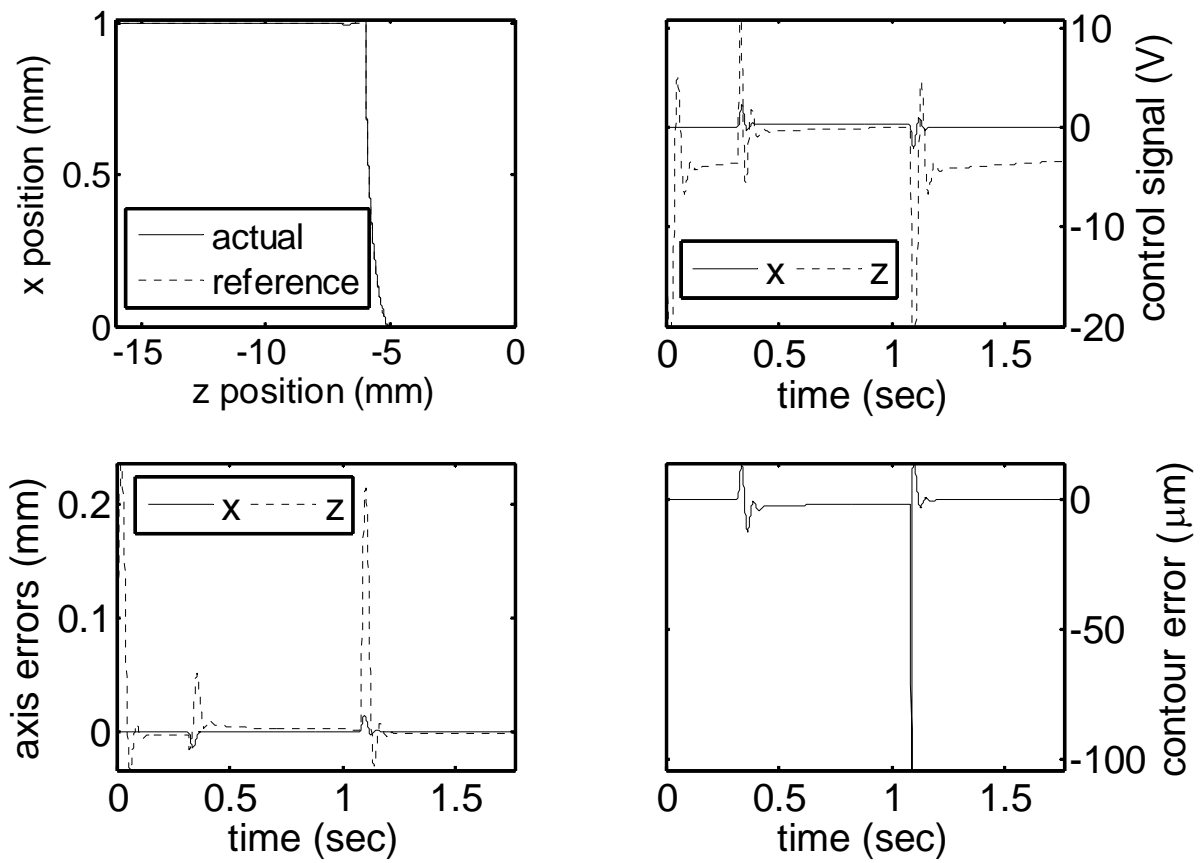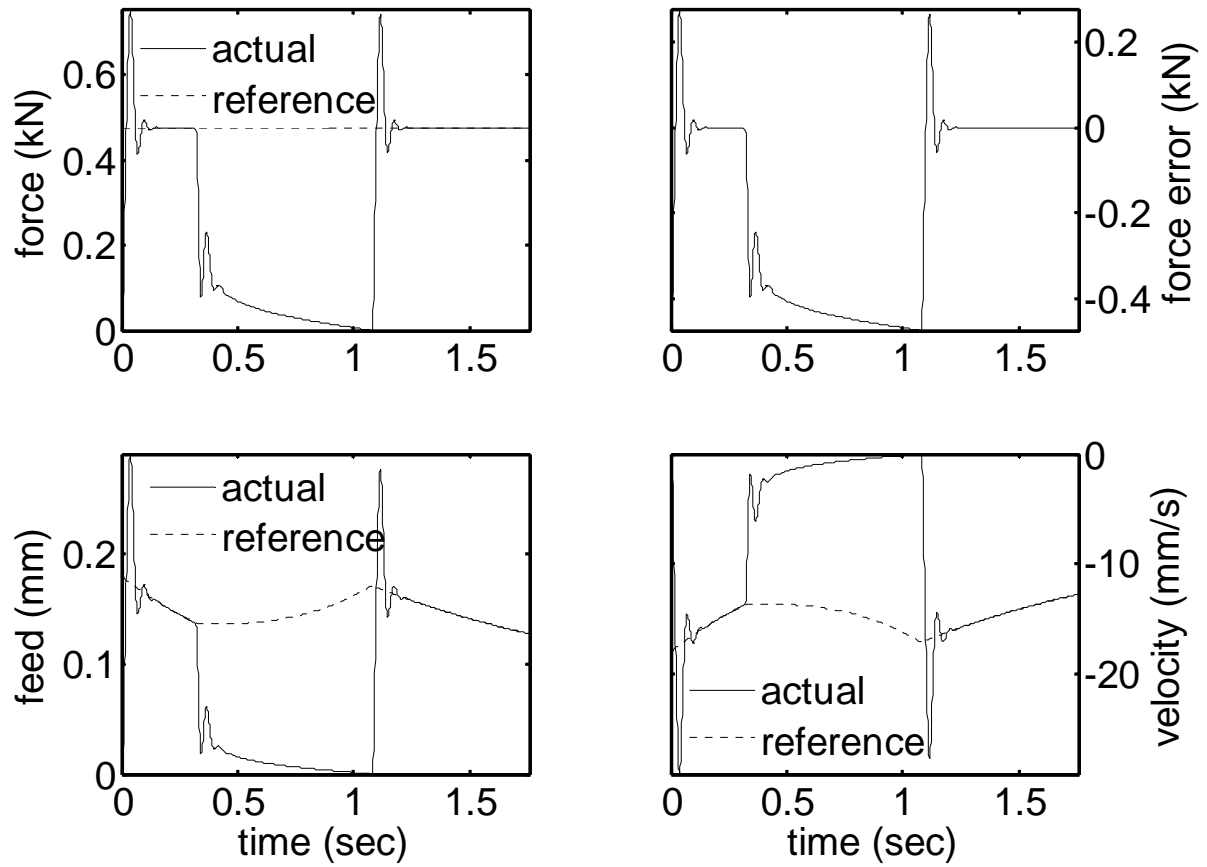
Figure 17 Case 6 (circular cut with variable force process gain) simulation results (servo)

Figure 18 Case 6 (circular cut with variable force process gain) simulation results (process)
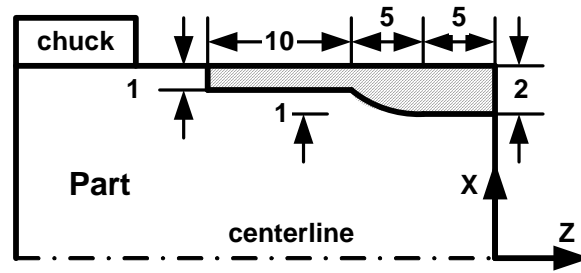
Figure 19 Operation IV

Operation IV

The contour of Operation IV (Figure 19) comprises three sections. The first and third sections are straight lines with depths–of–cut of 2 *mm* and 1 *mm*, respectively and lengths–of–cut of 5 *mm* and 10 *mm*, respectively. The second section is a quarter ellipse with a major radius of $a = 5$ *mm* and a minor radius of $b = 1$ *mm*. The contours in first and third sections have an infinite radius of curvature; thus, the reference angular velocity is zero in these sections. The reference angular velocity in the second section is the tangential reference angular velocity divided by the instantaneous radius of curvature. The reference angular velocity will constantly vary in this section since the reference feed will vary due to the changing depth–of–cut. The x and z–axis reference positions, respectively, are

$$r_x(t) = X_c + b\sin\left[\phi(t)\right], \tag{70}$$

$$r_z(t) = Z_c + a\cos\left[\phi(t)\right]. \tag{71}$$

The contour error is

$$\varepsilon(t) = \sqrt{\left[s_x(t) - X_{cc}(t)\right]^2 + \left[s_z(t) - Z_{cc}(t)\right]^2} - \rho(t), \tag{72}$$

and the actual x and z–axis positions, respectively, are

$$s_x(t) = r_x(t) + e_x(t), \tag{73}$$

$$s_z(t) = r_z(t) + e_z(t), \tag{74}$$

50

The instantaneous radius of curvature and the coordinates of the instantaneous center of curvature, respectively, are

$$\rho(t) = \frac{\left(a^2 \sin^2\left[\phi(t)\right] + b^2 \cos^2\left[\phi(t)\right]\right)^{1.5}}{ab}, \tag{75}$$

$$X_{cc}(t) = X_c + \frac{b^2 - a^2}{b} \sin^3\left[\phi(t)\right], \tag{76}$$

$$Z_{cc}(t) = Z_c + \frac{a^2 - b^2}{a} \cos^3\left[\phi(t)\right]. \tag{77}$$

Substituting equations (73) and (74) into equation (72) and expanding the resulting equation by a second order Taylor's series expansion, the contour error is

$$\begin{aligned}\varepsilon(t) &= \left\{ \frac{r_x(t) - X_{cc}(t)}{\rho(t)} + \frac{e_x(t)}{2\rho(t)} \right\} e_x(t) + \left\{ \frac{r_z(t) - Z_{cc}(t)}{\rho(t)} + \frac{e_z(t)}{2\rho(t)} \right\} e_z(t) \\ &= c_x(t) e_x(t) + c_z(t) e_z(t).\end{aligned} \tag{78}$$

The simulation results for Cases 7 and 8 are shown in Figure 20-Figure 23. In Case 7, the force process gain is constant and the depth–of–cut varies during the second section. Therefore, the force–feed relation is given by equation (64) and the steady–state value of $P_{bot}(t)$ is calculated at each sample period. In Case 8, the force process gain and depth – of – cut vary during the second section. Therefore, the force–feed relation is given by equation (59) and the steady–state value of $P_{bot}(t)$ is calculated at each sample period. The steady–state contour and force errors are zero in the first and third sections and for both cases since an exact contour error formulation was utilized and the feed was able to track the reference feed. The contour error magnitude in the second section was less than 4 μm and the machining force error went towards zero. The non zero contour error was due to the approximation in equation (78). The tangent to the contour in this section changes from being solely in the z direction at the beginning of the contour to being

solely in the *x* direction at the end of the contour. As a result, the reference *z*–axis velocity needed to maintain the machining force requires a *x*–axis reference velocity that exceeds its maximum value. Therefore, the *x*–axis reference velocity is set to its maximum value causing the reference *z*–axis velocity to decrease until it reaches zero at the end of the contour. This, in turn, causes the machining force to go towards zero. Again there is slight contour error at the transitions between the straight and elliptical sections due to the discontinuity in the reference velocity at these points and control signal saturation.
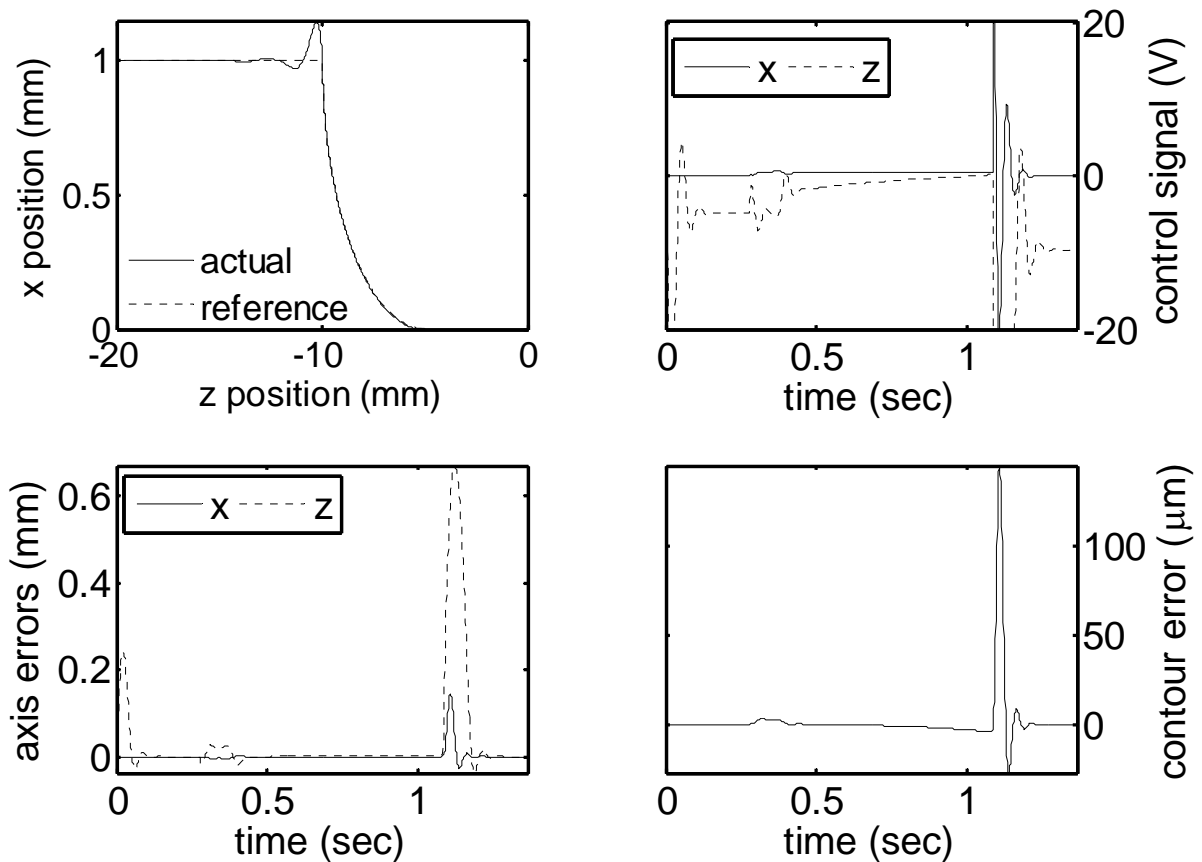

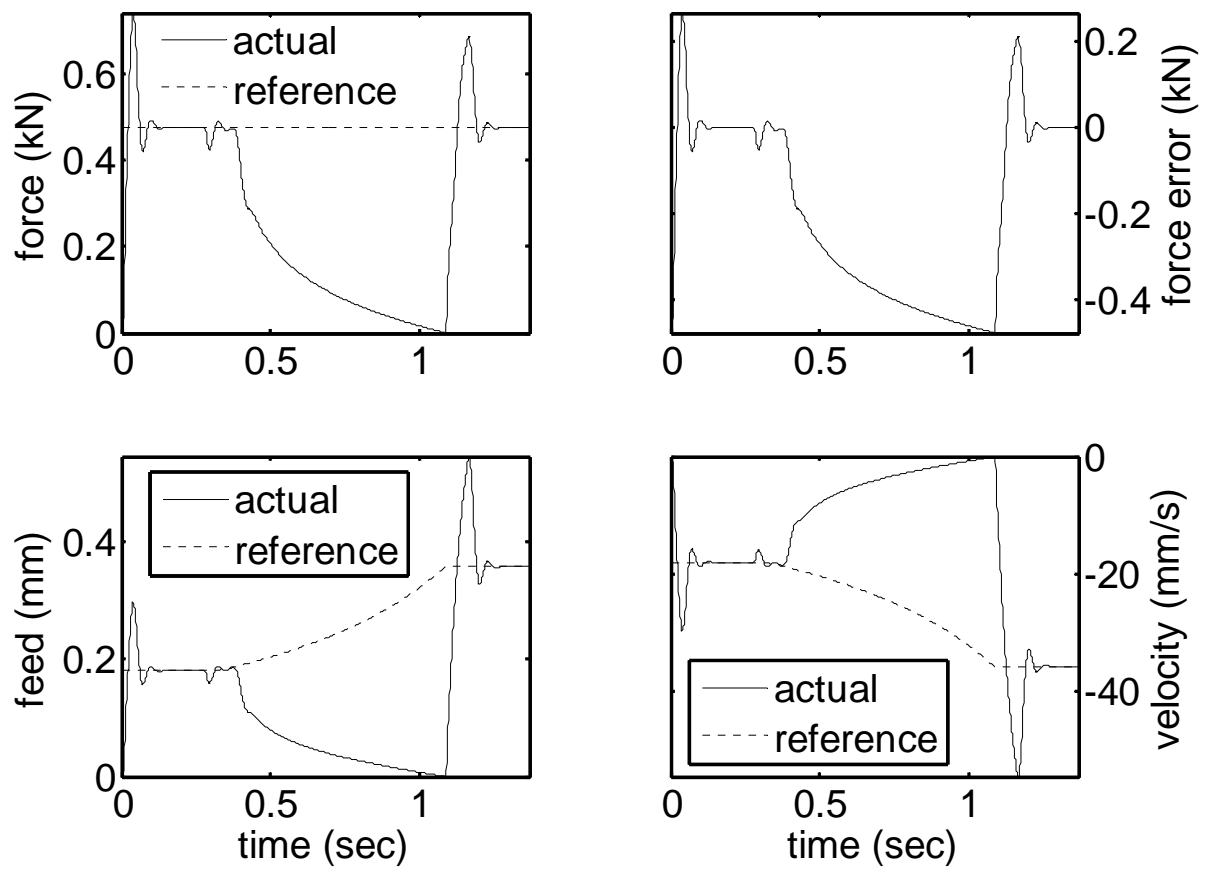**Figure 20 Case 7 (elliptical cut with constant force process gain) simulation results (servo)**

Figure 21 Case 7 (elliptical cut with constant force process gain) simulation results (process)
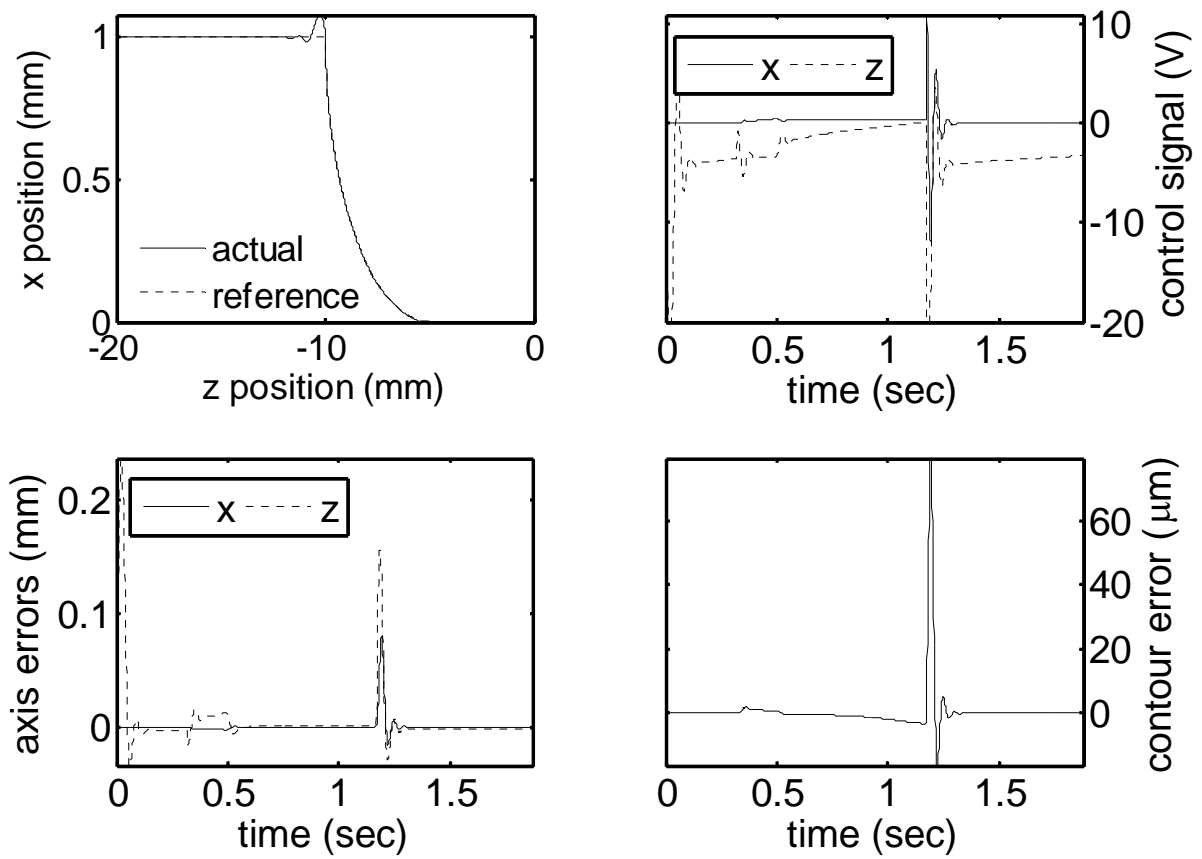
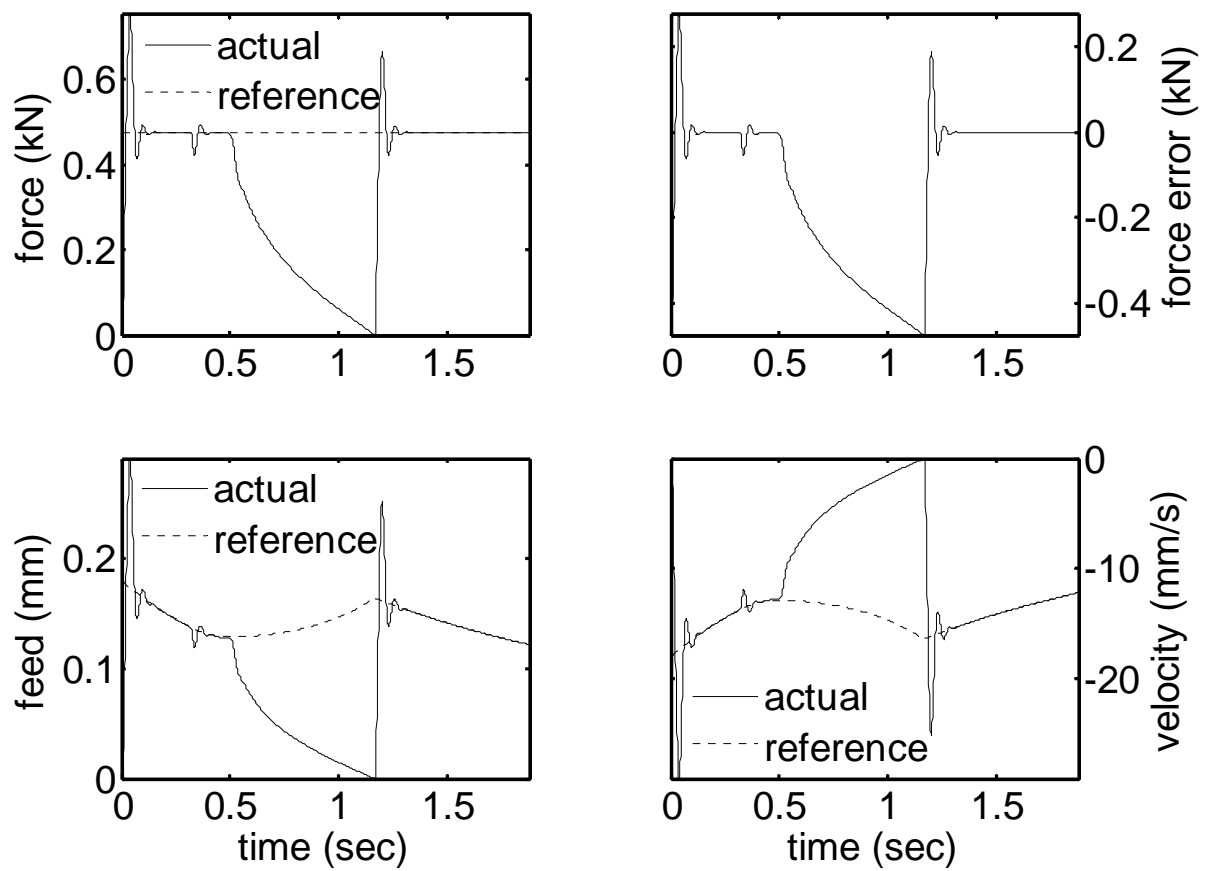**Figure 22 Case 8 (elliptical cut with variable force process gain) simulation results (servo)**

Figure 23 Case 8 (elliptical cut with variable force process gain) simulation results (process)

3.5   Summary and Conclusions

A direct integration of the servomechanism control and the process control was implemented via a hierarchical optimal control methodology. The developed controller can simultaneously regulate servomechanism position errors, contour error, and machining forces. The hierarchy contained two levels: the process level where the machining forces and contour error resided and the servo level where the servomechanism position errors resided. The requirements of a constant machining force and zero contour error were propagated to the bottom level via aggregation relationships between the machining force and contour errors and the servomechanism position errors. An optimal control problem was formulated and solved to construct a control law at the bottom level that simultaneously regulates the machining force, contour error, and servomechanism position errors. The hierarchical optimal control methodology was extended to account for variations in force process model parameters and process parameters.

The hierarchical optimal control methodology was applied to a two–axis lathing operation and simulations of four different operations were conducted to verify the developed methodology. Although the illustrative example was a two–axis lathing operation, the methodology can be applied to most machining operations. The results showed that the controller is able to simultaneously achieve machining force, contour error, and servomechanism position error requirements. Thus, the proposed technique greatly decreases the complexity of the overall control system as separate machining force process and contour controllers are not required. The simulation results showed that the developed methodology could be applied to complex contours where machining force model parameters and process parameters were changing simultaneously.

The hierarchical optimal control methodology presented in this paper provides a systematic strategy to integrate machining force process, contour, and servomechanism position control in machining operations.

CHAPTER 4 HELICAL END MILL DEFLECTION ANALYSIS

4.1   <u>Introduction</u>

In the previous chapter, the integration of control systems at the servo level and the process level is implemented through the parameter aggregation when the process parameters can be related to the servomechanism states directly. In some machining processes, however, such analytical aggregation is not available or difficult to obtain. Therefore, the process control cannot be aggregated in the servomechanism controller. On the other hand, some machining processes require real time modification of the tool path to compensate for the deformation errors between the cutting tool and the workpiece. Alternative servo-process control integration strategy should be developed to handle such case. The cutter deflection compensation in helical end milling is one example.

Cutter deflection is a common problem affecting machining accuracy in end-milling processes. End mills are cantilevered to the spindle through tool holder, and cutting takes place at the periphery of the free end. Although the cantilever beam structure facilitates automatic tool changers with flexibility in tool change, it deteriorates the machining accuracy when the cutter deflects under lateral cutting loads. Such structural feature makes accuracy an important subject in process control of end milling.

Literature review shows that process design and offline tool path offset are two commonly used strategies to improve accuracy in end-milling processes. The process design approach selects conservative machining conditions to avoid excessive deflection. So it is a strategy to improve accuracy at the cost of reducing productivity, which is not an optimal solution for mass production. Offline tool path offset approach, on the other hand, relies on the estimation accuracy of deflection, although it allows aggressive cutting conditions. The

estimation of deflection is based on the modeling of cutting forces, cutter geometry, and the cutting process. Due to the complexity of end milling processes, it is difficult to provide satisfactory deflection estimation. Therefore, the performance of offline tool path offset approach is questionable with the inherent modeling difficulty.

Online tool path offset may become an effective and economic strategy to improve accuracy in end milling. The tool path is offset during cutting according to deflection measurement from sensors. So the compensation effect mainly depends on the sensor performance, which was the obstacle for this approach. With the advances in reliable and economical optical sensors, the bottleneck will be overcome. Therefore, the online tool path offset would be a prospective process control approach to improve accuracy in end milling at no cost of productivity.

This process control, however, cannot be integrated with servomechanism control the same way as the approach introduced in the previous chapter. The difficulty arises from the fact that the surface accuracy error due to deflection cannot be associated with the servomechanism states directly. Recall that the force model used in Chapter 3 is static model which is defined as either maximum or average cutting force within one spindle revolution and is associated with process parameters such as feed f and depth of cut d. However, from the following analysis, it will be seen that the surface errors are associated with instantaneous cutting forces which are varying and cannot be modeled as function of process parameters. Due to the unavailability of aggregation relationship between the process and the servomechanism, the approach developed in Chapter 3 cannot be adopted for this case. A new servo-process control integration strategy should be developed. The strategy will be presented by two chapters. In this chapter, the complex impact of deflection on accuracy is analyzed to show the unavailability of aggregation between

surface errors due to cutter deflection and servomechanism states. The analysis will be provided through cutting force modeling, deflection model, and relationship between deflection and surface accuracy errors. Although such analysis is trivial for straight surfaces, milling of curved surfaces is rarely treated, and this void will be filled in this chapter. The analysis results will be used for developing integrated servo-process control for deflection compensation, which will be covered in the next chapter.

The chapter is organized as follows. The instantaneous cutting force model and simulation procedure are presented in section 4.2. Deflection model and resulting surface accuracy in milling of straight surfaces and curved surfaces are examined in section 4.3 and section 4.4, respectively. Section 4.5 concludes the chapter with summaries and conclusions.

4.2   Cutting Force Model

End mills deflect under lateral cutting forces applied at the free end, and excessive deflection will cause defects in machined parts. In order to analyze the impact of deflection on accuracy, we should start from modeling cutting forces in end milling. In this section, the cutting force model is presented, and then, deflection due to cutting forces is modeled by the cantilever beam theory.

In order of sophistication and accuracy, the available cutting force models are classified as *the average rigid force with static deflection model*, *the instantaneous rigid force model*, *the instantaneous rigid force with static deflection model*, *the instantaneous force with static deflection feedback model*, and *the regenerative force with dynamic deflection model* ([72]). Based on the relationship between metal removal rate (MRR) and the consumed average power in cutting, the average force model could be used only for rough estimation of deflection since the model is not able to reveal the relationship between deflection and the surface location error. So this model cannot be used in our deflection compensation study which requires such information. Similarly, the instantaneous rigid force model cannot be used either because the model is only used for cutting force prediction without considering deflection. Although the last two models would provide more accurate surface information, we only need a working model to associate the deflection with the surface location error so that we can proceed the online deflection compensation controller design. On the other hand, the online compensation strategy expects to get instantaneous deflection information from sensors rather than estimation from cutting force models. Otherwise, the performance of this strategy will also be problematic by the reliance on modeling accuracy as in the offline tool path offset approach. Therefore, the instantaneous force with static deflection model is used for the simulation study.

Combining the process geometry model developed by Martellotti and the mechanistic model of the end milling process proposed by Tlusty and MacNeil [43, 44, 73], the instantaneous force with static deflection model can predict the instantaneous force system characteristic [42]. As a multi-tooth cutting process, end milling removes metal by engagement of each tooth, and therefore cutting forces are computed from the chip load which is the product of the width of cut and the chip thickness generated from each tooth pass. Chip thickness in end milling can be derived from the process geometry, as an up-milling example shown Figure 24 [74]. Although the chip thickness varies during the cut, the maximum chip thickness is used for cutting force computation. It can be seen from Figure 24 that the maximum chip thickness for each tooth pass can be approximated as

$$h(\theta) \approx f_t \sin(\theta), \tag{79}$$

where θ is the rotation angle of the engaged tooth, and f_t is feed per tooth, given by

$$f_t = \frac{f_r}{N_t \cdot n}, \tag{80}$$

where f_r is the feed rate (mm/min), N_t is the flute number, and n is the spindle speed (rpm).

Due to the effect of helix angle of end mills, the rotation angle of each cutting point varies along the cutting edge. In order to reduce the influence of the helix angle, the cutter is divided to N_z number of equally distributed disks, each of which has the height of $dz = d_a / N_z$ with d_a is the axial depth of cut (see Figure 25). The rotation angle of the cutting point at the jth tooth of the kth disk can be represented by
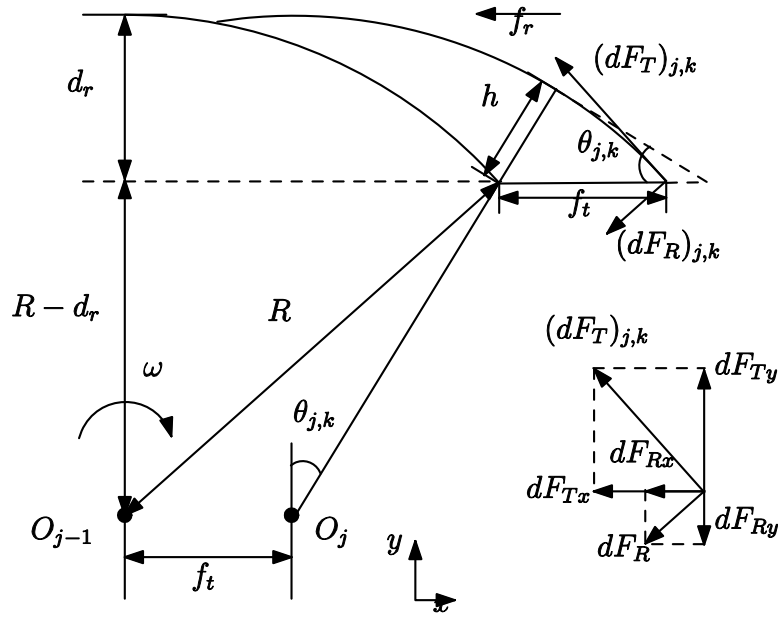
Figure 24 Chip Thickness and Cutting Forces
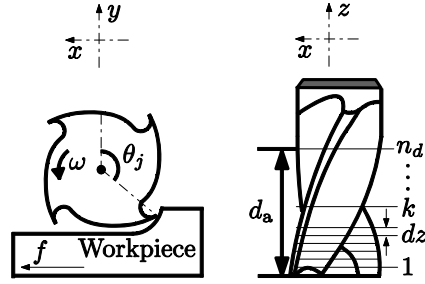
Figure 25 Process Geometry

$$\theta_{j,k}(t) = \theta(t) + (j-1)\theta_p - \frac{(k-1)\cdot dz \cdot \tan\beta}{R}, \tag{81}$$

where $\theta(t)$, as the reference angle, is the immersion angle of the leading point of the first tooth defined by the user, $\theta_p = 2\pi / N_t$ is the pitch angle of a cutter with N_t number of teeth, β is the helix angle of the cutter, and R is the radius of the cutter. Note that the addition operation on the second term in equation (81) conforms to the convention of tooth index in clockwise, and the subtraction operation on the third term in equation (81) indicates that a right hand helical end mill cutter is used.

63

The cutting forces will be computed on the teeth engaged in cutting. Cutting only occurs when

$$\theta_{st} \leq \theta_{j,k}(t) \leq \theta_{ex}, \tag{82}$$

where θ_{st} and θ_{ex} represent the entry angle and the exit angle, respectively (see Figure 25).During the steady state of cutting, $\theta_{st}=0$ and $\theta_{ex}=\arccos[(R-d_r)/R]$ are for up-milling; $\theta_{st}=\arccos[(R-d_r)/R]$ and $\theta_{ex}=\pi$ are for down-milling. Therefore, the engagement of any point on the cutting edge can be determined by equation(82).

Cutting forces, including the tangential and radial force, are computed on the cutting point of each disk. As seen from Figure 24, the elemental tangential cutting force dF_T and radial cutting force dF_R applied at tooth j on level k are given by

$$\left(dF_T(t)\right)_{j,k} = K_T \cdot dz \cdot h\left(\theta_{j,k}(t)\right), \tag{83}$$

$$\left(dF_R(t)\right)_{j,k} = K_R \cdot \left(dF_T(t)\right)_{j,k}, \tag{84}$$

where K_T is the specific tangential cutting force and K_R is the proportionality between the radial and the tangential cutting forces. Both K_T and K_R are estimated experimentally. Since the directions of both the tangential and the radial cutting forces change along the cutting edge, these forces are decomposed to the global x-y coordinates, where the x-axis is along with the feed direction and the y-axis is along with the cross-feed direction. The corresponding elemental cutting forces $(dF_x)_{j,k}$ and $(dF_y)_{j,k}$ are represented by

$$\left(dF_x\right)_{j,k} = -\left(dF_T(t)\right)_{j,k} \cdot \cos\left(\theta_{j,k}(t)\right) - \left(dF_R(t)\right)_{j,k} \cdot \sin\left(\theta_{j,k}(t)\right), \tag{85}$$

$$\left(dF_y\right)_{j,k} = \left(dF_T(t)\right)_{j,k} \cdot \sin\left(\theta_{j,k}(t)\right) - \left(dF_R(t)\right)_{j,k} \cdot \cos\left(\theta_{j,k}(t)\right). \tag{86}$$

By summing up cutting forces given in equations (85) and (86), the total cutting forces are given by

$$F_x = \sum_{j=1}^{N_t} \sum_{k=1}^{N_z} -\left(dF_T(t)\right)_{j,k} \cdot \cos\left(\theta_{j,k}(t)\right) - \left(dF_R(t)\right)_{j,k} \cdot \sin\left(\theta_{j,k}(t)\right), \tag{87}$$

$$F_y = \sum_{j=1}^{N_t} \sum_{k=1}^{N_z} \left(dF_T(t)\right)_{j,k} \cdot \sin\left(\theta_{j,k}(t)\right) - \left(dF_R(t)\right)_{j,k} \cdot \cos\left(\theta_{j,k}(t)\right). \tag{88}$$

Equations (87) and (88) provide instantaneous cutting forces generated by all engaged cutting points. Then, the cutting force profile can be obtained through numerical simulations so that we could gain insights on cutting behavior under different cutting conditions.

In order to gain insights of cutting forces under different cutting conditions, The simulated cutting forces with cutting conditions of up-milling in Table 1 are shown in Figure 26-Figure 33. For case 1, $K_T = 6.598 \times 10^9$ Pa and $K_R = 0.3$. For case 2, $K_T = 5.377 \times 10^9$ Pa and $K_R = 0.408$ ([41]). Case 1 and Case 2 are same in the cutter geometry, workpiece material and spindle speed while differ in cutting conditions such as the feed rate, the radial and axial depth of cut. Case 1 uses more conservative cutting conditions than Case 2. Such difference can be seen from the magnitude of cutting forces, as shown in Figure 26 and Figure 30. Note that positive F_y indicates that the direction of F_y is away from the workpiece according to the schematic of up-milling shown in Figure 24.

Figure 27-Figure 28 and Figure 31-Figure 32 show cutting forces applied on each cutting edge for two cases. Theses plots are useful in analyzing the engagement of cutting edge. For example, Figure 27-Figure 28 show that most of time there is only one cutting edge engaged but at most two cutting edges engaged simultaneously during cutting in Case 1, while Figure 31-Figure 32 indicate different phenomena in Case 2. Either three cutting edges or two cutting edges

65

simultaneously engage during the cutting. The engagement and cutting force information will be used for further analysis of deflection.

Due to the varying engagement of cutting edges, the instantaneous force center varies as well. Since the finished surface is parallel to the cutter axis, only deflection due to F_y may affect surface accuracy. So only the force center of F_y is considered. The force center is the point along the cutter axis where the resultant F_y produces the same bending moment about the tool holder as the distributed elemental forces on the cutting edges. The force center variations for Case 1 and Case 2 are shown in Figure 29 and Figure 33, respectively. It can be seen that the force center oscillate about the axial elevation at half of axial depth of cut.

Table 1 Cutting Conditions For End Milling Numerical Simulation ([41])

Cutting Prameters	Case 1	Case 2
Cutter diameter (mm)	25.4	25.4
Number of flutes	4	4
Helix angle (deg)	30	30
Radial depth of cut (mm)	6.3	12.7
Axial depth of cut (mm)	25.2	50.4
Spindle speed (rpm)	191	191
Feed rate (mm/min)	9.932	99.32
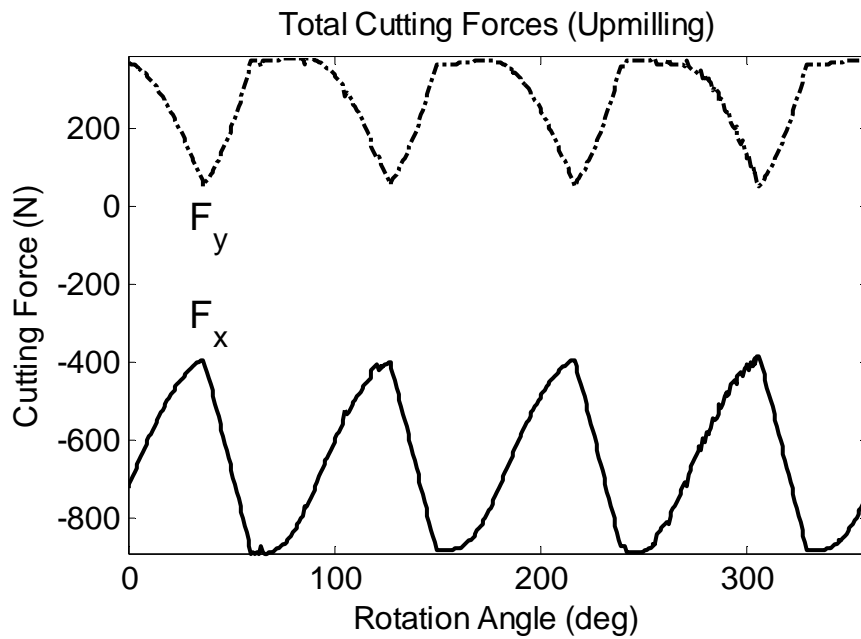
Figure 26 Total Cutting Forces for Case 1 in Table 1 (Up-milling)
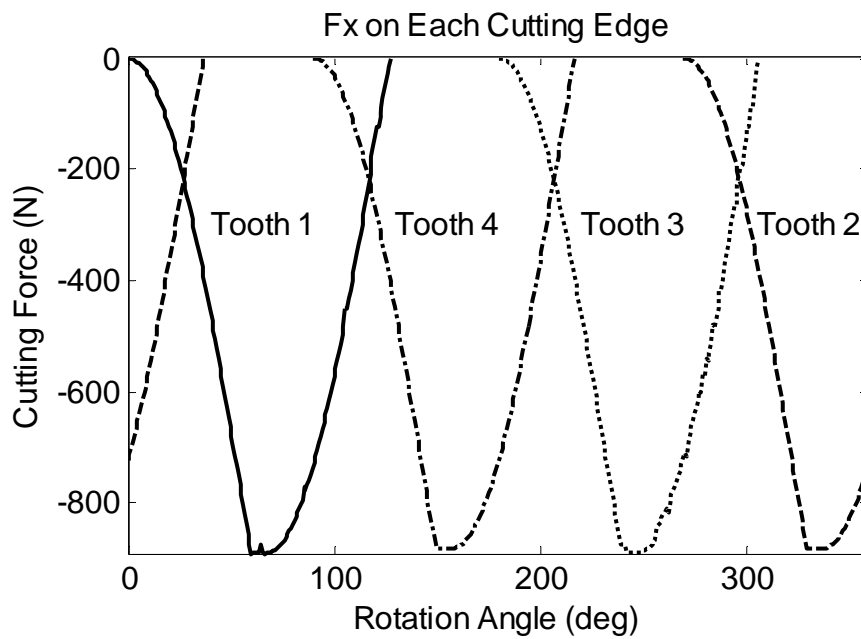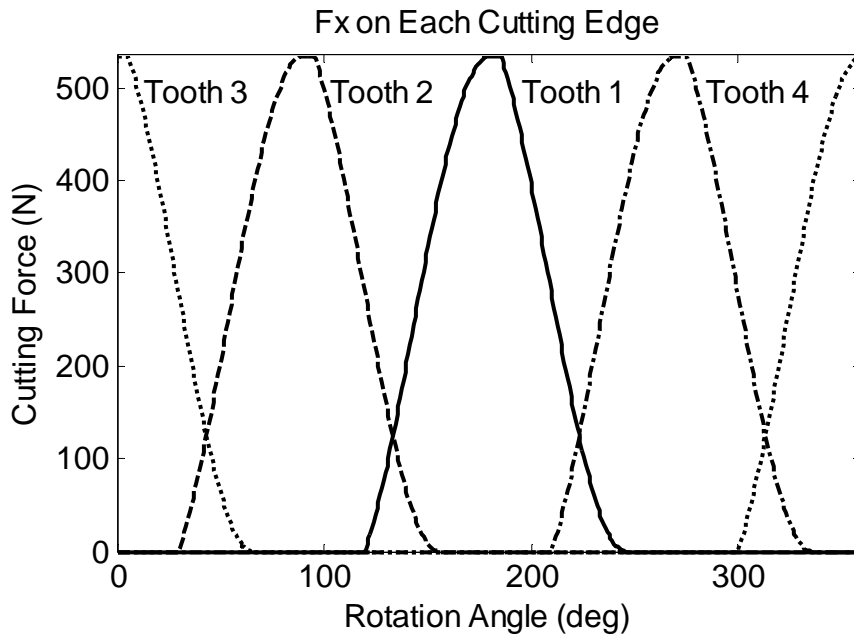

Figure 27 F_x on Each Cutting Edge for Case 1 in Table 1 (Up-milling)
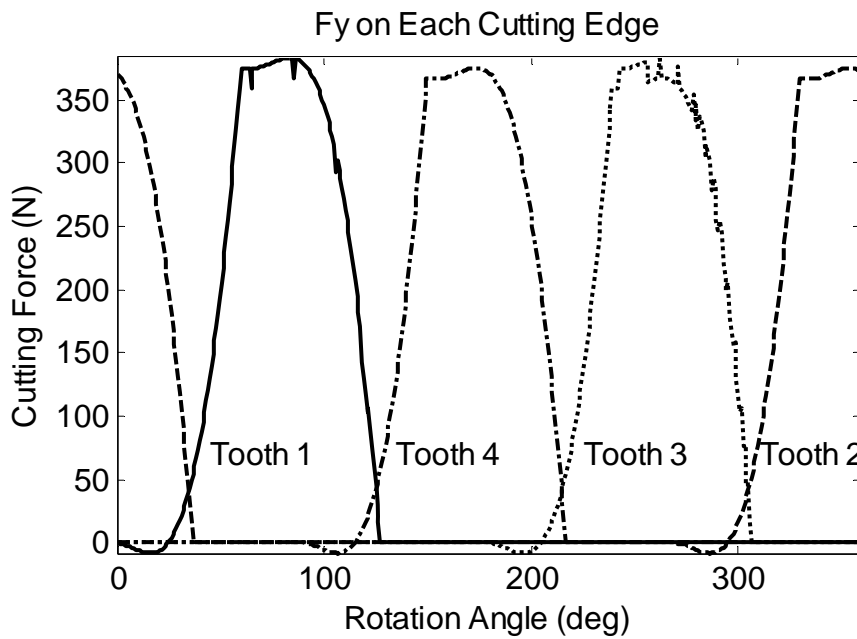
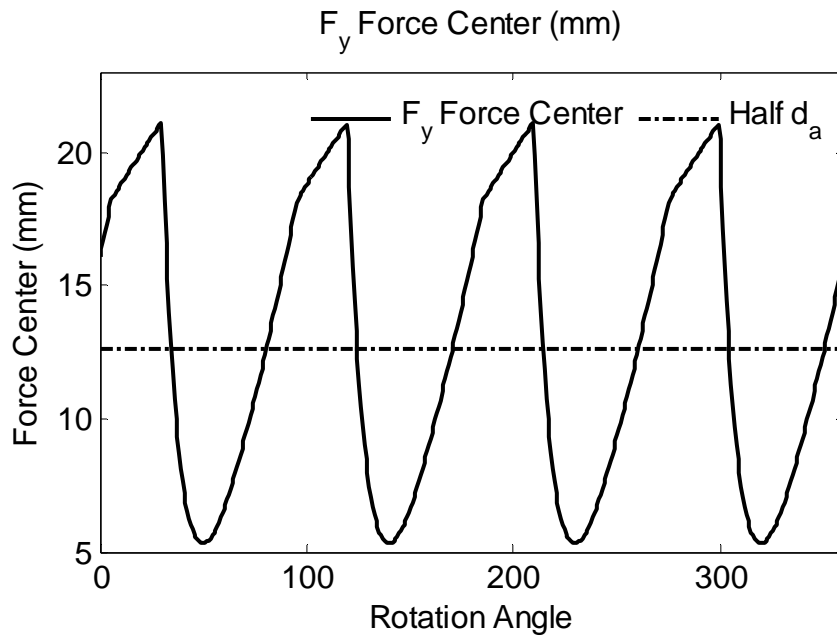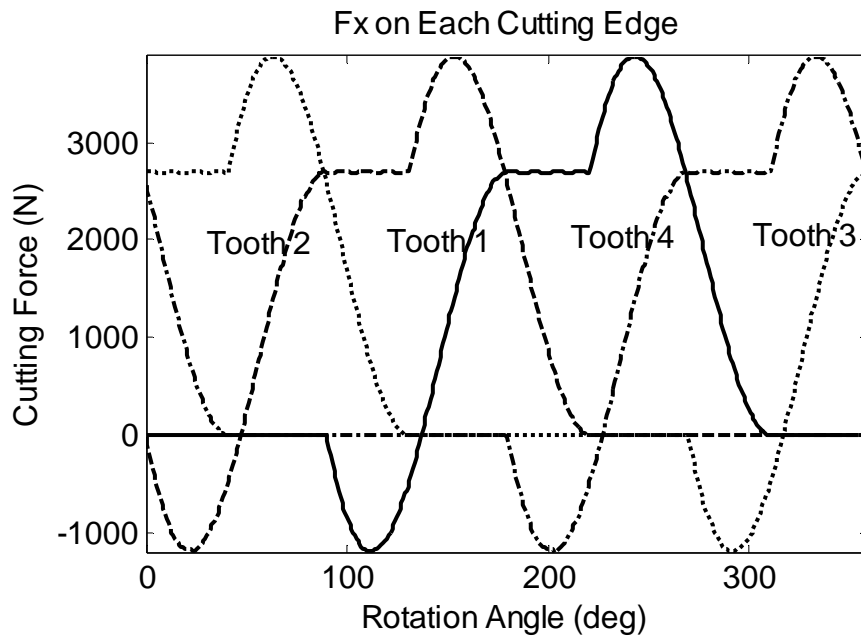**Figure 28** F_y **on Each Cutting Edge for Case 1 in Table 1 (Up-milling)**
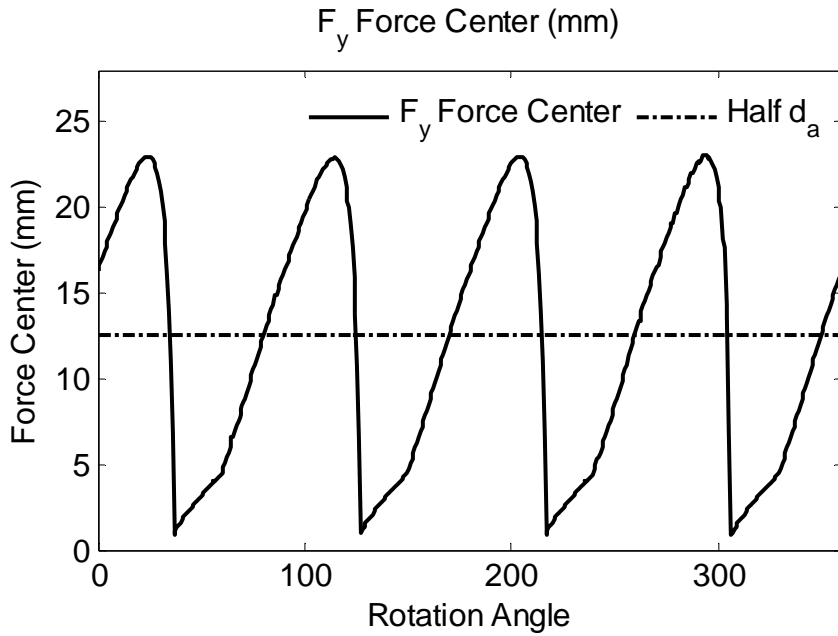
Figure 29 F_y **Force Center for Case 1 in Table 1 (Up-milling)**
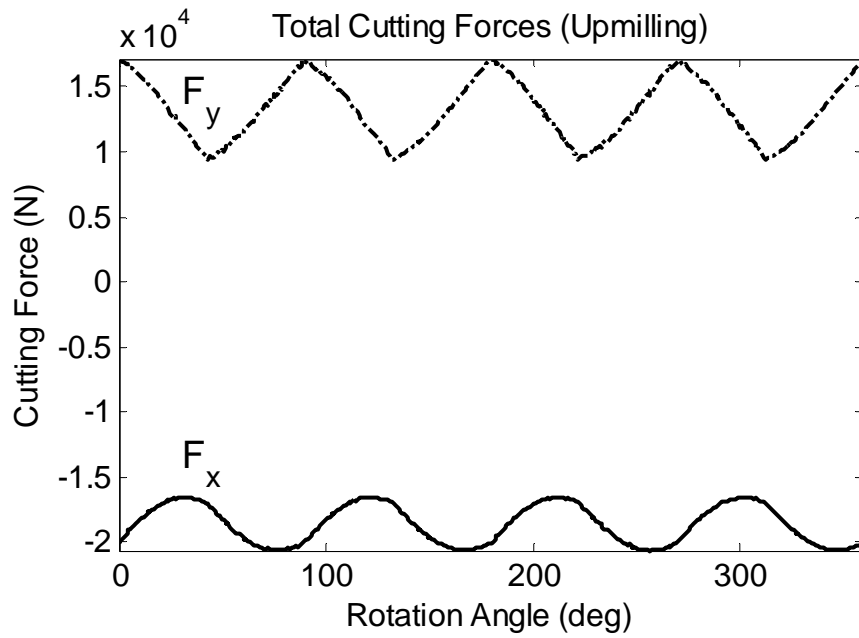
Figure 30 Total Cutting Forces for Case 2 in Table 1 (Up-milling)
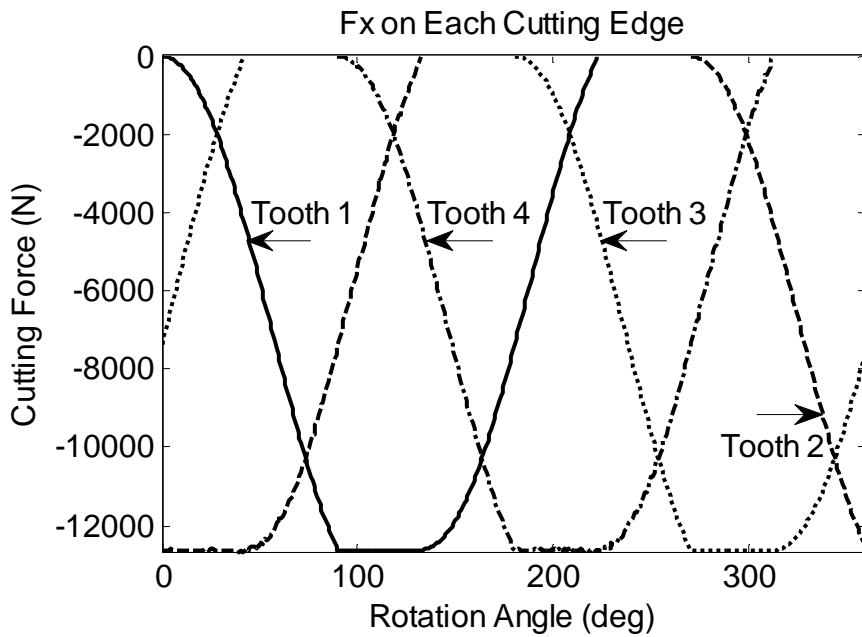
Figure 31 F_x on Each Cutting Edge for Case 2 in Table 1 (Up-milling)
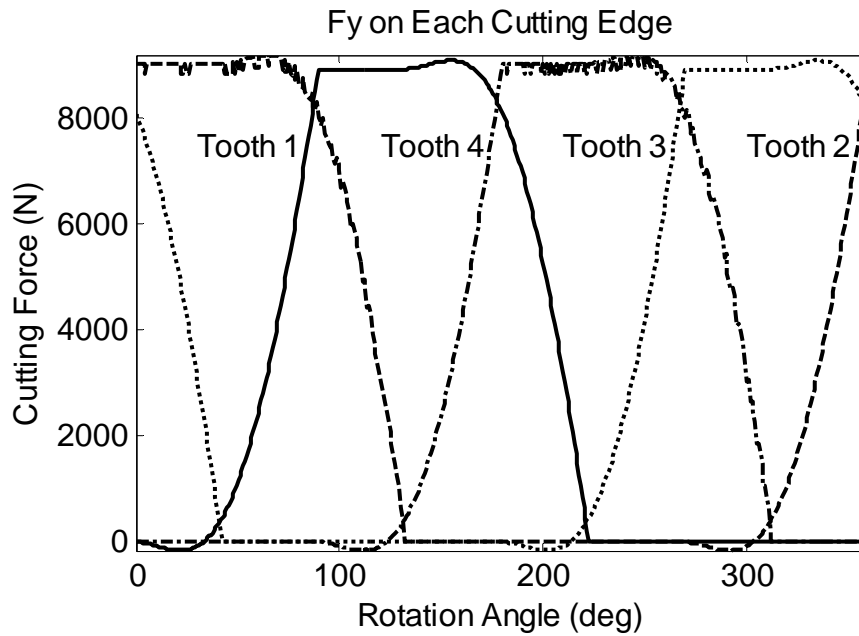
**Figure 32** F_y **on Each Cutting Edge for Case 2 in Table 1 (Up-milling)**
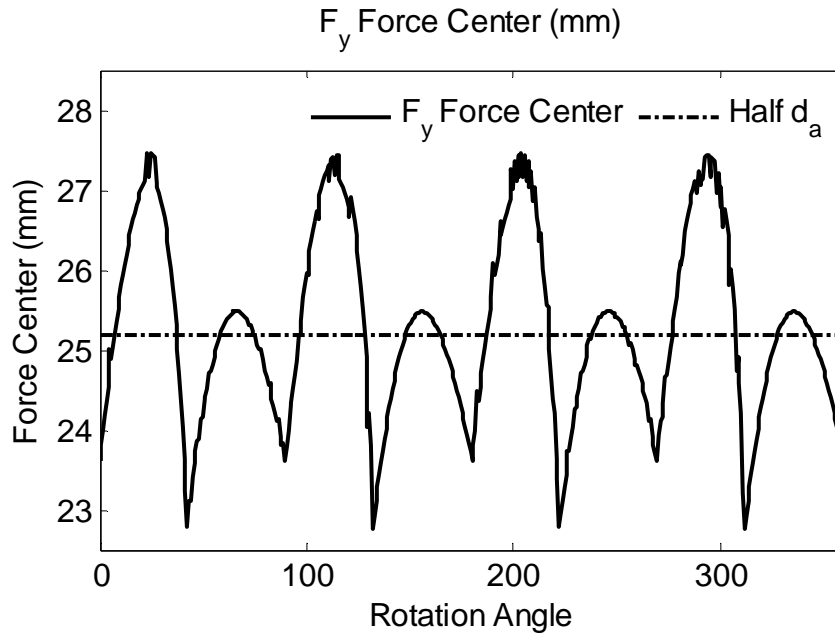
Figure 33 F_y **Force Center for Case 2 in Table 1 (Up-milling)**

In order to evaluate the influence of milling mode on cutting forces, simulations of cutting forces in down-milling (see Figure 34) are conducted as well. All the cutting conditions

in down-milling are same as those in Table 1with the exception on the milling mode. Simulation results of total cutting forces and cutting forces on individual cutting edges are shown in from Figure 35 to Figure 42.
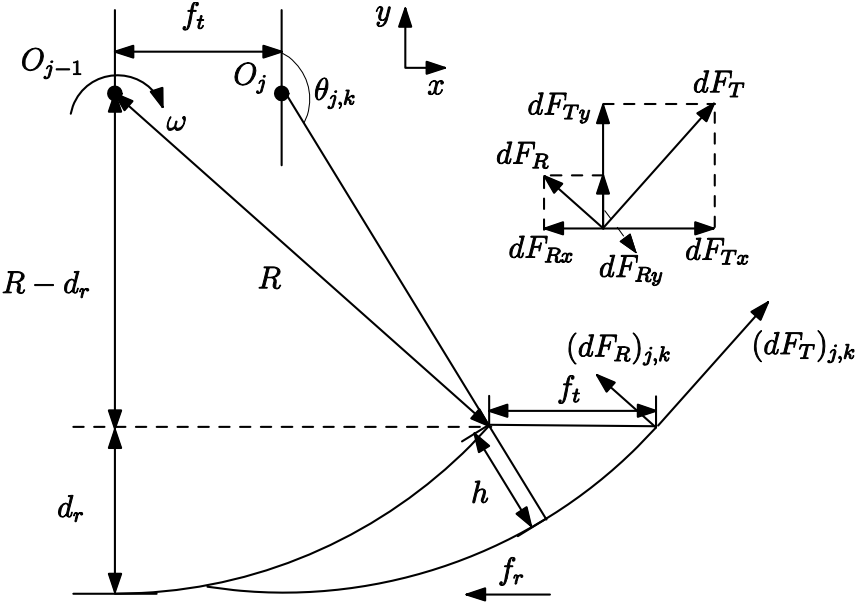
Figure 34 Schematic Diagram of Down-milling
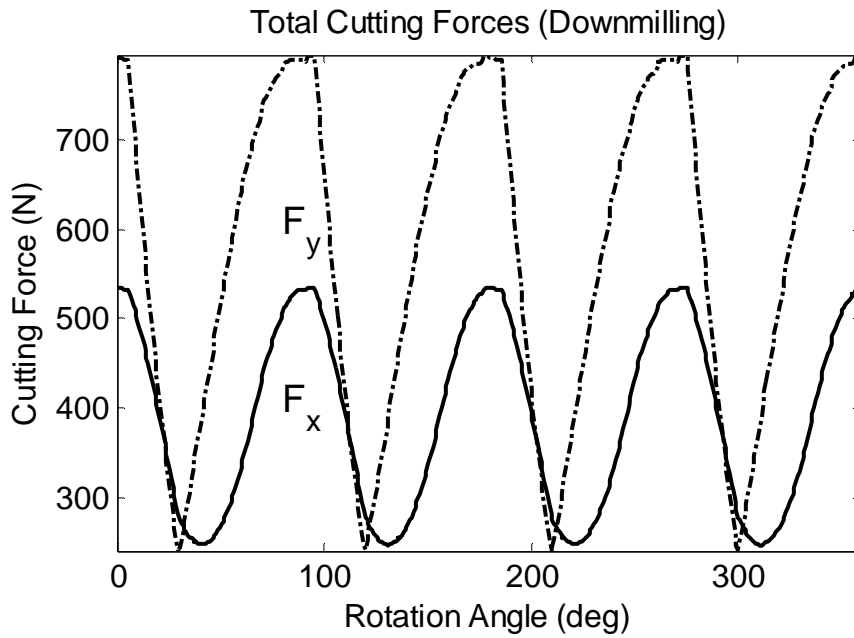
Figure 35 Cutting Forces for Case 1 in Table 1 (Down-milling)

Figure 36 F_x **on Each Cutting Edge for Case 1 in Table 1 (Down-milling)**
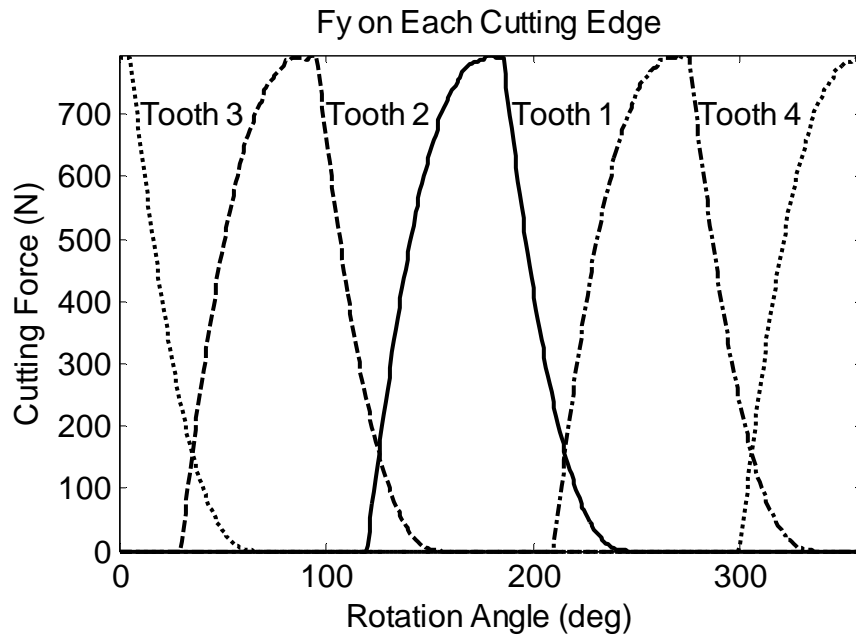
Figure 37 F_y **on Each Cutting Edge for Case 1 in Table 1 (Down-milling)**

Figure 38 F_y **Force Center for Case 1 in Table 1 (Down-milling)**
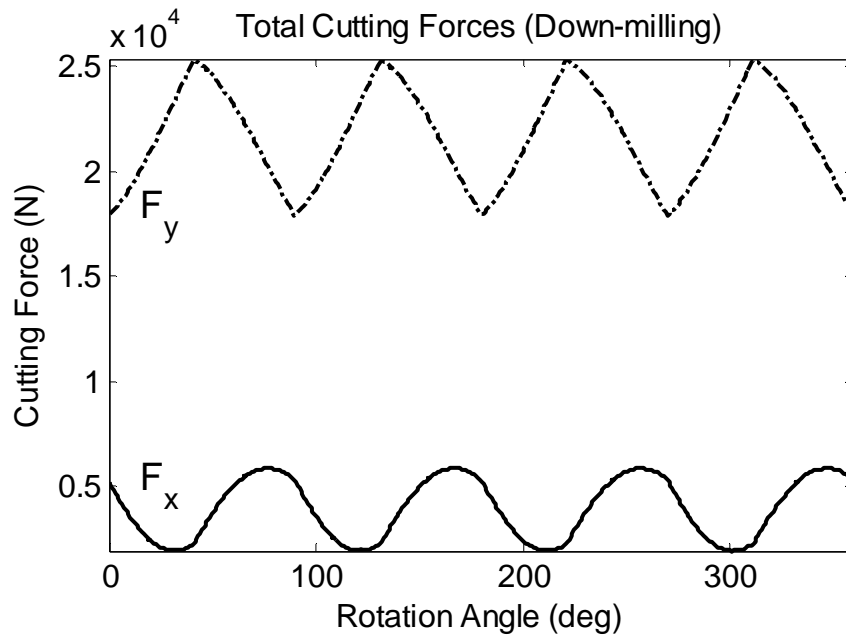
Figure 39 Cutting Forces for Case 2 in Table 1 (Down-milling)

Figure 40 F_x on Each Cutting Edge for Case 2 in Table 1 (Down-milling)
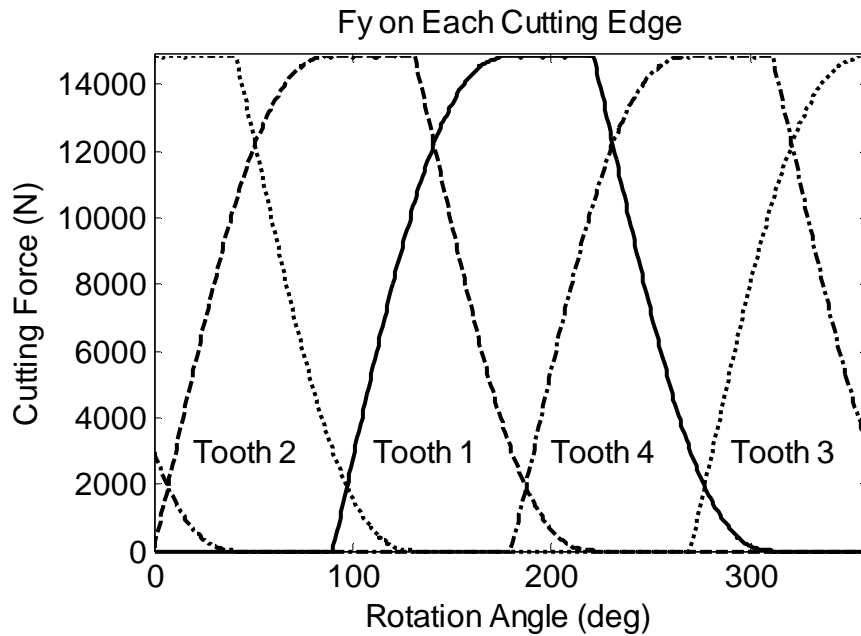
Figure 41 F_y **on Each Cutting Edge for Case 2 in Table 1 (Down-milling)**
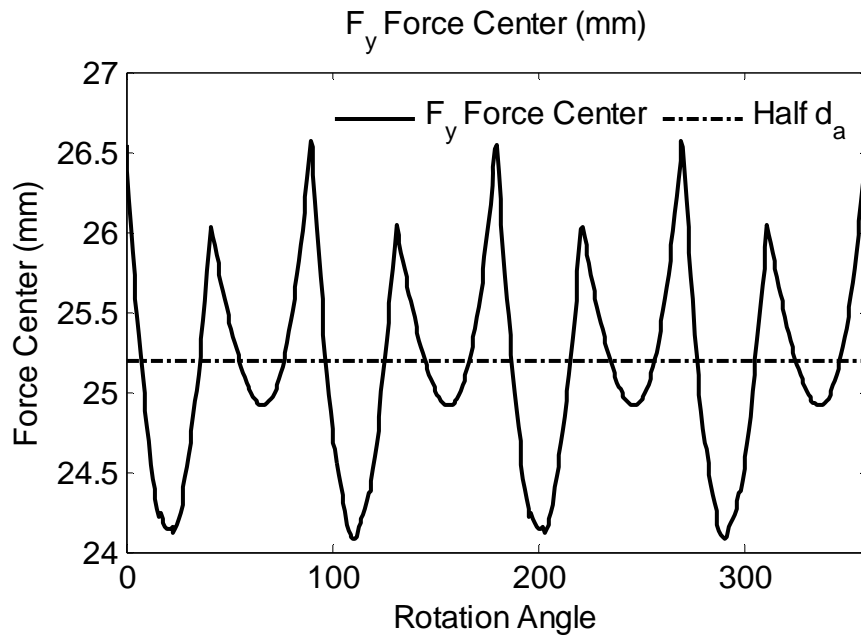
Figure 42 F_y **Force Center for Case 2 in Table 1 (Down-milling)**

By comparing F_y under the same cutting conditions for different milling mode, it can be

seen that the direction of F_y in down-milling is away from the workpiece while the direction of

F_y in up-milling is towards the workpiece. In addition to the difference in direction, force magnitudes differ as well under same cutting conditions while in different milling modes. Cutting forces in down-milling are greater than those in up-milling. Those differences will have different impacts on the surface location errors, which will be analyzed later.

The following conclusions about instantaneous cutting forces can be drawn from the above simulations:

1. In both up-milling and down-milling, cutting forces are periodic, and increase as the radial and axial depth of cut increase;

2. In both up-milling and down-milling, force center of F_y varies around half of the axial depth of cut;

3. In up-milling, the direction of F_y is towards the workpiece, while in down-milling, the direction of F_y is away from the workpiece.

The simulation friendly force model will be used for deflection analysis in the next section.

4.3   <u>Deflection and Surface Accuracy in Milling of Straight Surfaces</u>

As the most flexible part in the machine tool, the end mill is modeled as a cantilever beam with one end mounted on the spindle and the free end under laterally applied cutting forces. The periphery of end mills generates surfaces which are parallel to the cutter axis. The cutter under cutting load deflects towards or away from the surfaces, and therefore such deflection may cause machining error beyond tolerance. The machining error due to deflection, however, is complex , and does not have direct relationship with deflection ([72]). Therefore, the indirect relationship between deflection and the surface location error should be examined to provide required compensation. In this section, the cutter deflection due to cutting forces is simuated as well as the relationship between the deflection and surface accuracy.

Simulations from the previous section have shown that the magnitude and force center of resultant cutting forces vary during cutting. So end mills can be treated as cantilever beams under varying resultant force at any point rather than at the free end. On the other hand, as mentioned at the previous section, since the machined surface is parallel to the feed direction, only the deflection along the cross feed direction may affect the surface location error. Therefore, only the resultant force along cross-feed direction F_y will be considered for the analysis of deflection and surface location error.

Figure 43 illustrates an end mill subject to resultant cutting forces F_y applied at the axial elevation z_{F_y} which can be determined by

$$z_{F_y} = \frac{\sum\limits_{j=1}^{N_t}\sum\limits_{k=1}^{N_z}\left(dF_y\right)_{j,k}\cdot\left(L-z_{j,k}\right)}{F_y},\tag{89}$$

where $z_{j,k}$ is the elevation of applied elemental cutting force $(dF_y)_{j,k}$. According to the cantilever beam deflection theory, the cutter deflection $\delta(z)$ at the elevation z can be given by
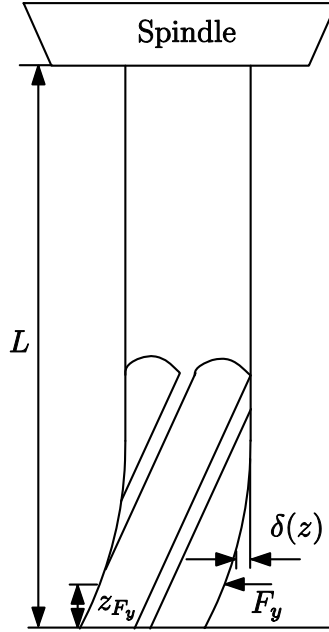

Figure 43 Cutter Deflection Under Cross-feed Load

$$\delta(z) = \begin{cases} \dfrac{F_y\left(L-z_{F_y}\right)^2}{6EI}\left(3(L-z)-\left(L-z_{F_y}\right)\right), & 0 < z < z_{F_y}; \\[4mm] \dfrac{F_y\left(L-z\right)^2}{6EI}\left(3\left(L-z_{F_y}\right)-(L-z)\right), & z_{F_y} < z < L, \end{cases} \tag{90}$$

where F_y is the resultant normal force, z_F is the force center where F_y is applied, E is the modulus of elasticity, I is the area moment of inertia, and L is the effective cutter length. The area moment of inertia I is computed with an equivalent tool diameter which is approximately 80% of the cutter diameter due to effect of flutes [75]. The effective cutter length L is slightly longer than the cutter length measured from the tool holder since it accounts for small deflections of the spindle and machine tool. L is usually obtained experimentally [76].

Note that the validity of using equation (90) to predict the cutter deflection is based on an assumption that cutting forces are static loads. According to [77], a load applied on a flexible structure can be treated as a static one when the lowest natural frequency of the structure is 10 times of the frequency of the applied load, which is N_t times of spindle rotation frequency. The lowest natural frequency of end mills can be computed by [78]

$$f_n = \frac{3.52}{2\pi} \sqrt{\frac{EI}{\rho A L^4}}, \tag{91}$$

where ρ is the mass density and A is the cross-sectional area of the beam. This assumption of static loads holds for conventional speed milling processes [76].

Next, the effect of cutter deflection on the surface accuracy will be investigated. It is mentioned above that the generated surface is parallel to the feed direction. In other words, only the cutting point whose rotation angle is either zero for up-milling or π for down-milling generates the finished surface. The intermediate surfaces generated by other cutting points will be removed by subsequent cuttings. According to equation (81), the axial location of the surface generation cutting points is given by

$$z(t) = \begin{cases} \dfrac{R\left[\theta_{j,k}(t) + (j-1)\theta_p\right]}{\tan\beta} , & \text{up-milling;} \\[4mm] \dfrac{R\left[\pi - \theta_{j,k}(t) - (j-1)\theta_p\right]}{\tan\beta} , & \text{down-milling.} \end{cases} \tag{92}$$

Then the surface accuracy is evaluated at these cutting points subjected to the instantaneous deflection given by equation (90).

Due to the helix angle of the cutter, surfaces are generated sequentially by cutting points sliding upward from the bottom to the location at axial depth of cut as the cutter rotates. Since cutting forces and corresponding cutter deflection vary, deflection will leave varying imprints on

79

the surface. Therefore, the surface location accuracy is related to both the location of the cutting

point and instantaneous cutter deflection. The cutting forces vary periodically with the frequency

N_t times of the spindle frequency, so do the cutter deflection and surface location accuracy. The

surface accuracy is simulated for operations in Table 1.
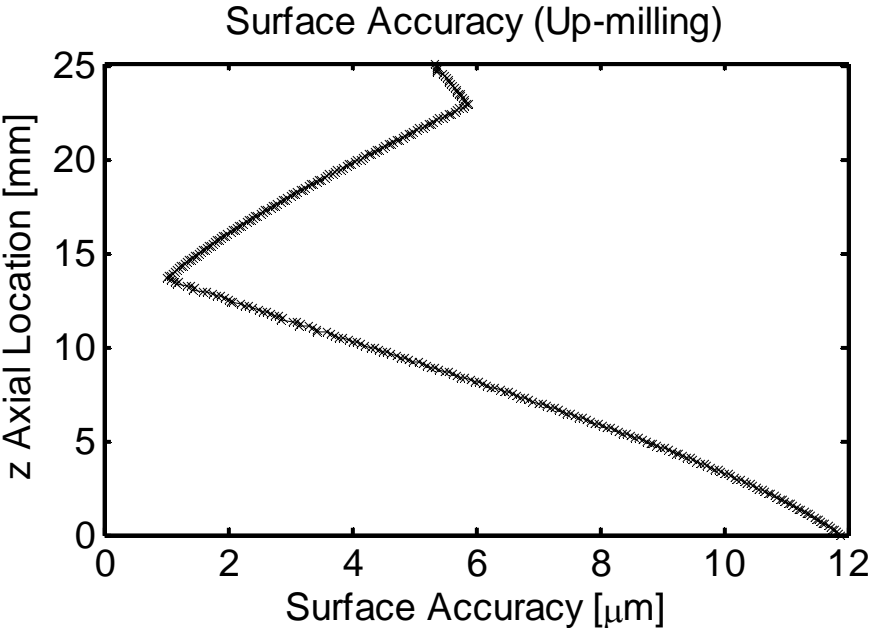
Figure 44 Surface Accuracy for Case 1 in Table 1 (Up-milling)

The simulation results of surface accuracy in up-milling are shown in Figure 44

and Figure 45, and results for down-milling are shown in Figure 46 and Figure 47. By comparing

the surface accuracy under same conditions in different milling modes, it can be seen that the

down-milling generates greater surface location error, which can be explained from the greater

cutting force magnitude in down-milling. On the other hand, the surface location errors of two

milling modes have different signs which indicate that the cutter deflects differently in these

modes. In up-milling, the cutter deflects towards the workpiece, while in down-milling, the

cutter deflects away from the workpiece. Since the down-milling is usually used in finishing cut,

the accuracy of down-milling is more important than that of up-milling, the compensation strategy will focus on down-milling operations only.

Surface Accuracy (Up-milling)
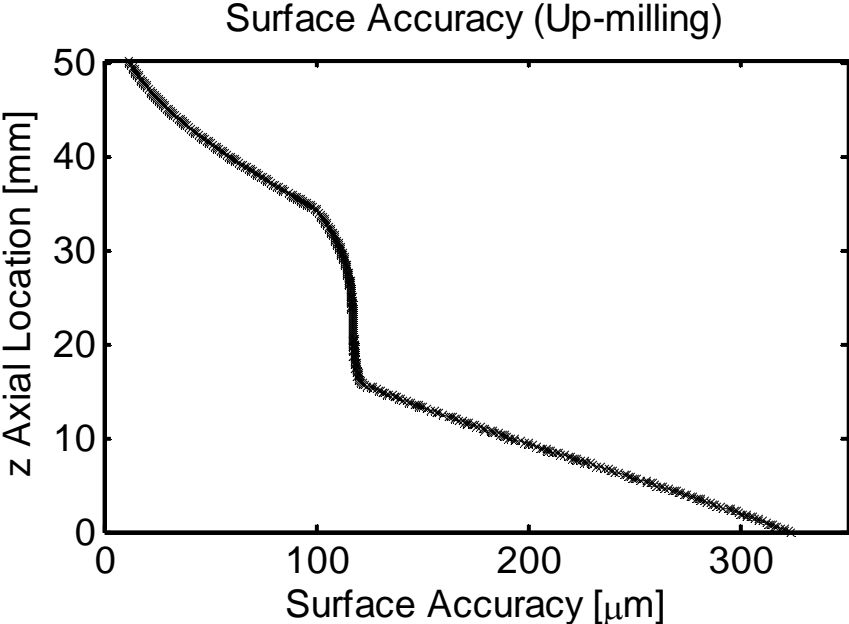
Figure 45 Surface Accuracy for Case 2 in Table 1 (Up-milling)

Surface Accuracy (Down-milling)
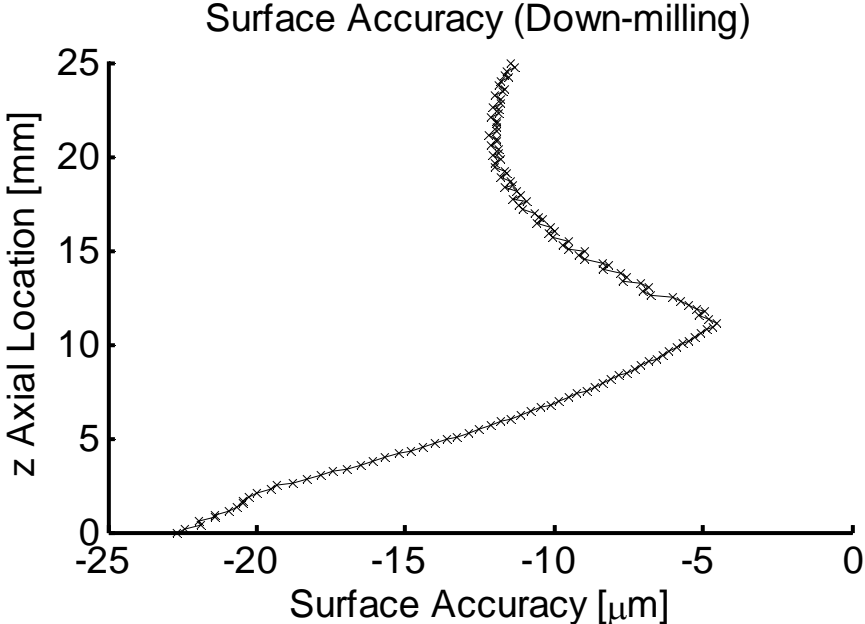
Figure 46 Surface Accuracy for Case 1 in Table 1 (Down-milling)
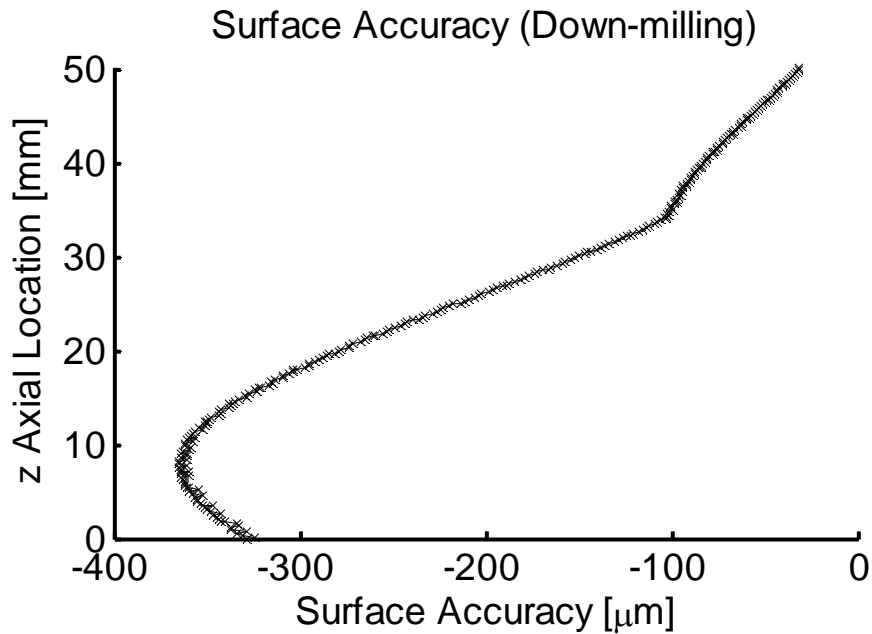
Figure 47 Surface Accuracy for Case 2 in Table 1 (Down-milling)

The surface accuracy for a commonly used milling operation slotting is also simulated since the operation involves both up-milling and down-milling. It is well known that cutting forces in slotting is a constant (see Figure 48), then the cutter deflection keep invariant during cutting. The results are shown in Figure 49 and Figure 50. The results indicate that the cutter deflects towards the up-milling side, and therefore, the surface accuracy errors at two sides are symmetric about the cutter axis.

With the above analysis and simulation results, the following conclusions can be drawn:

1. In up-milling, the cutter deflects towards the workpiece, while in down-milling, the cutter deflects away from the workpiece;

2. Under the same cutting conditions, deflection in down-milling is greater than that in up-milling;

3. The surface accuracy is associated with the locations of cutting points and instantaneous deflection other than maximum or average deflection;

82

4. Due to the periodicity of cutting forces and corresponding cutter deflection, the surface accuracy variation repeats for every tooth pass.

Cutting Force (Slotting)
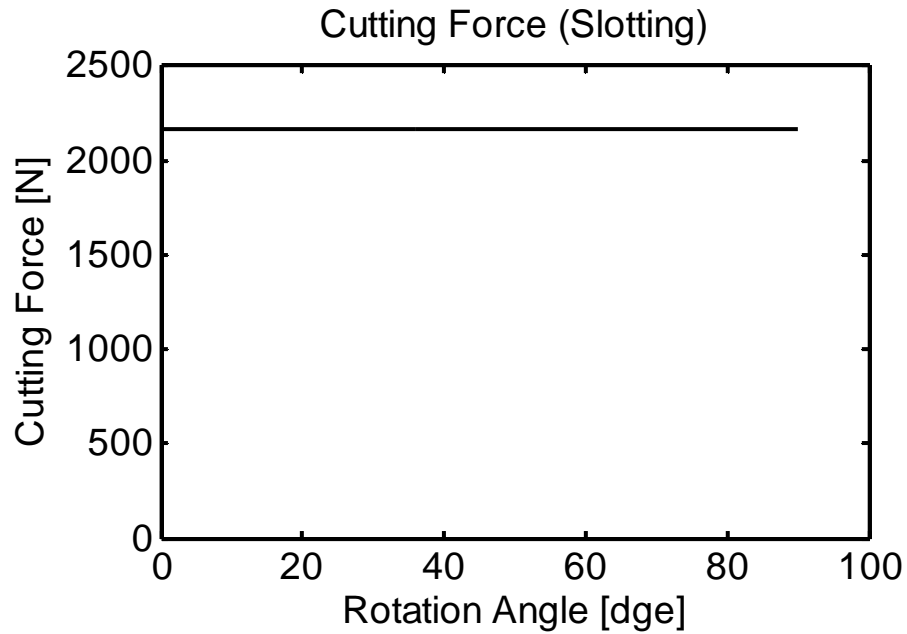
Figure 48 Cutting Forces in Slotting

Surface Accuracy (Slotting)
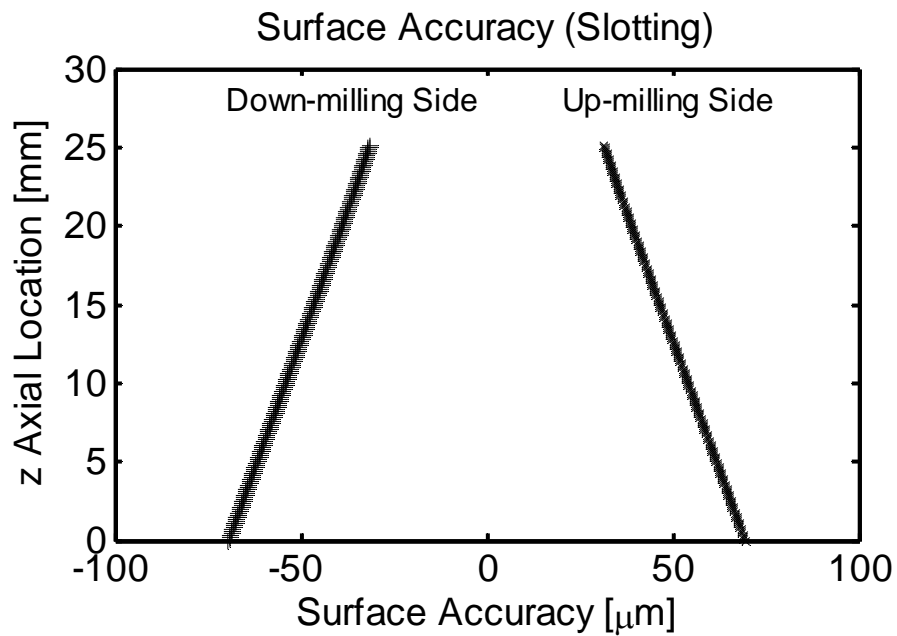
Figure 49 Surface Accuracy for Case 1 in Table 1 (Slotting)
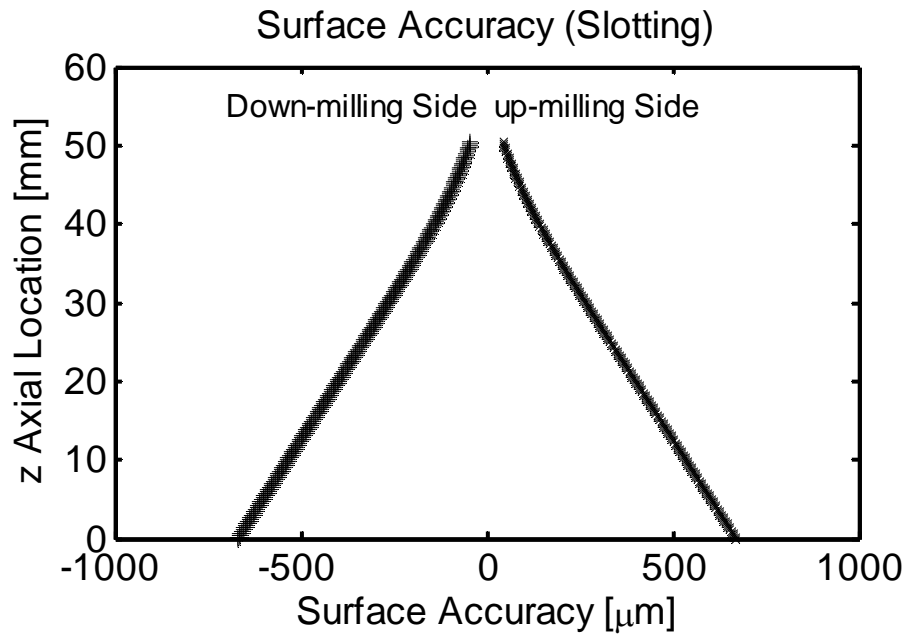
Figure 50 Surface Accuracy for Case 2 in Table 1 (Slotting)

4.4   Deflection and Surface Accuracy in Milling of Curved Surfaces

In the case of milling circular or free form surfaces, the non-straight tool path or workpiece curvature cause change in the feed per tooth and cutter engagement conditions [79]. Therefore, such change should be considered to predict cutting forces and corresponding cutter deflection. In this section, the cutter deflection and surface accuracy in milling of curved surfaces are examined. First, the change of the feed per tooth and the entry angle are investigated for both circular surface milling and free form milling. Then, the cutting forces and corresponding deflection are recomputed for both cases. Finally, surface accuracy is evaluated for two cases.

To facilitate cutting force and location representation, two Cartesian coordinate systems are used. The global Cartesian coordinates with x-y-z axes are fixed with the origin at either the center of the workpiece or a location as defined. The horizontal x-axis and y-axis are parallel to the longer and the shorter dimension of the machine tool table, respectively, and the z-axis is aligned with the spindle direction which is perpendicular to the x-y plane. The Cartesian coordinates x_F-y_N axes, denoted the feed and normal directions, respectively, are rotating together with the cutter. The kinematics is usually represented in the global Cartesian coordinates, while the cutting mechanics is studied in the rotating local Cartesian coordinates.

4.4.1   Milling of Circular Surfaces

With the Cartesian coordinates defined above, a down-milling of a circular surface is illustrated in Figure 51. The tool path and surfaces before/after machining are located on concentric circles with the center denoted O_W. The cutting tool moves along the path with radius as $R_W + R_T - d_r$, where R_W is the workpiece radius before machining, R_T is the cutter radius, and d_r is the radial depth of cut. O_T^i, $i=j-1$ and j, represent the centers of the cutter at successive instants. The distance between the successive centers is the nominal feed per tooth $\bar{f_t}$, which is given by

$$\bar{f}_t = \frac{f_r}{N_t \cdot n},$$ (93)

where f_r is the feedrate (mm/min), N_t is the flute number, and n is the spindle speed (rpm) as defined in equation (80).
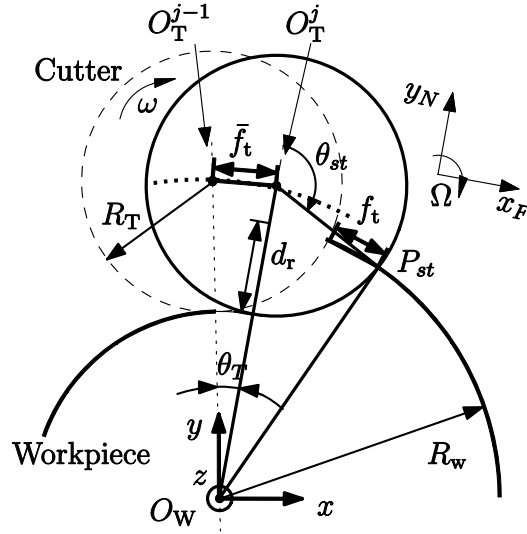
Figure 51 Milling of Circular Surfaces

As shown in Figure 51, the actual feed per tooth f_t, evaluated on the workpiece surface, does not equal to the nominal one $\bar{f}_t$ due to the effect of workpiece curvature. Since the tool path and the workpiece surface are in concentric circles, the actual feed per tooth f_t can be found from the process geometry, and f_t is given by

$$\frac{f_t}{\bar{f}_t} = \frac{R_W}{R_W + R_T - d_r}.$$ (94)

In down-milling, the exit angle $\theta_{ex} = \pi$, and the entry angle θ_{st} can be calculated by applying cosine formula in the triangle formed by O_W, O_T^j, and P_{st}, which is the contact point where the cutter enters the workpiece, and θ_{st} is given by

$$\theta_{st} = \pi - \arccos \frac{R_T^2 + \left(R_T + R_W - d_r\right)^2 - R_W^2}{2R_T\left(R_T + R_W - d_r\right)}.$$ (95)

86

Note that both ϕ_{st} and ϕ_{ex} are defined from normal direction. Equation (82) should be modified to determine the engagement condition since $\theta_{j,k}(t)$ is the rotation angle defined from the global y-axis other than the normal direction y_N. The process geometry shows that the normal direction rotates along the tool path at the angular velocity Ω given by

$$\Omega = \frac{f_r}{R_T + R_W - d_r}, \tag{96}$$

where f_r is the feed rate. Then the rotation angle $\overline{\theta}_{j,k}(t)$ of cutting point relative to the normal direction is given by

$$\overline{\theta}_{j,k}(t) = \theta_{j,k}(t) - \Omega t. \tag{97}$$

Cutting forces, including the tangential and radial force, are modified accordingly:

$$\left(dF_T(t)\right)_{j,k} = K_T \cdot dz \cdot h\left(\overline{\theta}_{j,k}(t)\right), \tag{98}$$

$$\left(dF_R(t)\right)_{j,k} = K_R \cdot \left(dF_T(t)\right)_{j,k}. \tag{99}$$

The engagement condition given in equation (82) should be modified to

$$\theta_{st} \leq \overline{\theta}_{j,k}(t) \leq \theta_{ex}. \tag{100}$$

Since the elemental cutting forces $(dF_x)_{j,k}$ and $(dF_y)_{j,k}$ are components of cutting forces on the fixed global x-y axes, equations (85)-(86) and (87)-(88) for straight surface milling are still applicable for circular surface milling. Note that $\overline{\theta}_{j,k}(t)$ is used to compute tangential and radial cutting forces since $\overline{\theta}_{j,k}(t)$ is measured in the rotating x_F-y_N coordinates, while $\theta_{j,k}(t)$ is used to compute F_x and F_y since $\theta_{j,k}(t)$ is measured in the fixed global x-y coordinates.
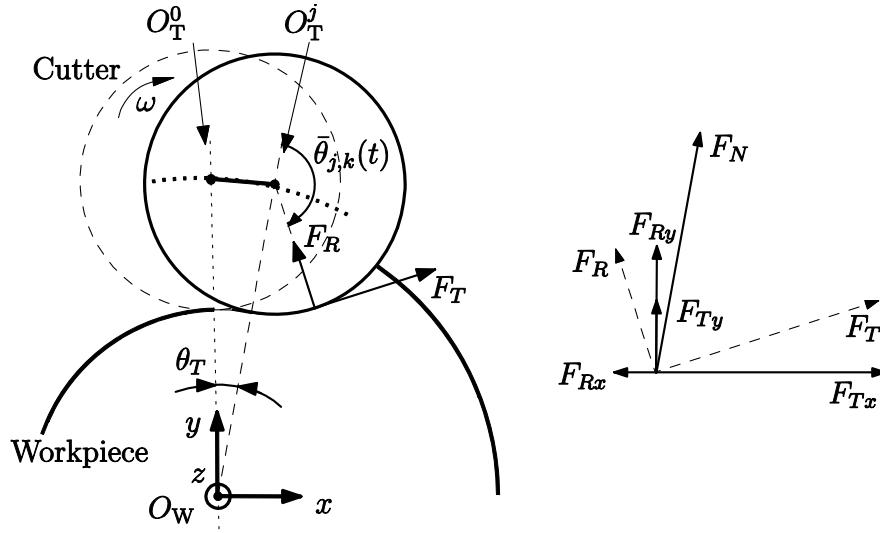
Figure 52 Cutting Forces in Milling of Circular Surfaces

In addition to the above changes, the direction of deflection which causes surface accuracy error varies as well. In straight surface cutting, surface accuracy is affected only by deflection due to normal force F_N along with y-axis which is perpendicular to the feed direction. In circular surface, however, the direction of normal force is rotating together with the cutter center. Normal forces are determined by both F_x and F_y (see Figure 52). Therefore, both F_x and F_y should be considered to evaluate surface accuracy. Accordingly, the deflection given in Equation (90) should be modified as

$$\delta(z) = \begin{cases} \dfrac{F_N \left(L - z_{F_N}\right)^2}{6EI}\left(3(L - z) - \left(L - z_{F_N}\right)\right), & 0 < z < z_{F_N} \\[4mm] \dfrac{F_N (L - z)^2}{6EI}\left(3\left(L - z_{F_N}\right) - (L - z)\right), & z_{F_N} < z < L \end{cases} , \tag{101}$$

where F_N is given by

$$F_N = F_x \sin\theta_T + F_y \cos\theta_T, \tag{102}$$

where θ_T is the rotation angle of the cutter center measured from the positive y-axis, and θ_T is given by

$$\theta_T(t) = \Omega t, \tag{103}$$

where Ω is defined by equation (96).

The axial location of the surface generation cutting points is modified as

$$z(t) = \begin{cases} \dfrac{R\left[\bar{\theta}_{j,k}(t) + (j-1)\theta_p\right]}{\tan \beta} & , \quad \text{up-milling}; \\[4mm] \dfrac{R\left[\pi - \bar{\theta}_{j,k}(t) - (j-1)\theta_p\right]}{\tan \beta} & , \quad \text{down-milling}. \end{cases} \tag{104}$$

Then the surface accuracy is evaluated at these cutting points subjected to the instantaneous deflection given by equation (101).

In order to illustrate the difference between circular surface milling and straight surface milling, cutting conditions of Case 2 in Table 1 is used for simulation. The comparison is shown in Figure 53 with the result of the same cutting conditions while for different surfaces. It can be seen that the circular surface milling leads to less deflection. This phenomenon can be explained by force contribution to cutter deflection. In straight surface milling, cutter deflection is due to F_y which has contribution of both tangential and radial cutting forces. While in circular surface milling, cutter deflection is mainly caused by radial cutting forces which are usually much smaller than tangential cutting forces. The difference between F_y and F_N is shown in
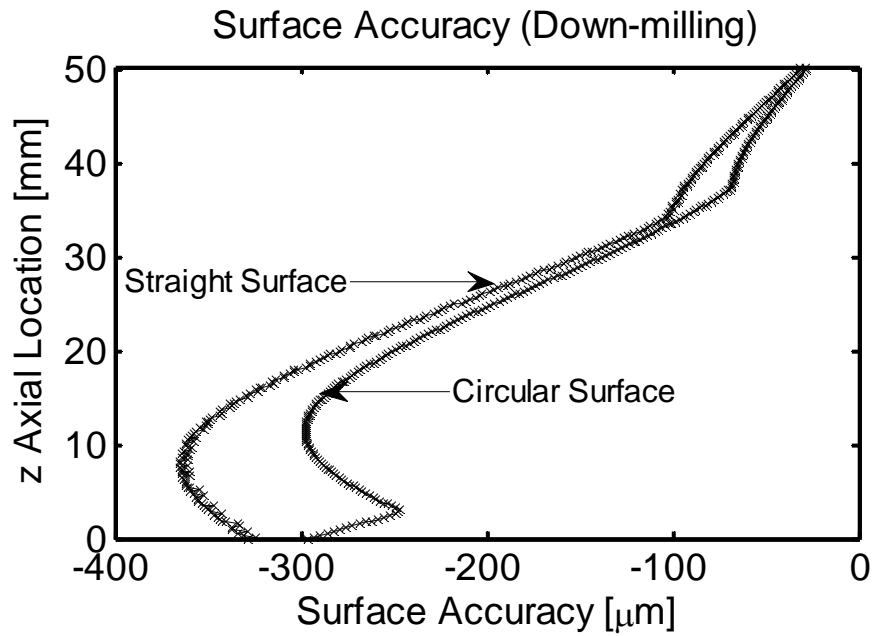
Figure 53 Surface Accuracy Comparison Between Circular Surface Milling and Straight Surface Milling Under Same Cutting Conditions.
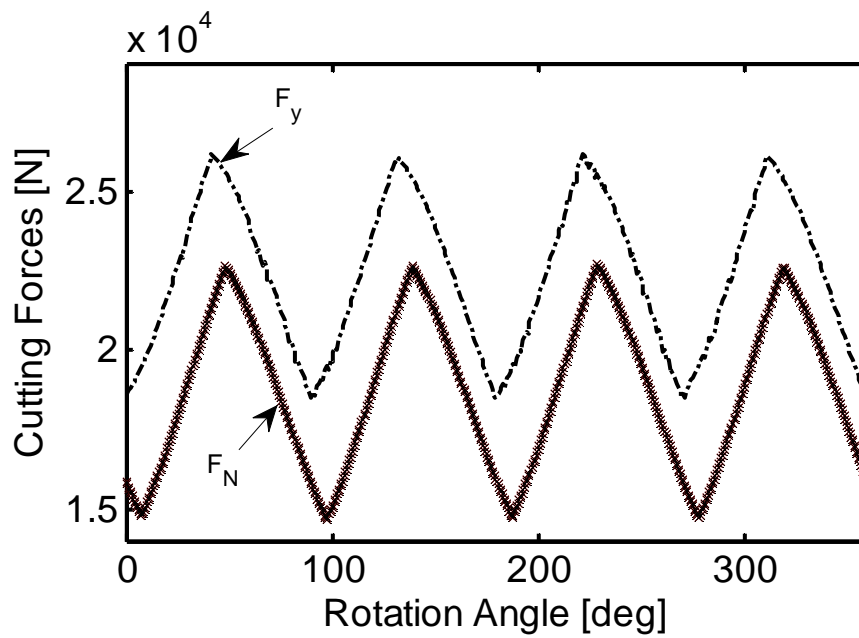
Figure 54 Cutting Force Comparison Between Circular Surface Milling and Straight Surface Milling Under Same Cutting Conditions.

In the next section, the more general case, free form surface milling, will be studied.

4.4.2 Milling of Free Form Surfaces

Free form milling is commonly seen in machining of parts in aerospace engineering, such as turbine blades and impellers etc. Until recently, the study of free form surface milling was initiated by Rao et. al in [64], but the surface error defined in [64] is cusp height due to cutter path geometry rather than cutter deflection which is targeted in this research. This section extends the analysis presented in [64] to study the effect of cutter deflection on the surface accuracy in free form surface milling. We will first study the effect of surface curvature on the immersion angle and corresponding engagement condition, then the cutting force and surface accuracy will be simulated according to the engagement condition.
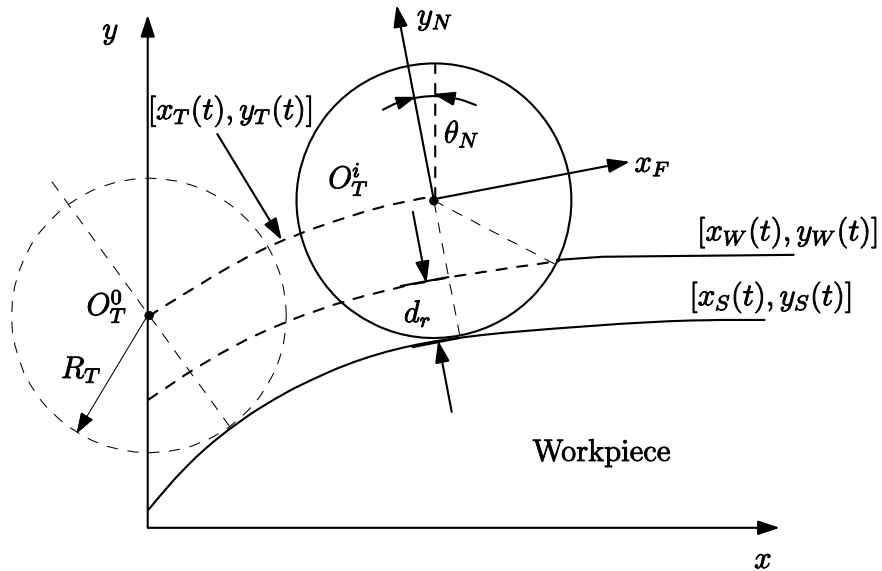
Figure 55 Milling of Curved Surface

The general curved surface after machining, denoted $[x_S(t), y_S(t)]$, can be described by parametric equations

$$x_S(t) = f(t),$$
$$y_S(t) = g(t).$$

(105)

91

Since the workpiece surface before machining, denoted $[x_W(t), y_W(t)]$, and the tool path, denoted $[x_T(t), y_T(t)]$, are parallel to the surface after machining, and the offset distances are d_r and R_T, respectively, $[x_W(t), y_W(t)]$ and $[x_T(t), y_T(t)]$ can be represented by

$$x_W(t) = f(t) - \frac{d_r g'(t)}{\sqrt{\left[f'(t)\right]^2 + \left[g'(t)\right]^2}},$$
$$y_W(t) = g(t) + \frac{d_r f'(t)}{\sqrt{\left[f'(t)\right]^2 + \left[g'(t)\right]^2}}.$$

$$(106)$$

and

$$x_T(t) = f(t) - \frac{R_T g'(t)}{\sqrt{\left[f'(t)\right]^2 + \left[g'(t)\right]^2}},$$
$$y_T(t) = g(t) + \frac{R_T f'(t)}{\sqrt{\left[f'(t)\right]^2 + \left[g'(t)\right]^2}}.$$

$$(107)$$

where d_r is the radial depth of cut, R_T is the tool radius, $f'(t)$ and $g'(t)$ are derivatives of $f(t)$ and $g(t)$ with respective to t, respectively. In order to calculate cutting forces, engagement condition and actual feed per tooth should be determined. From previous section on milling of circular surfaces, it is shown that the engagement condition depends on the cutter rotation angle relative to the cross-feed direction y_N which can be determined from constant angular velocity of the cutter along the tool path. In milling of general curved surfaces, however, the angular velocity along the tool path is no longer constant due to the varying instantaneous radius of curvature. Therefore, the cross-feed direction y_N should be evaluated instantaneously. Similarly, the actual feed per tooth is also varying along the path due to the variation in instantaneous radius of curvature. As a result, the cross-feed direction y_N and the instantaneous radius of curvature for curved surfaces should be solved first.

It can be seen from Figure 55 that the cross-feed direction y_N is normal to the surface, the slope of y_N at the instant t_i, denoted $k_{y_N}^{t_i}$, satisfies

$$k_{y_N}^{t_i} \cdot k_{[x_S(t_i), y_S(t_i)]} = -1, \tag{108}$$

where $k_{[x_S(t_i), y_S(t_i)]}$ is the slope of the tangent line at the machined surface $[x_S(t_i), y_S(t_i)]$ at the instant t_i, and $k_{[x_S(t_i), y_S(t_i)]}$ is

$$k_{[x_S(t_i), y_S(t_i)]} = \frac{g'(t_i)}{f'(t_i)}. \tag{109}$$

Therefore, the orientation of y_N relative to y axis, denoted θ_N can be solved by

$$\theta_N(t_i) = \begin{cases} \dfrac{\pi}{2} - \tan^{-1} \dfrac{-f'(t_i)}{g'(t_i)} & , \quad \dfrac{f'(t_i)}{g'(t_i)} \leq 0; \\[4mm] -\tan^{-1} \dfrac{-f'(t_i)}{g'(t_i)} - \dfrac{\pi}{2} & , \quad \dfrac{f'(t_i)}{g'(t_i)} > 0. \end{cases} \tag{110}$$

Then the rotation angle $\overline{\theta}_{j,k}(t)$ of cutting point relative to the normal direction is given by

$$\overline{\theta}_{j,k}(t) = \theta_{j,k}(t) - \theta_N(t). \tag{111}$$

where $\theta_{j,k}(t)$ is the rotation angle relative to y axis.

It can be In order to evaluate the actual feed per tooth, the instantaneous radius of curvature should be known. For the surface given by equation (105), the instantaneous radius of curvature is

$$R_S(t) = \frac{\left[(g'(t))^2 + (f'(t))^2 \right]^{3/2}}{|g'(t)f''(t) - g''(t)f'(t)|}. \tag{112}$$

And the actual feedrate f_t can be obtained by solving

$$\frac{f_t}{\overline{f}_t} = \frac{R_S(t) + d_r}{R_S(t) + R_T}, \tag{113}$$

93

where $\overline{f_t}$ is the nominal feed per tooth. Similarly, the entry angle

$$\theta_{st} = \pi - \arccos \frac{R_T^2 + \left(R_T + R_S(t)\right)^2 - \left(d_r + R_S(t)\right)^2}{2R_T\left(R_T + R_S(t)\right)}. \tag{114}$$

In summary, due to the effect of curvature, the immersion angle, the entry angle, and feed per tooth vary along the tool trajectory. Therefore, cutting forces are no long periodic as they are for milling of straight surfaces and circular surfaces. Cutting force variation is simulated for the cutting conditions given in Table 2. The workpiece material is 7075-T6 aluminum, and the workpiece geometry is defined by logarithmic spiral

$$\begin{aligned} x(t) &= a\sin(\theta)e^{b\theta}, \\ y(t) &= a\cos(\theta)e^{b\theta}, \end{aligned} \tag{115}$$

where a=48 mm and b=0.5, and θ varies from 0 to $\pi/2$ measured from y-axis. The profile of the workpiece is shown in Figure 56.
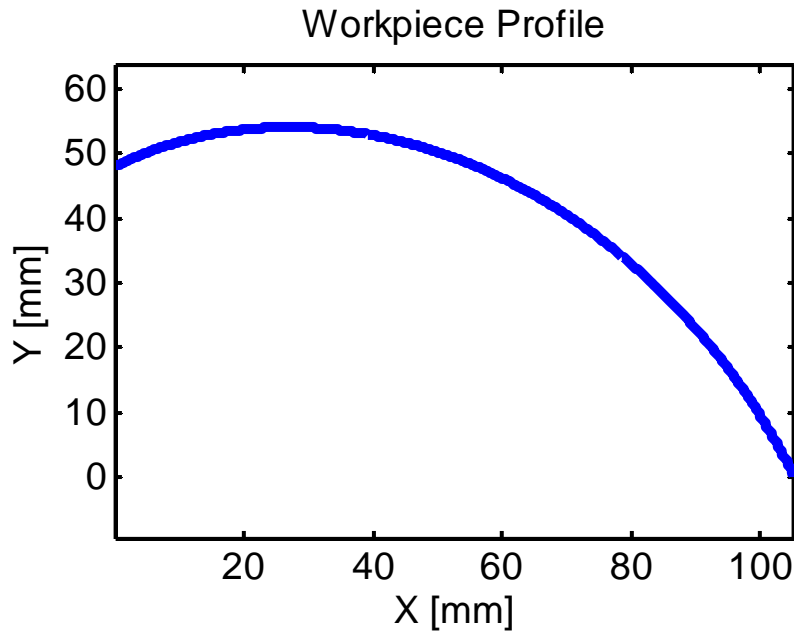
Figure 56 Workpiece Profile for Simulation of Free Form Milling

The the specific cutting pressure constants K_t and K_r, obtained from cutting experiments in [58], are related to average chip thickness t_a as

$$K_t = 435.9783 \left(t_a \right)^{-0.3672},$$
$$K_r = 0.2405 \left(t_a \right)^{-0.1062}.$$

(116)

The cutting forces along x- and y-axis, and the direction normal to the workpiece are shown in Figure 57-Figure 59

Table 2 Cutting Conditions of Free Form Milling [58]

Cutting Prameters	Values
Cutter diameter (mm)	10
Number of flutes	4
Helix angle (deg)	25
Radial depth of cut (mm)	2.5
Axial depth of cut (mm)	15
Spindle speed (rpm)	900
Feed rate (mm/min)	108
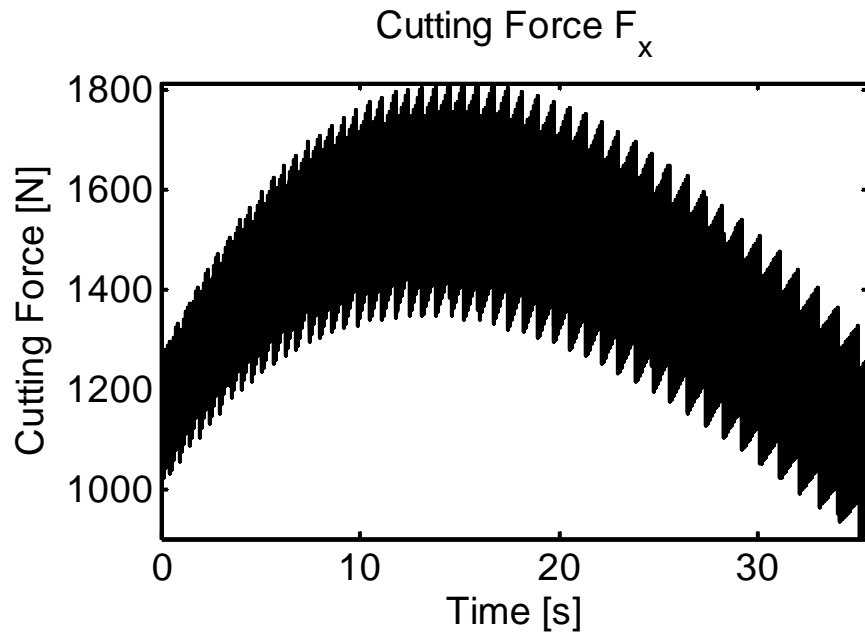
Figure 57 Cutting Force F_x for Cutting Conditions in Table 2
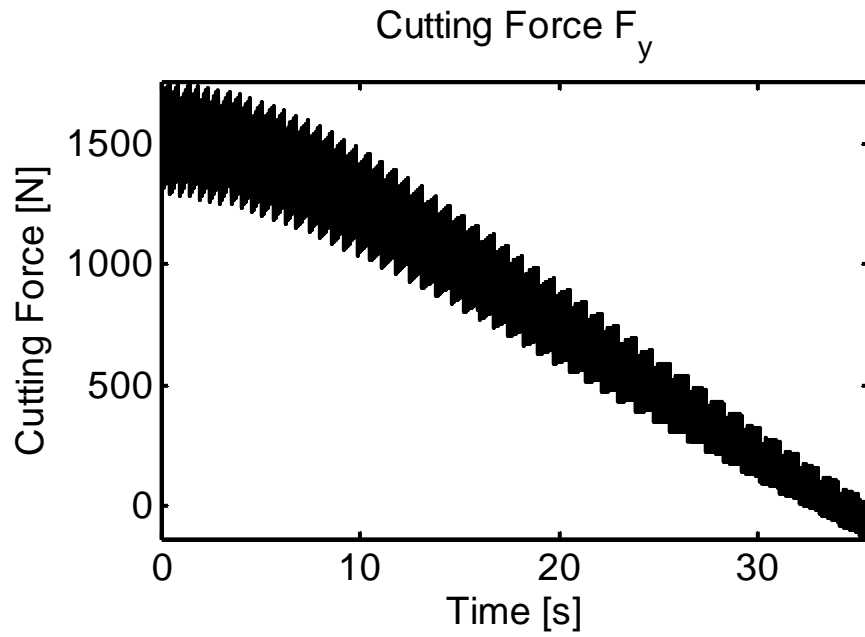
Figure 58 Cutting Force F_y for Cutting Conditions in Table 2
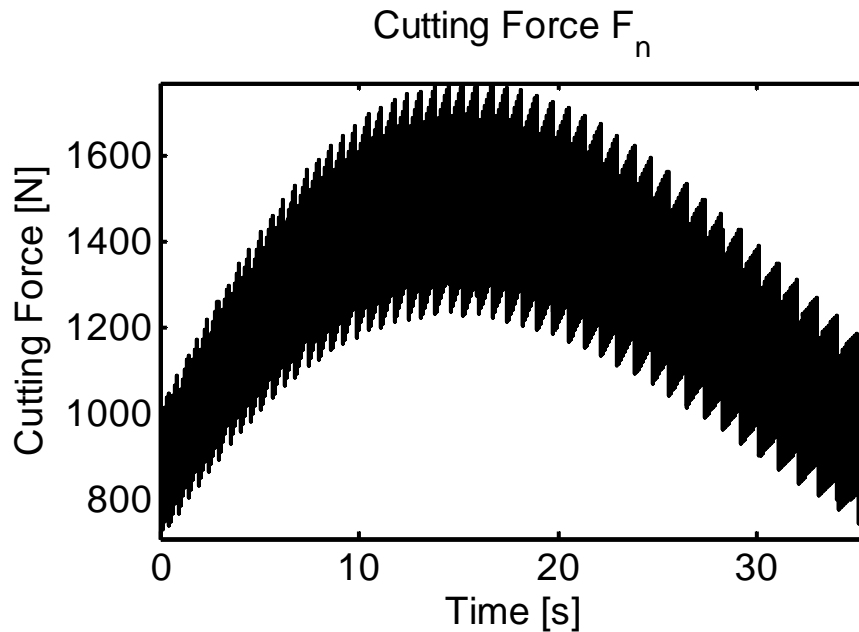
Figure 59 Cutting Force F_n for Cutting Conditions in Table 2

It can be seen from the above plots that the peak values of these cutting forces are influenced by the curvature of workpiece. Therefore, cutter deflection and corresponding workpiece accuracy will also vary along the tool path. As a representative example, the workpiece accuracy during each tooth pass within one revolution where maximum normal force F_n is displayed in Figure 60. Note that the tooth pass defined here is referred to the duration with which a tooth rotates for a pitch angle. It is obvious that the maximum normal force occurs at the second tooth pass of the revolution. In order to examine the variation of surface accuracy along the elevation during machining, the maximum and minimum surface accuracy are illustrated in Figure 61. The surface error at the height of axial depth of cut varies from 257.6 μm to 550.17 μm, and the error varies from 431.7 μm to 926.93 μm at the bottom end. Such variation shows the complexity and the non-periodic characteristics in free form milling when compared to milling of straight surfaces and circular surfaces where the surface accuracy repeats for each tooth pass.
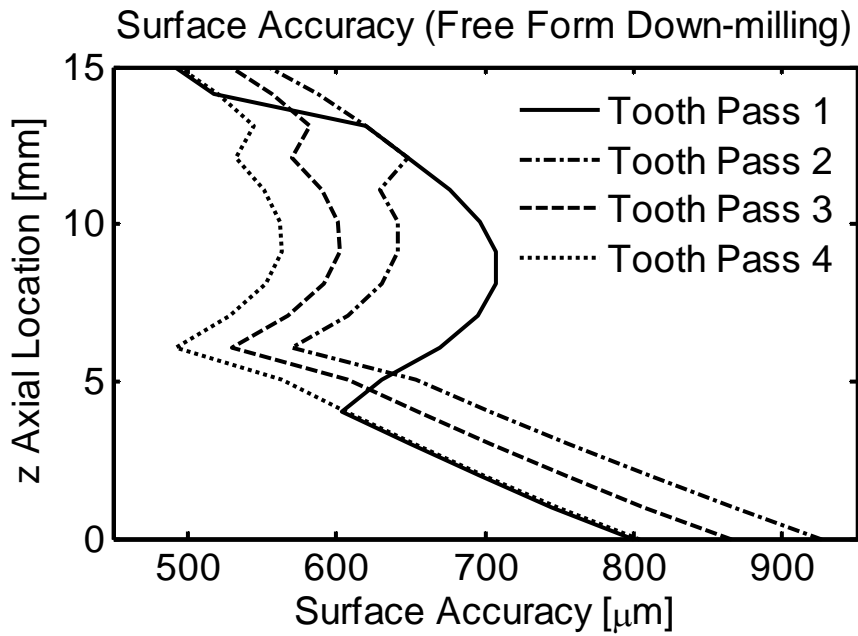
Figure 60 Surface Accuracy of Free Form Milling
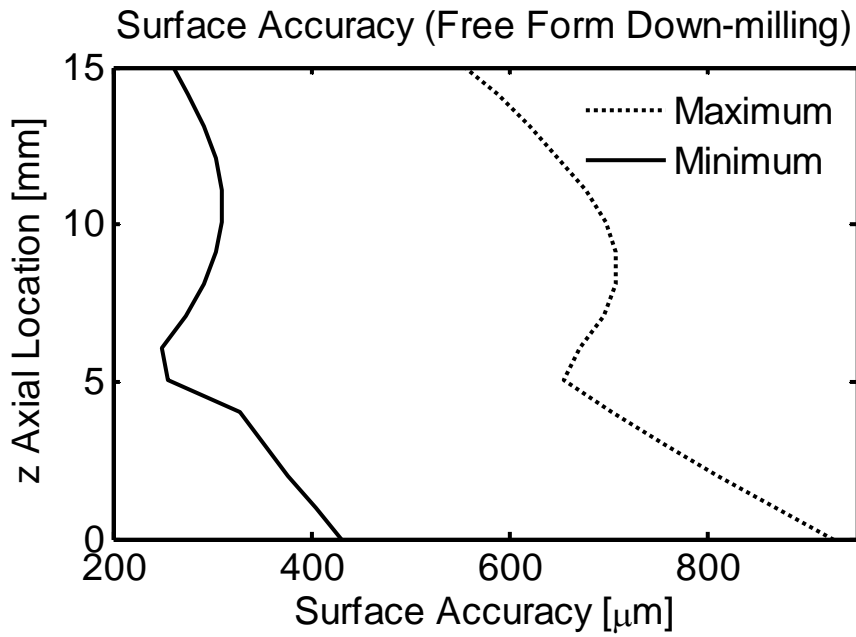
Figure 61 Minimum and Maximum Surface Accuracy in Free Form Milling

4.5   Summary and Conclusions

This chapter aims to study surface accuracy of helical end milling processes. The analysis of surface accuracy is based on the cutting force model, numerical simulation model for instantaneous cutting force, cutter deflection, and the surface generation condition. The Cutting force model and corresponding numerical simulation procedure are introduced in Section 4.2 along with the cutting force simulation results. Modeled as cantilever beam deflection, cutter deflection is analyzed in Section 4.3 and its effect on surface accuracy is simulated as well. In section 4.3, cutting force, cutter deflection and surface accuracy for milling of curved surfaces are provided. These results will be used to emulate the sensor information of cutter deflection for the design of deflection compensation.

CHAPTER 5 INDIRECT INTEGRATION OF SERVO AND PROCESS CONTROL

5.1 Introduction

In the previous section, helical end mill deflection and its influence on surface accuracy are analyzed and simulated. In practice, the surface accuracy is improved by either process design or offline tool path offset [58]. The advantages and drawbacks of these approaches have been reviewed in chapter 2, and it is concluded that online tool path offset will help improve the accuracy without sacrificing machining productivity. In this chapter, integrated servo-process control is developed to provide online tool path offset for deflection compensation. The strategy of direct integration of servo-process control presented in chapter 3 cannot be applied in this case because of the indirect relationship between deflection and servomechanism states. Cutter deflection is affected by many factors including cutter geometry, process geometry, and materials of cutter and workpiece. Unlike cutting force variation which can be associated with feed rate and depth-of-cut, deflection cannot be aggregated with the servomechanism states directly. Such indirect relationships impose challenges on the integration of the servo-process control. Alternative solution is expected to allow the servomechanism controller to simultaneously regulate axis positions and compensate for the cutter deflection.

Although cutter deflection and surface accuracy cannot be aggregated with servomechanism states as contour error and cutting forces variation, they can be measured through sensors. In open architecture machines tools which support process measuring, the surface accuracy and deflection could be measured by optical sensors or other high resolution proximity sensors. The measurement could be utilized as a media to integrate servomechanism control and deflection compensation. In this simulation-based study, we will use surface

accuracy simulation technique introduced in the previous chapter to emulate the measurement from sensors to discuss the integration approach.

Interpolators are programmed before machining to generate reference points along the tool path according to the part geometry and servomechanism limits such as speed and acceleration. During process control, interpolators are updated with the reference feed or feedrate sent from process controller according to the process variation. The updated interpolation will provide the new reference trajectory for servomechanisms. Therefore, interpolators are important media to implement process control which is not aggregated with the servomechanism control. The process variables are adjusted by updating the interpolator to change the interaction between the cutting tool and the workpiece. So the interpolation scheme considering both part geometry and tool path modification is important to implement combined servo control and process control to account for variations in the process. The interpolation scheme used in chapter 3 only considers contour geometry information since the process control is integrated in servo control and there is no need to offset tool path during machining. For cutter deflection compensation, however, the interpolation scheme should combine both part geometry and real time path offset information to implement the integrated servo-process control.

These reference points are usually generated in interpolators by approximating the trajectory with a series of linear segments or circular arcs, which will cause discontinuities along the path. The discontinuities are undesirable from the view of kinematics and dynamics. First, if acceleration and deceleration are utilized for linear segments and circular segments, it will take longer time to complete the trajectory [5]. Second, the discontinuities may generate high harmonics in the reference trajectory which may excite the natural modes of the machine tool structure [80]. Furthermore, such interpolation cannot provide constant tangential velocity along

the tool path which is required for processes like end milling to achieve constant maximum cutting forces. The interpolation scheme used in chapter 3, on the contrary, can provide constant tangential velocity. On the other hand, the angular velocity profile is required for the implementation of robust motion tracking control based on the error space approach. Furthermore, since only the deflection normal to the feed direction generates surface error, the tool path should be offset along the normal direction, which can be treated as changing the instantaneous radius. Therefore, the tool path offset can be accurately reflected in this interpolation scheme for constant tangential velocity. In this chapter, the interpolation scheme used in chapter 3 will be extended to include the path offset to implement deflection compensation.

The online deflection compensation approach is presented in this chapter. The interpolation scheme for milling of different surfaces is introduced in Section 5.2, followed by compensation strategy in Section 5.3. Simulation studies of milling of three different surfaces are conducted in Section 5.4 through Section 5.5. This chapter is concluded by summaries and conclusions in Section 5.6.

5.2   <u>Interpolation</u>

In this section, interpolation scheme for real time path offset is presented for end milling. The path offset is determined by how much surface error should be compensated. Simulation results in the previous chapter show that cutter deflection imprints varying surface errors along the axial depth of cut. If the tool path is offset to compensate for the minimum surface error, some of the surface will undergo undercuts. On the contrary, if the tool path is offset to compensate for the maximum surface error, some of the surface will undergo overcuts. The decision depends on the machining requirement. If the workpiece is machined by rough cuts, maximum surface error is more concerned for the purpose of productivity as long as the overcuts are still within tolerance requirement. On the other hand, if the workpiece is machined by finish cuts, minimum surface is more concerned for the purpose of product quality. So the quantity of path offset depends on the surface accuracy error and the dimensional tolerance requirement. In this research, a compromise is made for simplicity. Average surface error during a tool pass is used for tool path offset. The tool pass is defined as the period

$$T = \frac{1}{n \cdot N_t},$$
(117)

where n is the spindle speed and N_t is the number of tooth.

The cutter deflection compensation will be implemented for milling of three different surfaces, including straight surfaces, circular surfaces, and free-form surfaces. The interpolation schemes for milling of each surface will be presented to compensate for the average surface error.

Straight Surfaces

Since the generated surface is normal to the feed direction, it is required to offset the tool path in the normal direction to compensate for the error due to deflection. The offset scheme is based on the comparison between surface error and the tolerance requirement. The tool path is only offset along the normal direction opposite to the deflection to minimize the surface error when surface error exceeds the tolerance. Given the constant tangential velocity V_r and the sample period denoted T, the axis reference positions r_x and r_y are

$$
\begin{aligned}
r_x(t) &= r_x(t-T) + V_r \cdot T, \\
r_y(t) &= r_y(t-T) - \big(\varepsilon(t) - \Delta\big), \quad \varepsilon(t) > \Delta, \\
r_y(t) &= r_y(t-T), \quad \varepsilon(t) \le \Delta,
\end{aligned}
\tag{118}
$$

where $\epsilon(t)$ denotes the surface accuracy error, and Δ is the tolerance. From the deflection analysis in the previous section, it is know that the surface error repeats for each tooth pass. Therefore, r_y is only updated for each tooth pass rather than each interpolation sample period if the surface error is beyond the tolerance. The reference velocity along the normal direction for tool offset is implied to be

$$
V_N(t) = \frac{\varepsilon(t) - \Delta}{T}.
\tag{119}
$$

Circular Surfaces

The interpolator for straight surface utilizes the Cartesian coordinates to provide reference axis positions, while the circular interpolator uses polar coordinates to facilitate the representation of reference points. For circular surfaces, the constant angular velocity is required to maintain the

constant tangential velocity. Therefore, angular increment is constant during each interpolation sample period, and it is given by

$$\Delta\theta = \frac{V_r}{R}T. \tag{120}$$

If no deflection occurs, the constant radius R will be maintained. However, the deflection generates surface accuracy error $\epsilon(t)$ along the radial direction, and the tool path should be offset in the opposite direction. As a result, $R - \epsilon(t)$ should be used as the radius when the tooth path is offset. Since the surface accuracy error $\epsilon(t)$ is much smaller than $R,$ the tangential velocity is approximately constant when constant angular increment is used. The reference axis positions are

$$\begin{aligned}
r_x &= X_O + \left(R - \varepsilon(t)\right)\cos\left(\theta(t-1) + \Delta\theta\right), \\
r_y &= Y_O + \left(R - \varepsilon(t)\right)\sin\left(\theta(t-1) + \Delta\theta\right),
\end{aligned} \tag{121}$$

where (X_O, Y_O) is the circle center. against Therefore, the circular interpolator without considering deflection

Free-form Surfaces

The free-form surface used in the previous section is used as an example since the logarithmic spiral is commonly used form for turbine blades and impellers. The scheme can also be applied for other free-form surface by appropriate coordinate transformations.

In Cartesian coordinates, the surface profile defined by logarithmic spiral is represented by

$$\begin{aligned}
x(t) &= a\sin\left[\theta(t)\right]e^{b\theta(t)}, \\
y(t) &= a\cos\left[\theta(t)\right]e^{b\theta(t)},
\end{aligned} \tag{122}$$

where $\theta(t)$ is measured from y-axis clockwise to facilitate simulation since the rotation angle of the cutter is defined clockwise by convention. In order to maintain constant tangential velocity, the interpolator for this case should provide varying angular increment since the instantaneous radius varies along the tool path. On the other hand, since the surface error is normal to the tool path, the tool should be offset in the normal direction. The required interpolation scheme should maintain constant tangential velocity and provide necessary tool path offset to compensate for the dimensional error due to cutter deflection.

It is known from the geometry of logarithmic spirals that the arc length L corresponding to each interpolation interval dt is given by

$$
\begin{aligned}
L &= \int_{\theta}^{\theta+d\theta} \sqrt{\left(\frac{dx}{d\theta}\right)^2 + \left(\frac{dy}{d\theta}\right)^2}\, d\theta \\
&= \int_{\theta}^{\theta+d\theta} \sqrt{\left[a\left(\cos\theta e^{b\theta} + b\sin\theta e^{b\theta}\right)\right]^2 + \left[a\left(-\sin\theta e^{b\theta} + b\cos\theta e^{b\theta}\right)\right]^2}\, d\theta \\
&= a\sqrt{1+b^2}\, e^{b\theta}\left(e^{bd\theta} - 1\right) \\
&= f_r dt,
\end{aligned}
\tag{123}
$$

where f_r is the feedrate maintained along the path. Equation (123) shows that the angular increment $d\theta$ can be derived from previous angular position θ as

$$
d\theta = \frac{\ln\left[\dfrac{f_r \cdot dt}{a\sqrt{1+b^2} \cdot e^{b\theta}} + 1\right]}{b}.
\tag{124}
$$

Therefore, the interpolation for tool path without deflection is given by

$$
\begin{aligned}
x(t) &= a\sin\left[\theta(t-1) + d\theta\right]e^{b\left[\theta(t-1)+d\theta\right]}, \\
y(t) &= a\cos\left[\theta(t-1) + d\theta\right]e^{b\left[\theta(t-1)+d\theta\right]}.
\end{aligned}
\tag{125}
$$

When the dimensional error due to cutter deflection is beyond the tolerance requirement, the tool path should be offset along the normal direction which can be represented by the angle

θ_N given in equation (110). Assume the tool path should be offset by $\epsilon(t)$, the interpolation in equation (125) should be modified to

$$
\begin{aligned}
x(t) &= a\sin\left[\theta(t-1)+d\theta\right]e^{b\left[\theta(t-1)+d\theta\right]} - \delta(t)\cdot\sin(\theta_N), \\
y(t) &= a\cos\left[\theta(t-1)+d\theta\right]e^{b\left[\theta(t-1)+d\theta\right]} - \delta(t)\cdot\cos(\theta_N).
\end{aligned}
\tag{126}
$$

5.3   Error Space Motion Control

In Chapter 3, it shows that the error space motion control can drive the individual axis errors to zero. Therefore, this approach is utilized here to achieve zero errors between the axis position and real time modified reference path generated by the interpolator. The control law in Chapter 3 is found by LQR. In this case of cutter deflection, however, no optimal control problem is formulated so alternative state feedback other than LQR should be used to design the error space motion control for the servomechanism control.

The dynamics of the servomechanism system are given by

$$\tau_x \ddot{x}_x(t) + \dot{x}_x(t) = K_x u_x(t), \tag{127}$$

$$\tau_z \ddot{x}_z(t) + \dot{x}_z(t) = K_z u_z(t). \tag{128}$$

The state space representation is given by equation (1) where

$$\boldsymbol{x}^T(t) = \begin{bmatrix} x_x(t) & x_z(t) & \dot{x}_x(t) & \dot{x}_z(t) \end{bmatrix}, \tag{129}$$

$$\boldsymbol{u}^T(t) = \begin{bmatrix} u_x(t) & u_z(t) \end{bmatrix}, \tag{130}$$

$$\boldsymbol{y}^T(t) = \begin{bmatrix} x_x(t) & x_z(t) \end{bmatrix}, \tag{131}$$

$$A = \begin{bmatrix} 0 & 0 & 1 & 0 \\ 0 & 0 & 0 & 1 \\ 0 & 0 & -\dfrac{1}{\tau_x} & 0 \\ 0 & 0 & 0 & -\dfrac{1}{\tau_z} \end{bmatrix}, \quad B = \begin{bmatrix} 0 & 0 \\ 0 & 0 \\ \dfrac{K_x}{\tau_x} & 0 \\ 0 & \dfrac{K_z}{\tau_z} \end{bmatrix}, \quad H = \begin{bmatrix} 1 & 0 & 0 & 0 \\ 0 & 1 & 0 & 0 \end{bmatrix}. \tag{132}$$

The augmented servomechanism system is

$$\dot{\boldsymbol{x}}_{bot}(t) = \begin{bmatrix} E_{bot} & H_{bot} \\ 0_{(4)(4)} & A \end{bmatrix} \begin{bmatrix} \boldsymbol{e}(t) \\ \boldsymbol{\xi}(t) \end{bmatrix} + \begin{bmatrix} 0_{(4)(2)} \\ B \end{bmatrix} \boldsymbol{u}_{bot}(t), \tag{133}$$

where

$$e^T(t) = \begin{bmatrix} e_x(t) & e_z(t) & \dot{e}_x(t) & \dot{e}_z(t) \end{bmatrix}, \tag{134}$$

$$e_x(t) = x_x(t) - r_x(t), \tag{135}$$

$$e_z(t) = x_z(t) - r_z(t), \tag{136}$$

$$\xi^T(t) = \begin{bmatrix} \ddot{x}_x(t) + \omega^2 x_x(t) & \ddot{x}_z(t) + \omega^2 x_z(t) & \ddot{x}_x(t) + \omega^2 \dot{x}_x(t) & \ddot{x}_z(t) + \omega^2 \dot{x}_z(t) \end{bmatrix}, \tag{137}$$

$$E_{bot} = \begin{bmatrix} 0_{(2)(2)} & I_2 \\ -\omega^2 I_2 & 0_{(2)(2)} \end{bmatrix}, \qquad H_{bot} = \begin{bmatrix} 0_{(2)(4)} \\ H \end{bmatrix}, \tag{138}$$

$$u_{bot}(t) = \begin{bmatrix} \ddot{u}_x(t) \\ \ddot{u}_z(t) \end{bmatrix} + \omega^2 \begin{bmatrix} u_x(t) \\ u_z(t) \end{bmatrix}. \tag{139}$$

We know from Section 3.2.2.1 that $u_{bot}(t)$ in equation (139) can be found by state feedback since the augmented system is controllable. Therefore, the equation (48) for finding physical servomechanism control inputs can be written as

$$\begin{bmatrix} \ddot{u}_x(t) \\ \ddot{u}_z(t) \end{bmatrix} + \omega^2 \begin{bmatrix} u_x(t) \\ u_z(t) \end{bmatrix} = -Kx_{bot}(t), \tag{140}$$

where K can be found by one of state feedback control method, the pole placement technique.

5.4   Simulation Studies

The simulation studies are conducted under a variety of cutting conditions for three kinds of workpiece surface, *i.e.*, workpiece with straight surface, circular surface, and the free form surface. All the case studies are taken from the open literature. These simulation studies are intended to test the compensation effect subject to the variation in the spindle speed, the feedrate, and the radial depth of cut. The servomechanism parameters are from a laboratory–grade machine tool [70]: $\tau_x = 0.055$ *sec*, $\tau_z = 0.056$ *sec*, $K_x = 3.628$ *(mm/s)/V*, and $K_z = 3.706$ *(mm/s)/V*. For the convenience of comparison of compensation effects for three kinds of surfaces, all cutting simulations use the same four-fluted high-speed steel end mill with 30° helix angle and 16 mm diameter and aluminum alloy LY12 workpiece. The cutting pressure constants K_T and K_R are obtained from cutting tests [79]:

$$K_T = 578.912\left(\overline{t_c}\right)^{-0.141} \quad \text{N/mm}^2 ,$$
$$K_R = 0.6576\left(\overline{t_c}\right)^{-0.0238} . \tag{141}$$

Interpolators introduced in the previous section generate the reference axis trajectories. A Runge–Kutta fourth order integration routine with a sample period of 0.001 *sec* is utilized to solve the augmented system (133) in the error space and the control dynamic equation(140). The poles for the simulations are chosen by trial and error, and they are -79±83*i*, -125±20*i*, -200±50*i*, -100, and -210.

5.4.1   Milling of Straight Surfaces

In the simulation studies of straight surface milling, the effect of the interpolation and deflection compensation approach will be evaluated under variation in cutting conditions. It is shown in the previous chapter that the surface accuracy is affected by cutting conditions including the spindle speed, the feed rate, the radial and the axial depth of cut. Since both the radial depth of cut and

the axial depth of cut have influence on the engagement of the cutter, only the radial depth of cut is chosen for simplicity. For the three sets of simulations, the workpiece length is taken as 12.4 mm, and the origin is set as the initial position of the cutter center when cutting begins. The first set of simulations is performed to illustrate the improvement of average surface accuracy under four different feed rates of 25, 35, 50, and 65 mm/min. The other cutting conditions used are $n = 300$ rpm, $d_a = 5$ mm, and $d_r = 15$ mm. The simulation results for f_r=25 mm/min are shown in Figure 62-Figure 64. Note only the tool path and control signals during transient period are plotted to illustrate the transient behavior.
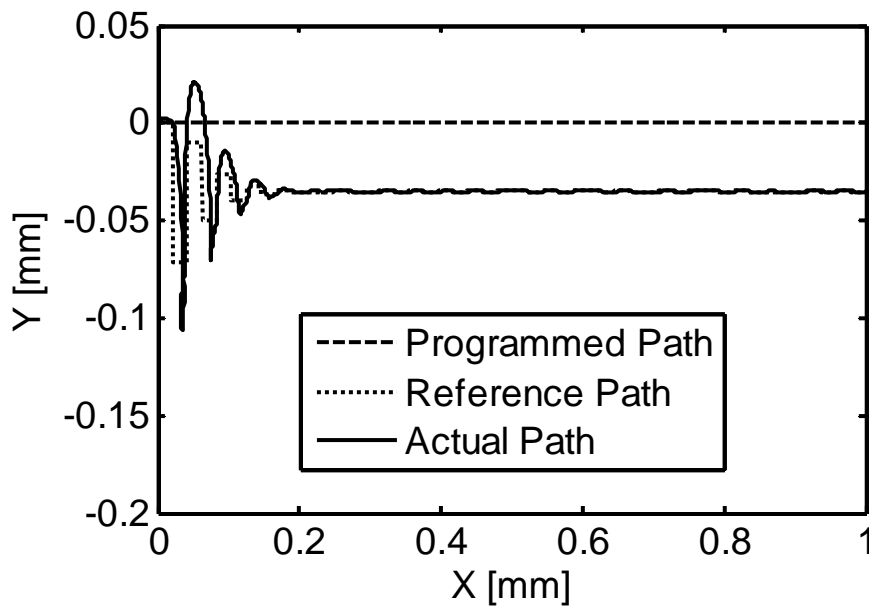
Figure 62 Tool Path (f_r=25 mm/min)
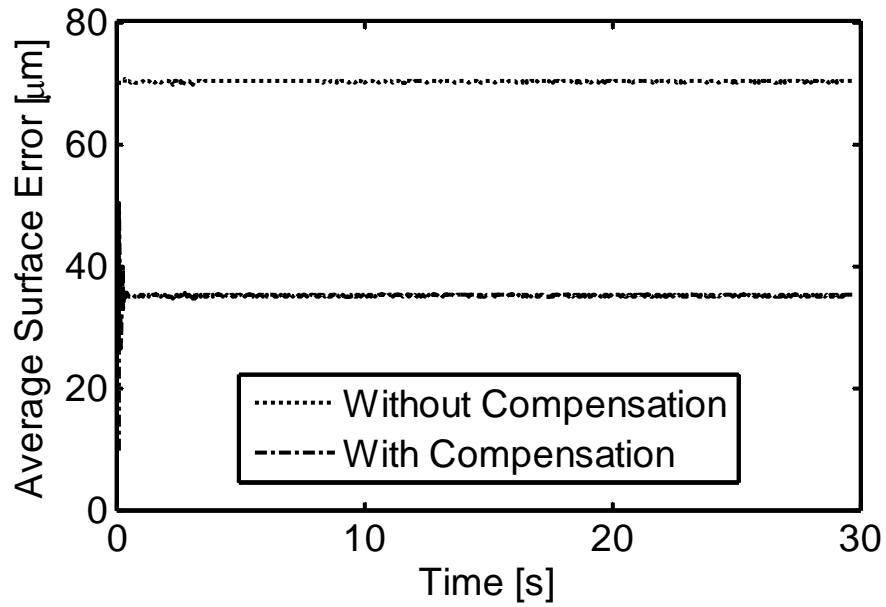
Figure 63 Average Surface Accuracy Error (f$_r$=25 mm/min)
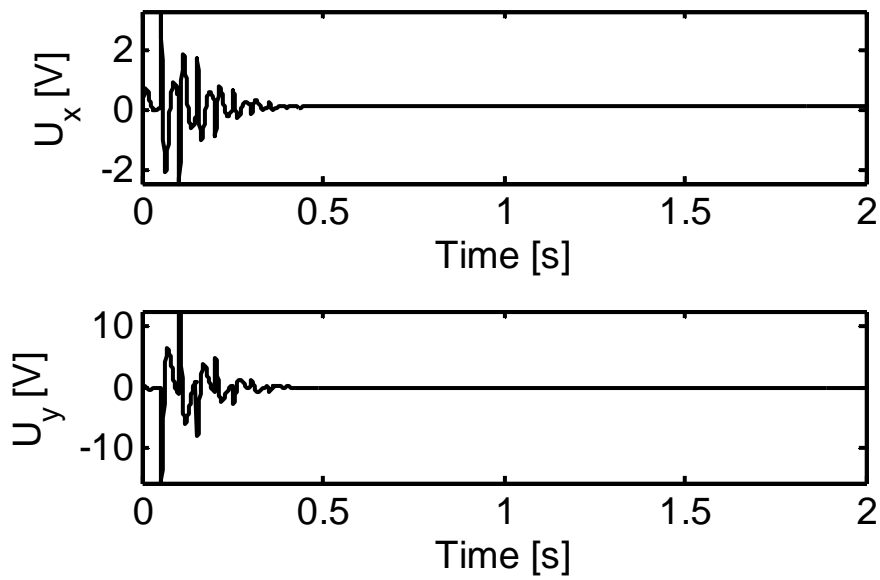
Figure 64 Control Signals (f$_r$=25 mm/min)

The simulation results for f$_r$=35 mm/min are shown in Figure 65-Figure 67.
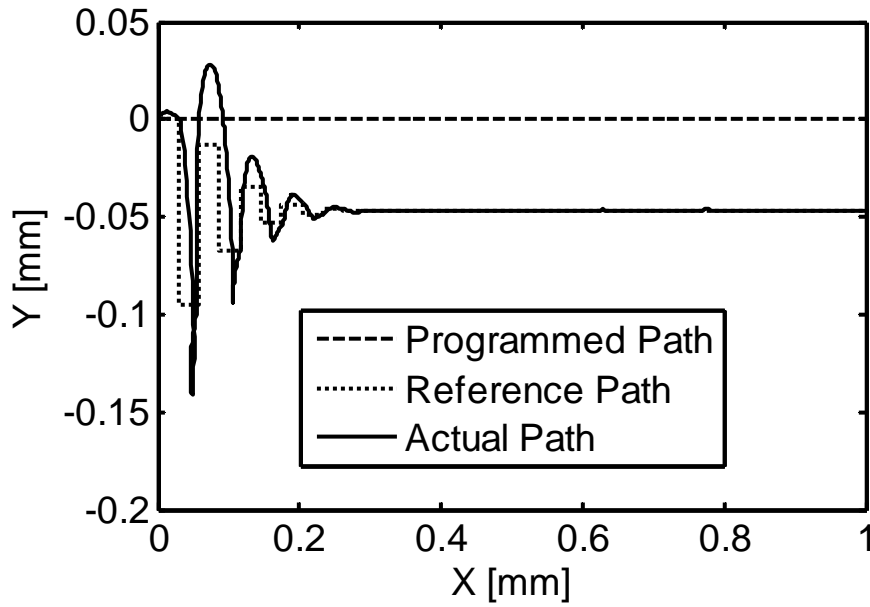
Figure 65 Tool Path (f$_r$=35 mm/min)
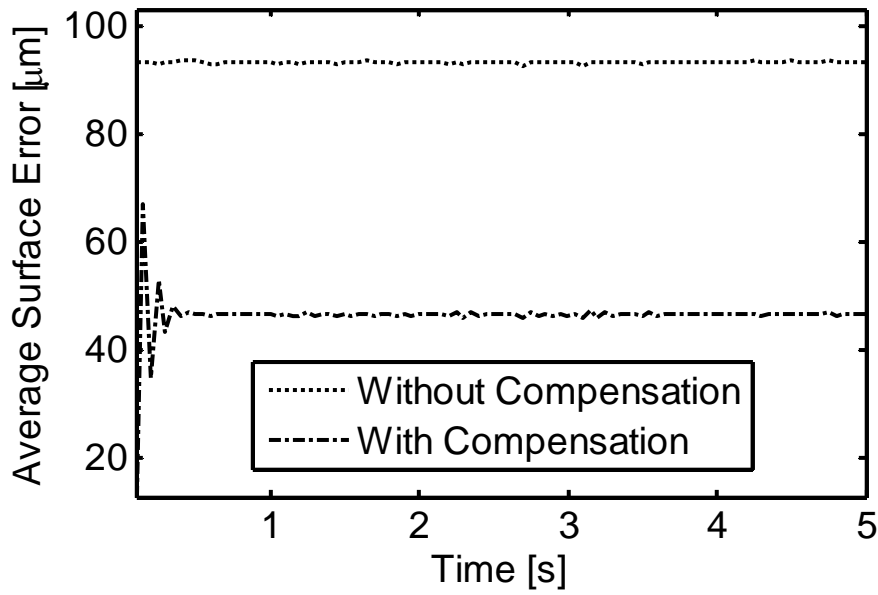
Figure 66 Average Surface Accuracy Error (f$_r$=35 mm/min)
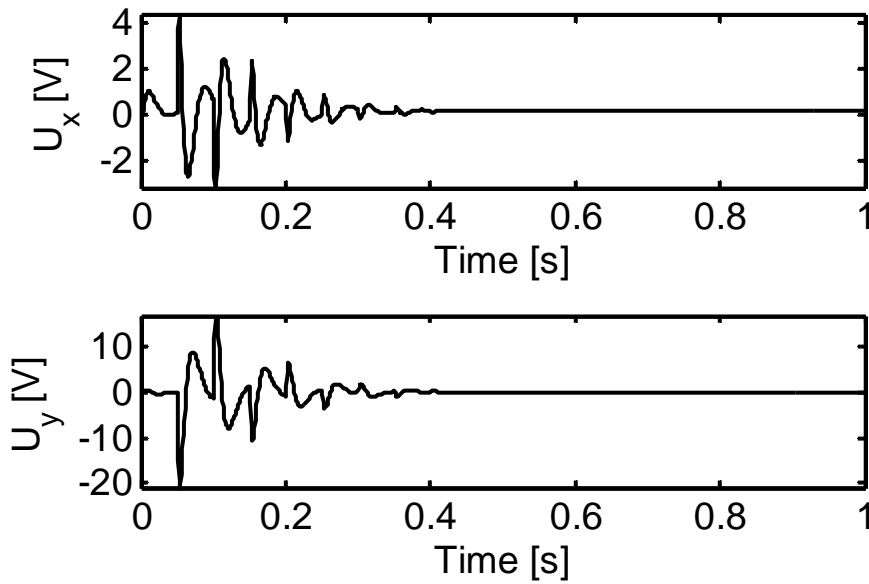
Figure 67 Control Signals (f$_r$=35 mm/min)

The simulation results for f$_r$=50 mm/min are shown in Figure 68-Figure 70.
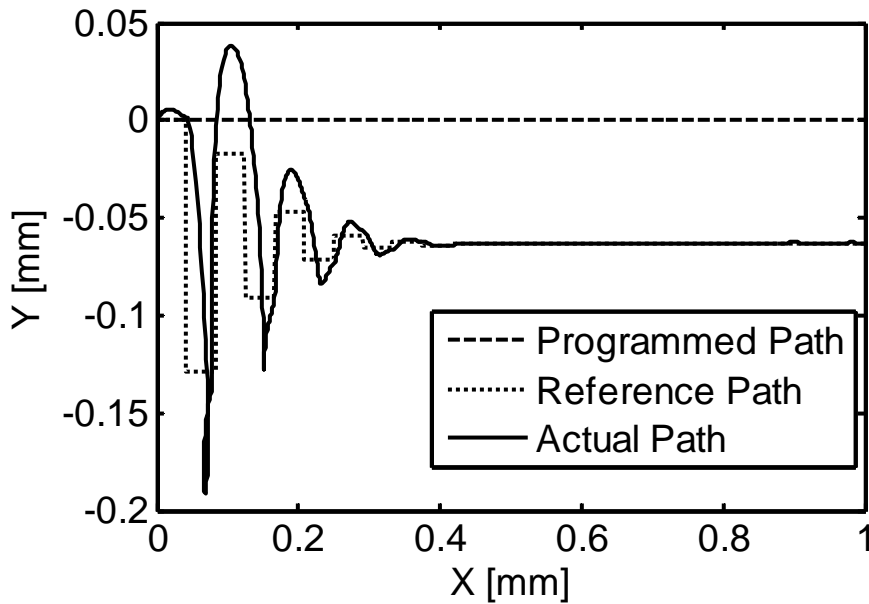
Figure 68 Tool Path (f$_r$ = 50 mm/min)
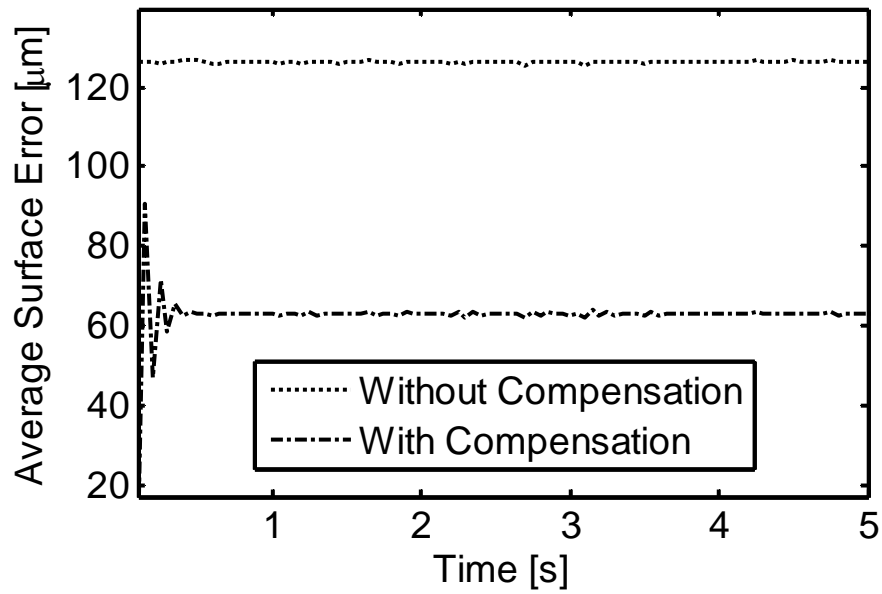
Figure 69 Average Surface Accuracy Error (f$_r$=50 mm/min)
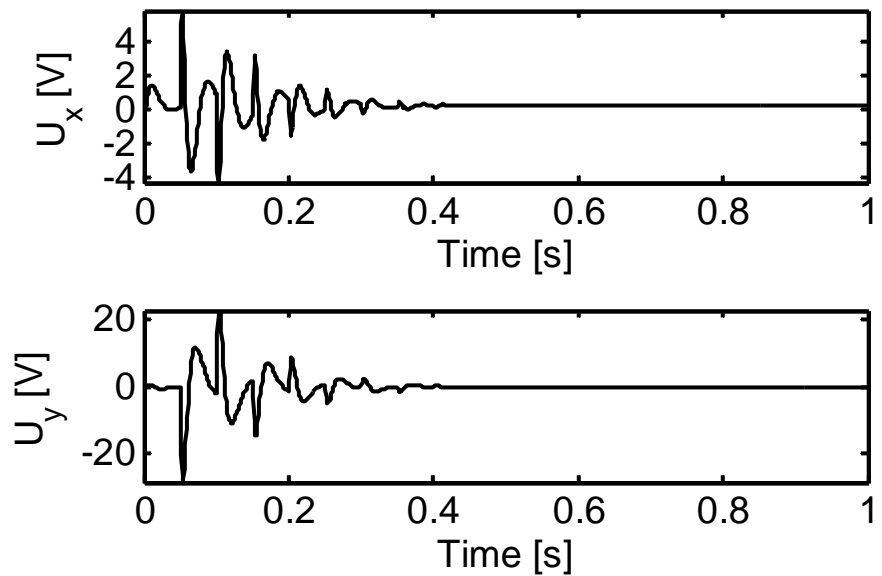
Figure 70 Control Signals (f$_r$ = 50 mm/min)

The simulation results for f$_r$=65 mm/min are shown in Figure 71-Figure 73.
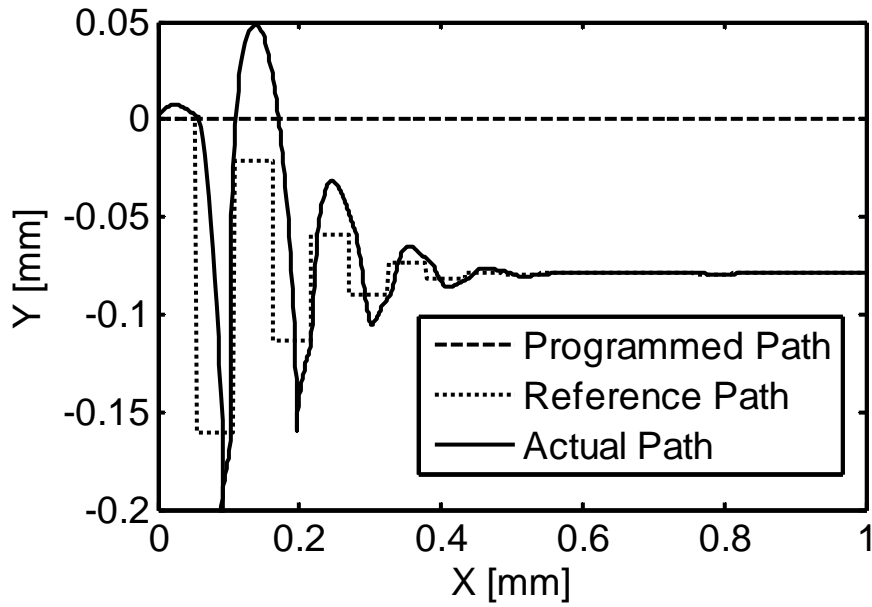
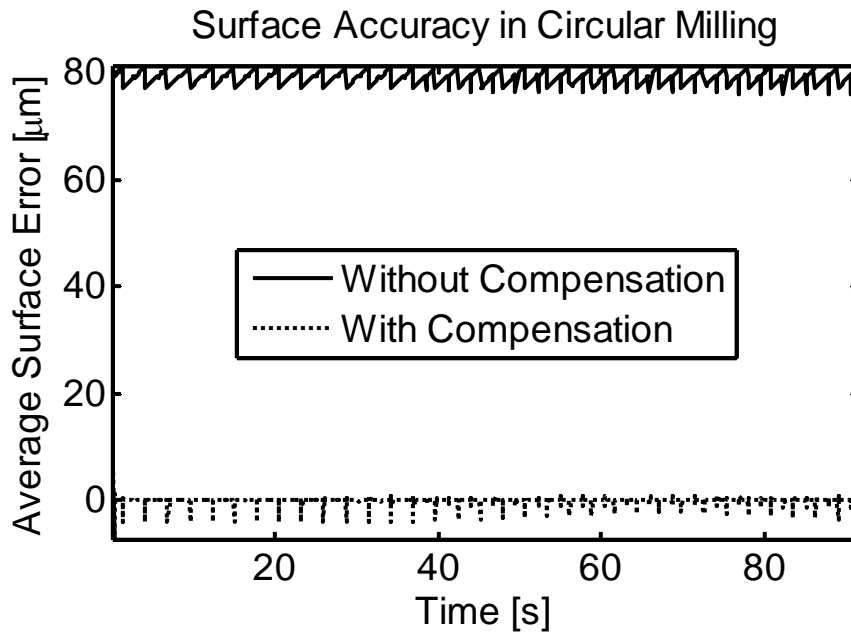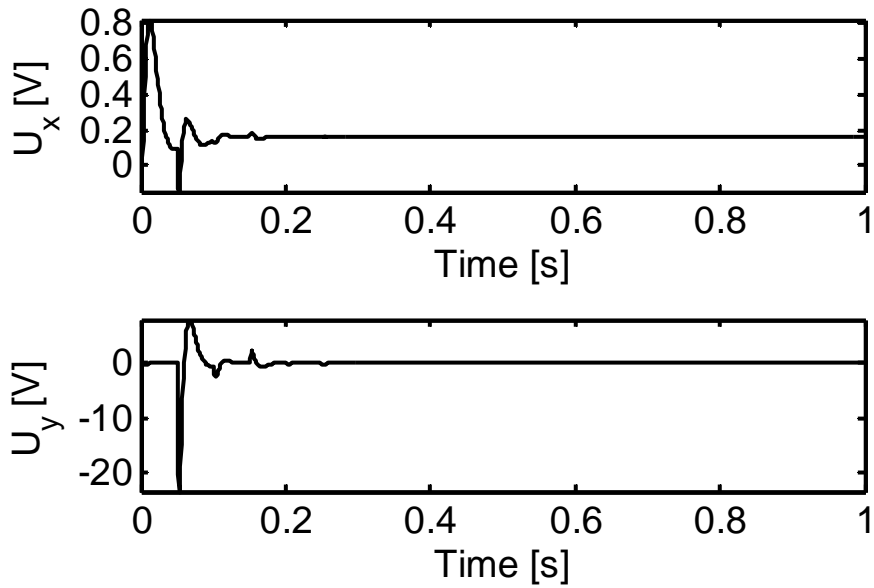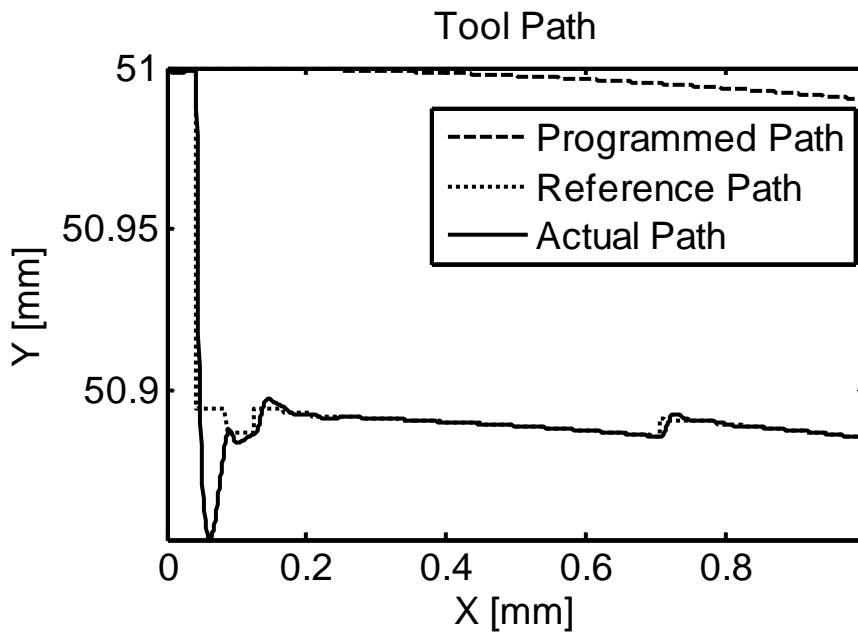**Figure 71 Tool Path (f_r = 65 mm/min)**
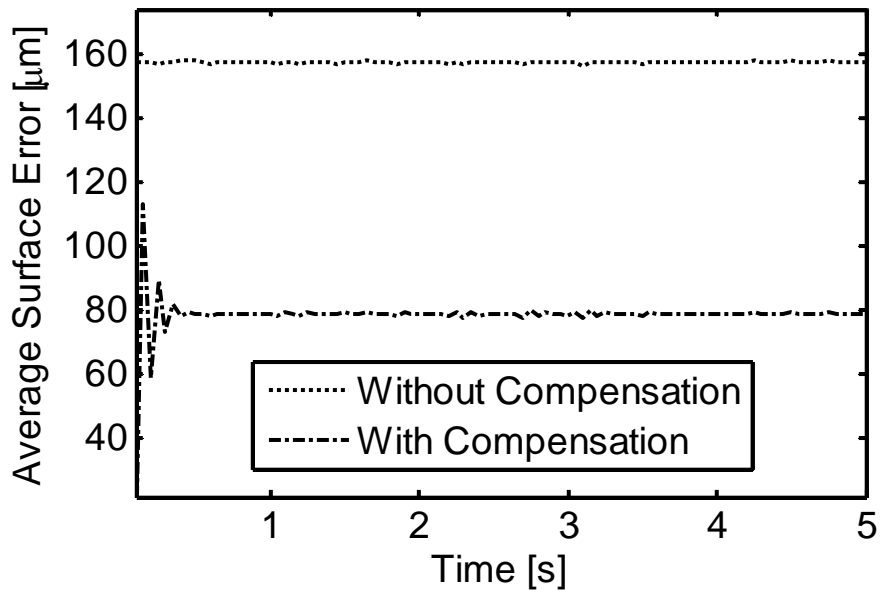
Figure 72 Average Surface Accuracy Error (f_r=65 mm/min)

116
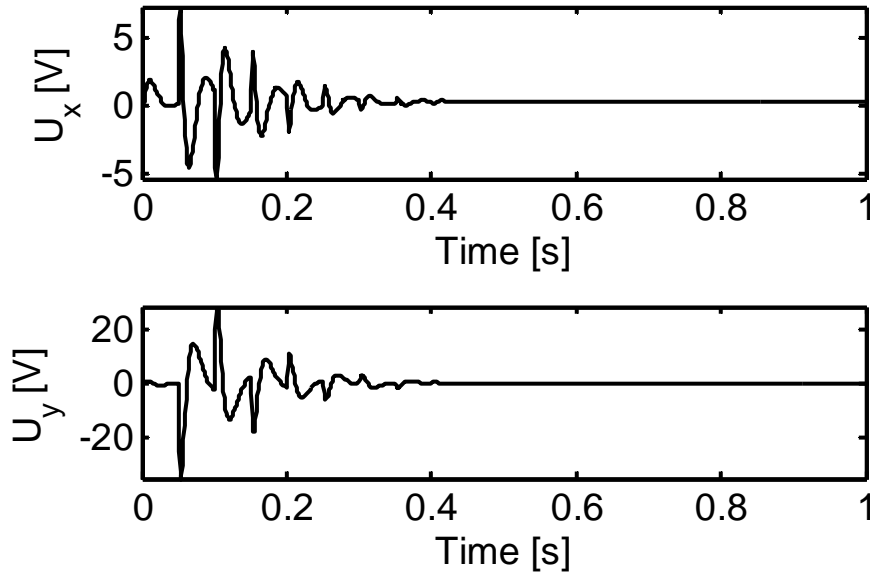
Figure 73 Control Signals (f$_r$=65 mm/min)

The second set of simulations is performed to illustrate the improvement of average surface accuracy under four different spindle speeds as 300, 420, 540 and 650 rpm. The other cutting conditions used are f$_r$ = 40 mm/min, $d_r = 5$ mm, and $d_a = 15$ mm. The simulation results for n=300 rpm are shown in Figure 74-Figure 76.
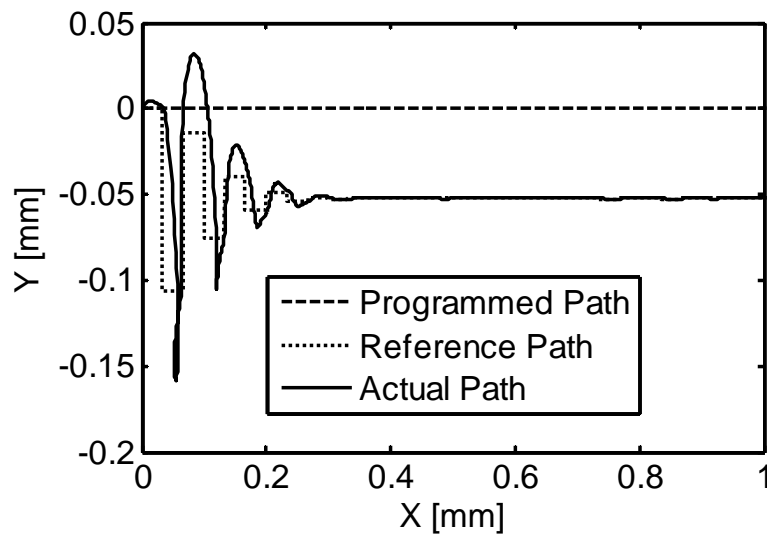
Figure 74 Tool Path (n=300 rpm)
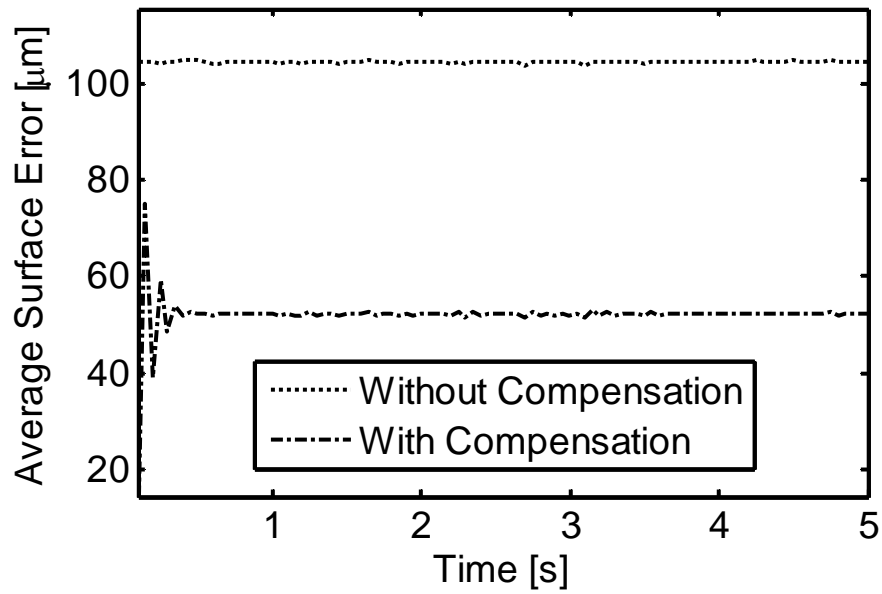
Figure 75 Average Surface Accuracy (n = 300 rpm)
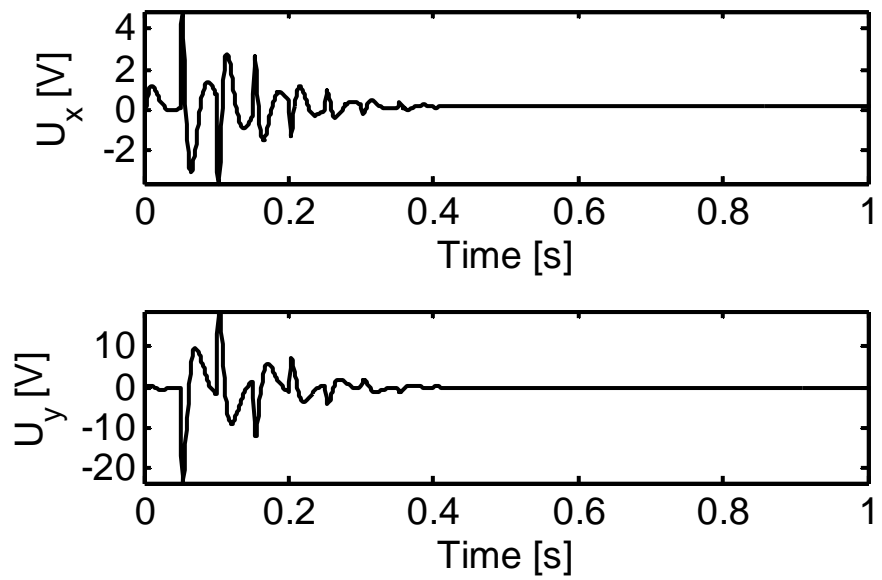
Figure 76 Control Signals (n = 300 rpm)

The simulation results for n=420 rpm are shown in Figure 77-Figure 79.
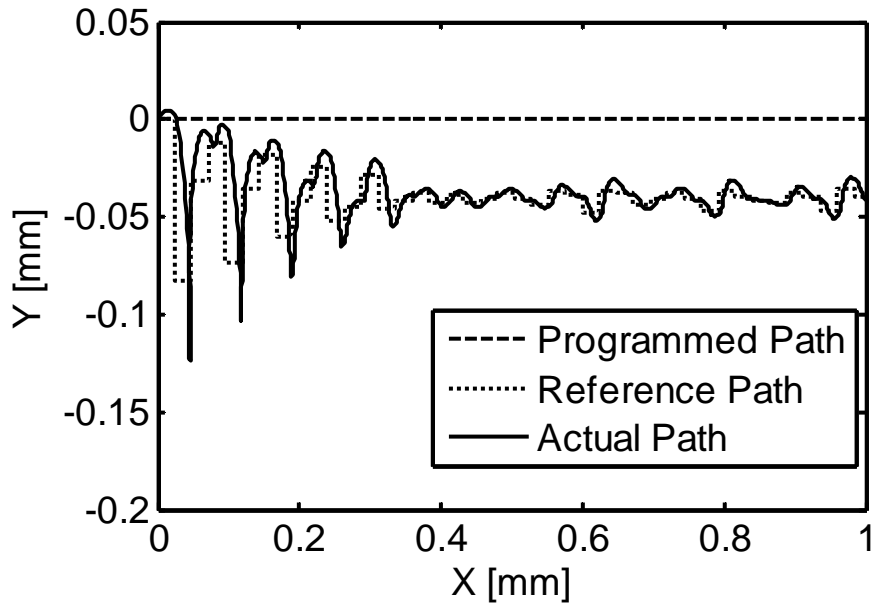
Figure 77 Tool Path (n = 420 rpm)
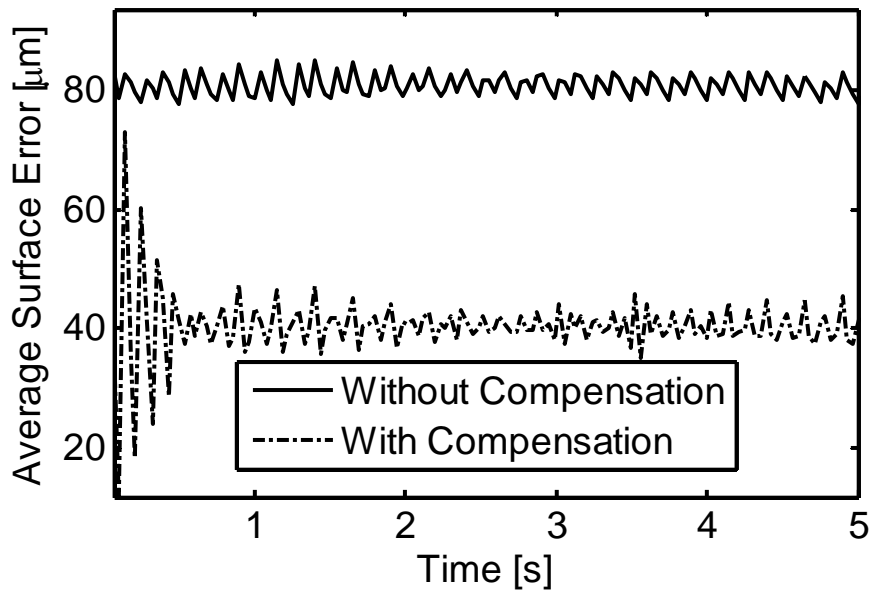
Figure 78 Average Surface Accuracy (n = 420 rpm)

119
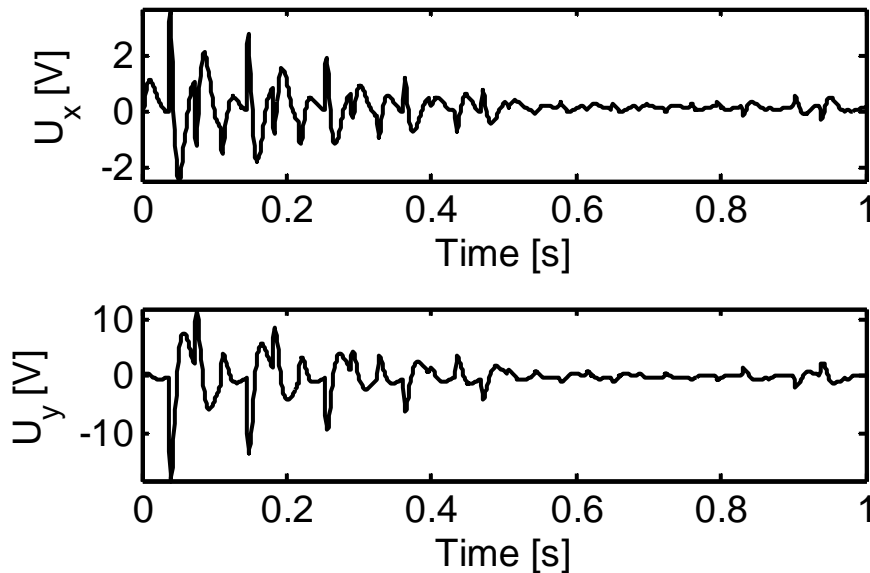
Figure 79 Control Signals (n = 420 rpm)

For n=540 rpm and n=650 rpm, the spindle speed is too fast for the servomechanism to shift the tool path since for the compensation is implemented for each tooth pass $T = 1/(nN_t)$. The system is unstable for high spindle speed. This trend can be observed from the oscillation in the results for n = 420 rpm.

The third set of simulations is performed to illustrate the improvement of average surface accuracy under three different radial depth of cut as 3, 4, 5 and 6 mm. The other cutting conditions used are n = 300 rpm, f_r = 50 mm/min, and $d_a = 15$ mm. The simulation results for $d_r = 3mm$ are shown in Figure 80-Figure 82.
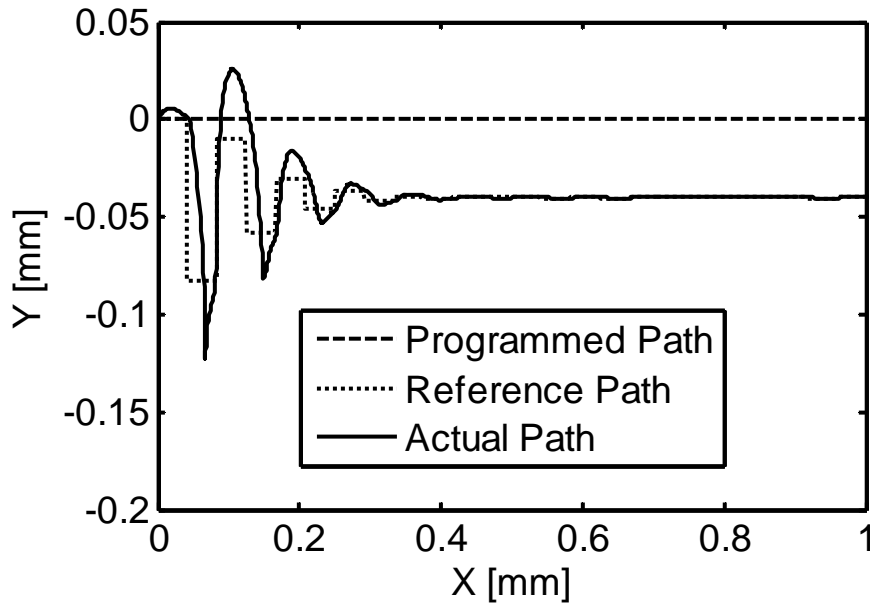
Figure 80 Tool Path (d$_r$ = 3 mm)
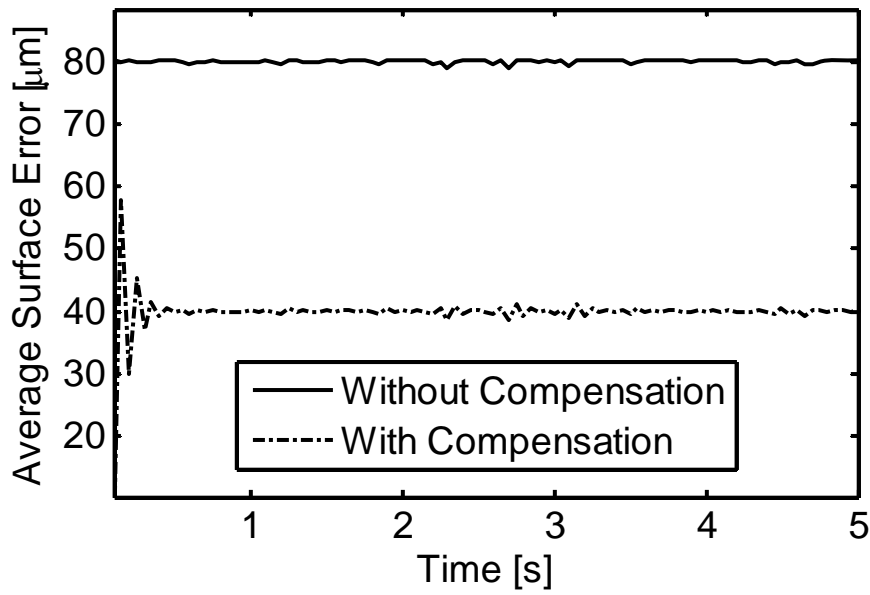
Figure 81 Average Surface Accuracy (d$_r$ = 3 mm)

121
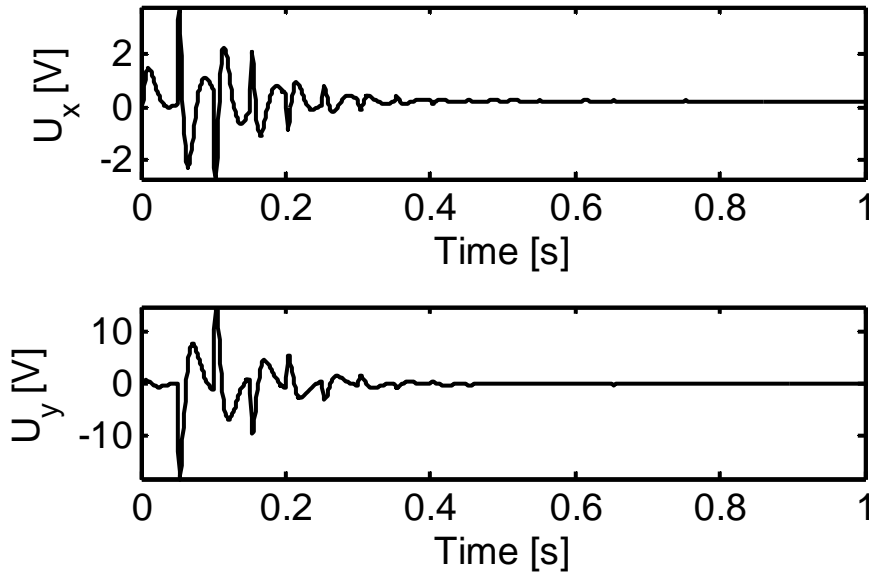
Figure 82 Control Signals (d$_r$ = 3 mm)

The simulation results for $d_r = 4mm$ are shown in Figure 83-Figure 85.
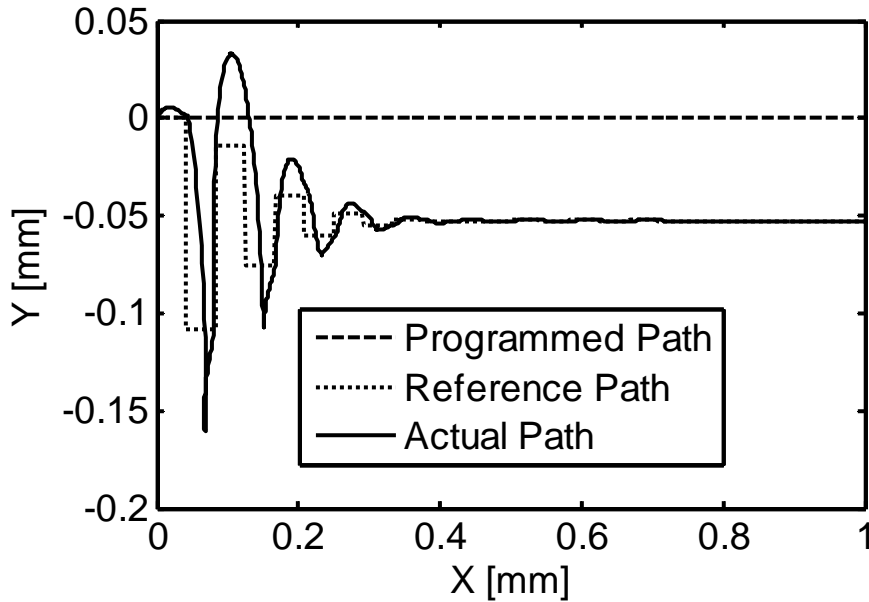
Figure 83 Tool Path (d$_r$ = 4 mm)
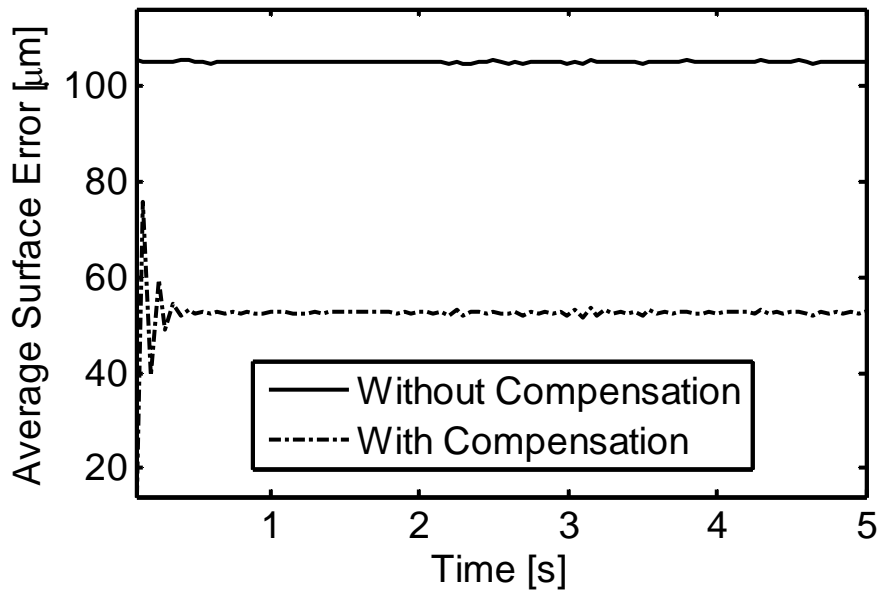
Figure 84 Average Surface Accuracy (d_r = 4 mm)
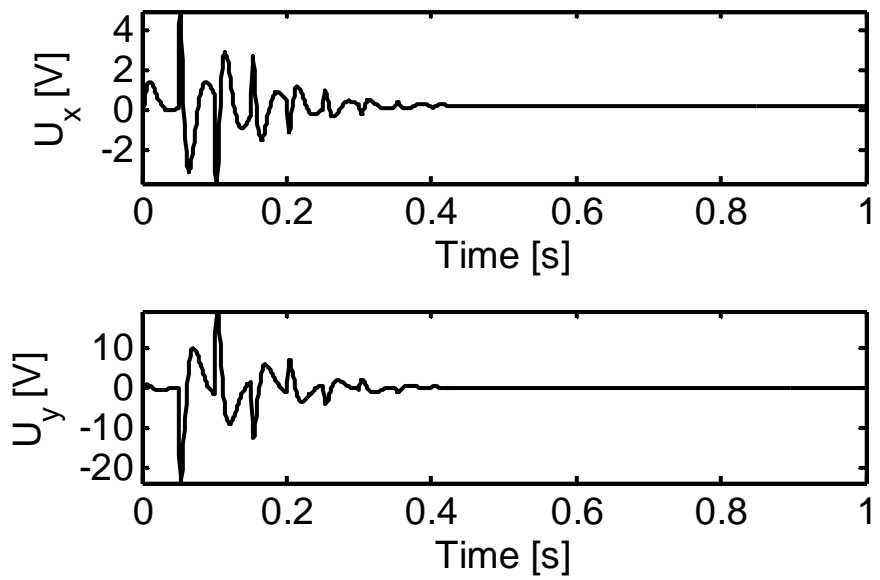
Figure 85 Control Signals (d_r = 4 mm)

The simulation results for $d_r = 5mm$ are shown in Figure 86-Figure 88.
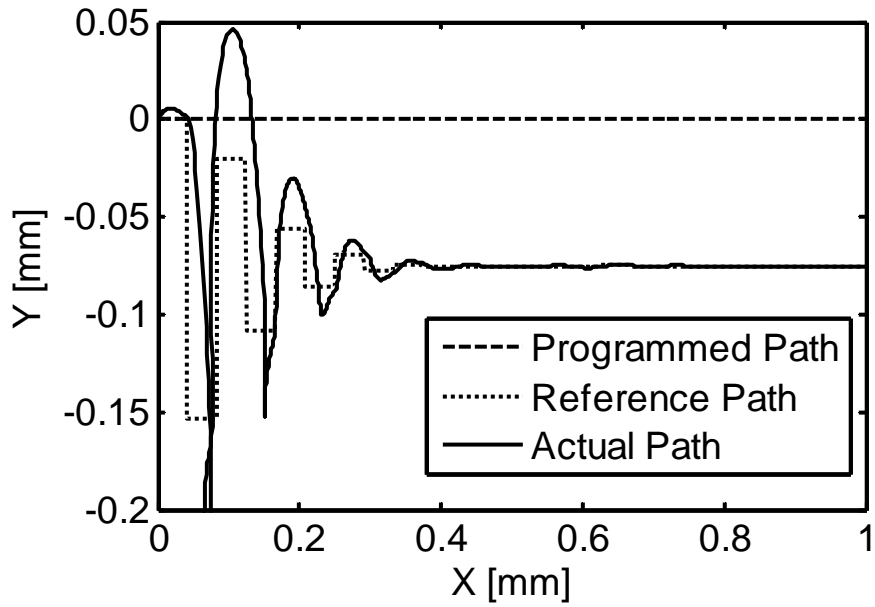
Figure 86 Tool Path (d_r = 5 mm)
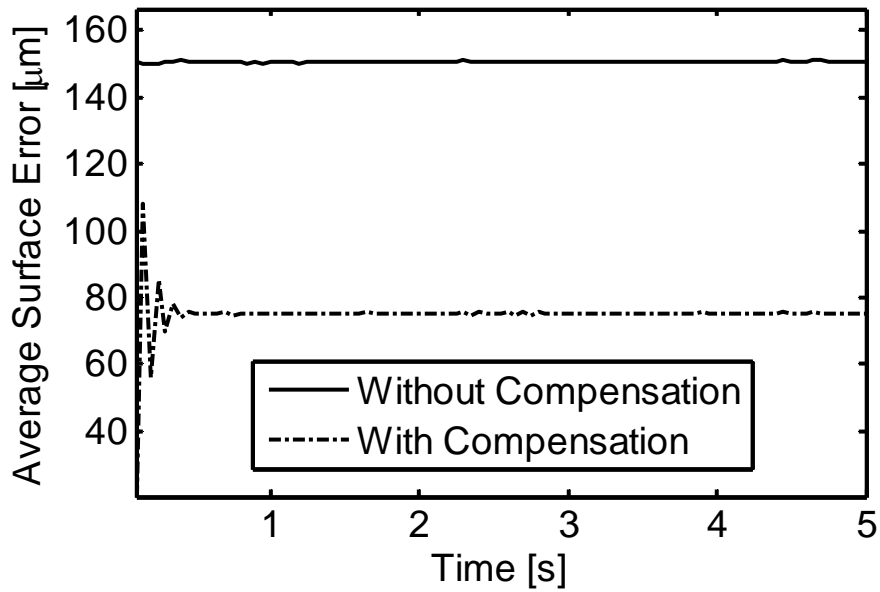
Figure 87 Average Surface Accuracy (d_r = 5 mm)
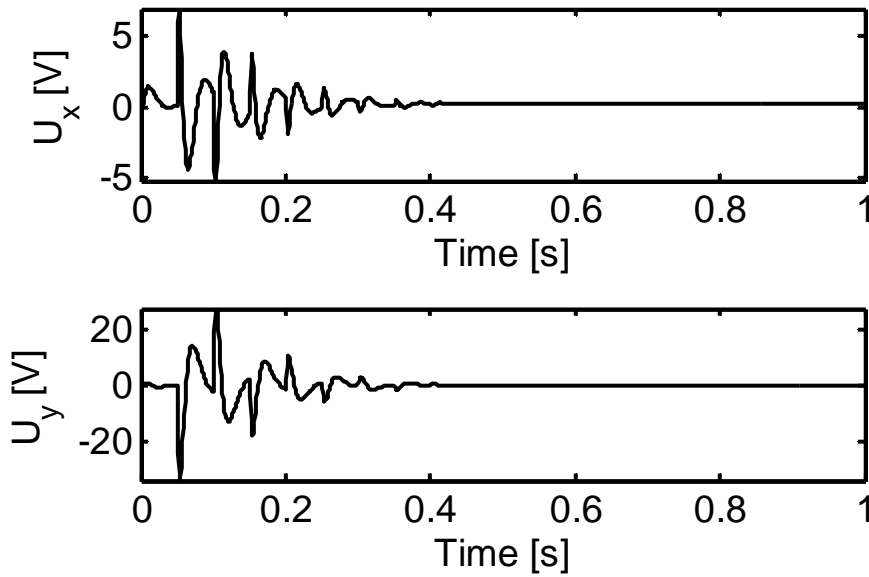
Figure 88 Control Signals (d$_r$ = 5 mm)

The simulation results for $d_r = 6mm$ are shown in Figure 89-Figure 91.
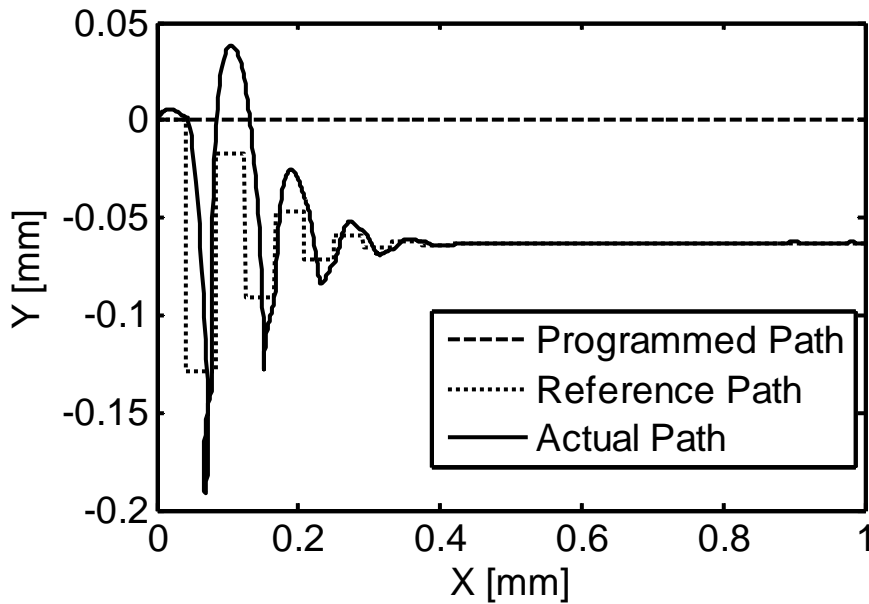
Figure 89 Tool Path (d$_r$ = 6 mm)
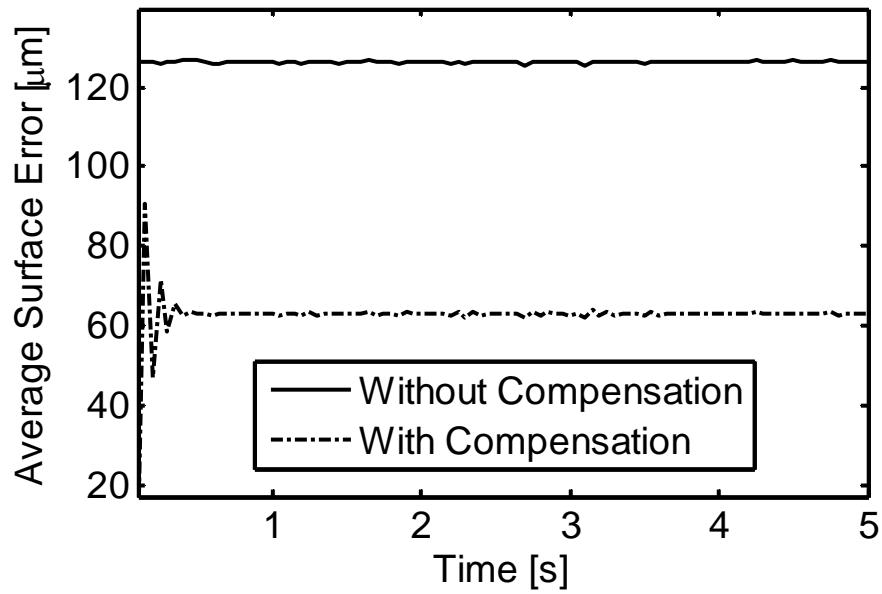
Figure 90 Average Surface Accuracy (d_r = 6 mm)
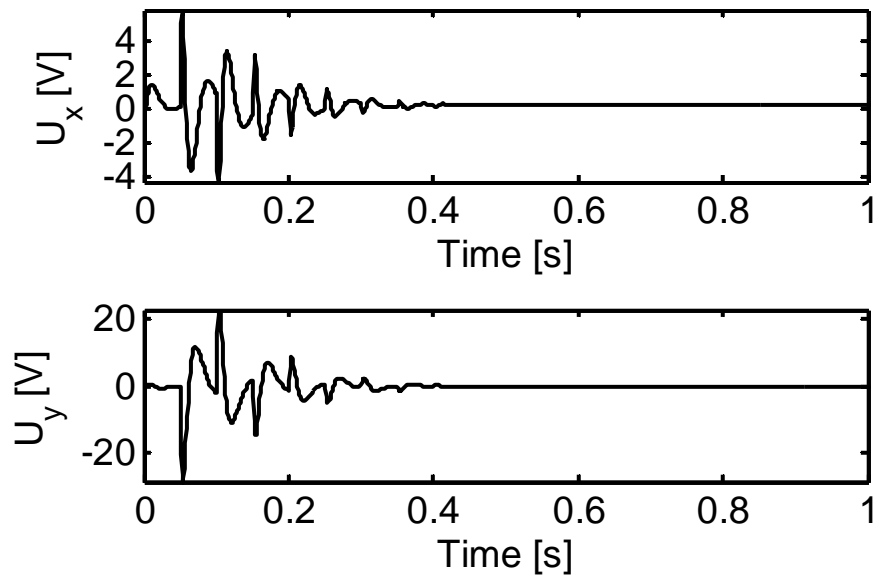
Figure 91 Control Signals (d_r = 6 mm)

5.4.2 Milling of Circular Surfaces

In the simulation studies of circular surface milling, the effect of the interpolation and deflection compensation approach will be evaluated under variation in cutting conditions including the spindle speed, the feed rate, and the radial depth of cut. For the three sets of simulations, the workpiece radius is taken as 48 mm, and the origin is set as the center of the workpiece for the simplicity of tool path representation. The first set of simulations is performed to illustrate the improvement of average surface accuracy under four different feed rates of 25, 35, 50, and 65 mm/min. The other cutting conditions used are $n = 300$ rpm, the workpiece radius $R_w = 46mm$, $d_r = 5$ mm, and $d_a = 15$ mm. The simulation results for f_r=25 mm/min are shown in Figure 92-Figure 94.
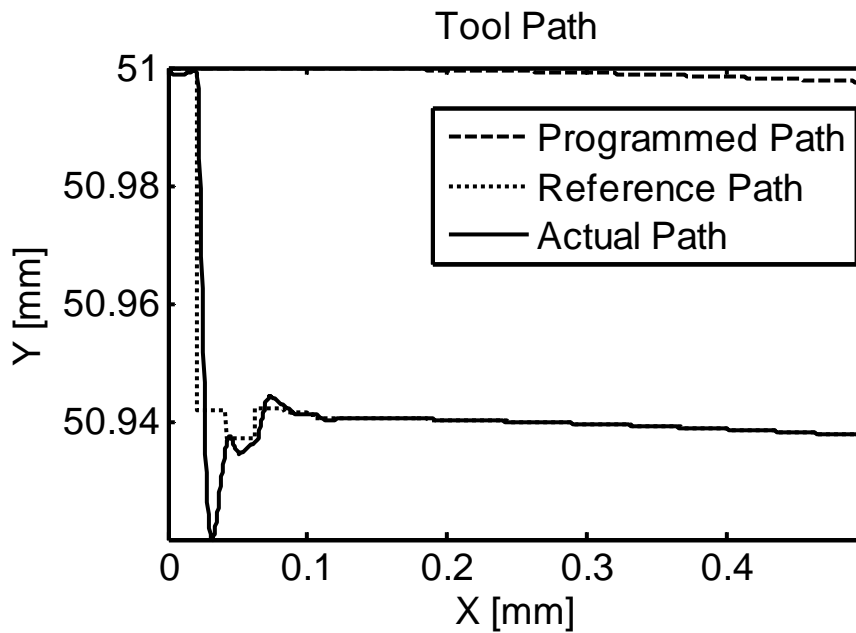
Figure 92 Tool Path ($f_r = 25$ mm/min)
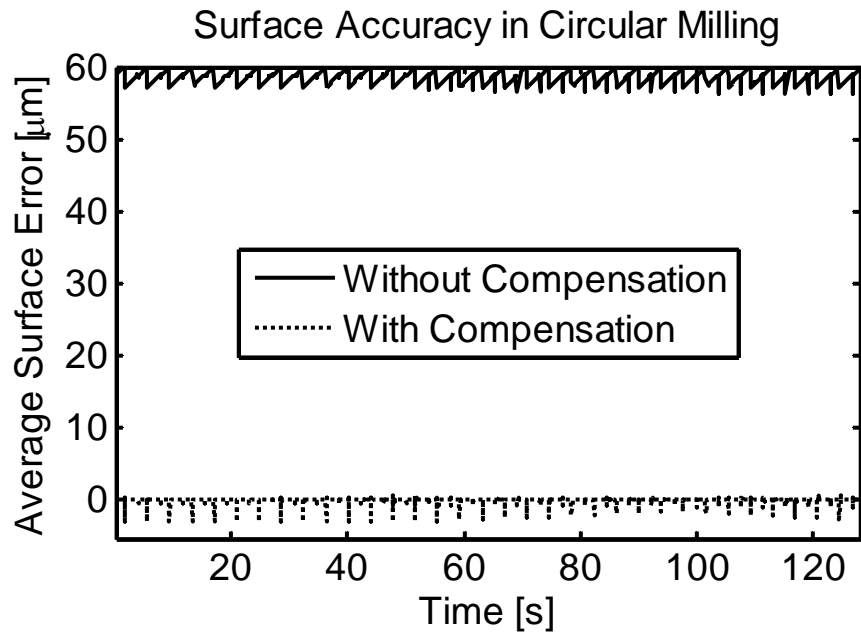
Figure 93 Average Surface Accuracy (f_r = 25 mm/min)
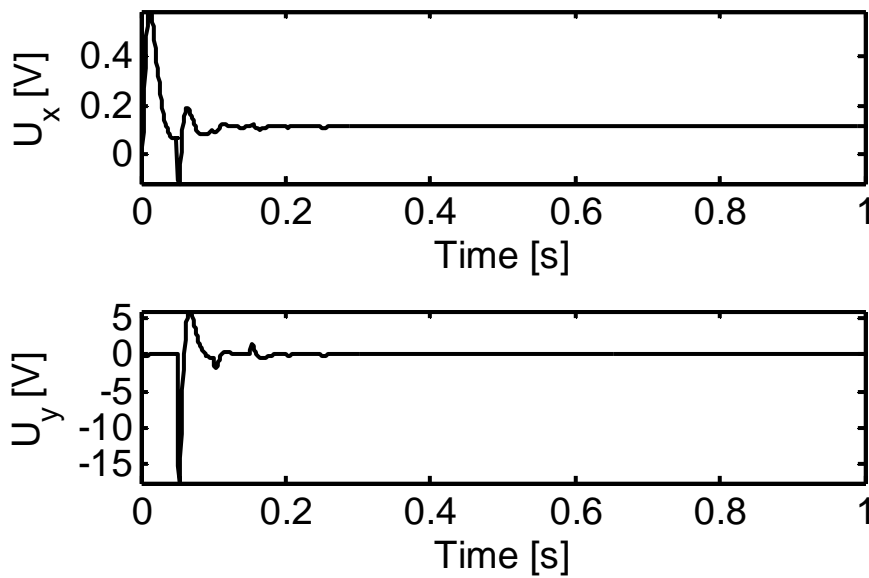
Figure 94 Control Signals (f_r = 25 mm/min)

The simulation results for f_r=35 mm/min are shown in Figure 95-Figure 97.
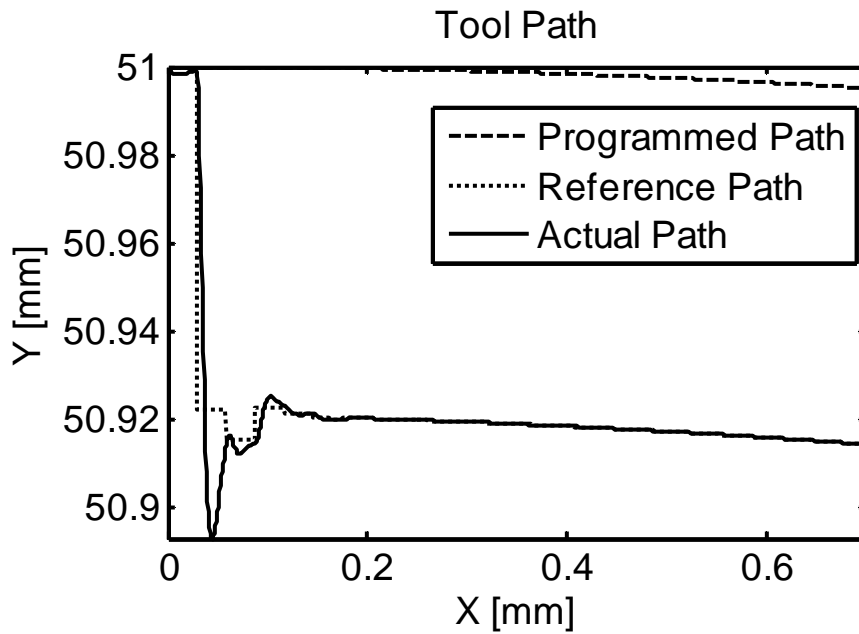
Tool Path

Figure 95 Tool Path (f_r = 35 mm/min)

Surface Accuracy in Circular Milling

Figure 96 Average Surface Accuracy (f_r = 35 mm/min)

Figure 97 Control Signals (f$_r$ = 35 mm/min)

The simulation results for f$_r$=50 mm/min are shown in Figure 98-Figure 100.

Figure 98 Tool Path (f$_r$ = 50 mm/min)
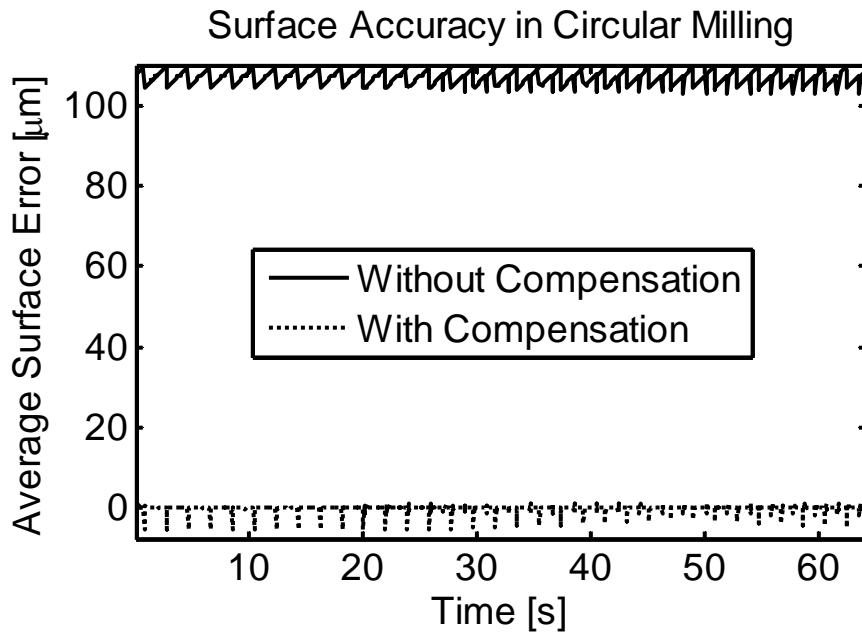
Figure 99 Average Surface Accuracy (f_r = 50 mm/min)
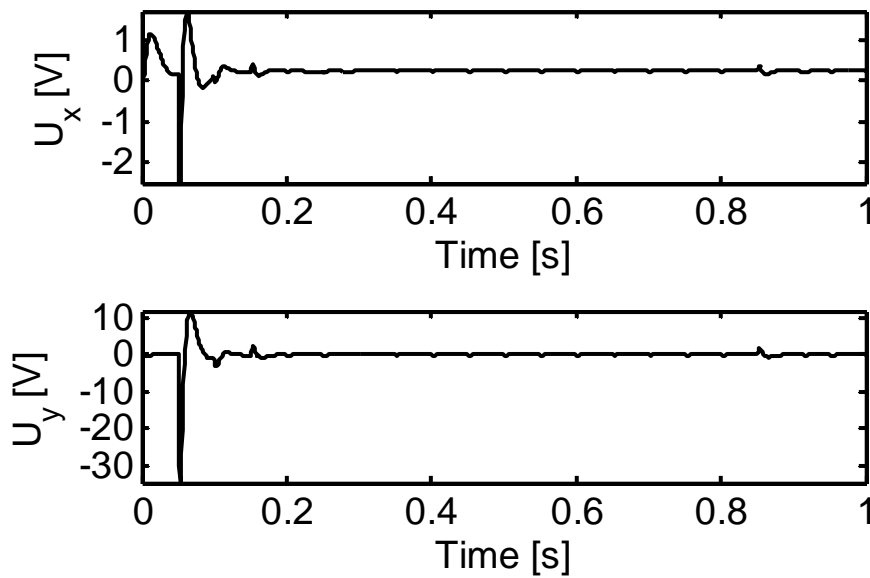
Figure 100 Control Signals (f_r = 50 mm/min)

The simulation results for f_r=65 mm/min are shown in Figure 101-Figure 103.
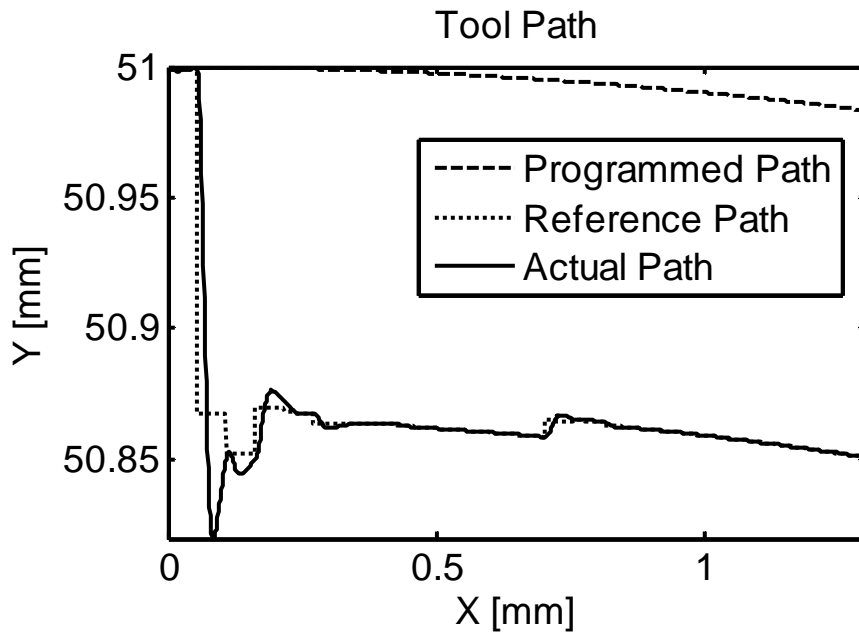
Figure 101 Tool Path (f$_r$ = 65 mm/min)
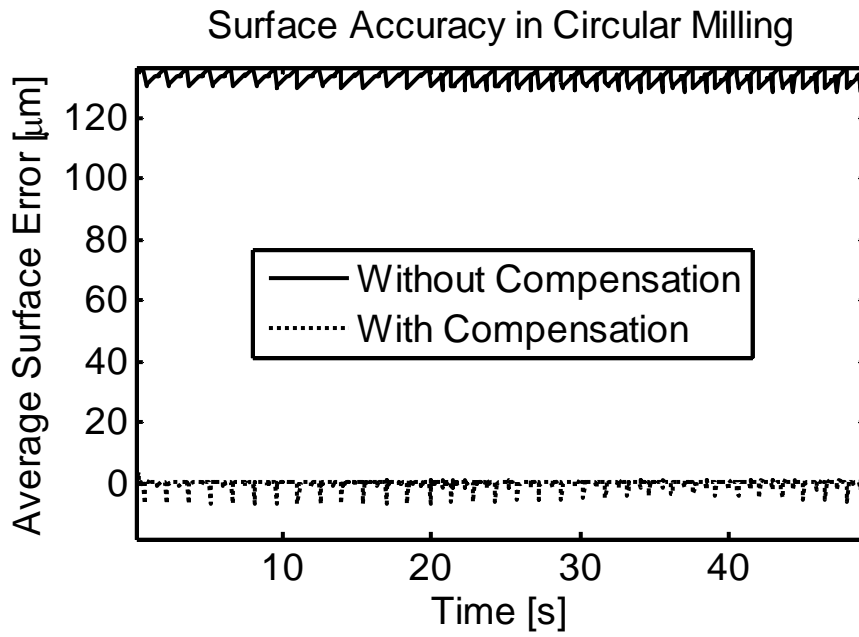
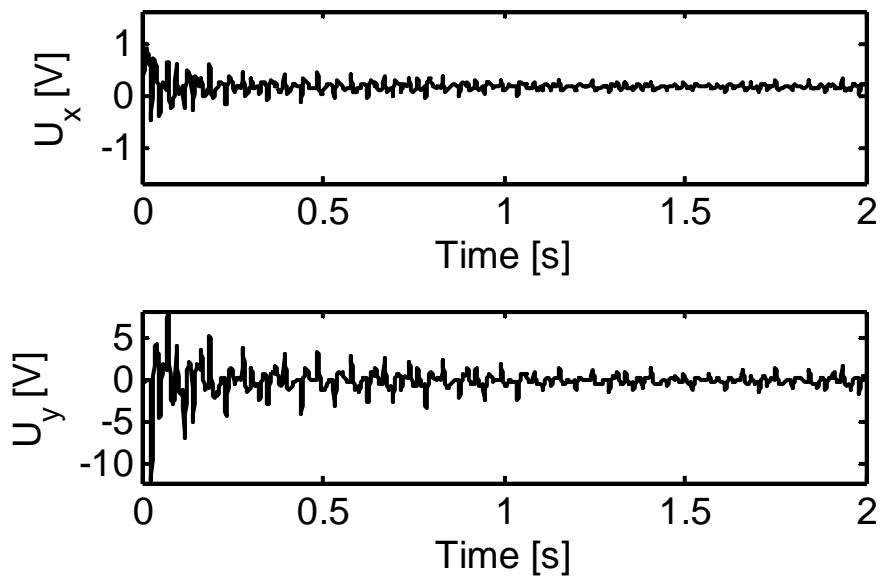**Figure 102 Average Surface Accuracy (f$_r$ = 65 mm/min)**
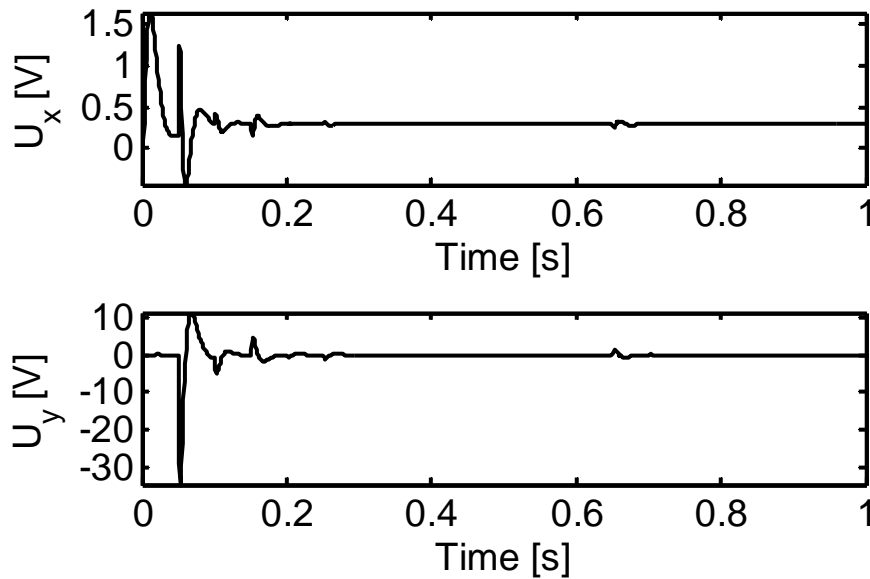
Figure 103 Control Signals (f$_r$ = 65 mm/min)

The second set of simulations is performed to illustrate the improvement of average surface accuracy under four different spindle speeds of 300, 420, 540, and 650 rpm. The other cutting conditions used are $f_r = 40$ mm/min, the workpiece radius $R_w = 46mm$, $d_r = 5$ mm, and $d_a = 15$ mm. The simulation results for n=300 rpm are shown in Figure 104-Figure 106.
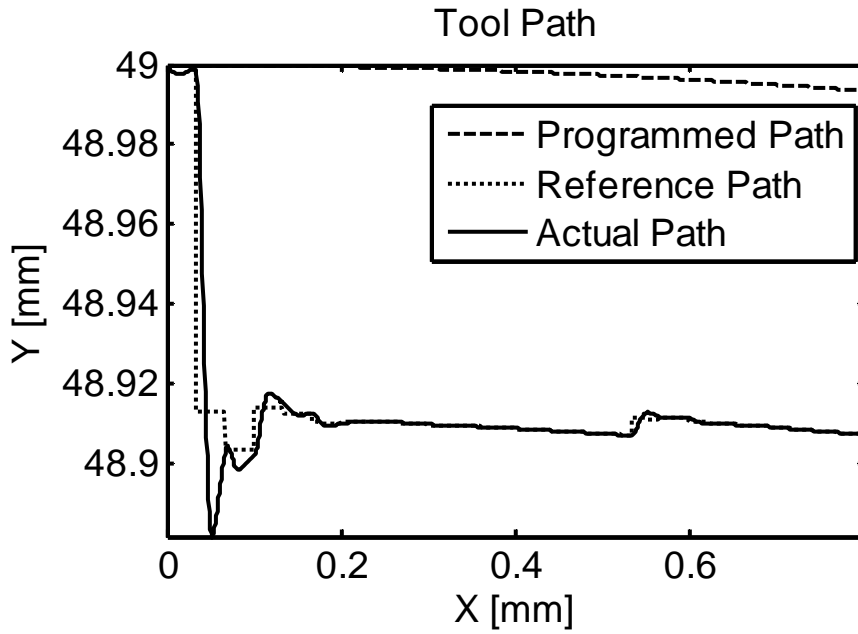
Figure 104 Tool Path (n = 300 rpm)
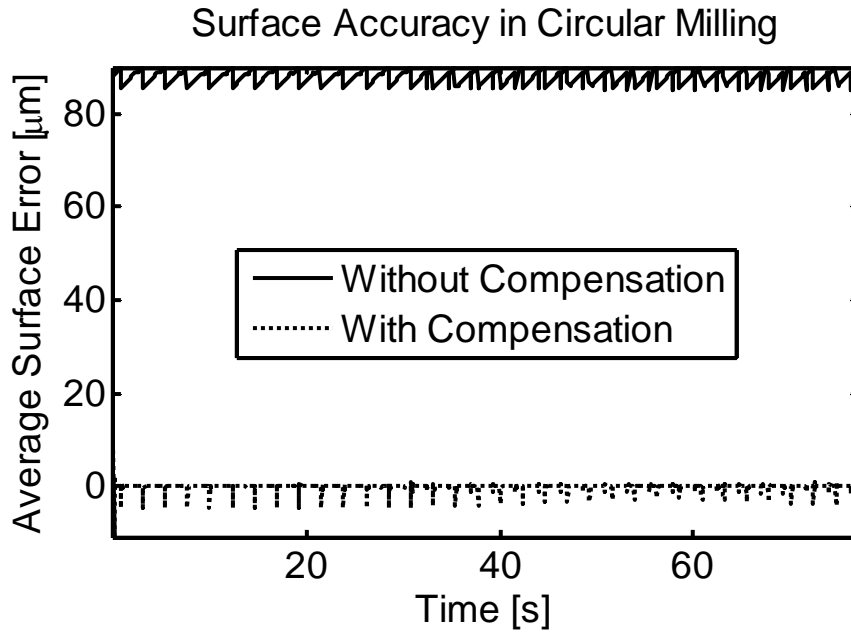
Figure 105 Average Surface Accuracy (n = 300 rpm)
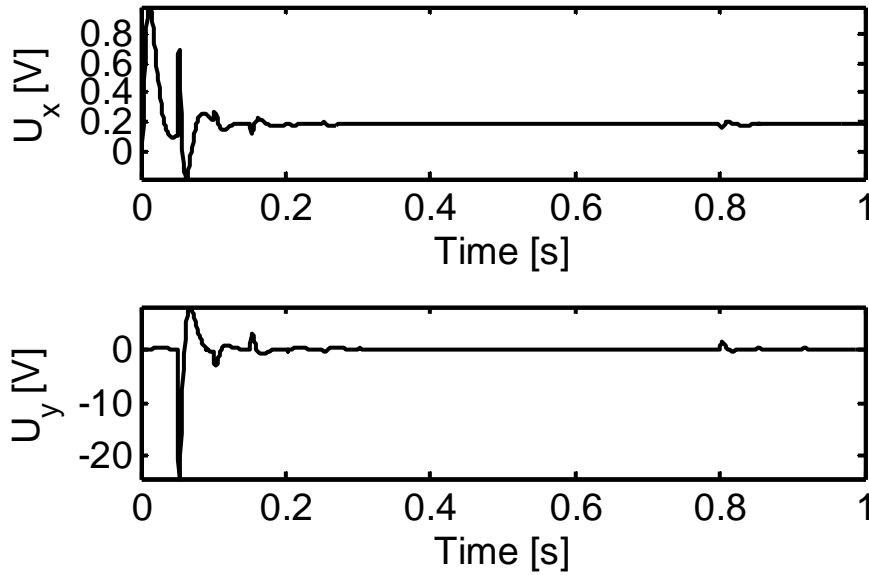
Figure 106 Control Signals (n = 300 rpm)

The simulation results for *n*=420 rpm are shown in Figure 107-Figure 109.
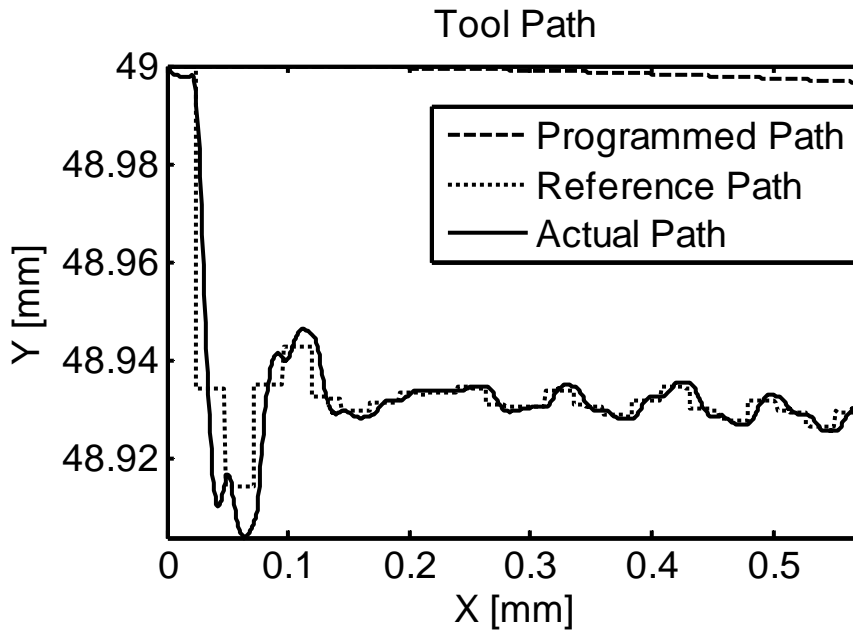
Figure 107 Tool Path (n = 420 rpm)
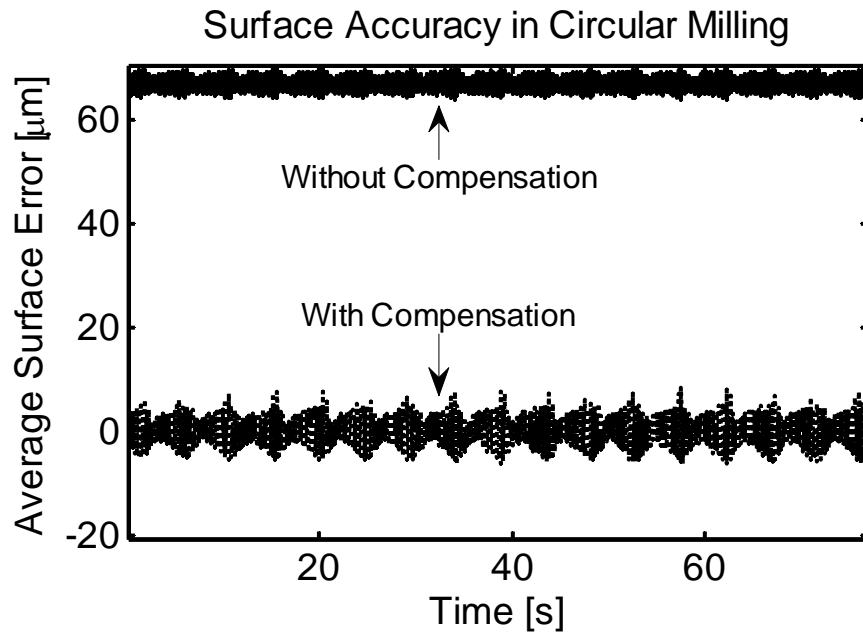
Figure 108 Average Surface Accuracy (n = 420 rpm)
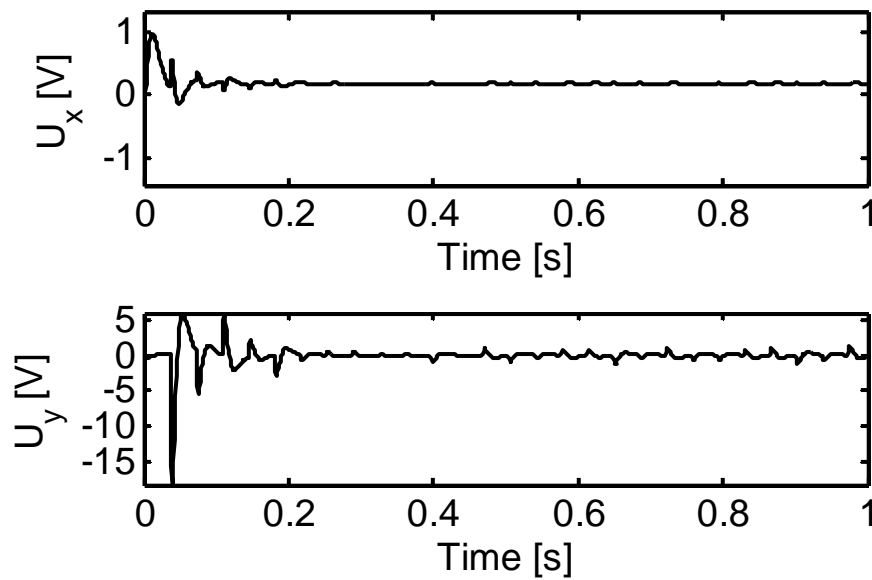
Figure 109 Control Signals (n = 420 rpm)

The simulation results for *n*=540 rpm are shown in Figure 110-Figure 112.
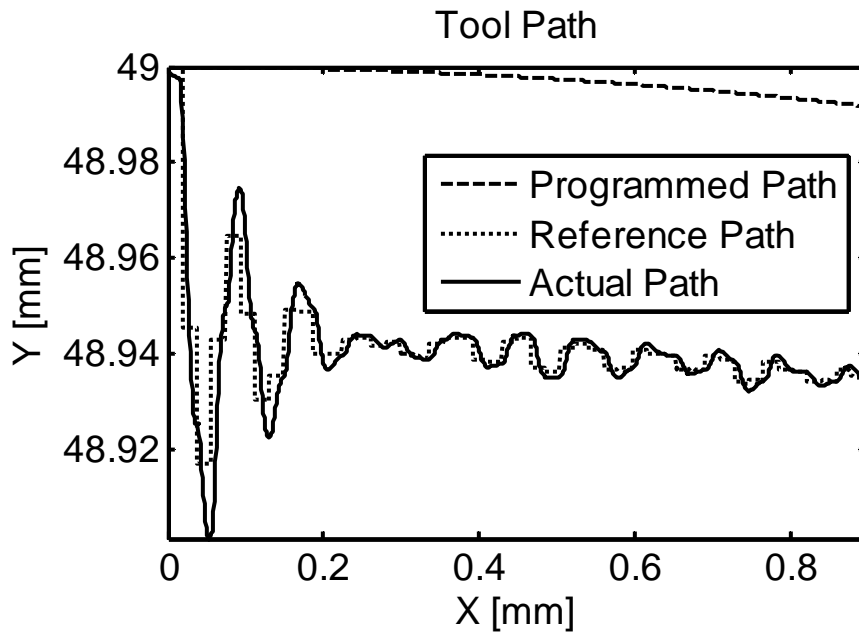
Figure 110 Tool Path (n = 540 rpm)
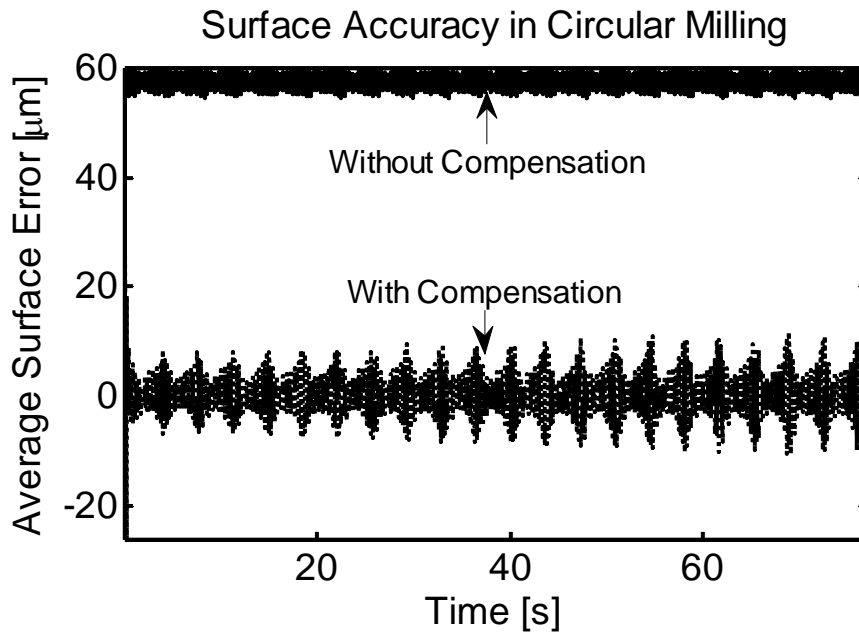
Figure 111 Average Surface Accuracy (n = 540 rpm)
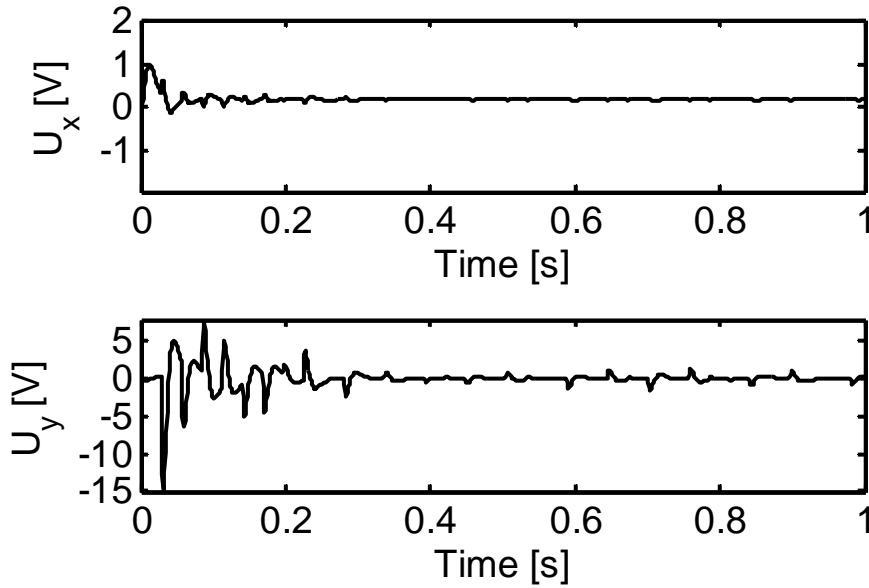
Figure 112 Control Signals (n = 540 rpm)

The simulation results for *n*=660 rpm are shown in Figure 113-Figure 115.
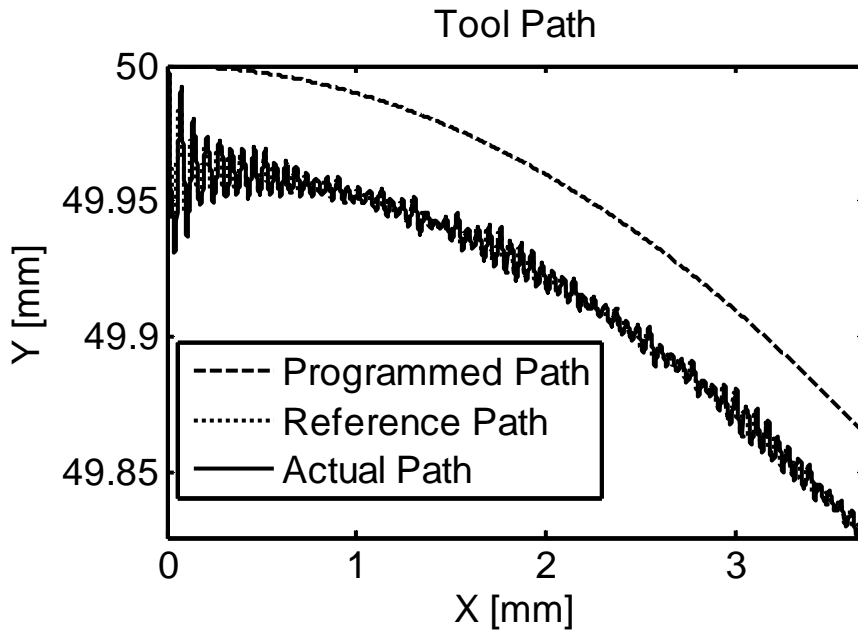
Figure 113 Tool Path (n = 660 rpm)
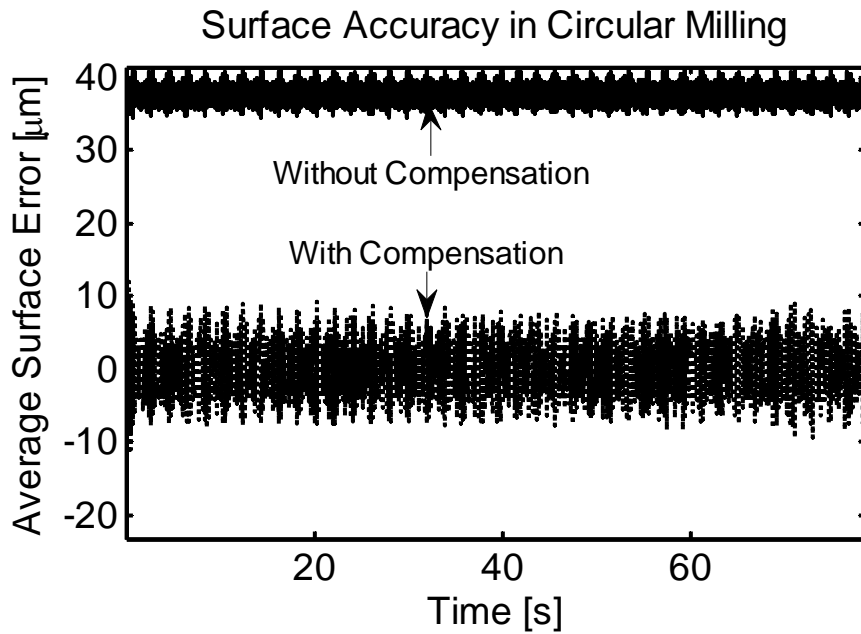
Figure 114 Average Surface Accuracy (n = 660 rpm)

Figure 115 Control Signals (n = 660 rpm)

The third set of simulations is performed to illustrate the improvement of average surface accuracy under four different radial depth of cut of 3, 4, 5, and 6 mm. The other cutting conditions used are the spindle speed $n = 300$ rpm, the feedrate $f_r = 50$ mm/min, the workpiece

radius $R_w = 48$ mm, the axial depth of cut $d_a = 15$ mm. The simulation results for d_r=3 mm are shown in Figure 116-Figure 118.
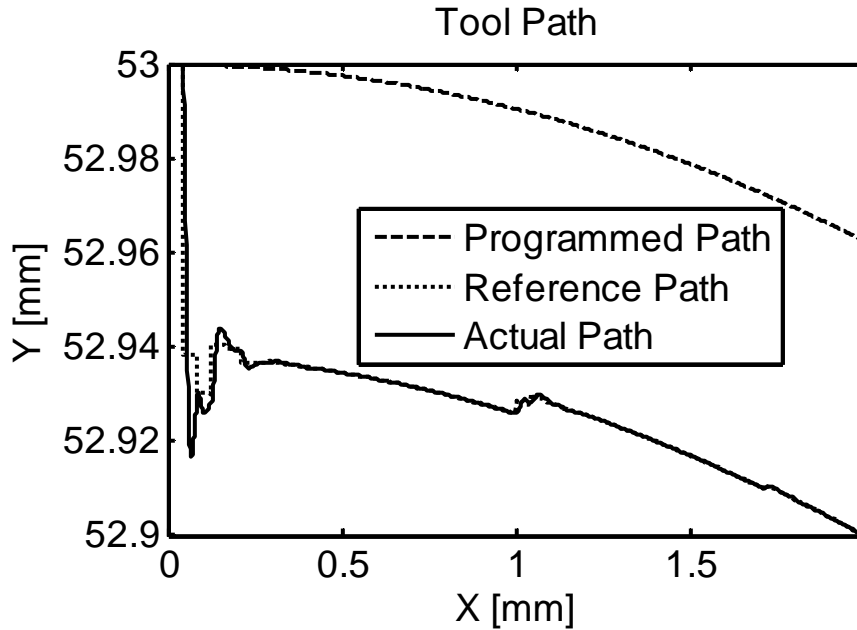
Figure 116 Tool Path (d$_r$ = 3 mm)
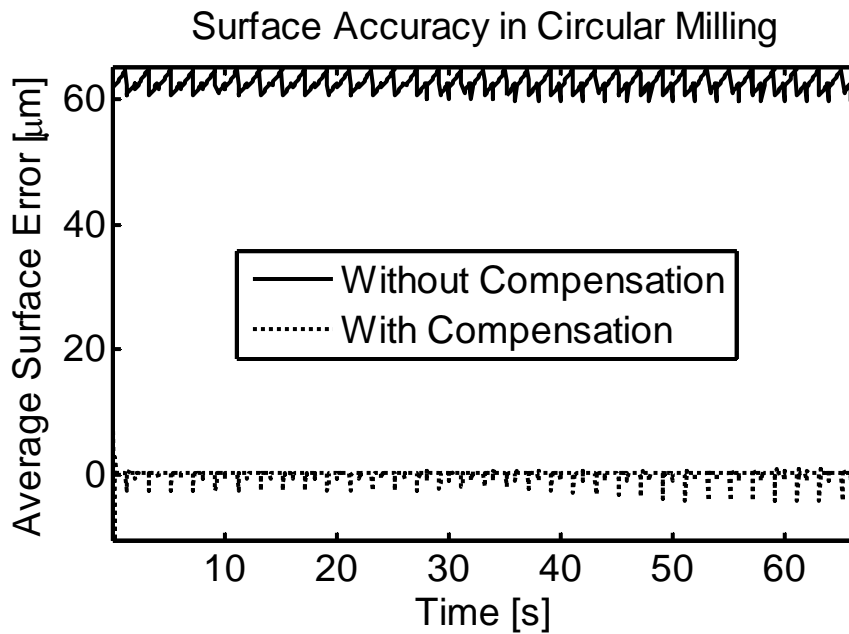
Figure 117 Average Surface Accuracy (d$_r$ = 3 mm)
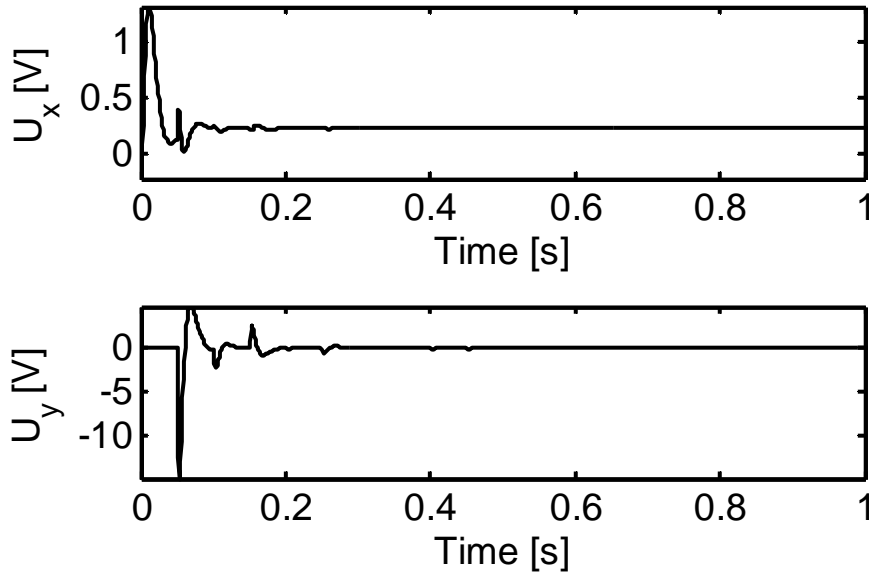
Figure 118 Control Signals (d$_r$ = 3 mm)

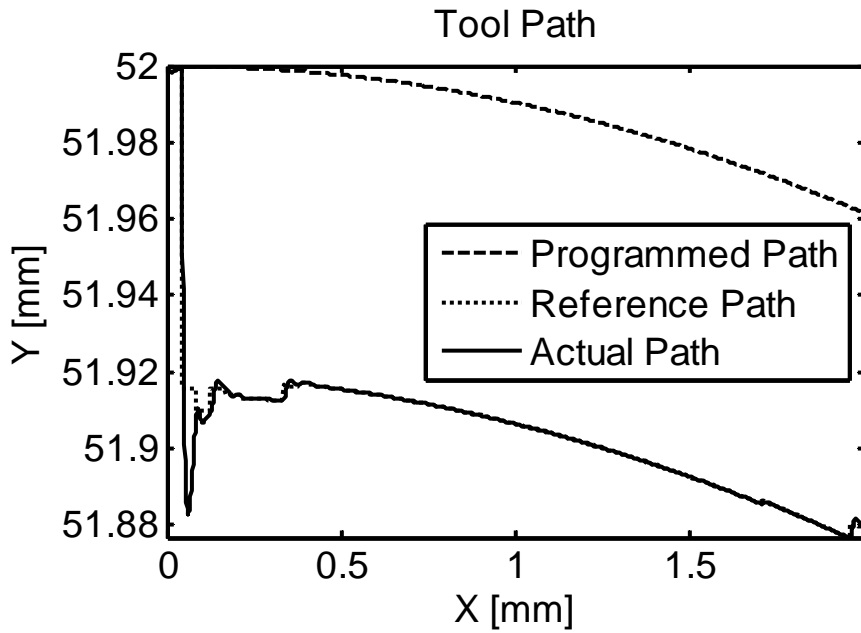The simulation results for d$_r$=4 mm are shown in Figure 119-Figure 121.
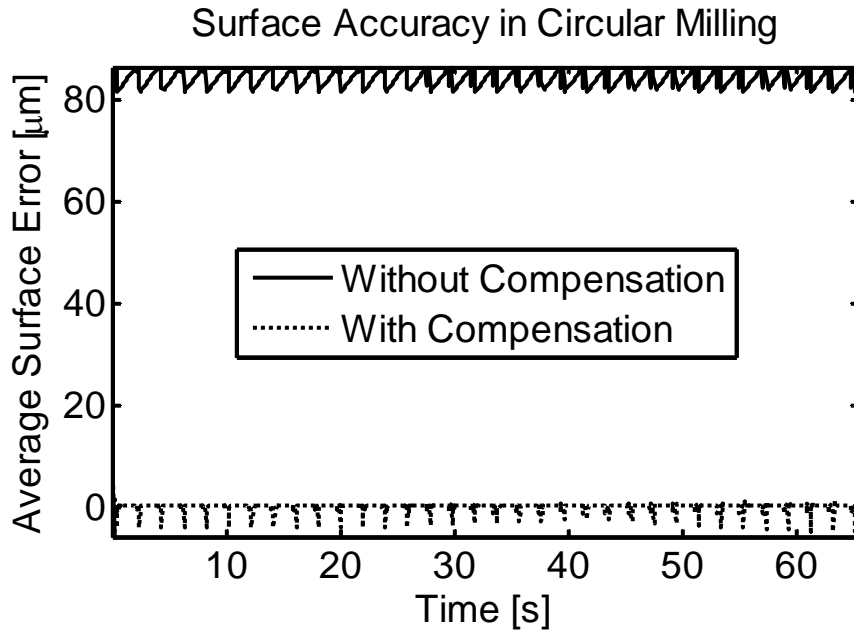

Figure 119 Tool Path (d$_r$ = 4 mm)

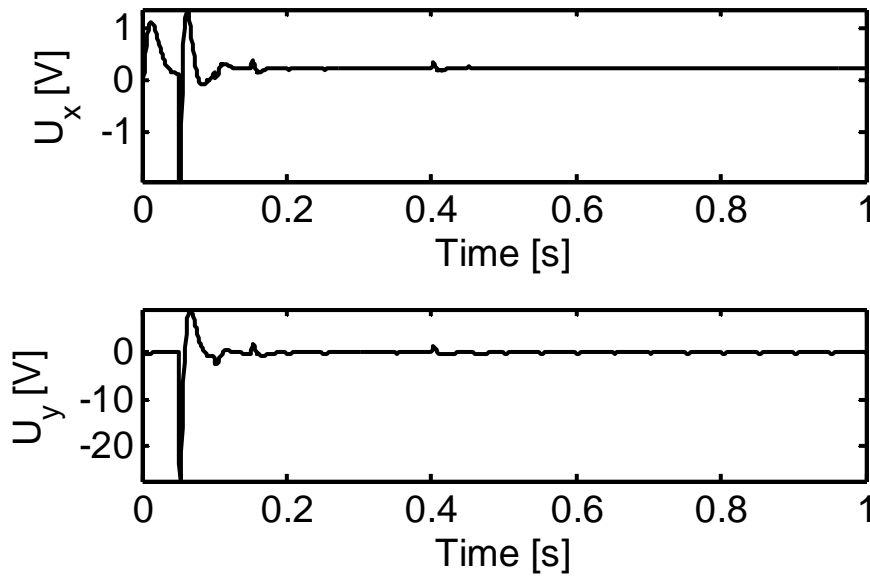**Figure 120 Average Surface Accuracy (d$_r$ = 4 mm)**

Figure 121 Control Signals (d$_r$ = 4 mm)

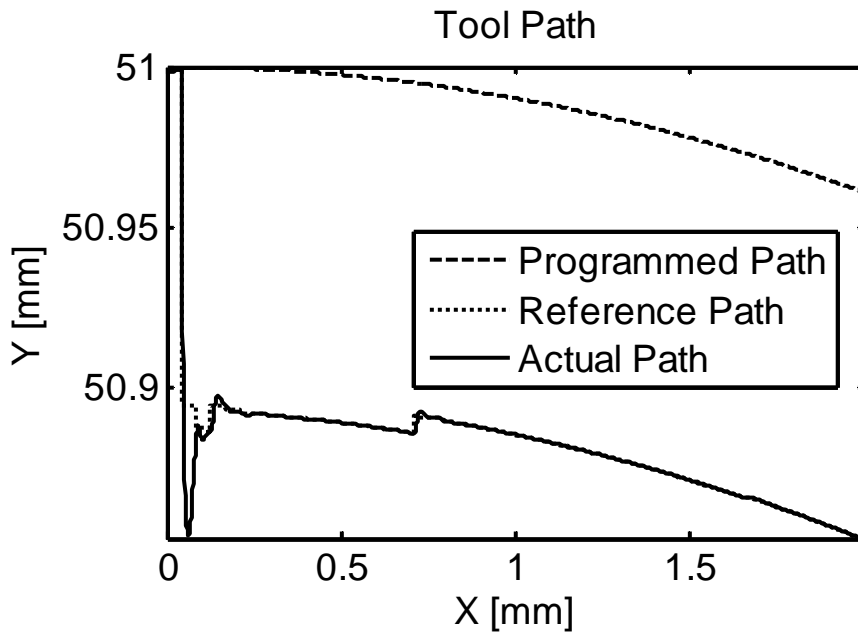The simulation results for d$_r$=5 mm are shown in Figure 122-Figure 124.
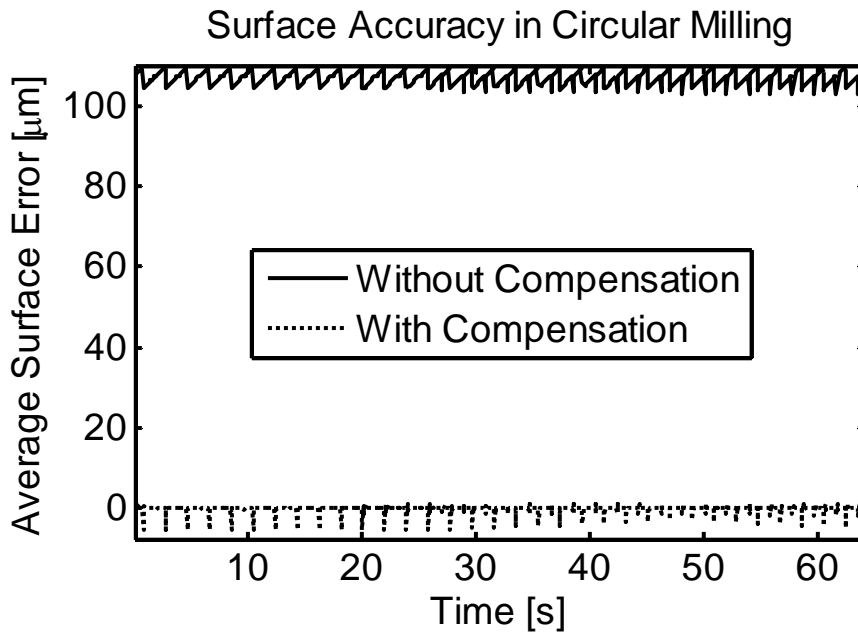
Figure 122 Tool Path (d_r = 5 mm)

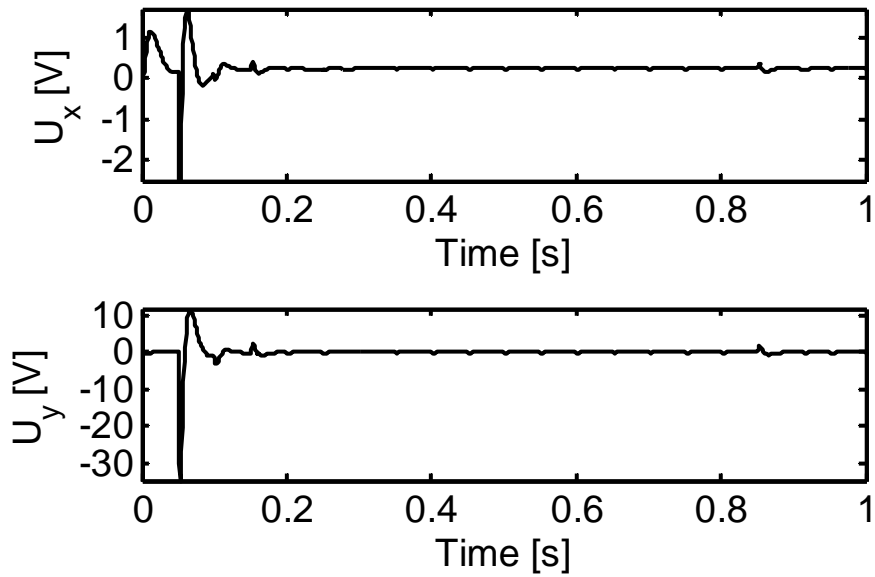**Figure 123 Average Surface Accuracy (d_r = 5 mm)**

Figure 124 Control Signals (d$_r$ = 5 mm)

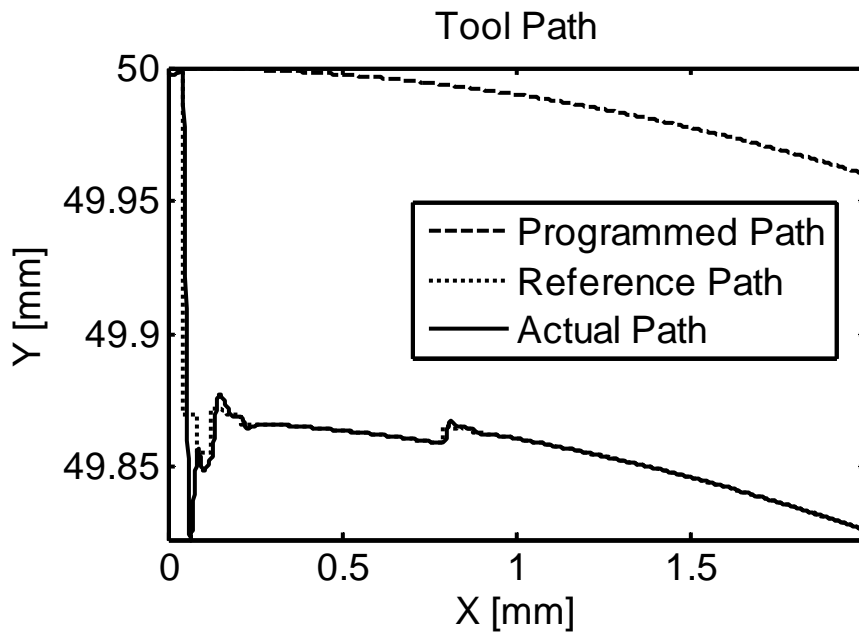The simulation results for d$_r$=6 mm are shown in Figure 125-Figure 127.
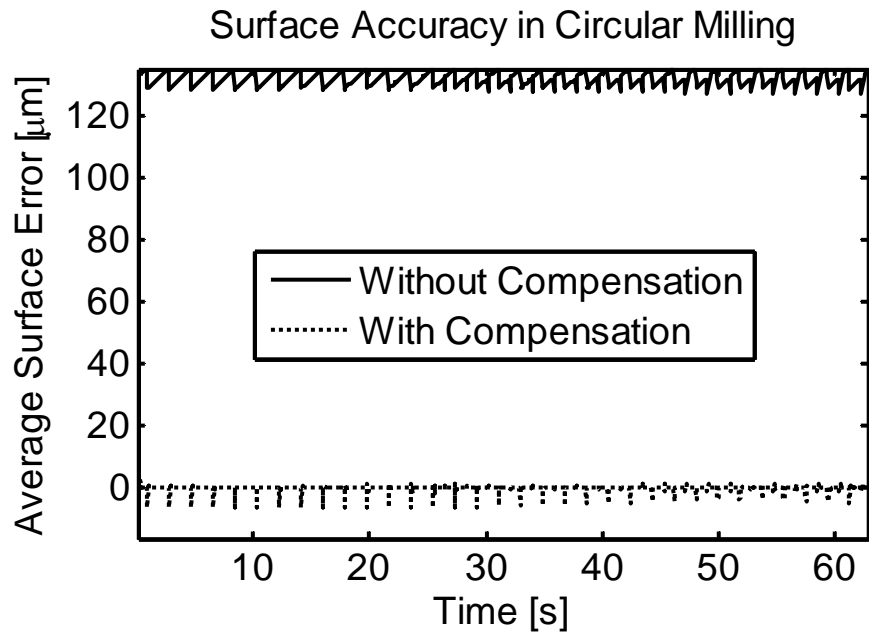

Figure 125 Tool Path (d$_r$ = 6 mm)

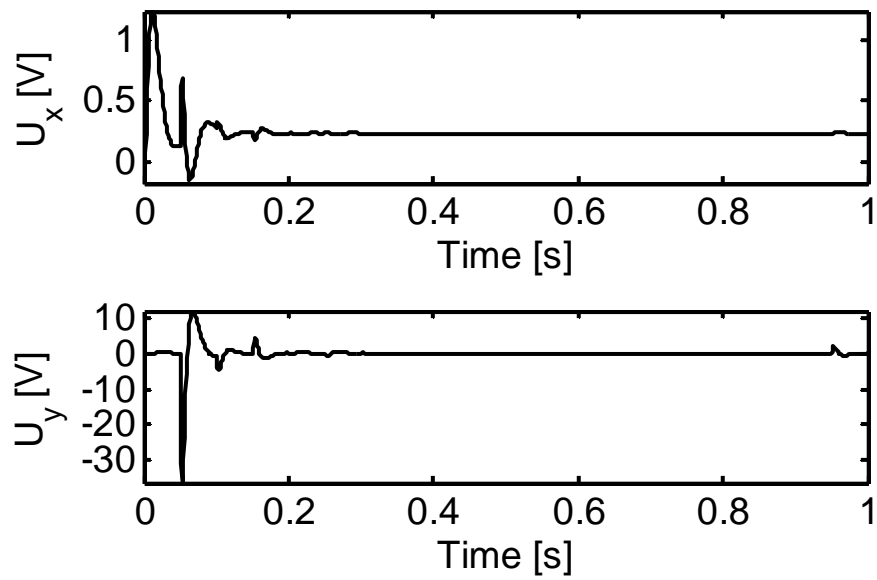**Figure 126 Average Surface Accuracy (d_r = 6 mm)**

Figure 127 Control Signals (d_r = 6 mm)

5.4.3 Milling of Free Form Surfaces

In the simulation studies of free form surface milling, the effect of the interpolation and deflection compensation approach will be evaluated under variation in cutting conditions including the spindle speed, the feed rate, and the radial depth of cut. Since the logarithmic spiral curve is widely used in turbine blades and impellers, it is adopted as an example of free form surface. The logarithmic spiral used in the simulation is represented by parametric equations given in equation (115) where $a = 0.048$, $b = 0.5$, and θ is measured from the positive y-axis. The first set of simulations is performed to illustrate the improvement of average surface accuracy under four different feed rates of 25, 35, 50, and 65 mm/min. The other cutting conditions used are $n = 300$ rpm, $d_r = 5$ mm, and $d_a = 15$ mm. The simulation results for f_r=25 mm/min are shown in Figure 128-Figure 130.

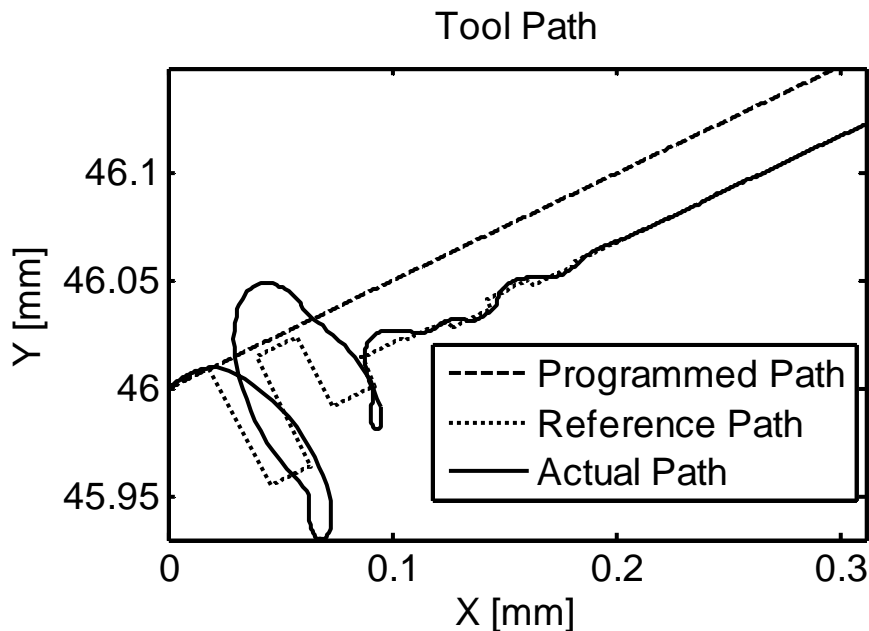
Figure 128 Tool Path (f$_r$ = 25 mm/min)

Figure 129 Average Surface Accuracy (f$_r$ = 25 mm/min)

Figure 130 Control Signals (f$_r$ = 25 mm/min)

The simulation results for f$_r$=35 mm/min are shown Figure 131-Figure 133.

Figure 131 Tool Path (f_r = 35 mm/min)

Figure 132 Average Surface Accuracy (f_r = 35 mm/min)
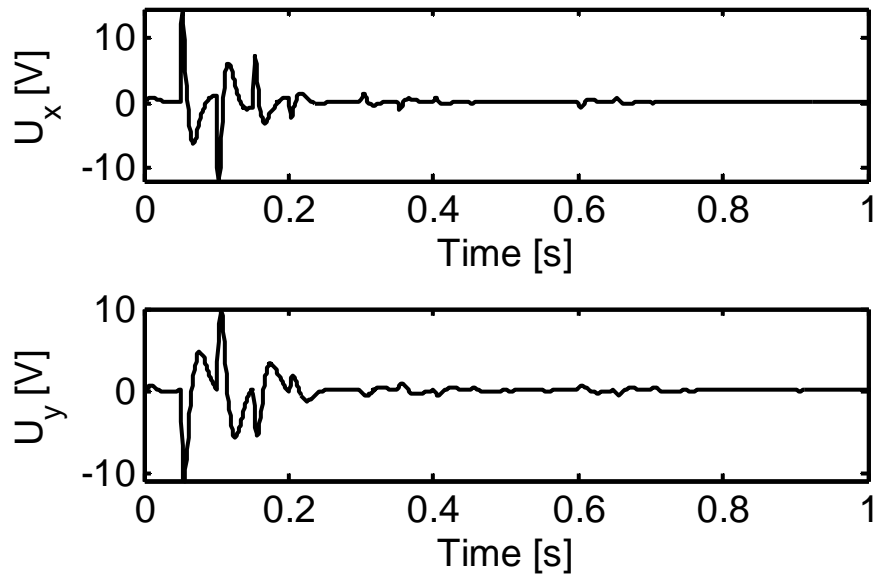
Figure 133 Control Signals (fr = 35 mm/min)

The simulation results for f_r=50 mm/min are shown Figure 134-Figure 136.
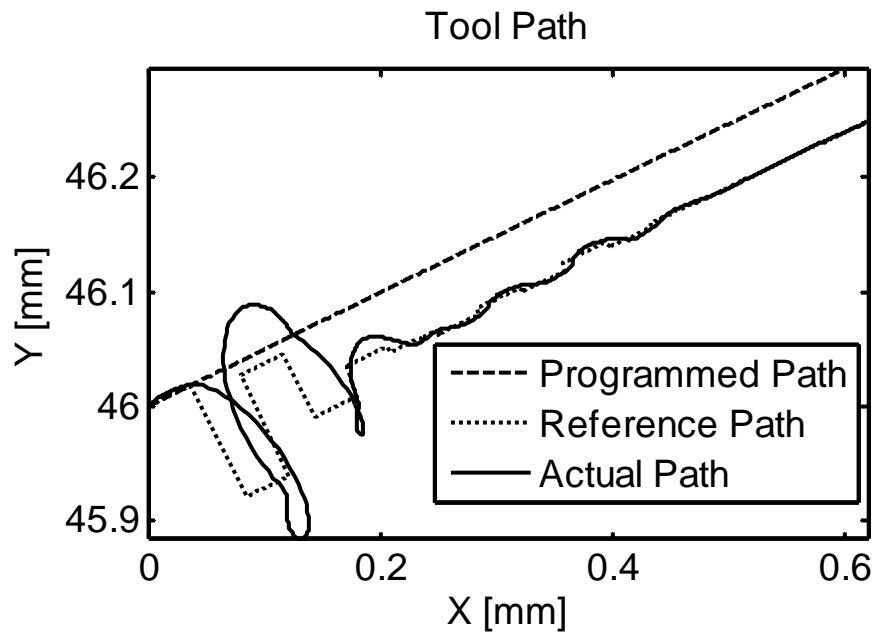
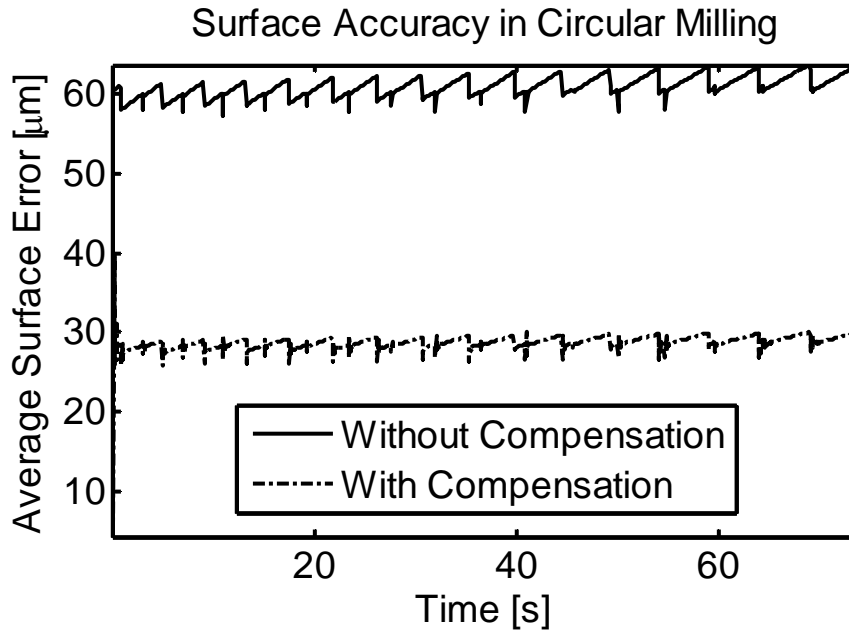**Figure 134 Tool Path (f$_r$ = 50 mm/min)**
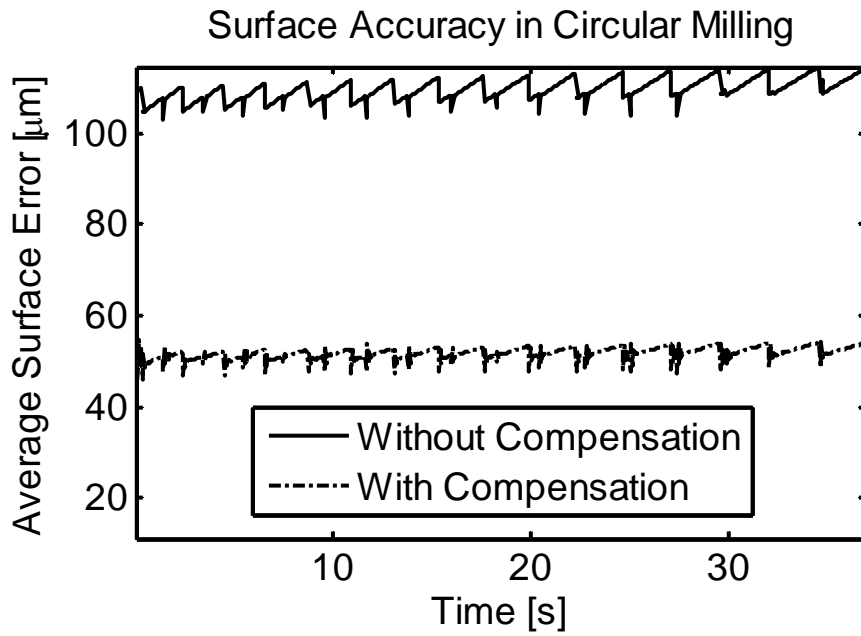
Figure 135 Average Surface Accuracy (f$_r$ = 50 mm/min)
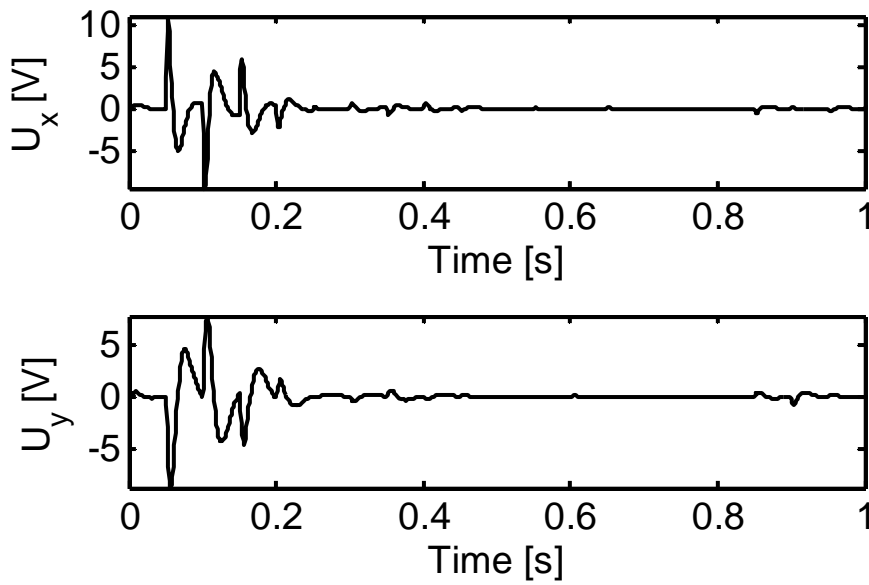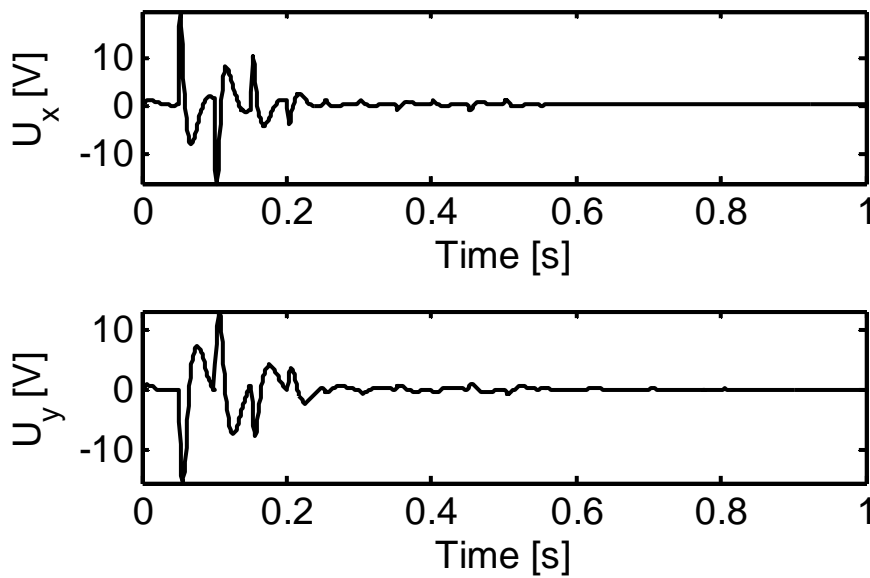

Figure 136 Control Signals (f$_r$ = 50 mm/min)

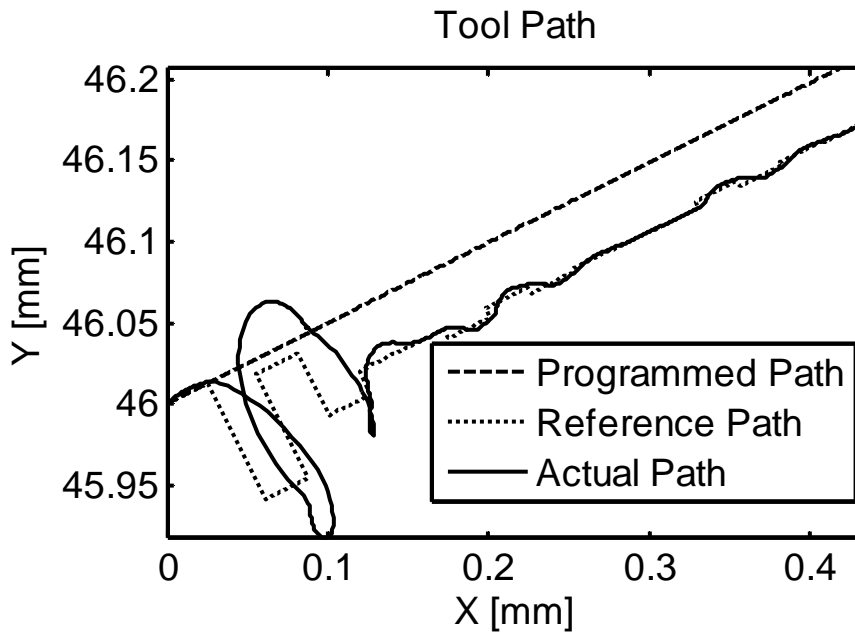The simulation results for f$_r$=65 mm/min are shown Figure 137-Figure 139.
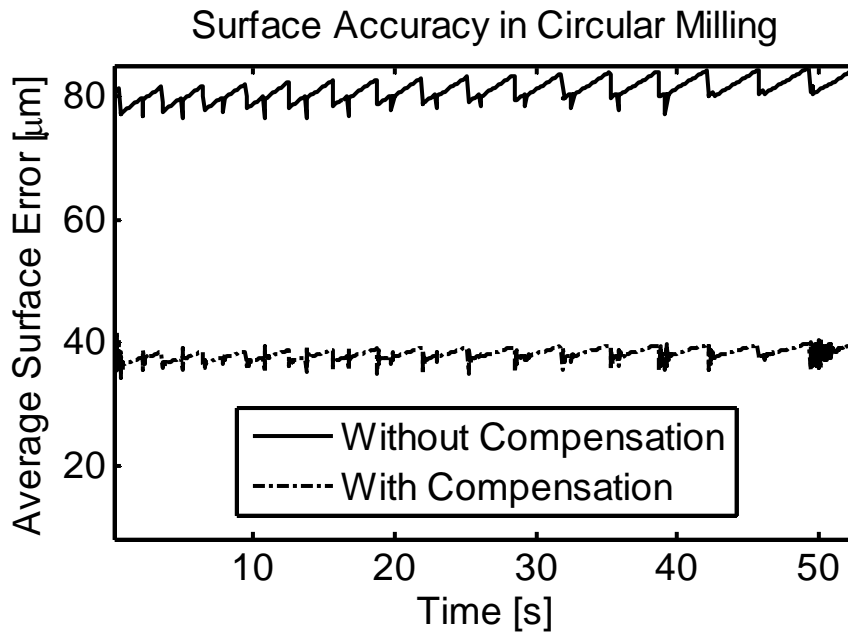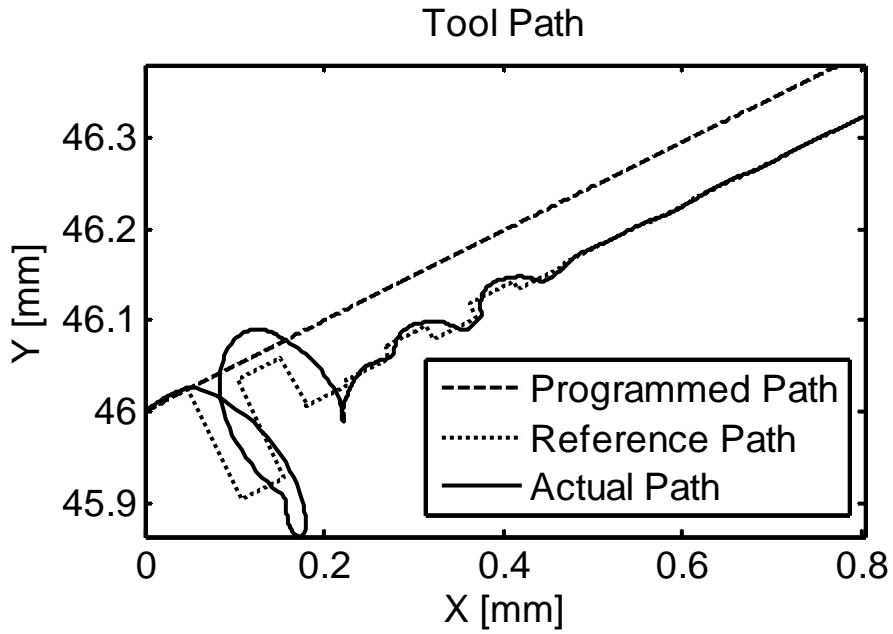
Figure 137 Tool Path (f$_r$ = 65 mm/min)
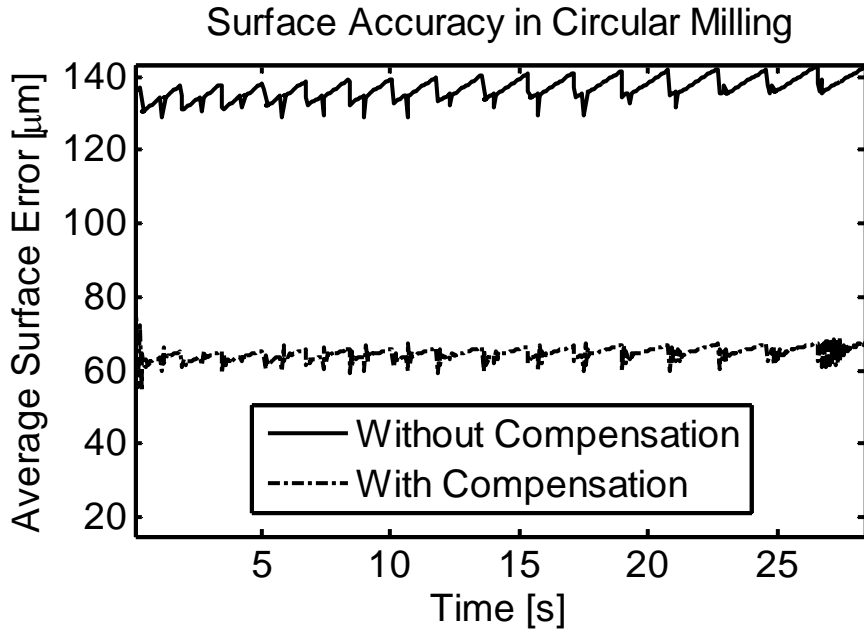
Figure 138 Average Surface Accuracy (f$_r$ = 65 mm/min)
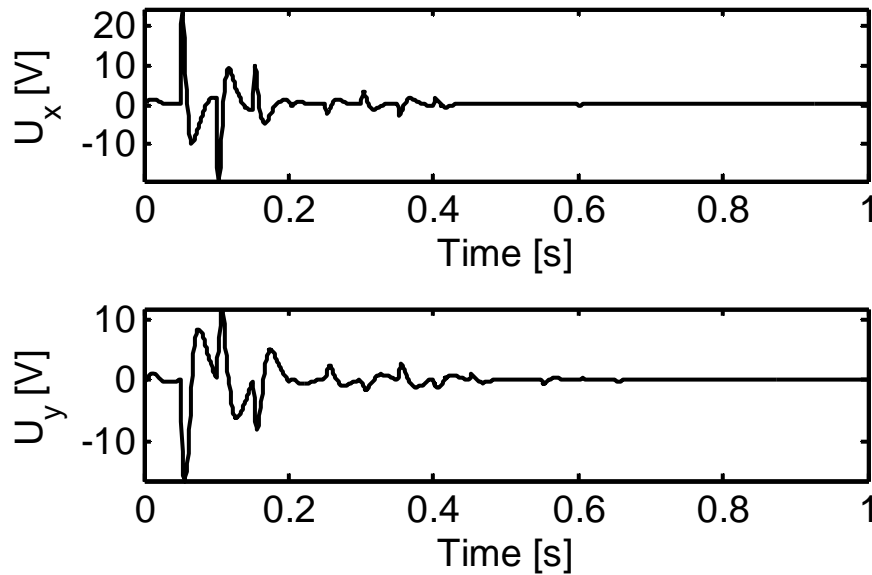
Figure 139Control Signals (f$_r$ = 65 mm/min)

The second set of simulations is performed to illustrate the improvement of average surface accuracy under four different spindle speeds of 300, 420, 540, and 650 rpm. The other cutting conditions used are $f_r = 40$ mm/min, $d_r = 5$ mm, and $d_a = 15$ mm. The simulation results for n=300 rpm are shown in Figure 140-Figure 142.
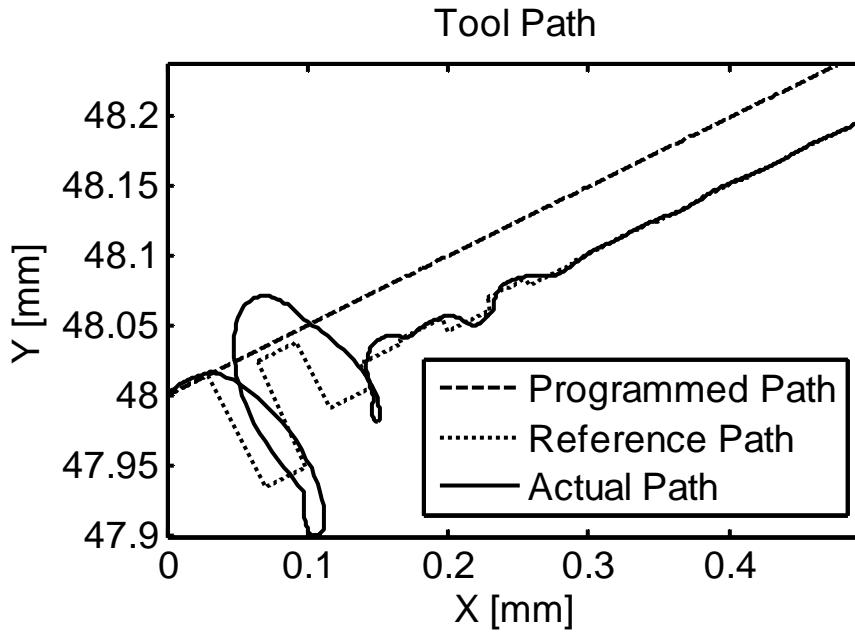
Figure 140 Tool Path (n = 300 rpm)
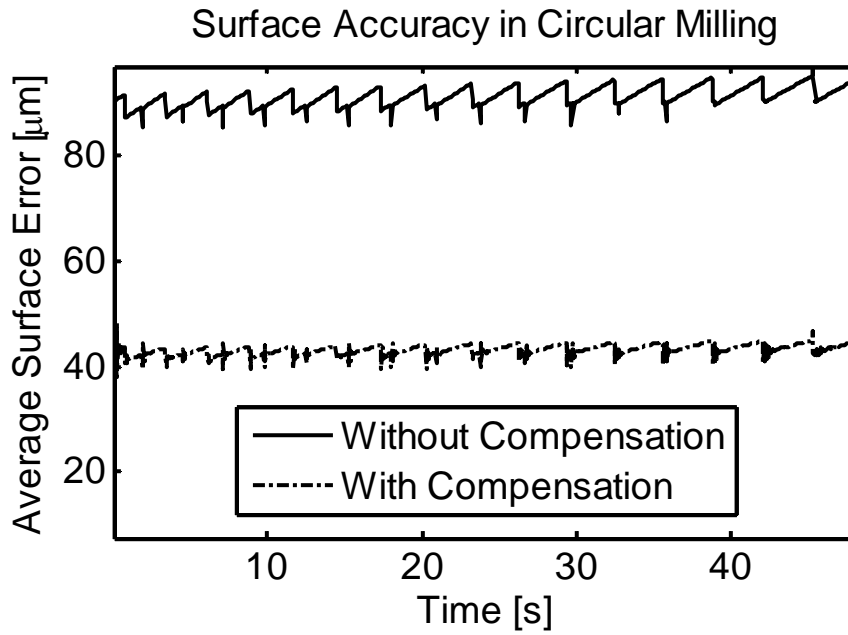
Figure 141 Average Surface Accuracy (n = 300 rpm)
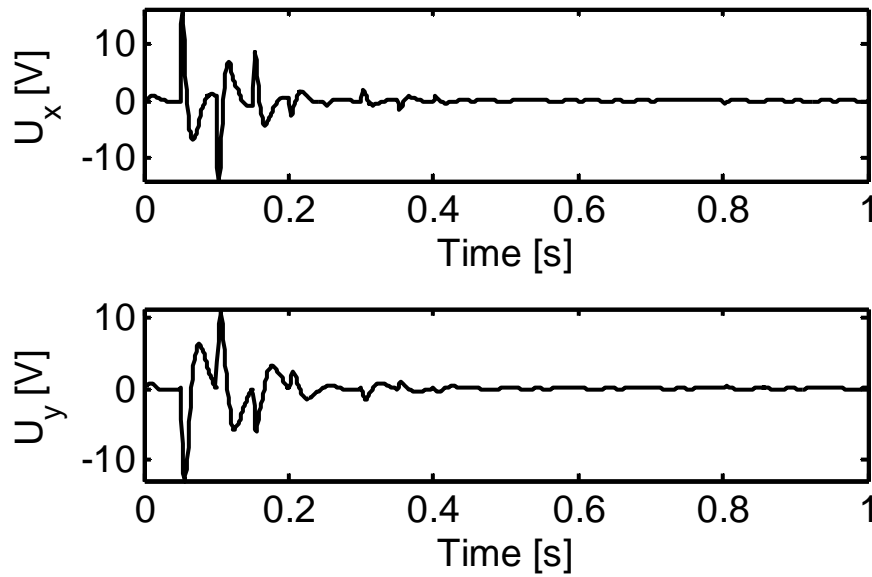
Figure 142 Control Signals (n = 300 rpm)

The simulation results for *n*=420 rpm are shown in Figure 143-Figure 145.
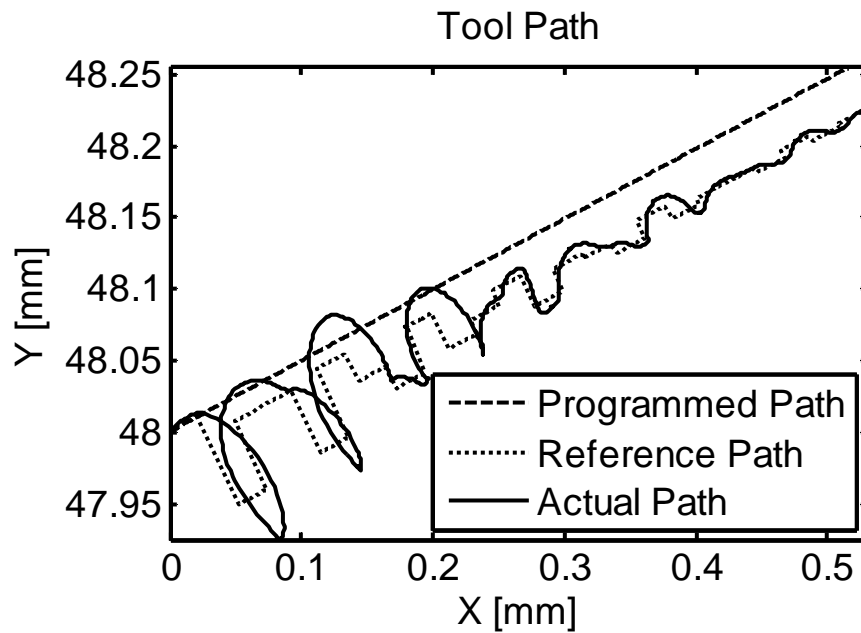
Figure 143 Tool Path (n = 420 rpm)
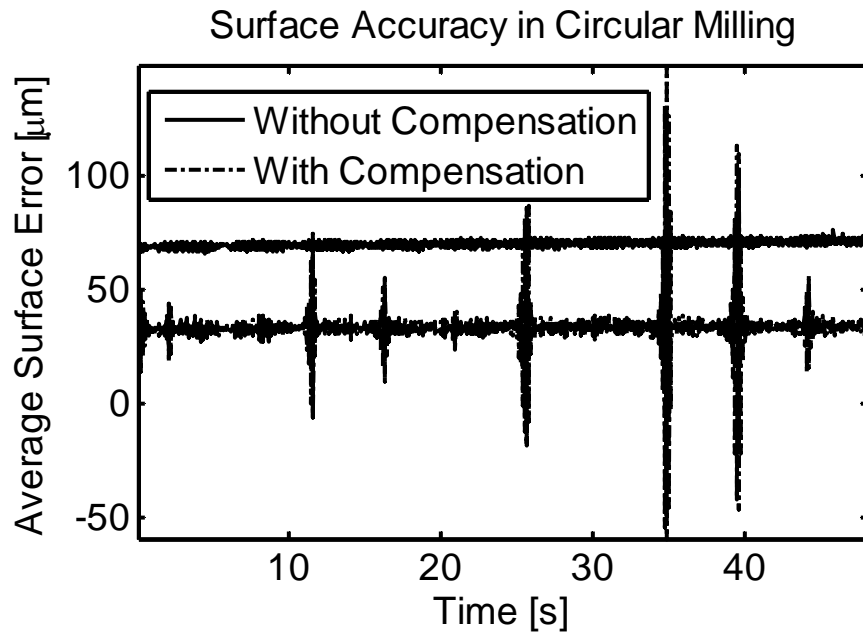
Figure 144 Average Surface Accuracy (n = 420 rpm)
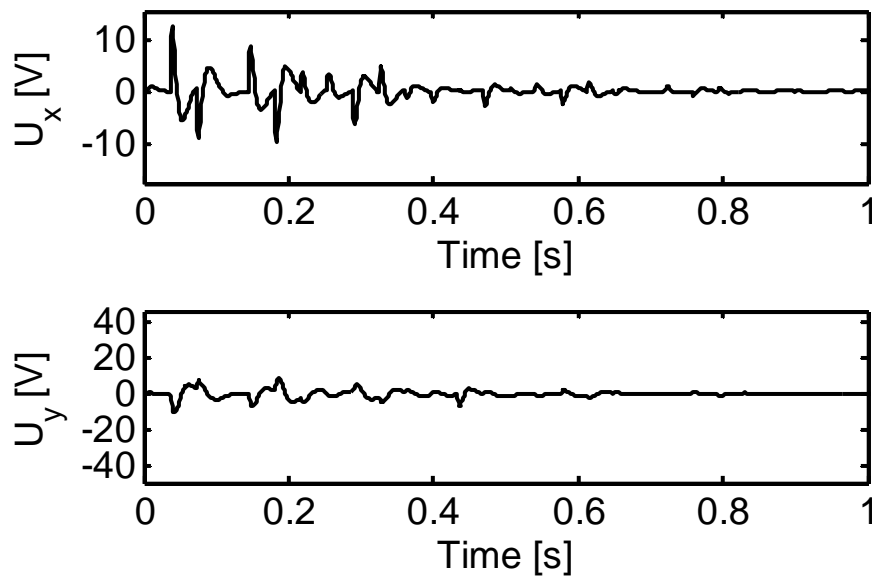
Figure 145 Control Signals (n = 420 rpm)

For n=540 rpm and n=650 rpm, the system is unstable, and the compensation scheme

failed. The possible reason is that the spindle speed is too fast for the servomechanism to shift

155

the tool path since for the compensation is implemented for each tooth pass $T = 1/(nN_t)$. This trend can be observed from the oscillation in the results for n = 420 rpm.

The third set of simulations is performed to illustrate the improvement of average surface accuracy under four different radial depth of cut of 3, 4, 5, and 6 mm. The other cutting conditions used are the spindle speed $n = 300$ rpm, the feedrate $f_r = 50$ mm/min, and the axial depth of cut $d_a = 15$ mm. The simulation results for d$_r$=3 mm are shown in Figure 146-Figure 148.
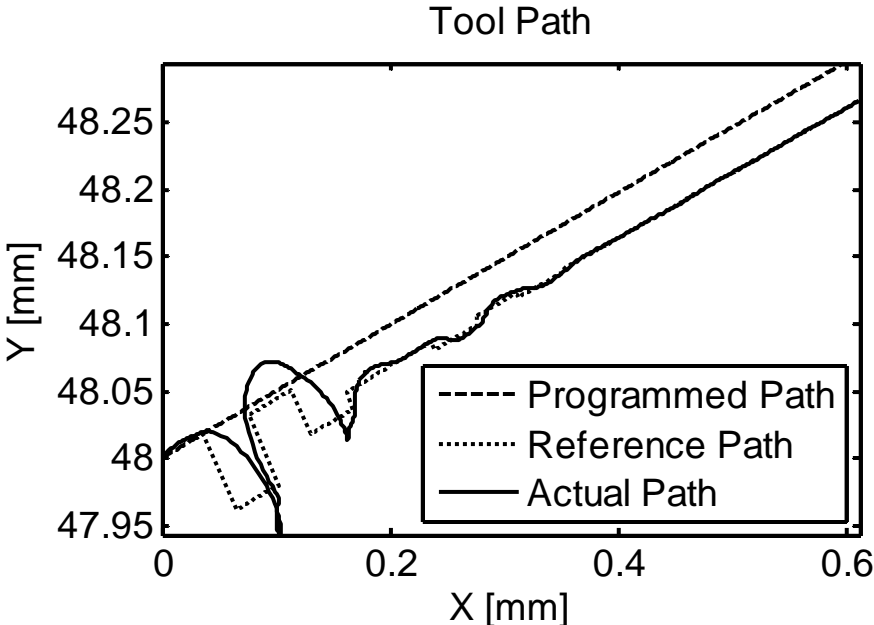
Figure 146 Tool Path (d$_r$ = 3 mm)
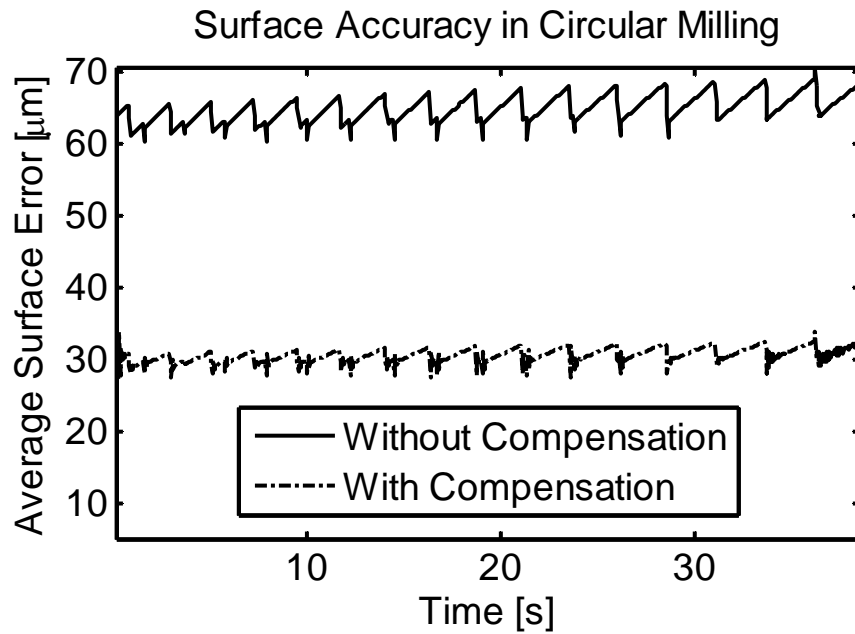
Figure 147 Average Surface Accuracy (d_r = 3 mm)
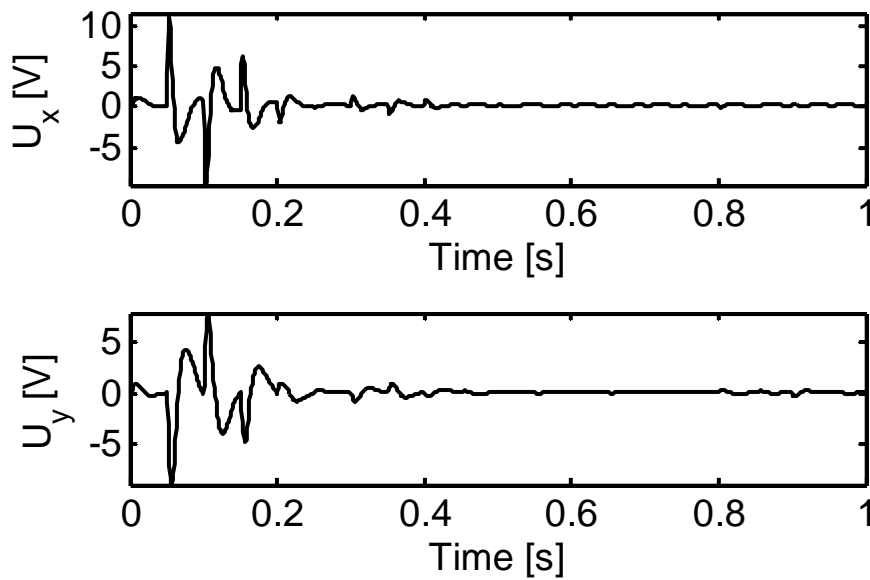
Figure 148 Control Signals (d_r = 3 mm)

The simulation results for d_r=4 mm are shown in Figure 149-Figure 151.

157
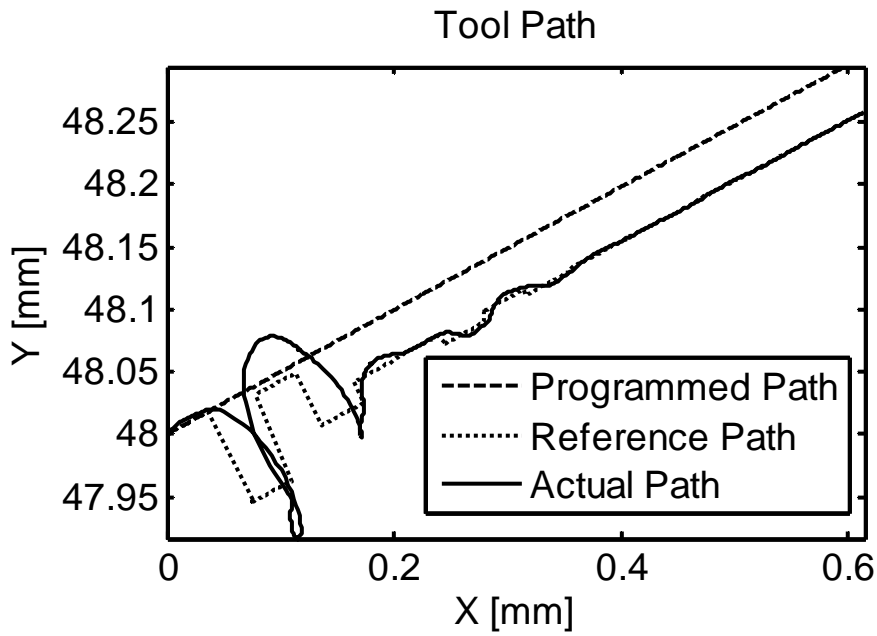
Figure 149 Tool Path (d$_r$ = 4 mm)
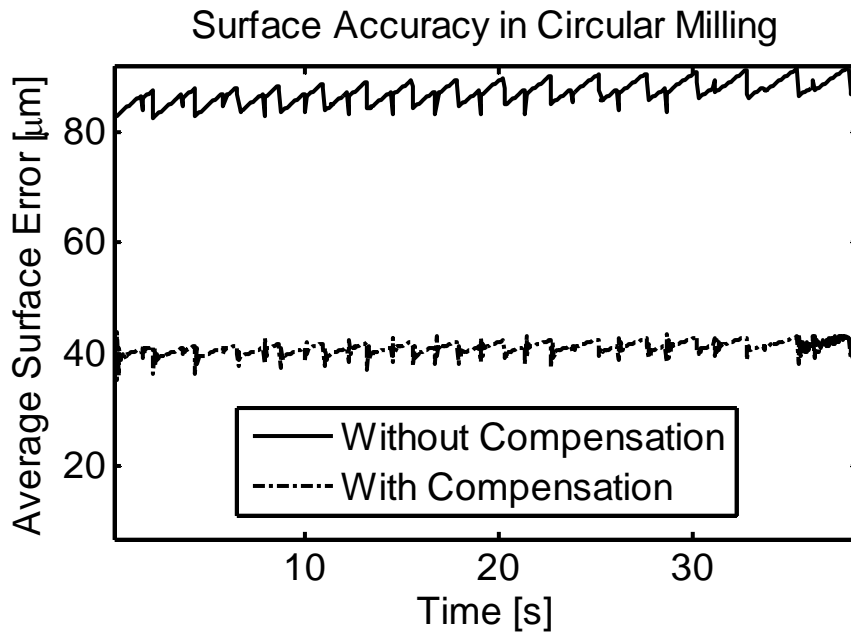
Figure 150 Average Surface Accuracy (d$_r$ = 4 mm)
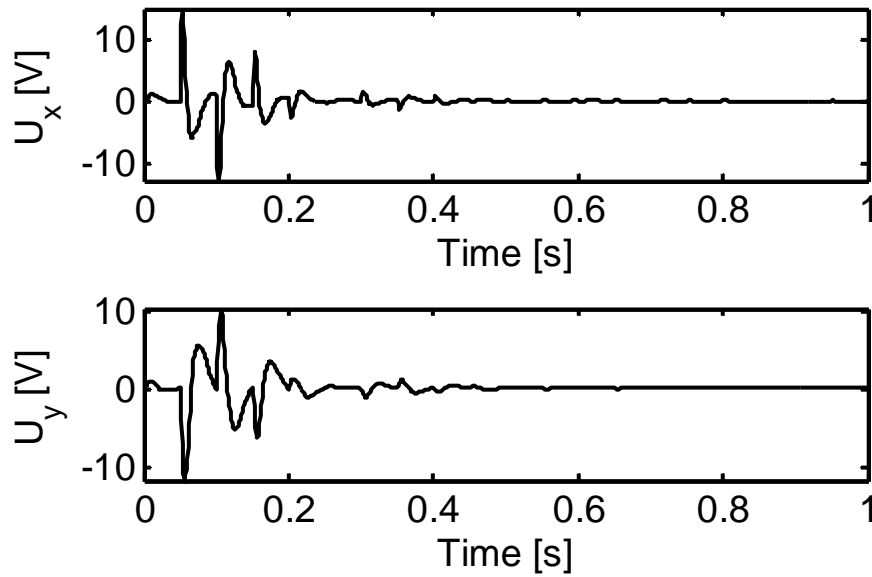
Figure 151 Control Signals (d_r = 4 mm)

The simulation results for d_r=5 mm are shown in Figure 152-Figure 154.
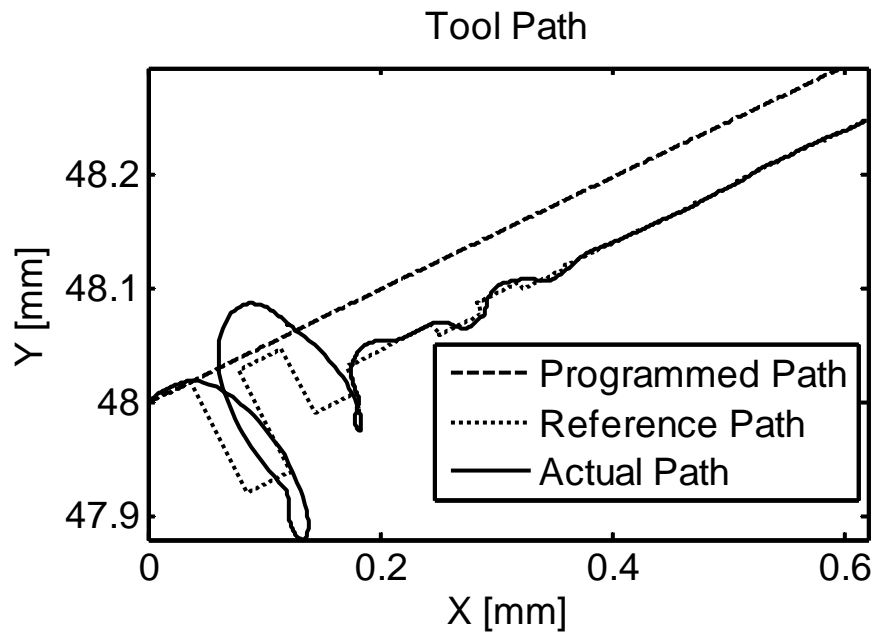
Tool Path

Figure 152 Tool Path (d_r = 5 mm)

159
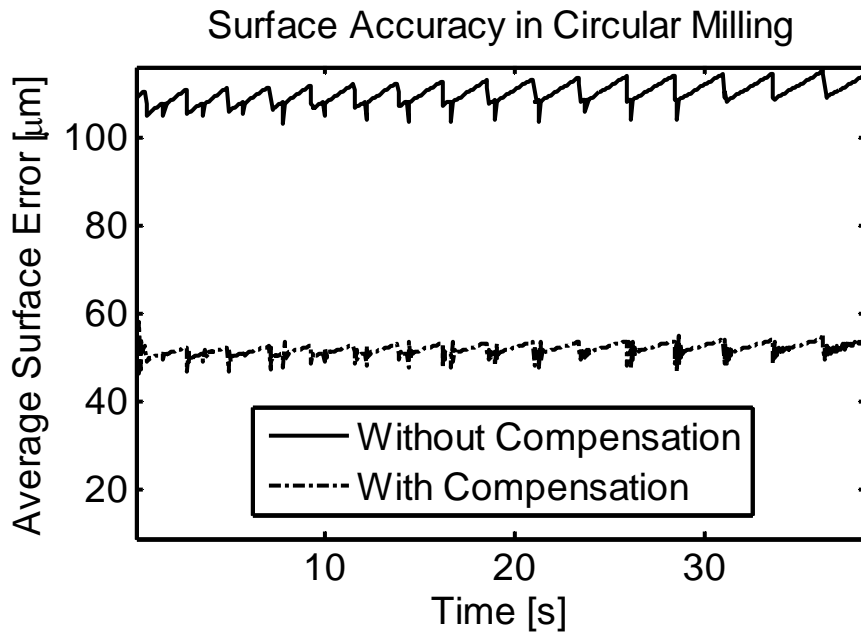
Figure 153 Average Surface Accuracy (d_r = 5 mm)
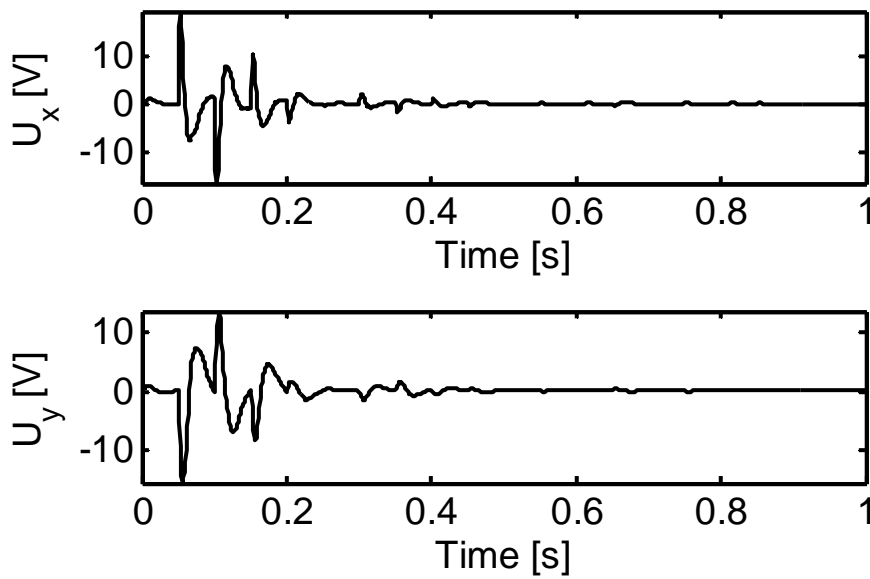
Figure 154 Control Signals (d_r = 5 mm)

The simulation results for d_r=6 mm are shown in Figure 155-Figure 157.
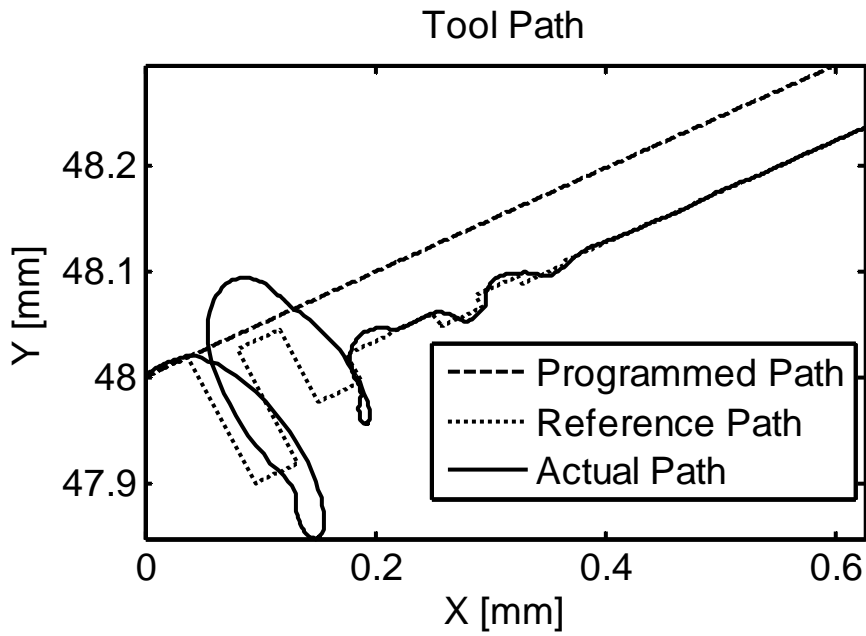
Tool Path

Figure 155 Tool Path (d_r = 6 mm)

Surface Accuracy in Circular Milling
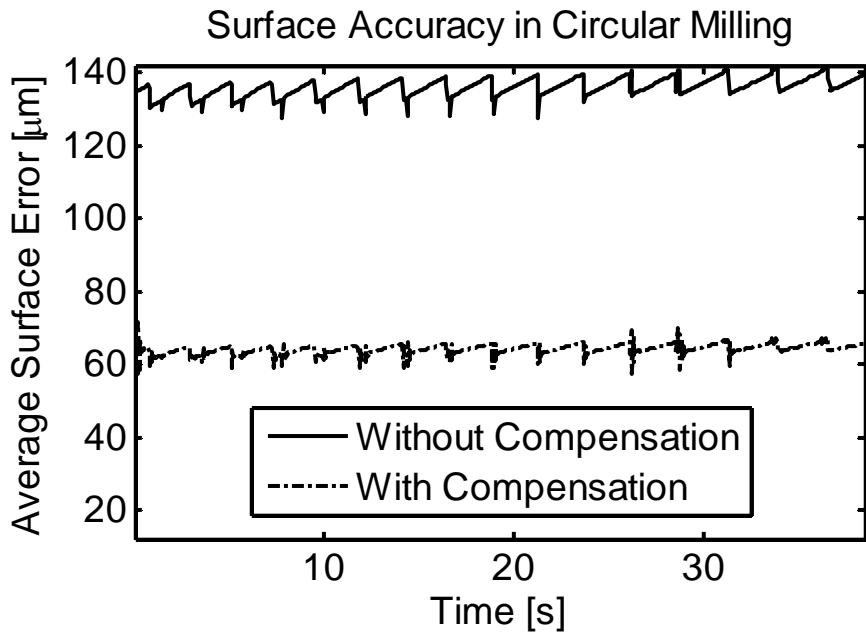
Figure 156 Average Surface Accuracy (d_r = 6 mm)
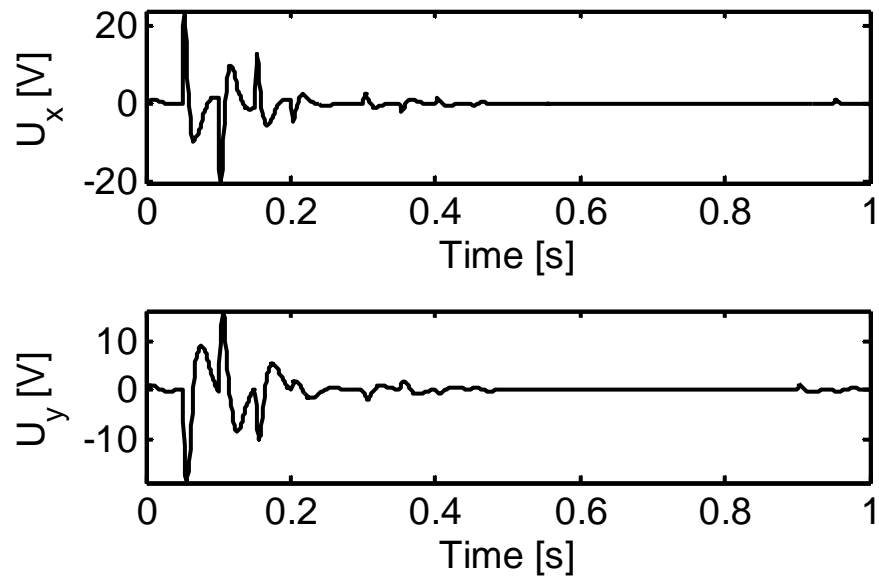
Figure 157 Control Signals (d$_r$ = 6 mm)

5.5   Summary and Conclusions

In this chapter, the online cutter deflection compensation in helical end millings is developed as an example of indirect integration of servomechanism and process control. The helical end mill deflection and its effect on surface accuracy cannot be modeled to be associated with the servomechanism states; therefore, the process control cannot be aggregated with the servomechanism control. The indirect integration is achieved through interpolation. The interpolator modifies the reference trajectory according to the process variation, i.e. surface accuracy in this case, and the servomechanism system will track the updated trajectory to implement cutter deflection compensation.

The cutter deflection compensation is studied for three kinds of workpiece surfaces including straight surface, circular surface, and free form surface. The interpolation scheme is developed first for each surface, and simulations are conducted over a variety of cutting conditions to demonstrate the effectiveness. The simulation results show that the cutter deflection can be well compensated at lower spindle speeds which determines the compensation period. The system is unstable for the spindle speeds higher than 500 rpm. This problem can only be solved by using the fast servomechanism which is capable of shifting the tool path as request.

CHAPTER 6 CONCLUSION AND FUTURE WORK

6.1   Summary and Conclusions

The objective of this research was to develop an integrated scheme for achieving process control and servomechanism control simultaneously for machining processes. The integration was investigated for two scenarios. One scenario is for the machining processes whose parameters can be associated with the servomechanism states and the tool path does not need offset during machining. The other scenario is for the machining processes which do not have direct relationship with servomechanism states and the tool path requires real time offset with the process variations. Different integration schemes for the two scenarios were propose.

A hierarchical optimal control was developed to aggregate the process control into the servomechanism control for the first scenario. The process control goal, maintaining maximum constant cutting forces, is propagated to the servomechanism level by aggregating variation in cutting forces and contour error with servomechanism states. Such aggregation is considered in the formation of the hierarchical optimal controller. The resulting controller can simultaneously achieve maximum cutting force, zero contour error, and servomechanism position control. The control performance and the robustness to parameter variations are tested via simulations for turning operations.

For the second scenario, the interpolation scheme is critical for real time tool path offset. Cutter deflection compensation in helical end milling processes is studied as one example for this case. The surface accuracy affected by cutter deflection is complicated, and cannot be associated with servomechanism states directly. Meanwhile, the tool path needs to be offset during machining to compensate for the surface accuracy error due to cutter deflection. Therefore, an effective interpolation scheme is required to generate the reference trajectory for the

servomechanism system. Interpolation schemes for three commonly used surfaces in milling are developed. The capability of tracking complex trajectory of the servomechanism control guarantees effective path offset to compensate for the surface error due to cutter deflection. The simulations are conducted for different cutting conditions.

The ultimate goal of the research is to provide an integrated servomechanism and process control module which can be bundled with open architecture machine tools. The proposed integrated servomechanism and process control can be used as a customized control module to achieve both servomechanism control and process control. With the advantage of interpolation scheme, motion control robustness and the integration, the proposed controller can be applied in the following machining processes:

(1) The process model can be represented by servomechanism states;

(2) The machining process requires constant tangential velocity;

(3) The tool path offset needs to be perpendicular to the part contour.

6.2   Future Work

As there exist various machining processes, it is impossible and impractical to generate a unified integrated servomechanism and process control scheme. It is encouraged to develop customer specific control strategy to make full use of the flexibility brought by open architecture machine tools. In order to enhance the integration of process control and the servomechanism control, the following future work is recommended:

1) Experimental studies should be conducted to demonstrate the practical effectiveness of the proposed methods;

2) To facilitate the controller design, an appropriate process dynamics model should be investigated under various cutting conditions. For instance, the integrated servo-process controller design for cutter deflection adopts trial-and-error approach to select the pole locations through simulations. The availability of the process dynamics model would provide rational recommendation for the pole locations;

3) Other servomechanism control approach should be studied for the integration with process control. The servomechanism control along with the interpolation scheme addressed in this research is suitable for machining processes requiring constant contour velocity. Other servomechanism control strategies should also be studied to enhance the integration of various process control and servomechanism control.

LIST OF REFERENCES

[1]   A. G. Ulsoy, "Monitoring and Control of Machining," in *Condition Monitoring and Control for Intelligent Manufacturing*, 2006, pp. 1-32.

[2]   S. Y. Liang, R. L. Hecker, and R. G. Landers, "Machining Process Monitoring and Control: The State-of-the-Art," *Journal of Manufacturing Science and Engineering,* vol. 126, pp. 297-310, 2004.

[3]   Y. Altintas, C. Brecher, M. Weck, and S. Witt, "Virtual Machine Tool," *CIRP Annals-Manufacturing Technology,* vol. 54, pp. 115-138, 2005.

[4]   K. Yoram, "Control of Machine Tools," *Journal of Manufacturing Science and Engineering,* vol. 119, pp. 749-755, 1997.

[5]   R. G. Landers, "Error Space Motion Control Methodology for Complex Contours," *Asian Journal of Control,* vol. 7, pp. 20-28, 2005.

[6]   Y. Koren, "Cross-coupled biaxial computer control for manufacturing systems," *ASME Journal of Dynamic Systems, Measurement, and Control,* vol. 102, p. 265?72, 1980.

[7]   A.-N. Poo, J. G. Bollinger, and G. W. Younkin, "Dynamic Errors in Type 1 Contouring Systems," *Industry Applications, IEEE Transactions on,* vol. IA-8, pp. 477-484, 1972.

[8]   Y. Koren, "Interpolator for a CNC System," *IEEE Transactions on Computers,* vol. 25, p. 32?7, 1976.

[9]   H. Bin, K. Yamazaki, and M. DeVries, "A Microprocessor-Based Control Scheme for the Improvement of Contouring Accuracy," *Annals of the CIRP,* vol. 32, pp. 275-279, 1983.

[10]   R. Doraiswami and A. Gulliver, "Control strategy for computer numerical control machine exhibiting precision and rapidity," *J. DYN. SYST. MEAS. CONTROL.,* vol. 106, pp. 56-62, 1984.

[11]   F. de Schepper, K. Yamazaki, T. Shigemura, M. Imai, and T. Hoshi, "Development of an Asic Performing High Speed Current Loop Processing of Servo Motor Control for Mechatronics Applications," *CIRP Annals - Manufacturing Technology,* vol. 38, pp. 355-358, 1989.

[12]   G. Pritschow and W. Philipp, "Direct drives for high-dynamic machine tool axes," *Annals of the CIRP,* vol. 39, pp. 413-416, 1990.

[13]   H. Makino and T. Ohde, "Motion control of the direct drive actuator," *Annals of the CIRP,* vol. 40, p. 1991, 1991.

[14]   S. Jee and Y. Koren, "Adaptive fuzzy logic controller for feed drives of a CNC machine tool," *Mechatronics,* vol. 14, pp. 299-326, 2004.

[15]   M. Tomizuka, "Zero phase error tracking algorithm for digital control," *J. DYN. SYST. MEAS. CONTROL.,* vol. 109, pp. 65-68, 1987.

[16]   T. Tsao and M. Tomizuka, "Adaptive zero phase error tracking algorithm for digital control," *J. DYN. SYST. MEAS. CONTROL.,* vol. 109, pp. 349-354, 1987.

[17]   M. Weck and G. Ye, "Sharp Corner Tracking Using the IKF Control Strategy," *CIRP Annals - Manufacturing Technology,* vol. 39, pp. 437-441, 1990.

[18]   B. Haack and M. Tomizuka, "The effect of adding zeroes to feedforward controllers," *Journal of Dynamic Systems, Measurement, and Control,* vol. 113, p. 6, 1991.

[19]   D. Torfs, J. De Schutter, and J. Swevers, "Extended bandwidth zero phase error tracking control of nonminimal phase systems," *Journal of Dynamic Systems, Measurement, and Control,* vol. 114, p. 347, 1992.

[20] M. Tomizuka, M. S. Chen, S. Renn, and T. C. Tsao, "TOOL POSITIONING FOR NONCIRCULAR CUTTING WITH LATHE," *Journal of Dynamic Systems Measurement and Control-Transactions of the Asme,* vol. 109, pp. 176-179, 1987.

[21] T. C. Tsao and M. Tomizuka, "ADAPTIVE ZERO PHASE ERROR TRACKING ALGORITHM FOR DIGITAL-CONTROL," *Journal of Dynamic Systems Measurement and Control-Transactions of the Asme,* vol. 109, pp. 349-354, 1987.

[22] G. Ellis and R. D. Lorenz, "Comparison of motion control loops for industrial applications," in *Industry Applications Conference, 1999. Thirty-Fourth IAS Annual Meeting. Conference Record of the 1999 IEEE*, 1999, pp. 2599-2605 vol.4.

[23] K. Srinivasan and P. Kulkarni, "Cross-coupled control of biaxial feed drive servomechanisms," *Journal of Dynamic Systems, Measurement, and Control,* vol. 112, p. 225, 1990.

[24] Y. Koren and C. C. Lo, "Advanced Controllers for Feed Drives," *CIRP Annals - Manufacturing Technology,* vol. 41, pp. 689-698, 1992.

[25] Y. Koren and C. Lo, "Variable-gain cross-coupling controller for contouring," *Annals of the CIRP,* vol. 40, pp. 371-374, 1991.

[26] R. Landers and S. Balakrishnan, "Hierarchical Optimal Contour-Position Control of Motion Control Systems," 2004, p. 13?9.

[27] Y. Koren, O. Masory, and S. Malkin, "Adaptive Control with Process Estimation," *CIRP Annals - Manufacturing Technology,* vol. 30, pp. 373-376, 1981.

[28] A. Ulsoy, Y. Koren, and F. Rasmussen, "Principal developments in the adaptive control of machine tools," *ASME Journal of Dynamic Systems, Measurement, and Control,* vol. 105, pp. 107-112, 1983.

[29]   S. J. Rober, Y. C. Shin, and O. D. I. Nwokah, "A Digital Robust Controller for Cutting Force Control in the End Milling Process," *Journal of Dynamic Systems, Measurement, and Control,* vol. 119, pp. 146-152, 1997.

[30]   S. I. Kim, R. G. Landers, and A. G. Ulsoy, "Robust Machining Force Control With Process Compensation," *Journal of Manufacturing Science and Engineering,* vol. 125, pp. 423-430, 2003.

[31]   L. Harder, *Cutting Force Control in Turning: Solutions and Possibilities*: Royal Institute of Technology, Department of Materials Processing, Production Engineering, 1995.

[32]   R. G. Landers and A. G. Ulsoy, "Model-Based Machining Force Control," *Journal of Dynamic Systems, Measurement, and Control,* vol. 122, pp. 521-527, 2000.

[33]   Y. Tarng, S. Hwang, and Y. Wang, "A neural network controller for contrast for constant turning force," *International Journal of Machine Tools & Manufacture,* vol. 34, pp. 453-460, 1994.

[34]   P. Hsu and W. Fann, "Fuzzy adaptive control of machining processes with a self-learning algorithm," *Journal of Manufacturing Science and Engineering,* vol. 118, p. 522, 1996.

[35]   R. Landers, A. Ulsoy, and Y. Ma, "A comparison of model-based machining force control approaches," *International Journal of Machine Tools and Manufacture,* vol. 44, pp. 733-748, 2004.

[36]   B. Pandurangan, R. Landers, and S. Balakrishnan, "Hierarchical optimal force-position control of a turning Process," *IEEE Transactions on Control Systems Technology,* vol. 13, pp. 321-327, 2005.

[37]   N. T. D. T. C. a. W. B. Company, "Use of Short End Mills Reduces Deflection," *Metal Cuttings,* vol. 3, 1956.

[38]   W. A. Kline and R. E. DeVor, "The effect of runout on cutting geometry and forces in end milling," *International Journal of Machine Tool Design & Research,* vol. 23, pp. 123-140, 1983.

[39]   W. A. Kline, R. E. DeVor, and J. R. Lindberg, "The Prediction of Cutting Forces in End Milling with Applications to Cornering Cuts," *International Journal of Machine Tool Design & Research,* vol. 22, p. 7, 1982.

[40]   J. W. Sutherland and R. E. DeVor, "An improved method for cutting force and surface error prediction in flexible end milling systems," *Journal of Engineering for Industry,* vol. 108, p. 269, 1986.

[41]   R. E. DeVor, W. A. Kline, and W. J. Zdeblick, "A Mechanistic Model for the Force System in End Milling with Applications to Machining Airframe Structures," in *Eighth North American Manufacturing Research Conference*, 1980, p. 297.

[42]   W. A. Kline, R. E. DeVor, and I. A. Shareef, "The Prediction of Surface Accuracy in End Milling " *Journal of Engineering For Industry, ASME,* vol. 104, pp. 272-278, 1982.

[43]   M. E. Martellotti, "An Analysis of the Milling Process," *Transactions of the ASME,* vol. 63, pp. 667-700, 1941.

[44]   J. Tlusty and P. Macneil, "Dynamics of cutting forces in end milling," *CIRP Annals - Manufacturing Technology,* vol. 24, pp. 21-25, 1975.

[45]   C. Sim and M. Yang, "The prediction of the cutting force in ball-end milling with a flexible cutter," *International Journal of Machine Tools and Manufacture,* vol. 33, pp. 267-284, 1993.

[46]   Y. S. Tarng and S. T. Cheng, "Fuzzy control of feed rate in end milling operations," *International Journal of Machine Tools and Manufacture,* vol. 33, pp. 643-650, 1993.

[47]   Y. Altintas, "Direct adaptive control of end milling process," *International Journal of Machine Tools and Manufacture,* vol. 34, pp. 461-472, 1994.

[48]   E. Budak and Y. Altintas, "Peripheral milling conditions for improved dimensional accuracy," *International Journal of Machine Tools and Manufacture,* vol. 34, pp. 907-918, 1994.

[49]   Z. Yazar, K.-F. Koch, T. Merrick, and T. Altan, "Feed rate optimization based on cutting force calculations in 3-axis milling of dies and molds with sculptured surfaces," *International Journal of Machine Tools and Manufacture,* vol. 34, pp. 365-377, 1994.

[50]   K. M. Y. Law, A. Geddam, and V. A. Ostafiev, "A process-design approach to error compensation in the end milling of pockets," *Journal of Materials Processing Technology,* vol. 89-90, pp. 238-244, 1999.

[51]   K. M. Y. Law and A. Geddam, "Prediction of contour accuracy in the end milling of pockets," *Journal of Materials Processing Technology,* vol. 113, pp. 399-405, 2001.

[52]   K. M. Y. Law and A. Geddam, "Error compensation in the end milling of pockets: a methodology," *Journal of Materials Processing Technology,* vol. 139, pp. 21-27, 2003.

[53]   T. Watanabe and S. Iwai, "A control system to improve the accuracy of finished surface in milling," *ASME Journal of Dynamic Systems, Measurement, and Control,* vol. 105, pp. 192-199, 1983.

[54]   M. Y. Yang and J. G. Choi, "A tool deflection compensation system for end milling accuracy improvement," *Journal of Manufacturing Science and Engineering-Transactions of the Asme,* vol. 120, pp. 222-229, 1998.

[55]   P. V. Saturley and A. D. Spence, "Integration of Milling Process Simulation with On-Line Monitoring and Control," *The International Journal of Advanced Manufacturing Technology,* vol. 16, pp. 92-99, 2000.

172

[56]   B. DENKENA, H.-C. MÖHRING, and J. C. WILL, "Tool deflection compensation with an adaptronic milling spindle," in *International Conference on Smart Machining Systems ICSMS*, 2007.

[57]   B. Denkena, O. Gummer, C. Will, and F. Hackeloer, "Compensation of Static and Dynamic Tool Deflections during Milling Processes by an Adaptronic Spindle System," 2008.

[58]   V. S. Rao and P. V. M. Rao, "Tool deflection compensation in peripheral milling of curved geometries," *International Journal of Machine Tools & Manufacture,* vol. 46, pp. 2036-2043, 2006.

[59]   C.-C. Lo and C.-Y. Hsiao, "A method of tool path compensation for repeated machining process," *International Journal of Machine Tools and Manufacture,* vol. 38, pp. 205-213, 1998.

[60]   T. I. Seo and M. W. Cho, "Tool trajectory generation based on tool deflection effects in flat-end milling process (I) - Tool path compensation strategy," *Ksme International Journal,* vol. 13, pp. 738-751, 1999.

[61]   T. I. Seo and M. W. Cho, "Tool trajectory generation based on tool deflection effects in the flat-end milling process (II) - Prediction and compensation of milled surface errors," *Ksme International Journal,* vol. 13, pp. 918-930, 1999.

[62]   M. W. Cho and T. I. Seo, "Machining error compensation using radial basis function network based on CAD/CAM/CAI integration concept," *International Journal of Production Research,* vol. 40, pp. 2159-2174, 2002.

[63]   S. Ratchev, S. Liu, W. Huang, and A. A. Becker, "Milling error prediction and compensation in machining of low-rigidity parts," *International Journal of Machine Tools and Manufacture,* vol. 44, pp. 1629-1641, 2004.

[64]   V. S. Rao and P. V. M. Rao, "Modelling of tooth trajectory and process geometry in peripheral milling of curved surfaces," *International Journal of Machine Tools and Manufacture,* vol. 45, pp. 617-630, 2005.

[65]   V. Rao and P. Rao, "Effect of workpiece curvature on cutting forces and surface error in peripheral milling," *Proceedings of the Institution of Mechanical Engineers, Part B: Journal of Engineering Manufacture,* vol. 220, pp. 1399-1407, 2006.

[66]   T. A. Dow, E. L. Miller, and K. Garrard, "Tool force and deflection compensation for small milling tools," *Precision Engineering,* vol. 28, pp. 31-45, 2004.

[67]   G. F. Franklin, J. D. Powell, and A. Emami-Naeini, *Feedback control of dynamic systems*. Upper Saddle River, N.J.: Pearson Prentice Hall, 2006.

[68]   F. Lewis and V. Syrmos, *Optimal control*: Wiley-Interscience, 1995.

[69]   K. Srinivasan and T. C. Tsao, "Machine Tool Feed Drives and Their Control---A Survey of the State of the Art," *Journal of Manufacturing Science and Engineering,* vol. 119, pp. 743-748, 1997.

[70]   R. G. Landers, "Supervisory machining control: A design approach plus chatter analysis and force control components," United States -- Michigan: University of Michigan, 1997.

[71]   J. E. Sandoval, R. G. Landers, and A. G. Ulsoy, "Reconfigurable CNC lathe simulation system," ERC/RMS Technical Report, 2001.

[72]   S. Smith and J. Tlusty, "An Overview of Modeling and Simulation of the Milling Process," *Journal of Engineering for Industry,* vol. 113, pp. 169-175, 1991.

[73]   M. E. Martellotti, "An Analysis of the Milling Process, Part II - Down Milling," *Transactions of the ASME,* vol. 67, pp. 233-251, 1945.

[74]   E. J. A. Armarego and R. H. Brown, *The Machining of Metals*: Prentice-Hall, 1969.

[75] Y. Altintas, *Manufacturing automation : metal cutting mechanics, machine tool vibrations, and CNC design*. New York: Cambridge University Press, 2000.

[76] W. A. Kline, "The Prediciton of Cutting Forces and Surface Accuracy for the End Milling Process," United States -- Illinois: University of Illinois at Urbana-Champaign, 1982.

[77] J. H. Faupel and F. E. Fisher, *Engineering design : a synthesis of stress analysis and materials engineering*. New York: Wiley, 1981.

[78] S. S. Rao, *Mechanical vibrations*. Upper Saddle River, NJ [u.a.]: Prentice Hall, 2004.

[79] L. Zhang, L. Zheng, Z. Zhang, Y. Liu, and Z. Li, "On cutting forces in peripheral milling of curved surfaces," *Proceedings of the Institution of Mechanical Engineers, Part B: Journal of Engineering Manufacture,* vol. 216, pp. 1385-1398, 2002.

[80] K. Erkorkmaz and Y. Altintas, "High speed CNC system design. Part I: jerk limited trajectory generation and quintic spline interpolation," *International Journal of Machine Tools and Manufacture,* vol. 41, pp. 1323-1345, 2001.